ISSN 1316-7081
ISSN Electrónico 2244-8780

CIENCIA e INGENIERÍA

Vicerrectorado Administrativo y
Académico
Mérida, Venezuela

UNIVERSIDAD DE LOS ANDES
(ULA)
Facultad de Ingeniería
Núcleo Universitario
«Pedro Rincón Gutiérrez»
Mérida - Venezuela

Vol. 46 Agosto – Noviembre 2025 No 3

Artículo de Investigación. Revista Ciencia e Ingeniería. Vol. 46, No. 3 pp.227-232, agosto-noviembre,2025.
ISSN 1316-7081. ISSN Elect. 2244-8780 Universidad de los Andes (ULA)

Emulgel as a transport and release system for clove oil (Syzygium aromaticum)

Emulgel como sistema de transporte y liberación del aceite de clavo de olor (*Syzygium aromaticum)*

Velásquez, Ingrid[*1,2]; Fortoul,Vanessa[3]

[1]Laboratorio de Investigación de Tecnología de Suelo y Ambiente, Departamento de Química, Facultad de Ingeniería, Universidad de Carabobo, Valencia, Venezuela.
[2]Laboratorio de Alimentos. Departamento de Química, Facultad Experimental de Ciencia y Tecnología, Universidad de Carabobo, Valencia, Venezuela.
[3]Escuela de Ingeniería Química, Facultad de Ingeniería, Universidad de Carabobo, Valencia, Venezuela

ivvelasquez@uc.edu.ve

Abstract

Clove (Syzygium aromaticum) is a plant that represents a rich source of phenolic compounds such as eugenol, eugenol acetate, and gallic acid. It has great potential for industrial applications due to its antimicrobial, antiviral, anti-inflammatory, hepatoprotective, anti-stress, contraceptive, and anesthetic properties. The essential oils obtained from this plant have direct applications in medicine, aromatherapy, fragrances, and perfumes, among others. To apply this compound, a system is required that not only protects it but also allows its release, thus allowing its diffusion and absorption appropriately, such as creams, lotions, or gels. The compound is obtained by Soxhlet extraction. A prototype emulgel is proposed, using carboxymethylcellulose for the hydrogel formulation and castor oil for the oleogel formulation, placing the extracted oil in one of the phases. The product's physicochemical characteristics were determined, including color, odor, homogeneity and consistency, pH, conductivity, viscosity, swelling index, spreadability, and stability. When evaluating the system, it was found that the bioactive compound within the emulgel could be released under the action of an external stimulus.

Keywords: cloves, emulgel, release system

Resumen

El clavo de olor (Syzygium aromaticum) es una planta que representa una rica fuente de compuestos fenólicos tales como eugenol, acetato de eugenol y ácido gálico, y posee un gran potencial de aplicaciones industriales dada sus propiedades antimicrobianas, antivirales, antiinflamatorias, hepatoprotectivas, anti estrés, anticonceptivas y anestésicas. El uso de los aceites esenciales obtenidos de esta planta tiene aplicaciones directas en medicina, aromaterapia, fragancias, perfumes, entre otras. Para aplicar este compuesto se requiere de un sistema que además de protegerlo permita su liberación, permitiendo así su difusión y absorción de manera apropiada, como cremas, lociones o geles. El compuesto se obtiene mediante extracción Soxhlet. Se propone un prototipo de emulgel, utilizando carboximetilcelulosa para la formulación de hidrogel y aceite de ricino para la formulación de oleogel, colocándose en una de las fases el aceite extraído. Se determinaron las características fisicoquímicas del producto, incluyendo color, olor, homogeneidad y consistencia, pH, conductividad, viscosidad, índice de hinchamiento, extensibilidad y estabilidad. Al evaluar el sistema se encontró que el compuesto bioactivo dentro del emulgel pudo ser liberado bajo la acción de un estímulo externo.

Palabras clave: clavo de olor, emulgel, sistema de liberación

1 Introduction

Clove (*Syzygium aromaticum L.)* is an aromatic flower of the Myrtaceae family, containing approximately 15–20% essential oil. More than 30 compounds have been identified in this oil, where eugenol is the main compound (50–90%), and the complement (10–40%) is composed mainly of β-caryophyllene and α-humulene (Haro-González *et al*., 2023).

Research shows that clove essential oil contains eugenol (83.6%); eugenyl acetate (11.6%) and caryophyllene (4.2%) as major components (Aguilar & López, 2013). This oil represents one of the main vegetable sources of phenolic compounds such as flavonoids, hydroxybenzoic acids, hydroxycinnamic acids and hydroxyphenylpropenes. Also found are caffeic, ferulic, ellagic, and salicylic acids. Flavonoids such as kaempferol, quercetin, and their (glycosylated) derivatives are also found in cloves at lower concentrations (Cortes-Rojas *et al*., 2014).

Eugenol is attributed with antimicrobial activity. This compound can denature proteins and simultaneously alter cell membrane permeability, resulting in the death of microorganisms. It also exhibits antioxidant capacity and free radical scavenging activity, forming complexes with reduced metals. It is also attributed with anti-inflammatory, antimutagenic, antiallergic, analgesic, and antitumor properties (Zari & Hamkeen, 2021).

Numerous physical and pharmacological benefits are attributed to it; in dentistry it is used in patients with toothache, pulpitis and dental hyperalgesia. (Gülçin, 2011). In the cosmetics industry it has been used for the treatment of skin infections, skin lesions and inflammatory disorders. (Nejad *et al*., 2017). However, the volatile nature, hydrophobicity and its impact on the organoleptic properties make it difficult to directly use this oil in food or pharmaceutical products (Franlyne *et al*., 2019).

Gels are a relatively new dosage form created by entrapment of large amounts of aqueous or hydroalcoholic liquid in a network of solid colloidal particles. Gel formulations generally provide a faster release of a compound compared to conventional ointments and creams. (Hiba *et al*., 2018). Emulgels are generally formed by dispersing an oil phase in a gel phase or by inducing gelation of the external phase of an oil-in-water emulsion, it is the approach that uses the help of both emulsion and gels, obtaining the double effect of controlled release (Kumar *et al*., 2016). This research proposes a prototype emulgel as a transport and release system for clove oil.

2 Experimental Procedure

2.1 Extraction and physicochemical characterization of clove oil

The extraction was performed using Soxhlet equipment. A sample was taken and placed in an extraction cartridge, in a 1:20 ratio with the solvent, using petroleum ether. The extraction was carried out at a circulation rate of 6 drops per minute for 6 hours. Once the extraction was complete, the flask was removed and transferred to a rotary evaporator to remove the solvent. The oil obtained was characterized as follows.

The refractive index of the extracted oil was determined using a refractometer (Thermo brand) according to COVENIN (702:2001). As well as its solubility, as proposed by Scotti *et al*., (2020), who used water and linear alcohols of different carbon numbers (C2-C7) by adding oil and solvent in a 1:3 ratios to a test tube, verifying its solubility or not.

The total polyphenol content was determined according to the Folin-Ciocalteu colorimetric method (analytical grade, Merck). For which a volume of 50 µL of the extract was taken to which 125 µL of the Folin-Ciocalteu reagent was added, the mixture was stirred and left to stand for 8 minutes. Subsequently, 400 µL of sodium carbonate (7.1% Na_2CO_3) was added and the solution was topped up with distilled water to 2,000 µL. After 1 hour of standing in the dark, the absorbance at 760 nm was read using a Genesis 20 UV/VIS spectrophotometer (Thermo Scintific, Waltham, Massachusetts, USA). A calibration curve was prepared with a Gallic Acid (Polyhydroxylated Organic Acid) standard. (Sigma-Aldrich, Berlín Alemania) at concentrations of 50, 100, 200, 300, 400, 500 and 1000 ppm**.**

The 2,2-diphenyl-1-picrylhydrazyl (DPPH) free radical method (Sigma Aldrich Co®) was used for antioxidant capacity determination using a 100 µM DPPH solution in 80% methanol. A glass cuvette contained 100 µL of extract and 2.9 mL of DPPH. Absorbance was monitored every 5 min for 30 min at a wavelength of 515 nm. Reference absorbance (A_0) was obtained by replacing the extract volume with 80% methanol.

2.2. Prototype of emulgel-type transport system. Characterization

For the development of the product prototype, carboxylmethylcellulose (CMC) was selected to form the gel in the aqueous phase, while castor oil was used for the oil phase. The emulsifiers used were Tween 80 and Span 20. The phase ratio was 9:1 (hydrogel:oleogel). The emulsifier was formed by mixing the hydrogel and oleogel using an UltraTurrax at 3500 rpm for 20 s.

The prototype was inspected for physical appearance, including color, homogeneity, and consistency. Its pH and conductivity were determined using a Digimed conductivity meter. A stability study was carried out by subjecting the product to mechanical stress, using a centrifuge at 500 rpm for 5 minutes, then at 1500 rpm for 0 minutes. If no significant changes were observed, the centrifuge was centrifuged at 3000 rpm for 15 minutes.

2.3. Evaluation of the oil release system incorporated in the emulgel

1 g of the emulgel was dissolved in an appropriate solvent and filtered to obtain a clear solution. A standard solution was prepared with a sample of commercial eugenol in the same solvent and a solution with the extracted oil. The concentration of oil in the product is determined by UV-visible spectrophotometry. The calibration curve was prepared with a commercial eugenol standard solution at concentrations of 5, 10, 15, 20 and 25 ppm at a wavelength of 280.5 nm.

3 Discussion and Results

3.1 *Physicochemical characterization of the oil*

The clove oil obtained was characterized by its appearance, as well as its refractive index as shown in table 1., which displays a characteristic odor, yellowish to brown color, pungent flavor, and oily texture, Nejad *et al*., (2017) points out that this oil acquires a brown color with aging or in contact with air, it is photosensitive and thermolabile, so its storage life is short if not properly protected.

Clove contains 15–20% volatile essential oil; 10–13% tannin (gallotanic acid), resin, chromone, and eugenin. The essential oil of clove buds contains eugenol (70–90%), eugenol acetate (2–17%), and caryophyllene as its main component (Misar *et al*., 2020).

The density of most oils is less than 1 g/cm³, which means they are less dense than water and will float on it, the presence of phenols or derivatives affect the density value. The refractive index obtained is within the range reported by Nejad *et al*., (2017) and Valladolid (2016) who indicate that the refractive index of this oil is between 1.515 and 1.535. Misar *et al.,* (2020) reports a refractive index1.529.

The oil is insoluble in water, partially soluble in ethanol, and soluble in linear alcohols (C2 to C7), given the structure of the predominant compounds in the extract, such as the presence of eugenol (Nejad, Özgünes, & Basaran, 2017). As the molecular weight of the alcohols increases, a decrease in polarity is observed. This can be attributed to the predominance of the nonpolar part of the molecule, i.e., the hydrocarbon chain, and the influence of the OH decreases, as is the case with the eugenol molecule.

Table 1. Physical and organoleptic characteristics of the essential oil

Parameters	Value obtained
Color	Dark yellow
Odor	Characteristic
Density (g /mL)	0,99 ± 0,05
refractive index	1,519 ± 0,001

Plant phenols are one of the main compounds that act as primary antioxidants or free radical scavengers. Eugenol, or 4-allyl-2-methoxyphenol, is a phenolic derivative composed of an aromatic hydroxyl nucleus. Table 2 shows the total phenol content found in the oil, as well as its antioxidant capacity. The principle of antioxidant activity is based on the availability of electrons to neutralize free radicals. Furthermore, antioxidant activity is related to the number and nature of the hydroxylation pattern on the aromatic ring. In general, the ability to act as a hydrogen donor and the inhibition of oxidation increase with the increasing number of hydroxyl groups on the phenolic ring. (Gülcin, 2011). Radünz *et al*. (2019) reported a percentage of 94.86% for the antioxidant capacity of this oil. In this study, the antioxidant and radical scavenging activities of eugenol were compared with those of a 6-hydroxy-2,5,7,8-tetramethylchromium-2-carboxylic acid solution.

Table 2. Physical and organoleptic characteristics of the essential oil

Parameters	Value obtained
Total polyphenols	(9321,93 ± 1,32)mg/L
Antioxidant capacity	(83,76 ± 0,32) %
Trolox	(96,43 ± 1,2) %

3.2. Characterization of the emulgel prototype

Emulgel consists of emulsions, either oil-in-water or water-in-oil, that gel when combined with a gelling agent. Emulgel is more effective in healing than conventional gel. Furthermore, this system features dual controlled release, attributed to both the emulsion and the gel (Malavi *et al.,*2022).

The product was formulated with organoleptic and rheological properties suitable for topical administration. An oil-in-water emulsion was proposed; the polymers and surfactants used to obtain the emulsion are used in the food and cosmetics industries. Upon mixing the aqueous and oily phases, a whitish product, a typical emulsion color, was obtained (Figure 1). The emulsion is homogeneous, with good spreadability and a characteristic clove odor due to its aromatic compounds.

Figure 1. Emulgel prototype

Spreadability is closely related to the ability to spread the product over a surface, Whader *et al*., (2018), who

reported a capacity of 1,875 g.cm/s, for a carbopol-based aqueous external phase emulsifier, this value is higher than that reported in this research (1.68 ± 0.05) g.cm/s, due to the polymer used (carboxylmethylcellulose), however, the result shows that it spreads easily when applied to a surface or to the skin, providing a suitable delivery system for the extracted oil.

The product has a pH of 6.0, which falls within the skin pH range of 5.5–6.5. The advantage of being slightly acidic is that it cannot attack skin tissue and does not cause skin disorders (Arshad *et al*., 2020) when used in cosmetics. The conductivity (1722 µS/cm) allows us to verify that the external phase is aqueous, based on the measurement of free ions and water present in the sample. The value obtained is higher than water, due to the presence of other components in the product, which causes a grouping of the globules in emulsion and the movement or exchange of ions within the aggregates (Mehta, Gurpeet, Bhasin, 2010). Regarding its viscosity, Wadher *et al*., (2018) point out that the viscosity of emulgel formulations that have more than 1% of gelling agent exceeds 10,000 cP, with that of this manufactured product being 19,500 cP, this value is in accordance with that described by the researcher.

Another characteristic that different gels have is their swelling capacity, due to their ability to form a three-dimensional polymeric network that allows them to absorb a large amount of liquid, swelling and considerably increasing their volume without losing their shape, until they reach their maximum degree of hydration or swelling index (Ramirez_*et al.*, 2016). The swelling index in an emulgel is associated with the structure and composition, as well as the medium where it is found. The value obtained was (9.82 ± 0.01) %, with indexes of 11.18% reported in the literature (Kapadiya *et al*., 2016).

On the other hand, the stability of the product was measured, finding that at 500 rpm for 5 min, and then 1500 rpm for 15 min there is no phase separation, however, at 3000 rpm for 15 min small oil droplets were observed on the surface. The emulgel behaves as a viscoelastic fluid, where the droplets that form part of the elaborated product are perfectly organized forming a hexagonal network with a negligible film thickness of the continuous phase, and is capable of storing the deformation energy and returning to its initial shape, just like the behavior of an elastic solid, dissipating part of that energy as if it were a viscous fluid. By increasing the shear stress for a considerable time, a greater kinetics of the dispersed agent (oil) is produced in the solution and the molecules in the dispersion proceed to join or agglomerate and the process known as flocculation is formed, where there is an increase in the drops due to their grouping, which leads to a breaking of the emulsion forcing it to a phase separation and due to the difference in densities, the oil being of lower density than the aqueous solution, a migration of the drops on the surface takes place (Nava, 2017).

3.3. Evaluation of the release system of the bioactive compound incorporated in the emulgel

The release of the compound was quantified by spectrophotometry showing its maximum absorbance at 280 nm (Olvera *et al*., 2019). A standard curve was constructed using commercial Eugenol as a standard. The emulgel was diluted, estimating an initial concentration of 200 ppm of eugenol in the clove extract. The emulgel dissolved and a concentration of 10.12 ppm was determined, which represented an absorbance of 0.408 a.u. This result shows that the compound trapped in the emulgel network can be released, suggesting that the system is capable of transporting and releasing the compound. The characteristics of the transport system can be modulated so that the compound is released under a certain external stimulus.

4 Conclusion

The resulting extract has a significant antioxidant capacity, providing excellent properties for use in cosmetic or pharmaceutical products. The designed prototype exhibits good properties as a topical product due to its good spreadability and pH. The proposed system is capable of transporting and releasing the compound present in cloves under external stimulation.

References

Aguilar, A. & Lopez, A. (2013). Extractos y aceite esencial del clavo de olor (*Syzygium aromaticum*) y su potencial aplicación como agentes antimicrobianos en alimentos. Temas selectos de Ingeniería de Alimentos. Vol. 7 (2), pp. 35-41

Arshad, W., Khan, H., Akhtar, & Mohammad, S. (2020). Polymeric emulgel carrying Cinnamomum tamalaextract: promising delivery system for potential topical applications. *Brazilian Journal of Pharmaceutical Sciences* Vol. 56. doi.org/10.1590/s2175-97902019000418318

Cortes-Rojas, D., Fernandes de Sousa, D., Pereira W. (2014). Clove (Syzygium aromaticum): a precious spice. Asian Pac J. Trop Biomed, Vol. 4(2), pp: 90-96. doi.org/10.1016/S2221-1691(14)60215-X

Franklyne, J.S. Lyer, S., Ebenazer, A., Mukherjee, A., Chandrasekaran, N. (2019). Essential oli nanoemulsions: antibacterial activity in contaminated fruit juice. Int.J.Food Sci. Technol, Vol. 54, pp. 2802-2810. doi.org/10.1111/ijifs.14195

Gülcin, I. (2011). Antioxidant Activity of Eugenol: A Structure–Activity Relationship Study. Journal of Medicinal Food, Vol. 14 (9), pp. 975-985. doi.org/10.1089/jmf.2010.0197

Haro-Gonzalez, J., Schlienger, B., Martinez-Velazquez, M., Castillo-Herrera, G., Esponosa-Andrews H. (2023). Optimization of Clove Oil nanoemulsions: Evaluation of antioxidant, antimicrobial, and anticancer properties. Colloids Interface, Vol. 7 (4) pp. 64-81. doi.org/10.3390/colloids7040064

Hiba, S., Kamal, A., Hameed, B., & Al-Anic, W. (2016). Formulation Design and Evaluation of Anti-Microbial Activity of Emulgel Containing Essential Oil of Myrtus communis L. *International Journal of Pharmaceutical Sciences Review and Research, Vol. 40 (2) pp.* 271-277.

Kapadiya, B., Gohil1, D., Patel, D., Patel, S., Aundhia, B., Shah, N., y otros. (2016). Formulation and Evaluation of Spironolactone Loaded Emulgel for Topical Application. *Journal of Pharmaceutical Science and Biocientific Research*, Vol. 12 (22), pp. 740-752. doi.org/.10.20959/wjpr202322-30742

Kumar, D., Singh, J., Antil, M., & Kumar, V. (2016). Emulgel-Novel Topical Drug Delivery System–A Comprehensive Review. *International Journal of Pharmaceutical Sciences and Research,* 4733-4742. doi.org/ 10.24327/ijrsr.2020.1104.5247

Mehta SK, Gurpeet K, Bhasin KK. (2010).Tween-embedded microemulsions-physicochemical and spectroscopic analysis for antitubercular drugs. *AAPS Pharm SciTech*. 11(1), pp.143-153. doi.org/10.1208/s12249-009-9356-5

Misar, K. S., Kulkarni, S. B., & Gurnule, W. B. (2020). Formulation and evaluation of antiacne cream by using Clove oil. Materials Today: Proceedings. Vol. 29, pp.1251-1258. doi.org/10.1016/j.matpr.2020.06.106

Nava, D. (2017). Formulación de un emulgel farmacéutico de un Aine. Trabajo de grado para optar por el título de Químico Farmacéutico Biólogo. Universidad Nacional Autónoma, México

Nejad, M., ÖzgÜnes, H., & Basaran, N. (2017). Pharmacological and Toxicological Properties of Eugenol. *Turk J Pharm Sci*, Vol. 14 (2), pp. 201-206. doi.org/10.4274/tjps.62207

Scotti E., Velásquez I., Ojeda L., Pacheco F., Noguera-Machado N. (2020) Characterization and incorporation of an extract of passion fruit seeds (Passiflora edulis) in a hydrogel. *Revista Ingeniería UC*, Vol. 27 (3), pp. 273 – 28. doi.org/10.54139/revinguc.v27i3.147

Radünz, M., Martins, M., Mota, T., Radünz, A., Dellinghausen, B., & Avila, E. (2019). Antimicrobial and antioxidant activity of unencapsulated and encapsulated clove (*Syzygium aromaticum, L.*) essential oil. *F*ood Chemistry, Vol. 276, pp.180-186. doi.org/10.1016/j.foodchem.2018.09.173

Ramirez, A., Benitez, J., Rojas, L., & Rojas, B. (2016). Materiales polimeros de tipo hidrogeles. *Revista Latinoamericana de Metalurgia y Materiales*, Vol. 36 (2), pp.108-130. Version impresa ISSN 0255-6952

Valladolid, A. (2016). Efecto del aceite esencial de clavo de olor *(Syzygium Aromaticum)* sobre la caracterización y vida útil de Tomates *(Solanum Lycopersicum)* frescos. Trabajo de grado para optar por el título de ingeniero agroindustrial e industrias alimentarias. Escuela Profesional De Ingeniería Agroindustrial E Industrias Alimentarias, Perú.

Wadher, K., Patel, D., Trivedi, S., & Umekar, M. (2018). Design, Formulation and Evaluation of Topical Nimesulide Emulgel. *International Journal of ChemTech Research*, Vol. 11 (10), pp. 52-59. doi.org/10.20902/IJCTR.2018.111008

Zari, T.A., & Hakeem, K.R. (2021). Anticancer properties of eugenol. A review. Molecules, 26 (23),pp. 7407. doi.org/ 10.3390/molecules26237407

Received: *January 26th, 2025*

Accepted: *June 22th, 2025*

Velásquez, Ingrid**:** *Doctor of Enginneerig, Chemical area, Scientific Research Soil and Environmental Technology Research Laboratory, and Food laboratory. Universidad de Carabobo, Valencia, Venezuela.* **https://orcid.org/0000-0002-5522-0161**

Vanessa Fortoul: *Chemical Engineering. Universidad de Carabobo. Valencia, Venezuela.*
Email:vanessafortouluc@gmail.com
https://orcid.org/0009-0000-0806-383X

Artículo de Investigación. Revista Ciencia e Ingeniería. Vol. 46, No. 3 pp. 233-240, agosto-noviembre, 2025.
ISSN 1316-7081. ISSN Elect. 2244-8780 Universidad de los Andes (ULA)

Chemical composition and antibacterial activity of essential oil *Pluchea carolinensis* (Jacq.) G. Don.(Asteraceae)

Composición química ctividad antibacteriana del aceite esencial de *Pluchea carolinensis* (Jacq.) G. Don. (Asteraceae)

Buitrago-Díaz Alexis[1,2]; Rojas-Vera, Janne[1]*; †Rojas, Luis[1]; Velasco, Judith[3]: Peñaloza, Yonel[4]
[1]Instituto de Investigaciones, Facultad de Farmacia y Bioanálisis, Universidad de Los Andes, Mérida-Venezuela.
[2]Departamento de Análisis y Control, Facultad de Farmacia y Bioanálisis, Universidad de Los Andes, Mérida-Venezuela.
[3]Departmento de Microbiología y Parasitología, Facultad de Farmacia y Bioanálisis, Universidad de Los Andes, Mérida-Venezuela. [4]Carrera de Economía, Facultad de Ciencias Administrativas y Económicas, Univeridad Técnica de Cotopaxi. Latacunga-Ecuador.
*janne.rojas24@gmail.com

Abstract

*Currently, plants continue to provide bioactive molecules used as alternative for the development of new drugs. Pluchea carolinensis (Asteraceae) species known as beach sage is used as ornamental plant in some Caribbean locations. Phytochemical studies have reported the presence of sesquiterpenes, lignans, triterpenes and flavonoids. In this regard, the essential oil contains mainly 3-thujopsanone, ß-caryophyllene, spathulenol and ß-chamigrene. Different parts of the plant are used in traditional medicine for the treatment of headache, fiber, stomach conditions, among others. Present study aims to determine the chemical composition of essential oil of P. carolinensis (Jacq.) G. Don collected from Michelena, Tachira State and to evaluate its activity against international reference bacterial strains. Gas chromatography coupled to mass spectrometry assay of the essential oil of the species under study revealed α-pinene (31.94%), thymol (13.60%), bicyclogermacrene (12.64%) and 2,5-dimethoxy-p-cymene (11.10%) as main components. Antibacterial activity assay carried out by agar disk diffusion method showed activity against Staphylococcus aureus ATCC 25923 at minimum inhibitory concentration (**MIC**) of 300 µL/mL and Enterococcus faecalis ATCC 29212 at 500 µL/mL.*

Keywords: *Pluchea carolinensis*, Asteraceae, essential oil, sesquiterpenes, antibacterial activity.

Resumen

*En la actiualidad las plantas continúan proporcionando moléculas bioactivas utilizadas como alternativas para el desarrollo de nuevos fármacos. La especie Pluchea carolinensis (Asteraceae) conocida como salvia de playa es utilizada como planta ornamental en algunas localidades del Caribe. Los estudios fitoquímicos reportan la presencia de sesquiterpenoides, lignanos, triterpenoides y flavonoides. Por su parte, el aceite esencial contiene principalmente 3-tujopsanona, ß-cariofileno, espatulenol y ß-chamigreno. Las diferentes partes de la planta son utilizadas en la medicina tradicional para el tratamiento de dolores de cabeza, fiebres, afecciones estomacales, entre otras. El presente estudio tiene como objetivo determinar la composición química del aceite esencial de la especie P. carolinensis (Jacq.) G. Don. colectada en la población de Michelena en el estado Táchira y evaluar su actividad frente a cepas de referencia internacional. El análisis por cromatografía de gases acoplado a espectrometría de masas del aceite esencial de la especie en estudio reveló como compuestos mayoritarios α-pineno (31,94%), timol (13,60%), biciclogermacreno (12,64%) y 2,5-dimetoxi-p-cimeno (11,10%). Los resultados del ensayo para la actividad antibacteriana realizados por el método de difusión en agar con discos, mostraron actividad frente a Staphylococcus aureus ATCC 25923 a la Concentración Inhibitoria Mínima (**CIM**) de 300 µL/mL y Enterococcus faecalis ATCC 29212 a 500 µL/mL.*

Palabras clave: *Pluchea carolinensis,* Asteraceae, aceite esencial, sesquiterpenos, actividad antibacteriana.

1 Introducción

Increasing bacterial resistance at hospital centers due to incorrect use of antibiotics is considered a worldwide public health problem. In order to counteract the effect of some multi-resistant strains to certain antimicrobial drugs, scientific organizations have the challenge to find new bioactive chemical structures with less secondary effects obtained from natural resources (Buitrago-Díaz et al., 2024; Rojas et al., 2024).

Pluchea Cass (Asteraceae) genus comprises about 80 species distributed in tropical areas of North America, Central America and South America, as well as some species reported in Africa, Asia and Australia (Ibrahim et al., 2022; Gonfa et al., 2022; Hussain et al., 2013; Sharma et al., 2011). Described as aromatic *matojos*, perennial with erect steams, simple leaves, altern and unisexual flowers. In traditional medicine, different parts of the plant, are used for the treatment of headache, fiber, stomach conditions, among others (Elgamal et al., 2021; García et al., 2011).

Pluchea carolinensis (Jacq.) G. Don. known as beach sage is used as ornamental plant in some locations of Cuba, Venezuela and Panamá. Phytochemical studies published about this species indicate the presence of eudesmane type sesquiterpenoids, as well as, lignans, triterpenes and flavonoids. Essential oils are mainly formed by 3-thujopsenone, *ß*-caryophyllene, spathulenol and *ß*-chamigrene (Roersch, 2018; Kerdudo et al., 2016).

Specialized literature stands out the activity of hydroalcoholic extract of *P. carolinensis* leaves against *Enterobacter faecalis*, *Staphylococcus aureus*, *Mycobacterium* sp., *Mycobacterium fortuitum*, *Pseudomonas* sp., *Escherichia coli* and *Klebsiella* sp at concentration values below 100 mg/mL (Pérez et al.; 2007). Another investigation carried out with the ethanolic extract of same species showed antifungal effect against *Candida kefyr*, *Malassezia* sp, *Trichophyton rubrum*, *Trichophyton interdigitale* and *Trichophyton mentagrophytes* with MIC values between 200 to 400 µg/mL (Biabiany et al. 2013).

Presence of flavonoids such as kaempferol, myricetin and quercetin in ethyl acetate and butanol extracts of *P. carolinensis* leaves might be responsible for the high scavenging capacity observed through the *In Vitro* DPPH and ABTS methods at concentrations below to 8.4 mg TE/g of dry extract (Perera et al., 2010).

Antileishmanicidal study with promastigotes of *L. amazonensis* carried out with the hydroalcoholic extract of *P. carolinensis* showed inhibition of 50% at concentration of 30 µg/mL (Garcia et. al., 2011). Compounds like caffeic acid, chlorogenic acid, ferulic acid, quercetin and rosmarinic acid, showed growth inhibition activity of promastigotes and intracellular amastigotes with IC_{50} values between 0.2 and 2.9 µg/mL (Montrieux et al., 2014).

Oral administration, 80 mg/kg, of tincture (30%) obtained from aerial parts of *P. carolinensis* to Wistar rats revealed a reduction of acute and chronic inflammatory process evaluated in two carrageenan-induced rat paw edema and the cotton-induced granuloma model (Rosales et al., 1999).

Present investigation aims to determine the chemical composition of *Pluchea carolinensis* (Jacq.) G. Don. essential oil and to evaluate the growth inhibitory effect on international reference ATCC bacterial strains through the agar diffusion method.

2 Procedimiento Experimental

2.1 Plant material:

Pluchea carolinensis (Jacq.) G. Don. (**Plc**) was collected from Michelena, Táchira state, at 1200 m.a.s.l. (7°56′30″N, 72°14′33″O) in November 2023, during the rainy season and flowering stage. Botanical identification was carried out by Dr. Pablo Meléndez, MERF Herbarium, Faculty of Pharmacy and Bioanalysis, University of Los Andes, Mérida, Venezuela. Voucher specimen was deposited under the following code **JR52**.

2.2 Isolation of essential oils:

Fresh leaves of **Plc** (1100 g) were cut into small pieces and subjected to hydrodistillation for 4 h, using a Clevenger-type apparatus. The oil 0.6 mL (0.05% w/v) was dried over anhydrous sodium sulfate and stored at 4°C until the analyses were performed.

2.3 Gas Chromatography (***GC***)*:*

GC analyses were performed on a Perkin-Elmer AutoSystem gas chromatograph equipped with flame ionization detectors. Two capillary columns of different polarities were used: a 5% phenylmethyl polysiloxane fused-silica column (AT-5, Alltech Associates Inc., Deerfield, IL) (60 m × 0.25 mm, film thickness 0.25 µm) and a polyethylene glycol fused-silica column (AT-WAX, Alltech Associates Inc., Deerfield, IL) of the same dimensions. The initial oven temperature was 60°C; it was then heated to 260°C at 4°C/min and the final temperature was maintained for 20 min. The injector and detector temperatures were 200°C and 250°C, respectively. The carrier gas was helium at 1.0 mL/min and the sample was injected using a split ratio of 1:100. Retention indices were calculated relative to C_8-C_{24} n-alkanes, using only the AT-5 capillary column and comparing values reported in the literature (Adams, 2007; Davies, 1990).

2.4 Gas Chromatography-Mass Spectrometry (***GC-MS***)*:*

GC-MS analyses were carried out on a Hewlett Packard GC-MS system, Model 5973, fitted with a 30 m long, crosslinked 5% phenylmethyl siloxane (HP-5MS, Hewlett Packard, USA) fused-silica column (0.25 mm, film thickness 0.25 µm). The following conditions were applied:

source temperature 230°C; quadrupole temperature 150°C; carrier gas helium, adjusted to a linear velocity of 34 m/s; ionization energy, 70 eV; scan range 40-500 amu; 3.9 scans/s. The injected volume was 1.0 µl of a 2% dilution of oil in n-heptane. A Hewlett-Packard ALS injector was used with a split ratio of 1:100. The identification of the oil components was based on the Wiley Registry of Mass Spectral Data (6th Ed.) and NIST 05 data base library, followed by comparisons of mass spectral (**MS**) data with published literature and the retention index calculation (Adams, 2007).

2.5 Bacterial strains:

The microorganisms used for the antibacterial method were *Staphylococcus aureus* (ATCC 25923), *Enterococcus faecalis* (ATCC 29212), *Escherichia coli* (ATCC 25922), *Klebsiella pneumoniae* (ATCC 23357) and *Pseudomonas aeruginosa* (ATCC 27853).

2.6 Antibacterial method:

The antibacterial activity was carried out according to the disc diffusion assay described by Velasco et al., (2007). The strains were maintained in agar conservation at room temperature. Each bacterial inoculum was incubated in 2.5 mL Müeller-Hinton broth (BBLTM®) at 37ºC for 18 h (Weng-Alemán et al., 2003). The bacterial inoculum was diluted in sterile 0.85% saline to obtain turbidity visually comparable to McFarland Nº 0.5 standard (1.5 x 10^{6-8} CFU/mL). Every inoculum was spread over plates containing Mueller-Hinton agar and a paper filter disc (6 mm) saturated with 10 µL of essential oil.

The plates were left for 30 min at room temperature and then incubated at 37ºC for 24h. The inhibitory zone around the disc was measured and expressed in mm. A positive control was also assayed to check the sensitivity of the tested organisms using the following antibiotics: Linezolid® (10 µg), Vancomycin® (30 µg), Tobramycin® (30 µg), Aztreonam® (10 µg) and Cefepime® (30 µg). A negative control was also included in the test using a filter paper disc saturated with dimethyl sulphoxide (**DMSO**) to discard any activity of this solvent against the microorganisms assayed. The experiments were repeated twice.

The minimal inhibitory concentration (**MIC**) was determined only with microorganisms that displayed inhibitory zones. **MIC** was determined by dilution of the essential oil in **DMSO** by pipetting 10 µL of each dilution onto a filter paper disc. Dilutions of the oil within a concentration range of 100-600 µL/mL were also carried out. **MIC** was defined as the lowest concentration that inhibited the visible bacterial growth (CLSI, 2024; Buitrago et al., 2023). A negative control was also included in the test using a filter paper disc saturated with **DMSO** to check possible activity of this solvent against the bacteria assayed. The experiments were repeated twice.

3 Results and discussion

Essential oil obtained through hydrodistillation of **Plc** collected from Michelena, Táchira state, was analyzed by by **GC** and **GC-MS**. The chemical profile (Table 1) showed that the oil was composed mainly by sesquiterpenes, where, 25% corresponded to bicyclic sesquiterpenes; 16.67% tricyclic sesquiterpenes; 16.67% oxygenated bicyclic sesquiterpenes and a minor occurrence of other hydrocarbons. Results showed α-pinene (31.94%), thymol (13.60%), bicyclogermacrene (12.64%) and 2,5-dimethoxy-*p*-cymene (11.10%) as major components, while (*E*)-caryophyllene (8.04%), spathulenol (5.00%) and modheph-2-ene (4.77%) showed a moderate presence.

Table 1. Chemical composition of essential oils from *Pluchea carolinensis* (Jacq.) G. Don. leaves.

Compounds	%A	RI
trans-2-hexenal[f]	0.37	846
α-pinene[a]	**31.94**	**932**
thymol[d]	**13.60**	**1289**
modheph-2-ene[c]	4.77	1382
α-isocomene[c]	1.33	1387
(*E*)-caryophyllene[b]	8.04	1417
2,5-dimethoxy-*p*-cymene[d]	**11.10**	**1424**
aristolochene[b]	2.55	1487
byciclogermacrene[b]	**12.64**	**1500**
butylated hydroxytoluene[f]	1.74	1514
spathulenol[e]	5.00	1577
caryophyllene oxide[e]	1.90	1582
[a]Bicylic monoterpene		1 (8.33%)
[b]Bicyclic sesquiterpenes		3 (25%)
[c]Tricyclic sesquiterpenes		2 (16.67%)
[d]Oxygenated monocyclic monoterpene		2 (16.67%)
[e]Oxygenated bicyclic sesquiterpenes		2 (16.67%)
[f]Other hydrocarbons		2 (16.67%)

*Chemical composition was determined by comparison of the MS of each component with Wiley GC/MS library data 6th edition and its retention index (**RI**).*La composición del aceite esencial se determinó por comparación de los EM de cada compuesto con la base de datos Wiley 6ta edición y sus tiempos de retenciòn (**IR**).

Previous investigations on *P. carolinensis* essentials oils of flowers and leaves collected from Cuba revealed through GC-MS analysis the presence 44 constituents representing (F: 64.6%, L: 84.2%) of the total oil analized. The major identified components were selin-11-en-4-α-ol (**F**: 17.7%, **L**: 33.4%), β-caryophyllene (**F**: 5.5%, **L**: 21.1%), 2,5-dimethoxycymene (**F**: 8.9%, **L**: 3.3%), caryophyllene oxide (**F**: 6.6%, **L**: 3.3%), α-pinene (4.7%) and spathulenol (**F**: 3.8%, **L**: 3.1%). Furthermore, two carvotanacetone derivatives were for the first time identified: 5-angeloyloxycarvotagetone and 5-isovaleroyloxycarvotagetone (Kerdudo et al., 2016).

Another investigation conducted with the essential oil of *P. ovalis* aerial parts revealed through **GC-MS** analysis the presence of 37 components, mainly sesquiterpenes. The major chemical components where *α*-cadinol (15.54%), *δ*-cadinene (12.93%), *β*-selinene (5.86%), *τ*-muurolol (4.70%), *β*-gurjurene (4.17%), cubebol (3.00%), *γ*-cadinene (2.99%) and epizonarene (2.69%) (Gonfa et al., 2022).

In another investigation, the essential oil of *P. carolinensis* flowers consisted mainly of aldehydes and esters. The main compound was selin-11-en-4a-ol (43.40%), followed in a smaller proportion by 2,5-dimethoxy-*p*-cymene (12.50%), neryl isovalerate (6.40%) and caryophyllene oxide (6.80%) (Pino et al., 2009). Likewise, the oil from the leaves of *Pluchea pteropoda* collected in Vietnam showed high concentrations of oxygenated monoterpenes and sesquiterpenes, among which 2,5-dimethoxy-*p*-cymene (43.50%), *β*-maaliene (14.00%) and *α*-isocomene (9.00%) were found (Ninh The et al., 2022).

The variation in the chemical composition of the essential oil has been related to biotic and abiotic factors. The type of chemical components biosynthesized by the plant is related to genetic patterns, growth stages, geographic location, soil chemical composition, water availability, seasonal factors, extraction method, storage conditions, among others (Rojas et al., 2023; Madboly et al., 2023; Buitrago et al., 2015). Likewise, some compounds are observed only in specific species, considered as chemotaxonomic markers for species identification and authentication (Rojas et al., 2025).

Antibacterial evaluation assayed in present investigation revealed that **Plc** essential oil was active against grampositive bacteria (Table 2). The oil obtained from the leaves caused growth inhibition of *S. aureus* (**MIC**: 300 µL⁄mL) and *E. faecalis* (**MIC**: 500 µL⁄mL).

Table 2. Antibacterial activity of leaf essential oils of *Pluchea carolinensis* (Jacq.) G. Don.

Microorganisms	Inhibition zone (mm)*						MIC µL/mL
	Essential oil	Antibiotics					
		LI	VA	TO	AZT	CEP	
Staphylococcus aureus (ATCC 25923)	**9***	40*					**300**
Enterococcus faecalis (ATCC 29212)	**8***		26*				**500**
Escherichia coli (ATCC 25922)	NA			34*			NT
Klebsiella pneumoniae (ATCC 23357)	NA				42*		NT
Pseudomonas aeruginosa (ATCC 27853)	NA					38*	NT

*Zone of inhibition (discs 6 mm in diameter), **NA**: not active, **NT**: not tested; **LI**: Linezolid® (10 µg); **VA**: Vancomycin® (30 µg); **TO**: Tobramycin® (30 µg); **AZT**: Aztreonam® (30 µg); **CE**: Cefepime® (30 µg); **MIC**: Minimum inhibitory concentration, Range: 100-600 µL/mL. *Zona de inhibición (discos 6 mm de diámetro). **NA**: no activo; **NP**: no probado; **LI**: Linezolid® (10 µg); **VA**: Vancomicina® (30 µg); **TO**: Tobramicina® (30 µg); **AZT**: Aztreonam® (30 µg); **CE**: Cefepime® (30 µg); **CIM**: Concentración inhibitoria mínima, Rango: 100-600 µL/mL.

According to the classification suggested by Kuete (2010), for natural products evaluation, results obtained in the present investigation show that **Plc** essential oil exhibit moderate (100 µg/mL < **MIC** < 600 µg/mL) activity against *S. aureus* and *E. faecalis* bacteria strains.

Previous investigation on *P. eupatorioides* essential oil demonstrated effectiveness against *Staphylococcus aureus* and *Candida albicans* with **MIC** value of 100 µg/mL. Moreover, the essential oil was also found to be effective against *Bacillus cereus* and *Escherichia coli* with a **MIC** of 200 µg/mL (Thinh et al., 2023).

The essential oil *P. carolinensis* and 3 isolated molecules (5-isovaleroyloxycarvotagetone, 5-angeloyloxycarvotagetone and selin-11-en-4-ol) were significantly active at 0.5 % (w/v) against *A. niger*, *C. albicans*, *S. aureus* and *B. cereus*. No activity was observed against *P. aeruginosa*, *E. coli*, *S. arizonae* and *L. innocua* (Kerdudo et al., 2016).

Another investigation carried out with extracts from fresh leaves of *Pluchea carolinensis* showed growth inhibition of *Klebsiella* sp. at the **MIC** of 1mg/mL. On the other hand, *P. carolinensis* extracts showed activity against *E. faecalis*, *S. aureus*, *Mycobacterium* sp., *M. fortuitum*, *Pseudomonas* sp. and *E. coli* with **MIC** value of 100 mg/mL (Pérez et al., 2007).

The antibacterial activity observed by essential oils could be related mainly to mono- and sesquiterpenes, which have the ability to inhibit bacterial growth through several mechanisms such as: cell membrane denaturation, nutrient transport interference, metabolic regulation, among others (Buitrago et al., 2023; Patra et al., 2016; Trombetta et al., 2005). Some studies have revealed that caryophyllene and caryophyllene oxide have the ability to diffuse the cell membrane causing inhibition of bacterial growth (Sarpietro et al., 2015).

4 Conclusions

The essential oil of *P. carolinensis* leaves is composed mainly by monoterpenes, thymol and *α*-pinene, observed as main components. The antibacterial activity revealed that the essential oil has activity against *S. aureus* and *E. coli* at concentrations of 300 and 500 µL/mL, respectively. According to the results observed, the essential oil of this species may represent an alternative for the treatment of some infectious processes associated with these grampositive bacteria.

References

Adams, R. 2007. Identification of essential oil components by gas chromatography/ mass spectrometry. Illinois, United States: Allured Publishing Corporation, Carol Stream.

Biabiany, M., Roumy, V., Hennebelle, T., François, N., Sendid, B., Pottier, M., …. & Bailleul, F. 2013. Antifungal activity of 10 Guadeloupian plants. Phytotherapy Research, 27, 1640-1645. https:// doi: 10.1002/ptr.4906

Buitrago, A, Rojas, J., Velasco, J., Morillo, M., Joly, N., Rojas, L., & Martin, Patrick. 2023. Chemical Composition and Antibacterial Activity of essential oils from fruits of *Vismia Baccifera* and *Vismia Macrophylla* collected at different locations in Venezuelan Andes. European Journal of Medicinal Plants 34 (12):45-56. https://doi.org/10.9734/ejmp/2023/v34i121182

Buitrago, A., Rojas, J., Rojas, L., Velasco, J., Morales, A., Peñaloza, Y., & Díaz, C. 2015. Essential oil composition and antimicrobial activity of *Vismia macrophylla* leaves and fruits collected in Táchira-Venezuela. Natural product communications, 10(2), 375-377. chrome-extension://efaidnbmnnnibpcajpcglclefindmkaj/https://journals.sagepub.com/doi/pdf/10.1177/1934578X1501000244

Buitrago-Díaz, A. A., Rojas-Vera, J., Velasco-Carrillo, J., & Meléndez-González, P. A. 2024. Estudio fitoquímico preliminar y evaluación de la actividad antibacteriana del extracto metanólico de las hojas de *Baccharis prunifolia* Kunt. Revista de la Facultad de Farmacia, 66(2), 3-12. http://www.saber.ula.ve/handle/123456789/51145

Clinical & Laboratory Standards Institute (2024). Performance Standards for antimicrobial susceptibility testing, 34th. Disponible en: https://clsi.org/standards/products/microbiology/documents/m100/

Davies, N. W. 1990. Gas chromatographic retention indices of monoterpenes and sesquiterpenes on methylsilicone and carbowax 20M phases, Journal of Chromatography A, 503, 1-24. https://doi.org/10.1016/S0021-9673(01)81487-4

Elgamal, A. M., Ahmed, R. F., Abd-ElGawad, A. M., El Gendy, A. E. G., Elshamy, A. I., & Nassar, M. I. 2021. Chemical profiles, anticancer, and anti-aging activities of essential oils of *Pluchea dioscoridis* (L.) DC. and *Erigeron bonariensis* L. Plants (Basel), 10(4), 667. https://doi: 10.3390/plants10040667

García, M., Perera, W. H., Scull, R., & Monzote, L. 2011. Antileishmanial assessment of leaf extracts from *Pluchea carolinensis*, *Pluchea odorata* and *Pluchea rosea*. Asian Pacific Journal of Tropical Medicine, 4(10), 836-40. https://doi: 10.1016/S1995-7645(11)60204-6

Gonfa, Y. H., Tessema, F. B., Bachheti, A., Tadesse, M. G., Eid, E. M., Abou Fayssal, S., …. & Bachheti, R. K. 2022. Essential oil composition of aerial part of *Pluchea ovalis* (Pers.) DC., silver nanoparticles synthesis, and larvicidal activities against fall armyworm. Sustainability, 14(23), 15785. https://doi.org/10.3390/su142315785

Hussain, H., Al-Harrasi, A., Abbas, G., Rehman, N. U., Mabood, F., Ahmed, I., …. & Ali, I. 2013. The genus *Pluchea*: phytochemistry, traditional uses, and biological activities. Chemistry & Biodiversity, 10(11), 1944-71. http://doi: 10.1002/cbdv.201200140

Ibrahim, S. R. M., Bagalagel, A. A., Diri, R. M., Noor, A. O., Bakhsh, H. T., & Mohamed, G. A. 2022. Phytoconstituents and pharmacological activities of indian camphorweed (*Pluchea indica*): A multi-potential medicinal plant of nutritional and ethnomedicinal importance. Molecules, 27(8), 2383. https://doi.org/10.3390/molecules27082383

Kerdudo, A., Gonnot, V., Ellong, E. N., Boyer, L., Chandre, F., Adenet, S., Rochefort, K., Michel, T., & Fernandez, X. 2016. Composition and bioactivity of *Pluchea carolinensis* (Jack.) G. essential oil from Martinique. Industrial Crops and Products, 89, 295-302. https://doi.org/10.1016/j.indcrop.2016.04.076.

Kuete, V. 2010. Potential of Cameroonian plants and derived products against microbial infections: a review. Planta Medica, 76(14), 1479-1491. https://doi: 10.1055/s-0030-1250027

Madboly, W., Saleh, H., El Khawas, S., Hassanin, R., Marzouk, M., & Hussein, S. 2023. Chemical composition of *Pluchea dioscoridis* (L.) DC. essential oils from different natural habitats with their anticancer and antimicrobial po-tential. Egyptian Journal of Chemistry, 66(4), 425-433. https://doi: 10.21608/ejchem.2022.161665.6942

Montrieux, E., Perera, W. H., García, M., Maes, L, Cos, P, & Monzote, L. 2014. *In vitro* and *in vivo* activity of major constituents from *Pluchea carolinensis*

against *Leishmania amazonensis*. Parasitology Research, 113(8), 2925-2932. https://doi.org/10.1007/s00436-014-3954-1

Ninh The, S., Le Tuan, A., Dinh Thi, T. T., Dinh Luyen, N., & Tran, T. T. 2022. Essential oils of the asteraceae plants *Blumea riparia* DC. and *Pluchea pteropoda* Hemsl. ex Hemsl. growing in Vietnam. Natural Product Communications, 17(6), 1-6. https://doi:10.1177/1934578X221110662

Patra, J. K., & Baek, K. H. 2016. Antibacterial activity and action mechanism of the essential oil from *Enteromorpha linza* L. against foodborne pathogenic bacteria. Molecules (Basel, Switzerland), 21(3), 388. https://doi.org/10.3390/molecules21030388

Perera, W. H., Tabart, J., Gómez, A., Sipel, A., Payo AL., Kevers, C., & Dommes, J. 2010. Antioxidant capacity of three Cuban species of the genus *Pluchea* Cass. (Asteraceae). Journal of Food Biochemistry, 34, 249-261. https://doi.org/10.1111/j.1745-4514.2009.00328.x.

Pérez, C., Balcinde, Y., Suárez, C., Hernández, V., Falero, A., & Hung, B. R. 2007. Ensayo de la actividad antimicrobiana de *Pluchea carolinensis* (salvia de playa). Revista CENIC Ciencias Biológicas, 38(2), 150-154. https://revista.cnic.edu.cu/index.php/RevBiol/article/view/1060

Pino, J. A., Perera, W. H., Sarduy, R., Oviedo, R., & Quijano, C. E. 2009. Essential oil from flowers of *Pluchea carolinensis* (Jacq.) G. Don. Journal of Essential Oil Research, 21(1), 45-47. https://doi.org/10.1080/10412905.2009.9700105

Roersch, C. 2018. Medicinal and aromatic plants of South: Brazil (Medicinal and aromatic plants of the world). Albuquerque, NM: Springer Nature B.V. https://doi.org/10.1007/978-94-024-1552-0_34.

Rojas, J., Buitrago Díaz, A., Ramírez, H., & Fernández-Moreira, E. 2025. Chemical composition and antibacterial activity of essential oil from *Baccharis nitida* (Ruiz & Pav.) Pers. (Asteraceae) leaves Collected in Mérida-Venezuela. Journal of Essential Oil Bearing Plants, 28(2), 340-351. https://doi.org/10.1080/0972060X.2025.247655

Rojas, J., Buitrago Díaz, A., Rojas, L., & Velasco, J. 2023. Composición química y actividad antibacteriana del aceite esencial de la especie *Hyptis mutabilis* (Rich.) Briq. (Lamiaceae) colectada en Mérida-Venezuela. Ciencia e Ingeniería, 44(2), 95-100. http://erevistas.saber.ula.ve/index.php/cienciaeingenieria/article/view/18868

Rojas-Vera, J., Buitrago-Díaz, A., Rojas, L., Velasco, J., & Peñaloza, H. 2024. Composición química y actividad antibacteriana del aceite esencial de *Hinterubera imbricata* Cuatrec. et Aristeg (Asteraceae). Revista Ciencia e Ingeniería, 45(3), 275-280. http://erevistas.saber.ula.ve/index.php/cienciaeingenieria/article/view/20326

Rosales, V. P., Gross, M. C., Rosales, R. A., García, R. C., & León, J. E. 1999. Evaluación farmacológica de *Pluchea carolinensis* Jacq. (Salvia de playa) en animales de experimentación. Revista Cuba Plantas Medicinales, 3(2), 65-67. http://scielo.sld.cu/scielo.php?script=sci_arttext&pid=S1028-47961999000200004

Sarpietro, M. G., Di Sotto, A., Accolla, M. L., & Castelli, F. 2015. Interaction of α-caryophyllene and α-caryophylleneoxide phospholipidbilayers: Differential with scanning calorimetry study. Thermochimica Acta, 600: 2834. https://doi:10.1016/j.tca.2014.11.029

Sharma, S. K., & Goyal, N. 2011. Biological studies of the plants from genus *Pluchea*. Annals of Biological Research, 2(3), 25-34. rome-extension://efaidnbmnnnibpcajpcglclefindmkaj/https://www.scholarsresearchlibrary.com/articles/biological-studies-of-the-plants-from-genus-pluchea.pdf

Thinh, B. B., & Thin, D. B. 2023. Essential oil composition, antimicrobial and antioxidant properties of *Pluchea eupatorioides* Kurz collected from Vietnam. Journal of Essential Oil Bearing Plants, 26(3), 653-663. https://doi.org/10.1080/0972060X

Trombetta, D., Castelli, F., Sarpietro, M. G., Venuti, V., Cristani, M., Daniele, C., …. & Bisignano, G. 2005. Mechanisms of antibacterial action of three monoterpenes. Antimicrobial Agents and Chemotherapy, 49(6), 2474-2478. https://doi.org/10.1128/AAC.49.6.2474-2478.2005

Velasco, J., Rojas, J., Salazar, P., Rodríguez, M., Díaz, T., Morales, A., & Rondón, M. 2007. Antibacterial activity of the essential oil of *Lippia oreganoides* against multiresistant bacterials strains of nosocomial origin. Natural Product Communications, 2(1), 85-88. https://doi.org/10.1177/1934578X0700200117

Weng-Alemán, Z., Álvarez, M. I., Díaz, O. E., & Rodríguez. M. 2003. Recobrado de *Salmonella* sp. conservadas por método simple a temperatura ambiente. VacciMonitor, 12(3), 1-6. https://www.redalyc.org/articulo.oa?id=203414597001

Received: *January 10th, 2025*

Accepted: *July 22th, 2025*

Buitrago Díaz, Alexis Alberto: *Farmacéutico, MSc en Química Analítica, Dr. en Química de Medicamentos, Profesor Asociado del Departamento de Análisis y Control de la Facultad de Farmacia y Bioanálisis e Investigador*

activo del grupo de "Biomoléculas Orgánicas". Correo electrónico: albertbuitre@gmail.com. Orcid, ID: Diaz, ***https://orcid.org/ 0000-0001-6482-5907***

Rojas Vera, Janne: *Farmacéutica, MSc. en Química de Medicamentos, Ph.D. en Fitoquímica, profesora Titular adscrita al Instituto de Investigaciones de la Facultad de Farmacia y Bioanálisis. Coordinadora del grupo de investigacion "Biomoléculas Orgánicas". Orcid, ID: Rojas,* ***https://orcid.org/0000-0001-5161-6778***

†***Rojas Fermín, Luis:*** *Farmacéutico, MSc. en Química de Medicamentos, Dr. en Química Orgánica, profesor Titular adscrito al Instituto de Investigaciones de la Facultad de Farmacia y Bioanálisis. Director del IIFF periodo xx-2020*†. Correo electrónico: rojasfermin33@gmail.com. ***https://orcid.org/0000-0003-4508-1927***

Velasco, Judith: *Bioanalista, Esp. en Microbiología Clínica, PhD en Ciencias Médicas Fundamentales, Profa.Titular adscrita a la Cátedra de Bacteriología, Dpto. de microbiología y Parasitología, Escuela de Bioanálisis, Facultad deFarmacia y Bioanálisis, Universidad de LosAndes, Mérida-Venezuela. Correo electrónico: judithvelasco2005@yahoo.es.* ***https://orcid.org/0000-0002-4579-2772***

Peñaloza Molina, Hermes Yonel: *Licenciado en Educación Mención Matemáticas, MSc. en Estadística, Personal Académico no Titular, Carrera de Economía, Facultad de Ciencias Administrativas y Económica, Universidad Técnica de Cotopaxi, Latacunga-Ecuador. Correo electrónico: hermes.penaloza8432@utc.edu.ec.* ***https://orcid.org/0000-0003-4120-6040***

Artículo de Investigación. Revista Ciencia e Ingeniería. Vol. 46, No. 3 pp. 241-250, agosto-noviembre, 2025.
ISSN 1316-7081. ISSN Elect. 2244-8780 Universidad de los Andes (ULA)

Diagrama de fases, T(z) y comportamiento magnético del sistema de aleaciones $Cd_{1-z}Mn_zGa_2Te_4$

T(z) diagram and magnetic behavior of the $Cd_{1-z}Mn_zGa_2Te_4$ alloy system

Lacruz Páez, María Alejandra[2]; Soto, Orielys[1]; Power, Chystiam[1], Villarreal, Manuel[3]; Quintero, Miguel[1]; Morocoima, Manuel[1*].
[1]Centro de Estudios de Semiconductores, Departamento de Física, Facultad de Ciencias, Universidad de Los Andes, Mérida, Venezuela.
[2]Laboratorio de Espectroscopia Analítica, Departamento de Química, Facultad de Ciencias, Universidad de Los Andes, Mérida, Venezuela.
[3]Instituto de Matemática, Estadística e Física. Universidad Federal do Rio Grande – FURG. Rio Grande do Sul, Brasil.
***morocoima@gmail.com**

Resumen

Se realizaron mediciones de difracción de rayos-X, análisis térmico diferencial (ATD) y susceptibilidad magnética χ, en el rango de temperatura de 2 a 300 K, en muestras policristalinas del sistema de aleación $Cd_{1-z}Mn_zGa_2Te_4$. Los patrones de difracción de rayos-X se utilizaron para comprobar las condiciones de equilibrio y estimar los valores de los parámetros cristalinos. Estos valores mostraron que existen al menos dos regiones con fases diferentes, una para muestras con concentración $z < 0.03$ en la cual se presenta la fase del $CdGa_2Te_4$, y otra para muestras con $z > 0.1$, donde se exhibe la estructura del $MnGa_2Te_4$. Los valores de temperatura de transición del ATD se representaron gráficamente en función de la composición de la aleación z. Las curvas $1/\chi$ vs. T indicaron que las muestras en todo rango de composición muestran un comportamiento tipo vidrio de espín. De estas curvas se determinaron los valores de la Temperatura y constante de Curie-Weiss. También se determinó la temperatura de transición, Tg, para valores de $z \geq 0.80$.

Palabras clave: Semiconductores, parámetros de red, diagrama de fases, susceptibilidad magnética.

Abstract

Measurements of X-ray diffraction, differential thermal analysis (DTA) and of magnetic susceptibility χ, in the temperature range from 2 to 300 K, were carried out on polycrystalline samples of the $Cd_{1-z}Mn_zGa_2Te_4$ alloy system. The X-ray diffraction patterns were used to check the equilibrium conditions and to estimate crystalline parameter values. These values showed the existence of at least two distinct phase regions: one for samples with a concentration $z < 0.03$, where the $CdGa_2Te_4$ phase is present, and another for samples with $z > 0.1$, where the MnG_2Te_4 structure is exhibited. The DTA transition temperature values were plotted as a function of alloy composition z. The $1/\chi$ vs. T curves indicated that the samples across all composition ranges exhibit spin-glass behavior. From these curves, the Curie-Weiss temperature and constant values were determined. The transition temperature, Tg, was also determined for values of $z \geq 0.80$.

Keywords: Semiconductors, cell parameters, phase diagram, magnetic susceptibility.

1 Introducción.

El estudio de los Materiales Semiconductores Magnéticos, MSM y sus aleaciones, ASM, (Aleaciones Semiconductoras Magnéticas) son de gran interés debido a la forma en la que el comportamiento magnético asociado con el ion magnético puede modificar y complementar las propiedades de los semiconductores, (Shapira y col. 1988, Furdyna y col. 1988) y por su potencial aplicación en dispositivos magnetoópticos y electrónicos. Además de que se pueden modular estas propiedades con la variación de la concentración, esto para una determinada aplicación.
Los materiales más estudiados han sido las ASM obtenidas de los compuestos semiconductores II-VI de coordinación tetraédrica, reemplazando una fracción de los cationes del grupo II por un ion magnético de Fe, Co Mn, Ni, etc., por ejemplo $Cd_{1-z}Mn_zTe$ (Furdyna y col. 1988). Podemos obtener aleaciones similares introduciendo iones magnéticos en los compuestos ternarios del tipo calcopirita I-III-VI_2, los cuales presentan coordinación tetraédrica, por ejemplo $CuInTe_2$, y formar aleaciones del tipo $(CuIn)_{1-z}Mn_{2z}Te_2$, la que conseguimos aleando MnTe con $CuInTe_2$, estas aleaciones han sido estudiadas ampliamente (Quintero y col. 1989, Neal y col. 1989, Quintero y col. 1989). Otro tipo de compuesto que presentan enlaces tetraédricos son los Mn-III_2-VI_4, por ejemplo, $MnIn_2Te_4$ y sus aleaciones, $Zn_{1-z}Mn_zIn_2Te_4$ (Morocoima y col. 2009), que presentan una estructura tetragonal defectuosa con grupo espacial $I\bar{4}2m$, la cual está estrechamente relacionada con la estructura $I\bar{4}2d$, todos estos también han sido ampliamente estudiados, (K.J. Range, H. Hubner, 1976, Quintero y col. 1991, Morocoima y col. 2009).
Se ha demostrado que este tipo de aleaciones muestran diferentes comportamiento magnético, dependiendo del orden de los iones magnéticos dentro de la red catiónica, estos pueden ser antiferromagnéticos puros, para iones totalmente ordenados en la subred catiónica, como en el caso de $MnGa_2Se_4$ hasta vidrio de espín (spin-glass) para iones totalmente desordenados en la subred catiónica, como en el caso de $MnIn_2Te_4$ (Woolley y col. 1995, 1997), también pueden presentar efectos magnético-ópticos muy grandes, polarones magnéticos ligados, entre otros (Shapira y col. 1988, Furdyna y col. 1988, McCabe y col. 1997, Quintero y col. 2007). Se mostró que estas condiciones también aplican para el caso de varios sistemas de aleaciones y se encontró (Woolley y col. 1995, 1997) que los valores de la temperatura de Curie-Weiss, θ, determinadas a partir de las medidas de susceptibilidad magnética, dan buena indicación del ordenamiento de los iones magnéticos, Mn, en los distintos materiales estudiados. En nuestro caso, el sistema de aleaciones $Cd_{1-z}Mn_zGa_2Te_4$ pertenece a la familia II-III_2-VI_4, que involucra aleaciones semiconductoras magnéticas (ASM), producidas a partir de la sustitución de átomos no magnéticos de Cd por iones magnéticos de Mn.

Los compuestos extremos de este sistema de ASM: el $CdGa_2Te_4$ (z = 0) y el $MnGa_2Te_4$ (z = 1), presentan la misma estructura cristalina (tetragonal $I\bar{4}$)), (Calver 1.993, Garbato y col. 1987, 1993), pero parámetros de celda que difieren mucho entre ellos, por lo que es de esperar que en el diagrama de fases a bajas temperaturas se presenten regiones donde coexistan las dos fases y que separa a ambas. Se espera que, en los rangos de solución sólida, los parámetros de celda y las propiedades magnéticas varíen de forma controlada con la composición z.

2 Detalles experimentales

2.1 Preparación de las muestras.

Las muestras fueron preparadas en lingotes de 1 gramo mediante el método de síntesis y recocido [Morocoima y col. 2009, Moreno y col 2021, Correa y col, 2025], el cual consiste en depositar en cápsulas de cuarzo las cantidades previamente pesadas de los elementos para formar la muestra adecuada con una determinada composición. Las cápsulas son recubiertas en su interior con una capa de carbono, esto se logra mediante una pirólisis a la acetona. Esta capa impide que el manganeso reaccione con el cuarzo y deteriore la cápsula en el proceso de fundición. Luego las cápsulas son selladas al vacío (aproximadamente 10^{-5} Torr) y depositadas en hornos en los cuales son llevadas hasta una temperatura de 1150 °C aproximadamente, al alcanzar esta temperatura se apaga el horno y se deja enfriar, este proceso dura 24 horas aproximadamente. Para el recocido las muestras son introducidas en hornos a una temperatura de 500 °C y dejadas bajo estas condiciones por un lapso de 50 días, luego de este tiempo las muestras son enfriadas muy lentamente a una rata de 50 °C/día, con esto se buscaba que las muestras alcanzaran su equilibrio termodinámico. En nuestro caso se prepararon muestras del sistema $Cd_{1-z}Mn_zGa_2Te_4$ correspondientes a las siguientes concentraciones: 0.0, 0.025, 0.1, 0.15, 0.2, 0.25, 0.3, 0.4, 0.5, 0.6, 0.7, 0.8, 0.85, 0.9, 0.925, 0.95, 0.975, 1.0.

2.2 Determinación estructural. Difracción de rayos-X.

Para la determinación de las estructuras, los parámetros de red y número de fases presentes, se utilizó la técnica de difracción de rayos-x, mediante el método del polvo con una cámara de Guinier. La radiación utilizada fue la línea $K_{\alpha 1}$ del cobre, $Cu_{K\alpha 1}$ =1.5405 Å y se usó Silicio como sustancia patrón interno para corregir las desviaciones angulares. De las películas o patrones de difracción se extrajo la información referente a la desviación angular de los rayos difractados por el cristal, cada una de estas desviaciones angulares corresponde a una determinada familia de planos. Las medidas se realizaron a temperatura ambiente y se usó un programa de ajuste por mínimos cuadrados para determinar los parámetros de red.

2.3 Análisis Térmico Diferencial, (ATD)

Dado que cualquier cambio de fase está acompañado por una emisión o absorción de calor sin que la temperatura, de la muestra que experimenta el cambio de fase, varíe durante el proceso, se utiliza este principio para estudiar los cambios de fases de los materiales, usando la técnica de análisis térmico diferencial (ATD), y así construir los diagramas de fase correspondientes. Para esto, pequeñas cantidades de muestra, aproximadamente 100 mg, se depositan en cápsulas de cuarzo y se sellan al vacío, para luego introducirlas en un equipo DTA-7 PELQUIN ELMER. De los termogramas para cada muestra se extraen las temperaturas a la que se da cada transición de fase. El rango de temperatura de trabajo del DTA-7 es de 20 °C hasta 1200 °C.

2.4 Susceptibilidad Magnética.

La susceptibilidad de un material magnético se encuentra midiendo su magnetización cuando está bajo la influencia de un campo magnético, en nuestro caso se usó un magnetómetro SQUID DC MPMS-5 de la Quantum Design. La alta sensibilidad del SQUID permite medir la magnetización de muestras pequeñas, tal como 0.02 grs (20 mg), ya que el equipo no está diseñado para alojar grandes cantidades de muestras. Otra ventaja que tiene el magnetómetro SQUID, es que se necesita solo un pequeño campo magnético aplicado para detectar la magnetización. Este equipo puede ser utilizado para medir pequeños campos magnéticos con una gran exactitud. Está basado en dos principios físicos principales: La cuantización del flujo en el interior de un superconductor y el efecto Josephson (Rose-Innes y Rhoderick, 1.978). Básicamente el SQUID puede pensarse como un contador de flujo, el cual cuenta el "quanta" de flujo a través de la bobina. Este "quantum" es igual a h/2e, este valor es del orden de 2 x 10^{-7} G/cm^2. El equipo particular usado en estas medidas puede medir pequeñas fracciones de un quantum. Los rangos de temperatura y campo magnético que podemos manejar en el Squid son: de 1.8 K a 300 K y entre -5T y +5T.

3 Resultados, análisis y discusión.

3.1 Estructura cristalina del sistema $Cd_{1-z}Mn_zGa_2Te_4$.

En el sistema $Cd_{1-z}Mn_zGa_2Te_4$ encontramos para z=0, el compuesto $CdGa_2Te_4$, del cual Calver (Calver 1.993) reporta que presenta una estructura tetragonal con grupo espacial $I\bar{4}$ y parámetros de red, a=6.093 Å, c=11.81 Å y c/a=1.9383, datos sobre el diagrama de fase de éste no se han encontrado en la literatura. Para el extremo z=1, encontramos el compuesto $MnGa_2Te_4$, para éste, Garbato (Garbato y col. 1987, 1993) reporta que posee una super estructura tetragonal, $I\bar{4}$, con parámetros a_0=8.486 Å y c_0=48.40 Å, la cual está relacionada con una estructura calcopirita por las relaciones $a = \sqrt{2}a_0$ y c = 4c_0, sin embargo es importante mencionar que los autores no reportan el indexado de las líneas para este compuesto. En este mismo trabajo Garbato reporta que la estructura tetragonal de este compuesto se mantiene hasta 600 °C aproximadamente, por encima de esta temperatura la estructura $I\bar{4}$ empieza a desordenarse gradualmente, transformándose cerca de 690 °C en una estructura cúbica totalmente desordenada del tipo zinc-blenda, a 820 °C el compuesto funde congruentemente.

3.1.1 Análisis y discusión

Los patrones de rayos-x de Guinier para cada una de las muestras preparadas, se obtuvieron mediante el proceso indicado anteriormente. Estos mostraron que en las muestras los parámetros de la red se habían aproximado lo suficiente a sus valores de equilibrio termodinámico como para proseguir con el análisis de esos patrones y los demás experimentos, esto se infiere por la agudeza de los picos de difracción. Dado que no conocemos el indexado para todo el patrón de difracción del $MnGa_2Te_4$, tomamos las líneas que correspondían a la estructura tetragonal de otro compuesto ($MnGa_2Se_4$) y con ellas calculamos los parámetros de red para el compuesto y para las aleaciones donde se presentara este tipo de estructura. El análisis visual de las fotografías mostró que a baja concentración de Cd el rango de solución sólida es muy pequeño, entre 0.0 y 0.03 aproximadamente, luego existe una región monofásica desde z=0.05 hasta z=1.0, con la estructura del $MnGa_2Te_4$. Las líneas de difracción de cada aleación fueron indexadas y los parámetros de la red a, c y c/a determinados como se indicó anteriormente.

Para los compuestos $CdGa_2Te_4$ y $MnGa_2Te_4$ los parámetros calculados son a=6.108 Å, c=11.796 Å y c/a=1.931 y a=6.033 Å, c=11.984 Å y c/a= 1.986 con desviaciones estándares de ± 2e-3 y ± 1e-3. Como se puede ver, los resultados del compuesto $CdGa_2Te_4$ están de acuerdo con los reportados por Calver (Calver 1.993), así como también para el compuesto $MnGa_2Te_4$, ya que los valores encontrados concuerdan y cumplen con las relaciones dadas por Garbato (Garbato y col. 1987, 1993), como podemos apreciar de la Fig. 1 y de las relaciones 1 y 2.

$$\frac{a_G}{a_N} = \frac{8.486\ \text{Å}}{6.033\ \text{Å}} = 1.4066 \cong \sqrt{2} \ \rightarrow\ a_G = \sqrt{2}a_N \quad (1)$$

y

$$\frac{c_G}{c_N} = \frac{48.40\ \text{Å}}{11.98\ \text{Å}} \cong 4 \ \rightarrow \ c_G = 4c_N \qquad (2)$$

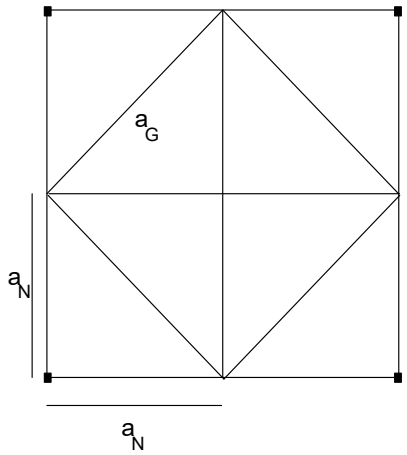

Fig. 1. Diagrama representativo de una proyección sobre el plano xy donde se aprecia la relación existente entre los parámetros de red reportados por Garbato y col. y los calculados en este trabajo.
Representative diagram of a projection on the xy plane showing the relationship between the lattice parameters reported by Garbato et al. and calculated in this work.

donde a_N, c_N, a_G y c_G son los parámetros a y c calculados en este trabajo y reportados por Garbato respectivamente. De la Fig. 1 y de las relaciones 1 y 2, se ve claramente que las líneas de estructura escogidas coinciden con la subcelda reportada por Garbato y col. En el caso de las aleaciones, los parámetros a, c y c/a fueron calculados de la misma manera y su variación con respecto a z se muestra en las Fig. 2, 3 y 4.

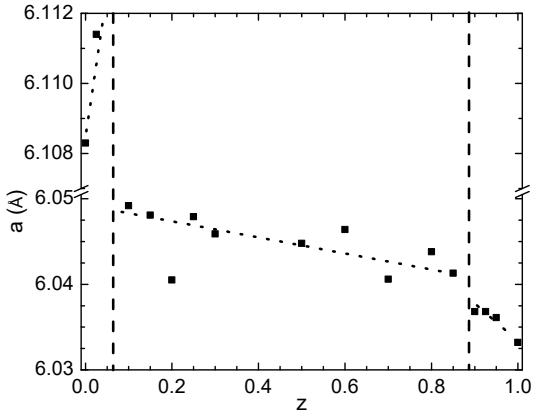

Fig. 2 Variación del parámetro de red a del sistema $Cd_{1-z}Mn_zGa_2Te_4$ con la composición z, los puntos representan los valores experimentales mientras que la línea punteada se usa para guiar la vista.
Variation of the lattice parameter a of the Cd1-zMnzGa2Te4 system with composition z, the points represent the experimental values while the dotted line is used to guide the view.

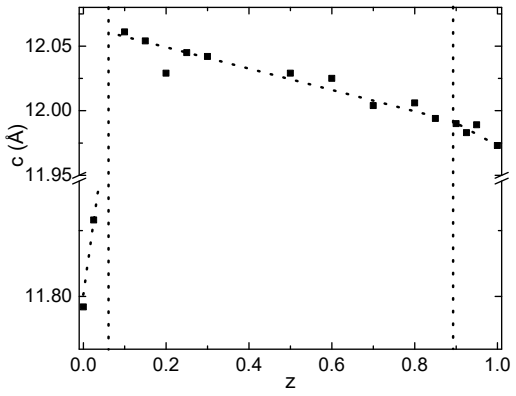

Fig. 3 Variación del parámetro de red c del sistema $Cd_{1-z}Mn_zGa_2Te_4$ con la composición z, los puntos representan los valores experimentales mientras que la línea punteada se usa para guiar la vista.
Variation of the lattice parameter c of the Cd1-zMnzGa2Te4 system with composition z, the points represent the experimental values while the dotted line is used to guide the view.

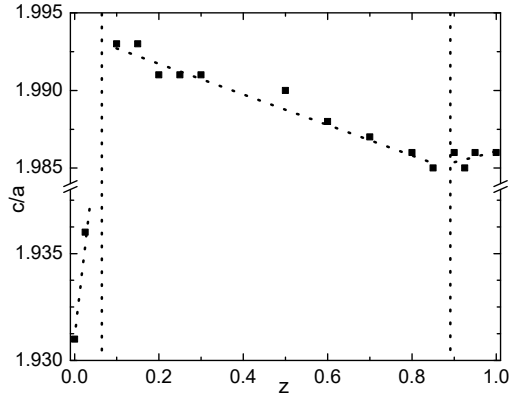

Fig. 4 Variación de la relación c/a del sistema $Cd_{1-z}Mn_zGa_2Te_4$ con la composición z, los puntos representan los valores experimentales mientras que la línea punteada se usa para guiar la vista.
Variation of the ratio c/a with of the Cd1-zMnzGa2Te4 system with composition z, the points represent the experimental values while the dotted line is used to guide the view.

Se observa de las figuras 2 a 4 que en el rango $0.1<z<1.0$ los parámetros a y c disminuyen linealmente con z, es decir, cuando se sustituyen los iones de Mn^{2+} por los de Cd^{2+}. Se observa de ambas figuras un pequeño quiebre cerca de z=0.9. La relación c/a, disminuye en el rango $0.1<z<0.9$, para valores mayores a 0.9 observamos un incremento en la variación hasta z=1.0

La pequeña dispersión de los puntos experimentales que se

observa se debe, quizás, al hecho de trabajar con un número pequeño de líneas de difracción, al hacer el cálculo futuro con todas las líneas y el indexado adecuado esta dispersión debe disminuir. También se observa de estas Figs. que existen tres regiones bien definidas, la primera comprendida entre z=0.0 y z=0.03 donde la estructura presente corresponde a la fase α, del $CdGa_2Te_4$, la segunda está comprendida entre z=0.03 y z=0.9 en la cual las aleaciones presentan estructuras γ', que corresponde a la estructura del $MnGa_2Te_4$ con algún tipo de rearreglo de los cationes, por último observamos una región que va desde z=0.9 hasta z=1.0, donde la estructura cristalina es γ, típica del $MnGa_2Te_4$, aunque no se observa de estas figuras, por el número de muestras preparadas, debe existir una región de dos fases aproximadamente entre z=0.03 y z=0.12, esta información será de importancia a la hora de construir el diagrama de fases.

3.2 Diagrama de fases del sistema $Cd_{1-z}Mn_zGa_2Te_4$.

En este sistema encontramos para la composición z=0.0 al compuesto $CdGa_2Te_4$, de éste no se han encontrado reportes de su diagrama de fases, sólo se conoce que a bajas temperaturas presenta una simetría $I\bar{4}$ (Calver 1.993). El extremo opuesto, es decir, $MnGa_2Te_4$, fue estudiado por Garbato (Garbato y col. 1987, 1993) quien reporta para este compuesto una estructura tetragonal γ con grupo espacial $I\bar{4}$, la cual es estable a bajas temperaturas, cerca de los 600 °C la fase γ empieza a desordenarse progresivamente hasta alcanzar una estructura totalmente desordenada tipo blenda de zinc a los 690 °C, para luego fundir congruentemente a los 820 °C.

3.2.1 Análisis y discusión.

En la Fig. 5 se muestra un termograma típico de ATD correspondiente a la concentración z=0.5.

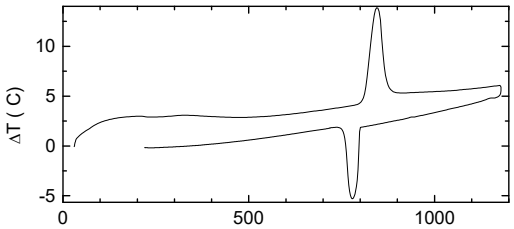

Fig. 5. Termogramas de calentamiento y enfriamiento del $Cd_{0.5}Mn_{0.5}Ga_2Te_4$. z=0.5
DTA thermograms for $Cd_{0.5}Mn_{0.5}Ga_2Te_4$. z=0.5, heating run and cooling run.

El diagrama de fases resultante del sistema, obtenido a partir de los termogramas de ATD y difracción de rayos-x, se muestra en la Fig. 6. Para z=0, es decir el compuesto $CdGa_2Te_4$, se observan 3 transiciones de fase, las cuales ocurren a las temperaturas de 426, 524 y 820 °C. Por debajo de los 426 °C el compuesto tiene una estructura tetragonal α, con grupo espacial $I\bar{4}$. Esta información se extrajo de los análisis de difracción de rayos-x y están de acuerdo con lo reportado por Calvert (Calver 1.993); por encima de esta temperatura y hasta 524 °C existe una fase α_2, posiblemente tetragonal pero con los aniones desordenados y las vacancias ordenadas, esta fase aún no ha sido identificada adecuadamente. Luego existe una fase β, que se extiende hasta 800 °C, esta fase β, corresponde a un desorden total de los aniones en la cual la muestra exhibe una simetría $F\bar{4}3m$ típica de la blenda de zinc; a lo 800 °C el compuesto funde congruentemente.

También se observa de la Fig. 6 que para el extremo z=1.0, existen tres transiciones, las dos primeras, a temperaturas por debajo de 700 °C, por su forma en los termogramas corresponden a transiciones continuas o una mezcla de transiciones continuas discontinuas, (en los termogramas no se observa un pico pronunciado en un corto rango de temperatura, por el contrario, se ve un lomo muy pequeño en el termograma y que puede extenderse en un rango de entre 50 y 150 K), estas transiciones se dan en los rangos de temperatura entre 420 °C y 480 °C y entre 600 °C y 688 °C, para temperaturas inferiores a 420 °C el compuesto exhibe una estructura tetragonal, γ, con grupo espacial $I\bar{4}$, de acuerdo con la reportada por Garbato, luego de la primera transición, es decir, por encima de los 480 °C, la fase debe ser del tipo α_2, y por encima de los 688 °C la fase es β, como se indicó anteriormente, Garbato reporta que este compuesto presentaba solo dos transiciones una progresiva cerca de 600 °C lo que está de acuerdo con los resultados encontrados en este trabajo y la de fusión a 820 °C aproximadamente, de lo termogramas podemos apreciar que el compuesto funde congruentemente como lo reporta Garbato pero a una temperatura ligeramente inferior de 780 °C. En lo que respecta a las aleaciones tenemos que a bajas temperaturas el diagrama de fases presenta cuatro regiones, la primera región es monofásica α, comprendida entre z=0.0 y z=0.02 aproximadamente, la estructura que presentan las aleaciones en esta región es tetragonal con grupo $I\bar{4}$ típica del $CdGa_2Te_4$, entre z=0.02 y z=0.12 debe existir una región de transición de dos fases, α + γ',

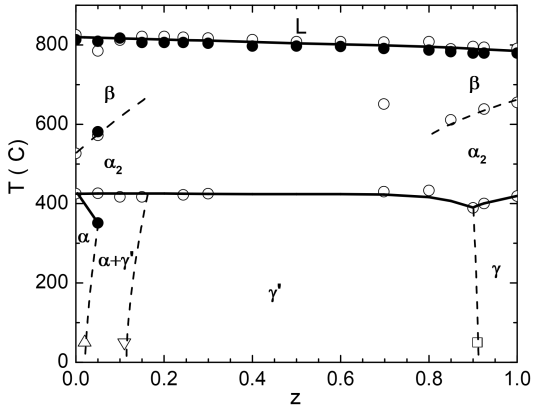

Fig. 6. Diagrama de fases del sistema $Cd_{1-z}Mn_zGa_2Te_4$, los círculos blancos fueron obtenidos durante el calentamiento y los negros durante el enfriamiento, los triángulos corresponden a las medidas de difracción de rayos-x y el cuadrado a las medidas de susceptibilidad magnética.
Phase diagram of the Cd1-zMnzGa2Te4 system, the white circles were obtained during heating and the black ones during cooling, the triangles correspond to the X-ray diffraction measurements and the square to the magnetic susceptibility measurements.

de z=0.12 y hasta z=1.0, las medidas de difracción de rayos-x y ATD, no mostraron cambio de fase alguno, sólo un cambio en la pendiente de la relación c/a cercano a z=0.9, pero las medidas de susceptibilidad magnética, que serán discutidas más adelante, indican que existe un cambio de fase magnético a z=0.9, γ '- γ , este cambio de fase está asociado a algún tipo de reordenamiento de los iones de Mn dentro de la subred catiónica; la región monofásica γ ' se extiende como se dijo anteriormente desde z= 0.12 hasta z=0.9 y desde temperatura ambiente hasta 420 ° C aproximadamente. La fase presente entre los 420 °C y por debajo de los 600 °C, posiblemente corresponde a la fase α_2, con cationes y/o vacancias parcialmente desordenados. Para todas las aleaciones existe un rango por sobre la segunda transición, T > 600 °C aproximadamente, del tipo continua en la cual la estructura presente es del tipo blenda de zinc, β, fase a la cual decaen todas estos compuestos diamantino con estructura tetragonal a temperaturas intermedias en los diagramas de fase.
Por último, se observa del diagrama de fases que todas las aleaciones incluyendo los compuestos terminales funden congruentemente entre 820 °C en z=0 y 780 °C en z=1.0

3.3 Susceptibilidad magnética del sistema $Cd_{1-z}Mn_zGa_2Te_4$.

Para el sistema bajo estudio se realizaron medidas de magnetización para muestras enfriadas sin campo magnético o Zero Field Cooling (ZFC) y para muestras enfriadas con campo magnético, Field Cooling (FC). Este tipo de medidas se realizó para las muestras en las que se observó la temperatura de transición. Para las muestras que tienen un comportamiento antiferromagnético puro, estas dos curvas no presentan ninguna diferencia, pero para las muestras que tienen un comportamiento antiferromagnético con cierto desorden en la subred catiónica, las curvas para temperaturas por encima de la temperatura de transición (región paramagnética) son iguales, pero por debajo de la temperatura de transición (región antiferromagnética) el desorden en la subred catiónica hace que los iones magnéticos no se compensen uno a uno y que descienda la susceptibilidad magnética, por el contrario, esta tiende a aumentarla. Así, esta es la primera evidencia de que un determinado material presente desorden en la subred catiónica y por ende un comportamiento tipo vidrio de spin (spin glass).

Para el caso del $MnGa_2Te_4$, su estructura cristalina ha sido reportada como tetragonal con grupo espacial $I\overline{4}$, Garbato (Garbato y col. 1987, 1993) indica que éste presenta una simetría tetragonal que se mantiene desde temperatura ambiente hasta 600 °C aproximadamente. De las medidas de susceptibilidad magnética, ZFC y FC, se deduce que los Mn se encuentran al azar en la subred catiónica, dado que de la gráfica de $1/\chi$ contra T se observa un comportamiento típico de spin-glass semejante al $MnIn_2Te_4$; esto se aprecia de la desviación de la linealidad a bajas temperaturas (Woolley y col. 1995, 1997, Morocoima y col. 2009) con un valor máximo de θ de -130K aproximadamente. También se observa para las muestras un mínimo agudo en la gráfica de $1/\chi$ contra T, correspondiente a Tg, el valor encontrado fue de 3.8K.
En la Fig. 7 se muestra lo descrito anteriormente, para la aleación con z=0.9, se observa de ella y de la extrapolación al eje de las temperaturas, que para esta concentración el valor de θ es de aproximadamente -136K y el valor de Tg, de 2.8 K; también se observa que las curvas ZFC y FC se separan una de la otra, típico del comportamiento de vidrio de espín.

De las curvas de $1/\chi$ contra T extraemos los valores de θ, C y cuando es posible Tg. La extrapolación de la parte lineal de la curva $1/\chi$ contra T al eje de las temperaturas nos da el valor de θ , un valor negativo nos indica que el comportamiento entre los iones magnéticos es del tipo antiferromagnético y la pendiente de la recta es 1/C, todo esto se extrae de la expresión de la ley de Curie-Weiss, ecuación (3). La temperatura de transición T_g (o T_N) la encontramos en el cambio de pendiente de la curva de $1/\chi$ contra T (o de χ contra T), en el mínimo (o máximo)

$$\chi = \frac{c}{T - \theta} \qquad (3)$$

En esta ecuación, χ es la susceptibilidad magnética del material, θ es la temperatura de Curie-Weiss y nos da una idea sobre el ordenamiento de los iones magnéticos y C es la constante de Curie.

Para el sistema que nos ocupa en este momento, conocemos del diagrama de fases que aparentemente hay una solución sólida desde z=0.15 hasta z=1.0, por lo que procedemos a hacer medidas de susceptibilidad magnética a todas las muestras de este rango de concentración. En regiones de dos o más fases, no es conveniente ni práctico hacer medidas de susceptibilidad o de alguna otra propiedad física, dado que no conocemos el aporte de cada fase a la propiedad medida.

Todas las gráficas de $1/\chi$ mostraron un comportamiento similar al reportado anteriormente para el $MnIn_2Te_4$ (Woolley y col. 1995), es decir, un comportamiento tipo spin-glass.

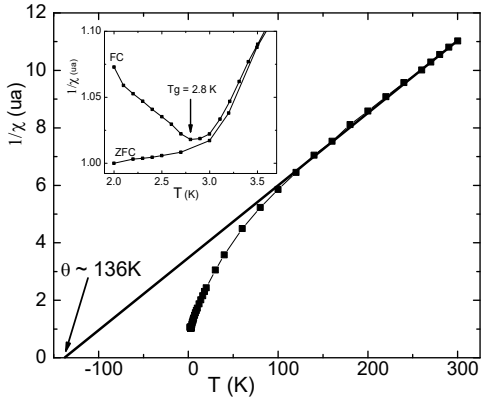

Fig. 7. Variación del inverso de la susceptibilidad, $1/\chi$, con la temperatura para la muestra z=0.9 del sistema $Cd_{1-z}Mn_zGa_2Te_4$.
Variation of reciprocal susceptibility, $1/\chi$, with temperature for the sample z=0.9 of the $Cd_{1-z}Mn_zGa_2Te_4$ alloys system.

Los valores de θ encontrados para las diferentes muestras y su variación con la composición en el rango de solución sólida, se muestran en la Fig. 8, de ella se observa una pequeña dispersión en los valores de θ para muestras entre z=0.95 y z=1.0, esto se debe quizás a un cambio en la posición de los iones Mn, en el rango entre z=0.15 y z=0.925 se observa que los valores de θ decrecen con la composición, pero no de manera lineal con z sino de manera parabólica, este comportamiento sólo se ha observado en esta aleación. Estos resultados serán usados más adelante para determinar de manera exacta la estructura cristalina de las aleaciones, dado que de la posición de los iones magnéticos en la subred catiónica, dependen estos valores.
Los valores de la constante de Curie, C, fueron calculados y su variación con z se muestra en la Fig. 9. Estos valores serán usados en trabajos futuros para determinar el momento magnético efectivo con que los iones de Mn contribuyen a las propiedades magnéticas de estos materiales estudiados.

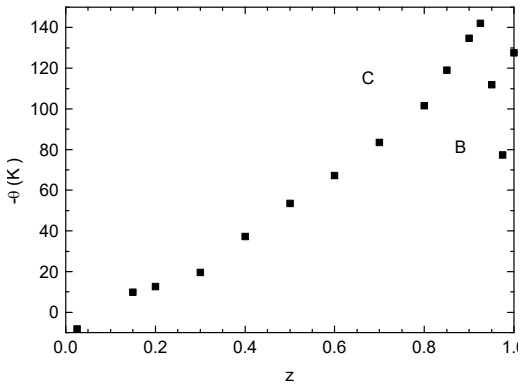

Fig. 8. Variación de la Temperatura de Curie-Weiss, θ, con la composición z, para el sistema $Cd_{1-z}Mn_zGa_2Te_4$
Variation of Curie-Weiss temperature, θ, with composition z, for the $Cd_{1-z}Mn_zGa_2Te_4$ alloys system

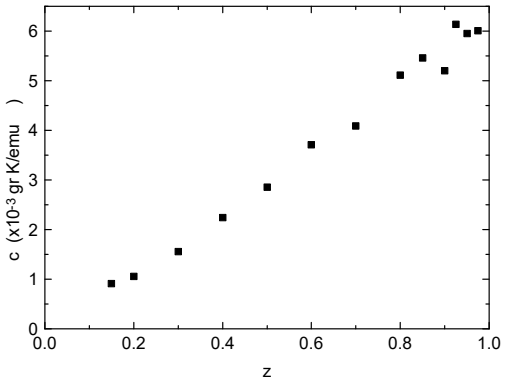

Fig. 9. Variación de la constante de Curie, C, con la composición para el sistema $Cd_{1-z}Mn_zGa_2Te_4$.
Variation of Curie constant, C, with composition for the $Cd_{1-z}Mn_zGa_2Te_4$ alloys system

Las curvas de $1/\chi$ vs T mostraron mínimos correspondientes

a la temperatura de transición Tg, estos mínimos se observaron para concentraciones mayores a z=0.8 y los resultados se muestran en la Fig. 10, de ella observamos que existen dos regiones claramente distinguibles, la primera entre z=0.9 y z=0.1, en la cual los valores de Tg varían de forma parabólica con la composición y la segunda entre z=0.8 y z=0.9 en la cual la variación es lineal con z. Con esto verificamos el cambio de fases que se presenta en el diagrama de fases del sistema $Cd_{1-z}Mn_zGa_2Te_4$.

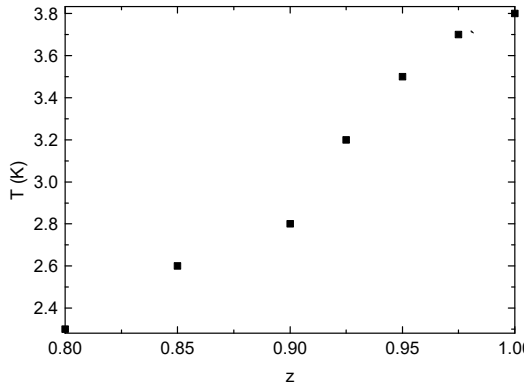

Fig. 10. Valores de la temperatura de transición, T_g, para el sistema $Cd_{1-z}Mn_zGa_2Te_4$.
Variation of transition temperature, Tg, for the $Cd_{1-z}Mn_zGa_2Te_4$ alloys system.

4 Conclusiones

Los resultados mostraron que a pesar de que ambos extremos presentan la misma simetría, la gran diferencia en el tamaño de las celdas de ambos compuestos hace que se presente un cambio de fases a muy bajas concentraciones de z, aproximadamente z=0.03, por debajo de este valor, las muestras exhiben un fase típica del $CaGa_2Te_4$ y para valores por encima de este la estructura es típica del $MnGa_2Te_4$, estos cambios en la simetría se observan en las gráficas de a vs z y c vs z, a bajas concentraciones de z (z≈0.03) y en la gráfica de c/a vs z para altas concentraciones de z (z≈0.09). El diagrama de fases propuesto, muestra un complejo cambio de estructuras que deberá ser verificado más adelantes con estudios in situ de la estructura a temperaturas en las diferentes regiones que se observan. También se observa del diagrama de fases que todas las muestras funden congruentemente a temperaturas de 820 °C para z=0 hasta 780 °C para z=1.0

Por último, las medidas de susceptibilidad magnética muestran que para todo el rango de composición las muestras exhiben un comportamiento tipo vidrio de espín. Lo que nos indica un desorden entre los iones magnéticos dentro de la subred catiónica. La variación de la temperatura de transición Tg mostró un cambio de fase magnético para z=0.9, con lo que se ratifica lo propuesto en el diagrama de fases para esta concentración y a bajas temperaturas.

Referencias

Shapira y. E.J. McNiff Jr., N.F. Oliveira Jr., E.D. Honig, K. Dwight, A. Wold, (1988) Magnetic properties of $Cu_2Zn_{1-x}Mn_xGeS_4$: Antiferromagnetic interactions in the wurtz-stannite structure. Phys. Rev. B 37, 411. DOI: https://doi.org/10.1103/PhysRevB.37.411

Furdyna, J.K., J. Kossut, in: R.K. Willardson, A.C. Beer (Eds.), (1988), Diluted Magnetic Semiconductors, Semiconductors and Semimetals, Vol.25, New York, Academic Press. https://doi.org/10.1063/1.341700

M. Quintero, E. Guerrero, P. Grima, J.C.Woolley, J . Electrochem. Soc. 136 (1989) 1220. https://doi.org/10.1016/0925-8388(94)01511-2

C. Neal, J.C. Woolley, R. Tovar, M. Quintero, J. Phys. D: Appl. Phys. 22 (1989) 1347. **DOI** 10.1088/0022-3727/22/9/016

M. Quintero, R. Tovar, H. Dhesi, J.C. Woolley, Phys. Stat. Sol. (a) 115 (1989) 157. https://doi.org/10.1016/S0022-3697(96)00109-6

M. Morocoima, F. Pineda, M. Quintero, E. Quintero, E. Moreno, P. Grima, R. Tovar, P. Bocaranda, J.A. Henao, Physica B 404 (2009) 1819–1825 https://doi.org/10.1016/j.physb.2009.02.027

K.J. Range, H. Hubner, Z. Naturforsch. 31b (1976) 886 http://www.znaturforsch.com/ab/v31b/c31b.htm

M. Quintero, M. Morocoima, E. Guerrero, R. Tovar, M. Delgado, J.C. Woolley, P. Conflant, J. Cryst. Growth 114 (1991) 661. https://doi.org/10.1016/0022-0248(91)90413-Y

J.C. Woolley, S. Bass, A.-M. Lamarche, G. Lamarche, M. Quintero, M. Morocoima, P. Bocaranda, J. Magn. Magn. Mater. 150 (1995) 353. https://doi.org/10.1016/0304-8853(95)00294-4

J.C. Woolley, R. Brun del Re, M. Quintero, Phys. Stat. Sol. (a) 159 (1997) 361. https://onlinelibrary.wiley.com/doi/abs/10.1002/1521-396X(199702)159:2%3C361::AID-PSSA361%3E3.0.CO;2-%23

McCabe G.H., T. Fries, M.T. Liu, Y. Shapira, L.R. Ram-Moham, R. Kershaw, A. Wold. C. Fau, M. Averous, E.J. McNiff Jr. (1997), Bound magnetic polarons in *p*-type $Cu_2Mn_{0.9}Zn_{0.1}SnS_4$, Phys. Rev. B 56 6673. https://doi.org/10.1103/PhysRevB.56.6673

E. Quintero, M. Quintero, M. Morocoima, and P. Bocaranda, (2007), Bound magnetic polaron in p-

type $Cu_2Cd_{0.25}Fe_{0.75}GeSe_4$ and $Cu_2FeGeTe_4$, J. Appl. Phis. 102, 083905. DOI: https://doi.org/10.1103/PhysRevB.56.6673

Calver Larson, PDF-2 Sets 1-43 database, file 28-187 (1.993) https://www.icdd.com/pdfsearch/

L. Garbato, A. Geddo-Lehmann, F. Ledda, M. Cannas and O. Devoto, Jpn. J. Phys. 32, 3, 389-390, (1.993) https://scispace.com/papers/t-x-diagram-of-the-mnte-1-x-ga2te3-xsystem-3c0j6nj9xw

Garbato L., F. Ledda and Rucci, (1987), Structural distortions and polymorphic behaviour in abc_2 and ab_2c_4 tetrahedral compounds, Prog. Crysta/ Growth and Charact. 15, pp. 1-41 https://doi.org/10.1016/0146-3535(87)90008-6

E. Moreno, M. Quintero, M. A. Villarreal, E. Quintero, M. Morocoima, G. E. Delgado, J. Contreras, M. Chourio; Rev. LatinAm. Metal. Mat. 2021; **41** (1): 50-59 https://rlmm.org/ojs-files/full_pdf/RLMM-2021-V41N1.pdf

Correa Pizano, Ana; Lacruz, María Alejandra; Sánchez, María Angélica; Caldera, Dayana; Quintero, Miguel; Marín, Giovanni; Morocoima, Manuel, Revista Ciencia e Ingeniería. Vol. 46, No. 2 pp. 173-178, abril-julio, 2025. http://erevistas.saber.ula.ve/index.php/cienciaeingenieria/article/view/19776

Rose-Innes, A.C; Rhoderick, H.E. (1.978). Introduction to superconductivity, Secon Edition, Pergamon Press, Toronto. https://www.sciencedirect.com/book/9780080216515/introduction-to-superconductivity

Received: February 12th, 2025

Accepted: June 25th, 2025

***Lacruz Páez, María Alejandra**, Licenciada en Química, 2006, Magíster en Química Aplicada, Opción Nuevos Materiales, 2009, Profesora Asistente, Laboratorio de Espectroscopía Analítica, Departamento de Química, Facultad de Ciencias, Universidad de Los Andes, Mérida, Venezuela.*
Correo: alejandra030707@gmail.com
https://orcid.org/ 0009-0001-5888-2160

***Soto, Orielys.** Licenciada en Física. Profesora Instructor, adscrita al Centro de Estudio de Semiconductores.*
Correo: orielys1012@gmail.com
https://orcid.org/ 0009-0001-5075-5239

***Power, Chrystian**, Licenciado en Física por la Universidad de Los Andes, MSc en Química Aplicada y Dr. En química Aplicada, PIQA, por la Universidad de Los Andes y Dr. En Física por la Universidad de Toulouse III, Paul Sabatier (Francia). Su investigación se enfoca en el estudio de propiedades ópticas de nuevos materiales semiconductores bajo Altas Presiones. Profesor Titular, e Investigador del Centro de Estudios de Semiconductores (CES-ULA), Departamento de Física, Facultad de Ciencias, Universidad de Los Andes, Mérida, Venezuela.*
Correo: ch.power.medina@gmail.com
https://orcid.org/ 0009-0008-5298-2532

***Villarreal, Manuel.** Se tituló en Física y obtuvo los grados de Magister Scientiae y Doctor en Química Aplicada, Mención: Estudio de Materiales, por la Universidad de Los Andes (Venezuela) en 2011. Adscrito al Instituto de Matemática, Estatística e Física. Universidad Federal do Rio Grande, FURG. Rio Grande do Sul, Brasil. Su investigación se enfoca en el estudio de nuevos materiales semiconductores, propiedades eléctricas, ópticas y magnéticas; la enseñanza de la Física y la didáctica de las Ciencias Naturales*
Correo: mavu8473@gmail.com
https://orcid.org/ 0000-0002-3863-4856

***Quintero, Miguel.** Licenciado en Física por la Universidad de Los Andes y PhD en Física, por la Universidad de Ottawa, Canadá en 1985. Su investigación se enfoca en el estudio de nuevos materiales semiconductores, síntesis, caracterización, diagramas de fases, propiedades térmicas, eléctricas, ópticas y magnéticas. Profesor Titular, e Investigador del Centro de Estudios de Semiconductores (CES-ULA), Departamento de Física, Facultad de Ciencias, Universidad de Los Andes, Mérida, Venezuela.*
Correo: marparra61@gmail.com
https://orcid.org/ 0009-0001-5468-2196

***Morocoima, Manuel.** Licenciado en Física, MSc y Dr. en Química Aplicada, en la Opción de Nuevos Materiales, miembro del Centro de Estudios de Semiconductores, (Director), Profesor Titular del Departamento de Física, Facultad de Ciencias, Universidad de Los Andes, Venezuela. Línea de investigación: Semiconductores Magnéticos. Caracterización estructural y propiedades ópticas, térmicas y magnéticas de semiconductores magnéticos.*
https://orcid.org/0000-0003-3571-5906

Artículo de Investigación. Revista Ciencia e Ingeniería. Vol. 46, No. 3 pp. 251-264, agosto-noviembre, 2025.
ISSN 1316-7081. ISSN Elect. 2244-8780 Universidad de los Andes (ULA)

Chitosan-based biomaterials for hydrogels in bone tissue regeneration

Biomateriales a base de quitosano para hidrogeles de regeneración del tejido óseo

Rondón, Jairo[1,2]; Ramirez-Vargas, Kimberly[1]*; Saucedo-Vazquez, Juan Pablo[3]; Ávila, Edward E.[4]
[1]Chemical Engineering Department, Universidad Politécnica de Puerto Rico, PR 00918 USA
[2]Biomedical Engineering Department, Universidad Politécnica de Puerto Rico, PR 00918 USA
[3]CATS Research Group, School of Chemical Sciences and Engineering, Yachay Tech, Urcuqui 100119, Ecuador
[3]GIAMP, School of Chemical Sciences and Engineering, Yachay Tech, Urcuqui 100119, Ecuador
*ramirez_106541@students.pupr.edu

Abstract

Bone regeneration remains a major challenge in biomedical engineering, particularly due to the clinical limitations of autologous and allogeneic grafts. In this context, chitosan-based hydrogels (CHs) have emerged as promising platforms due to their biocompatibility, gelation capacity, structural porosity, and ease of functionalization. This review presents a comprehensive analysis of the biological fundamentals of bone regeneration, the physicochemical properties of chitosan, and the hydrogel fabrication techniques employed to emulate the bone extracellular matrix. Alternative sources of chitin (crustaceans, insects, fungi) are examined, along with deacetylation methods (chemical, enzymatic, microwave-assisted, and deep eutectic solvents) and their impact on the degree of deacetylation (DD), molecular weight, and mechanical behavior of the material. Advanced approaches such as electrospinning, freeze-drying, and 3D bioprinting are described, highlighting their influence on porous architecture, controlled release of osteoinductive factors, and cell viability. Current challenges are also identified, including limited solubility, lack of standardization of structural parameters, and the clinical scalability of CHs, proposing research lines oriented toward personalized therapies and multifunctional bioactive platforms. Furthermore, application perspectives in osteochondral regeneration, targeted drug delivery, and tissue bioprinting are discussed, reinforcing the potential of chitosan as a strategic biopolymer in regenerative medicine.

Keywords: hydrogels, chitosan, chemical properties, mechanical properties, tissue engineering.

Resumen

La regeneración ósea sigue siendo un gran desafío en la ingeniería biomédica, debido principalmente a las limitaciones clínicas de los injertos autólogos y alogénicos. En este contexto, los hidrogeles basados en quitosano (CHs) han surgido como plataformas prometedoras gracias a su biocompatibilidad, capacidad de gelación, porosidad estructural y facilidad de funcionalización. Esta revisión ofrece un análisis exhaustivo de los fundamentos biológicos de la regeneración ósea, las propiedades fisicoquímicas del quitosano y las técnicas de fabricación de hidrogeles empleadas para emular la matriz extracelular ósea. Se examinan fuentes alternativas de quitina (crustáceos, insectos y hongos), junto con los métodos de desacetilación (químicos, enzimáticos, asistidos por microondas y con disolventes eutécticos profundos) y su impacto en el grado de desacetilación (DD), el peso molecular y el comportamiento mecánico del material. Se describen enfoques avanzados como el electrohilado, la liofilización y la bioimpresión 3D, destacando su influencia en la arquitectura porosa, la liberación controlada de factores osteoinductivos y la viabilidad celular. También se identifican los retos actuales como la solubilidad limitada, la falta de estandarización de parámetros estructurales y la escalabilidad clínica de los CHs) y se proponen líneas de investigación orientadas hacia terapias personalizadas y plataformas bioactivas multifuncionales. Además, se discuten las perspectivas de aplicación en regeneración osteocondral, liberación dirigida de fármacos e impresión de tejidos, reforzando el potencial del quitosano como biopolímero estratégico en la medicina regenerativa.

Palabras clave: hidrogeles, quitosano, propiedades químicas, propiedades mecánicas, ingeniería de tejidos

1 Introduction

The need to restore lost bone tissue remains a significant challenge in biomedical engineering and clinical practice. Although autologous and allogeneic bone grafting procedures are effective, they are associated with significant complications, such as donor site morbidity, risk of cross-infection, and limited material availability (Ansari, 2019). In this context, tissue engineering has emerged as a promising strategy, proposing the design of biomimetic scaffolds capable of emulating the extracellular matrix (ECM) while simultaneously promoting in situ bone regeneration (De León-Oliva *et al*., 2023; Rondón *et al*., 2025).

Among the candidate biomaterials, chitosan-based hydrogels stand out due to their remarkable biocompatibility, hydrophilic nature, and ability to form highly porous three-dimensional networks—key properties that support cell adhesion, migration, and differentiation (Aguilar *et al*., 2019; Kim *et al*., 2023). Chitosan, a polysaccharide obtained by the deacetylation of chitin derived from marine waste, insects, and fungi, contains free amino groups that confer a positive charge under physiological conditions. This facilitates electrostatic interactions with ECM proteins and promotes bone mineralization (Aranaz *et al*., 2021). Furthermore, chitosan can be chemically modified to tune its solubility, responsiveness to stimuli, and degradation profile, thereby expanding its applicability in advanced therapeutic approaches (Novikov *et al*., 2023).

Literature reports indicate that chitosan hydrogels—whether injectable, self-healing, or structured via 3D bioprinting—enable the controlled incorporation of osteoinductive factors, hydroxyapatite nanoparticles, or osteoprogenitor cells, thus enhancing bone neogenesis and integration with host tissue (Li *et al*., 2023; Lazaridou *et al*., 2022). Their porous architecture and high-water content (>90%) recreate a physiological microenvironment that facilitates nutrient and metabolite exchange—an essential feature in critical-size bone defects where vascularization is often compromised (Nallusamy & Das, 2021).

However, the versatility of chitosan strongly depends on its source and degree of deacetylation (DD). These parameters influence its molecular weight, crystallinity, and mechanical and biological properties (Huq *et al*., 2022). Therefore, standardization of purification and characterization methods is essential to ensure reproducibility and clinical safety. In this context, the present review article aims to:

1. Critically analyze the sources, extraction methods, and chemical modifications of chitosan, emphasizing their impact on physicochemical properties relevant to bone regeneration.
2. Summarize recent advances in the design and fabrication of chitosan hydrogels—including electrospinning, lyophilization, and 3D printing techniques—and their relationship with cellular responses and new bone formation.
3. Identify knowledge gaps and technical challenges that still hinder the clinical translation of these systems, proposing future research directions aligned with trends in personalized medicine and biofabrication.

The discussion is structured into sections covering (i) the biological fundamentals of bone regeneration, (ii) the intrinsic characteristics of chitosan, (iii) hydrogel synthesis methodologies, and (iv) their main biomedical applications. This comprehensive overview aims to help researchers and clinicians assess the real potential of these biomaterials and guide the development of more effective therapeutic strategies.

2 Methodology

2.1 Search strategy and databases

A systematic literature search was conducted following the PRISMA guidelines for reviews (Page *et al*., 2021; Moher *et al*., 2009). Search was performed between January and March 2025 across the following electronic databases: PubMed/MEDLINE, Scopus, Web of Science, ScienceDirect, Wiley Online Library, Royal Society of Chemistry, MDPI, IEEE Xplore, SciELO, RedALyC, and Google Scholar. Additionally, indexed conference proceedings and the reference lists of key articles were screened to identify further relevant literature.

Search queries used Boolean operators and truncation; a representative example was: (bone regeneration OR "bone tissue engineering") AND (chitosan OR "chitosan hydrogel*" OR quitosano) AND (scaffold* OR hydrogel* OR biomaterial*).

2.2 Inclusion and exclusion criteria

Table 1 summarizes the inclusion and exclusion criteria used in this review.

2.3 Data extraction and organization

For each eligible study, the following information was recorded:

- Source and type of chitin/chitosan (crustacean, insect, fungus)
- Degree of deacetylation (DD) and molecular weight
- Hydrogel synthesis method (physical crosslinking, chemical crosslinking, self-assembly, 3D printing,

electrospinning, freeze-drying, etc.)
- Chemical properties (surface charge, solubility, crystallinity) and mechanical properties (elastic modulus, tensile strength, porosity)
- Biological model design (cell lines, animal models, growth factors, mineralization, evaluation times)
- Main outcomes and reported limitations

The reference manager Mendeley was used to filter and classify articles according to the thematic focus of this review:

a. Composition and origin of chitosan (source, DD, purity)
b. Physicochemical and mechanical properties relevant to osteogenesis
c. Hydrogel fabrication techniques and their impact on biological performance

2.4 Qualitative synthesis

Data were grouped according to the classification scheme proposed by Nallusamy and Das (2021) for hydrogels, complemented by the chemical modification taxonomy proposed by Aranaz *et al*. (2021). An analysis was conducted on the relationship between the production method, resulting properties, and preclinical outcomes. This approach allowed for identifying correlations and knowledge gaps, which will be discussed in subsequent sections.

Table 1. Inclusion and exclusion criteria of the study.

Category	Inclusion Criteria	Exclusion Criteria
Document Type	Original research articles, systematic or narrative reviews, and peer-reviewed experimental reports with full text	Abstracts without full text, non-peer-reviewed short communications, and patents
Language	English or Spanish	Other languages
Time Frame	Publications between January 1, 2004, and March 31, 2025	Publications outside this time range
Content	Studies describing chitosan-based hydrogels for bone regeneration (*in vitro*, *in vivo*, or *ex vivo*), including data on composition, synthesis, physicochemical properties, or biological performance	Studies have not focused on chitosan or are not related to bone tissue.
Quality	Clear experimental design and minimum quantitative data ($n \geq 3$)	Insufficient methodological information or duplicate studies

3 Results and discussion

3.1 Biological fundamentals of bone regeneration

Bone regeneration is a highly coordinated process that fundamentally mimics the mechanisms of embryonic skeletal development. It is considered a model of complete tissue regeneration, as the newly formed tissue preserves the original's structure and functionality (Ansari, 2019). This process is crucial for fracture healing and tissue engineering applications aimed at restoring bone volume lost due to trauma, degenerative diseases, or tumor resections.

3.1.1 Physiological process of bone regeneration

Bone regeneration (Figure 1) occurs in three sequential but interrelated phases: inflammation, new bone formation, and remodeling (Henry & Bordoni, 2023). In the inflammatory phase, tissue rupture triggers the release of cytokines and growth factors (such as TGF-β, BMPs, and PDGFs), which initiate the hemostatic cascade, followed by the recruitment of inflammatory cells to the injury site. This phase establishes a key pro-regenerative environment for the next stage. During callus formation, fibrous tissue and cartilage (soft callus) are initially produced and mineralized into immature bone (hard callus). This process critically depends on the osteogenic activity of progenitor cells and a microenvironment that provides adequate oxygenation, nutrients, and structural support.

Remodeling involves the resorption of primary bone and its replacement with mature lamellar bone, restoring the original osteonal architecture. Depending on mechanical, hormonal, and cellular factors, this process can last for months or even years (Yue *et al*., 2020).

3.1.2 Cells involved in bone regeneration

Bone tissue is highly dynamic and depends on the coordinated action of multiple cell types. Among the most relevant in bone regeneration are:

- Osteoprogenitor or osteogenic cells: Mesenchymal stem cells located in the periosteum and endosteum. They can differentiate into osteoblasts under appropriate mechanical and biochemical stimuli

(Henry & Bordoni, 2023).

- Osteoblasts: Bone-forming cells derived from mesenchymal progenitors. They secrete osteoid matrix rich in type I collagen and play an active role in bone mineralization. They also express alkaline phosphatase and osteocalcin, key osteoblastic phenotype markers (Li *et al*., 2023).
- Osteocytes: Mature osteoblasts that become embedded in the mineralized matrix. They communicate through canaliculi and play roles in mechanotransduction, mineral homeostasis, and signaling for bone remodeling. Osteocytes are the most abundant cells in bone tissue (Nahian *et al*., 2023).
- Osteoclasts *(though not osteogenic)*: Multinucleated cells derived from the hematopoietic lineage, responsible for bone resorption. Their functional balance with osteoblasts ensures appropriate physiological bone remodeling.

The activation and coordination of these cells are regulated by systemic factors (hormones, vitamins), local signals (cytokines, growth factors), and the physicochemical microenvironment of the bone niche.

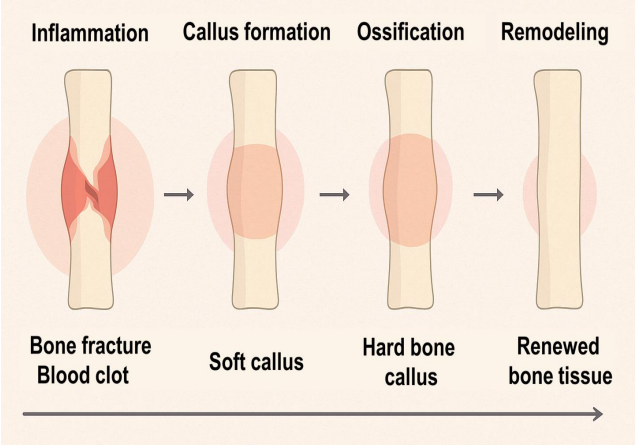

Figure 1. Physiological process of bone regeneration.

3.1.3 Composition of the bone matrix

The bone extracellular matrix (ECM) constitutes the biological scaffold that provides mechanical strength and biochemical signaling. Its composition can be divided into three main fractions:

- Organic fraction (~30% of dry weight): Predominantly composed of type I collagen (90–95% of the organic matrix), along with type V collagen, proteoglycans (such as decorin and biglycan), glycoproteins (osteonectin, osteopontin), growth factors, and bone morphogenetic proteins (BMPs) (De León-Oliva *et al*., 2023). These components mediate cell–matrix interactions and modulate cell adhesion, migration, and differentiation processes.
- Inorganic fraction (~60%): Primarily composed of hydroxyapatite crystals [$Ca_{10}(PO_4)_6(OH)_2$], which are responsible for bone mineralization and stiffness. This phase provides the tissue with its ability to withstand compressive forces.
- Water (~10%): Essential for nutrient transport, ion exchange, and maintenance of osmotic balance within the tissue.

Accurately replicating these characteristics in a biomaterial is essential for the design of functional scaffolds. For this reason, chitosan-based hydrogels—offering a hydrated polymeric matrix with tunable chemical functionality—have emerged as promising candidates to mimic the bone ECM (Aranaz *et al*., 2021; Kim *et al*., 2023).

3.2. Hydrogels as platforms for bone tissue engineering

Hydrogels have assumed a central role in designing biofunctional platforms for tissue engineering, particularly in bone regeneration. Thanks to their high water content, soft yet crosslinked structure, and capacity for chemical functionalization, hydrogels efficiently mimic the properties of the bone's natural extracellular matrix (ECM), thus facilitating cell adhesion, proliferation, and differentiation (Li *et al*., 2023; Aranaz *et al*., 2021). In the specific case of chitosan, its polysaccharide structure with primary amino groups allows a wide range of physicochemical modifications, making it a versatile material for biomedical applications.

3.2.1 Functional characteristics of hydrogels

Hydrogels are three-dimensional networks of hydrophilic polymers capable of absorbing large amounts of water or biological fluids without losing their structural integrity. This feature enables them to create microenvironments similar to soft tissues, thus promoting cell regeneration and favorable biological interactions (Nallusamy & Das, 2021).

From a functional perspective, chitosan hydrogels exhibit:

- High swelling capacity supports the transport of nutrients and the removal of cellular waste.
- Selective permeability is proper for gas exchange and controlled diffusion of biomolecules.
- Enzymatic biodegradability, due to the action of lysozyme in the human body, enables gradual integration with host tissue (Nguyen *et al*., 2023).
- Intrinsic antimicrobial properties, related to their positive surface charge, which helps prevent postoperative infections (Szymańska & Winnicka, 2015).

- Ease of modification, allowing for incorporating osteoinductive agents, nanoparticles, or progenitor cells through mild encapsulation techniques (Kim *et al*., 2023).

3.2.2 Role as 3D scaffolds: biocompatibility, porosity, and bioactivity

The design of three-dimensional (3D) scaffolds is an essential component of tissue engineering, as these structures must replicate the biochemical and structural environment of the bone matrix. Chitosan hydrogels fulfill several key requirements for this purpose (Figure 2):

- Biocompatibility: It is well documented that chitosan does not induce adverse immune responses under physiological conditions. Additionally, its cationic charge facilitates cell adhesion through interactions with ECM proteins and cell membranes (Freier *et al*., 2005).
- Porosity and interconnected architecture: The porous structure of hydrogels allows for efficient nutrient transport, metabolite removal, and cell migration—all critical factors in bone regeneration. For instance, pore sizes greater than 100 µm are optimal for vascularized bone tissue formation (Madihally & Matthew, 1999).
- Bioactivity: Through functionalization with peptides (e.g., RGD, BMP), hydroxyapatite nanoparticles (nHA), or growth factors, the hydrogel can be transformed into a bioactive system that not only supports but actively induces osteogenesis (Aguilar *et al*., 2019; Oliveira *et al*., 2021).
- Adaptable mechanical properties: While hydrogels alone do not exhibit the rigidity of cortical bone, they can be reinforced with bioceramics or inorganic phases to increase their elastic modulus without compromising biocompatibility (Kumar *et al*., 2019).

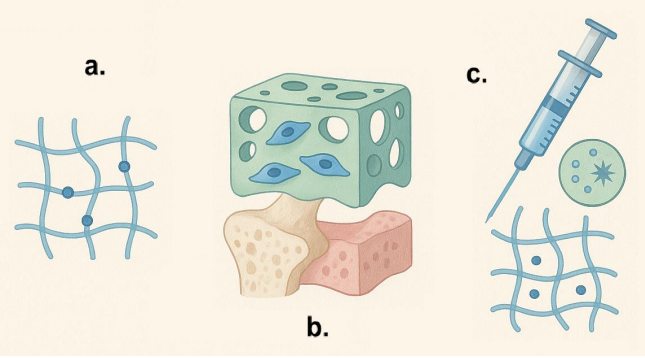

Figure 2. Hydrogels as bone tissue engineering platforms: a. functional characteristics of hydrogels; b. role as 3D scaffolds: biocompatibility, porosity, and bioactivity; c. injectable hydrogels, controlled release, and growth factors.

3.2.3 Injectable hydrogels, controlled release, and growth factors

One of the most promising innovations in this field is the development of injectable hydrogels, which can be applied to bone defects minimally invasively. These hydrogels can conform *in situ* to the shape of the defect and solidify via physical (thermogelation) or chemical (in situ crosslinking) mechanisms (Patois *et al*., 2009).

Furthermore, these systems can serve as controlled-release vehicles for bioactive agents. It has been demonstrated that growth factors such as:

- Bone morphogenetic proteins (BMP-2, BMP-7)
- Platelet-derived growth factors (PDGFs)
- Vascular endothelial growth factors (VEGFs)
- Transforming growth factors beta (TGF-β)

can be loaded into the hydrogel matrix and released in a sustained manner, thereby promoting not only osteogenesis but also angiogenesis, which is critical for the integration of newly formed tissue (Oliveira *et al*., 2021). These smart systems also allow the co-encapsulation of osteoprogenitor cells, leading to the development of multifunctional platforms capable of regenerating bone in complex environments with minimal surgical intervention (Li *et al*., 2023).

3.3 Origin of chitosan and extraction methods

Chitosan is a biopolymer derived from chitin, the second most abundant natural polysaccharide in the biosphere after cellulose. Chitin is found in a wide variety of invertebrates and microorganisms, and its conversion to chitosan through deacetylation processes is a critical step for biomedical applications. The origin of chitin directly influences the structural, physicochemical, and functional characteristics of the resulting chitosan. Therefore, it is essential to consider both the source and the extraction method when designing hydrogels for tissue engineering (Aguilar *et al*., 2019; Pellis *et al*., 2022).

3.3.1 Chitin sources: crustaceans, insects, fungi

a. Crustaceans: The most common commercial source of chitin is marine crustacean waste (shrimp, crabs, lobsters). This chitin is usually of the α-type, characterized by a highly crystalline and ordered structure, making it more resistant but also more difficult to deacetylate (Huq *et al*., 2022). It remains the most widely available option due to the large volume of waste generated by the fishing industry.
b. Insects: The exoskeletons of insects such as beetles, crickets, and larvae also contain chitin, generally with fewer minerals and allergens than crustaceans. Chitin extracted from insects typically presents a mix of α and β forms with a less compact structure, which may

facilitate its transformation into chitosan (Mohan *et al*., 2020; Hahn *et al*., 2020).

c. Fungi: Chitin from filamentous fungi and yeasts often exists as a chitin–glucan complex. It offers advantages such as being a more sustainable and low-allergen source and is independent of seasonality. However, its extraction is more complex, and the chitin content per unit of biomass is relatively low (Huq *et al*., 2022).

3.3.2 Source comparison

Table 2 summarizes the advantages, limitations, and degree of deacetylation (DD) for chitosan derived from the main biological sources:

3.3.3 Deacetylation processes: chemical, enzymatic, microwave, des

Transforming chitin into chitosan requires the removal of acetyl groups from N-acetylglucosamine units. This reaction can be performed using chemical, biological, or hybrid methods, each with different impacts on the degree of deacetylation (DD), molecular weight, and polymer chain distribution.

a. Chemical Method (alkaline and acidic): This is the most widely used industrial approach. It involves concentrated sodium hydroxide (NaOH) solutions at elevated temperatures (80–120 °C). It can achieve DD values above 80%, although it may degrade the polymer (Pellis *et al*., 2022). Pre-acidification with HCl is used for demineralization. Example: 50% NaOH at 100 °C for 1 hour (Pellis *et al*., 2022; Novikov *et al*., 2023).
b. Enzymatic Method: This approach uses chitinase and chitin deacetylase under mild conditions. While more environmentally friendly, it results in low DD values (10–30%) and slow kinetics, making it currently unfeasible for mass production (Harmsen *et al*., 2019).
c. Microwave-Assisted: This method relies on rapid, uniform heating of the sample in the presence of NaOH. It can accelerate the reaction within minutes, reaching up to 75% DD with reduced structural degradation (Tahir *et al*., 2024).
d. Steam Explosion: Involves high-pressure steam followed by rapid decompression to break down chitin structure, facilitating subsequent deacetylation. It is mainly used with shrimp and crab shell waste (Sugiyanti *et al*., 2019).
e. Deep Eutectic Solvents (DES): An emerging method using mixtures of hydrogen bond donors and acceptors (e.g., choline: malic acid) that melt at low temperatures. It enables controlled and environmentally friendly deacetylation. However, current efficiency remains limited (maximum ~40% DD in 24 hours) (Pellis *et al*., 2022).

3.4 Chemical and mechanical properties of chitosan

The performance of chitosan as a biomaterial for tissue engineering applications largely depends on its physicochemical properties. These characteristics determine its behavior in biological environments, its processability into forms such as hydrogels or films, and its compatibility with cells and tissues. The most relevant properties of chitosan for the design of hydrogels intended for bone regeneration are described below.

3.4.1 Chemical structure and functional groups

Chitosan is a linear polysaccharide composed of repeating units of D-glucosamine and N-acetyl-D-glucosamine, linked by β-(1→4) glycosidic bonds, similar to cellulose. Its structure results from the partial deacetylation of chitin (Figure 1). The degree of deacetylation (DD), typically ranging from 50% to 95%, defines the proportion of units with free amino groups (–NH_2), which are responsible for many of its functional properties (Aranaz *et al*., 2021; Ioelovich, 2014). Key functional groups include:

- Primary amino group (–NH_2) at carbon 2 of D-glucosamine → imparts positive charge in acidic media, enabling interactions with cell membranes and proteins.
- Hydroxyl groups (–OH) at carbons 3 and 6 → enable crosslinking and chemical modifications.
- Glycosidic bond (C1–O–C4) → provides structural integrity to the polymer chain.

These functional groups allow for crosslinking with aldehydes, organic acids, or ionic agents, and facilitate the incorporation of bioactive molecules, granting chitosan significant versatility in hydrogel formulation (Kim *et al*., 2023).

Table 2. Chitosan characteristics according to its source.

Source	Advantages	Limitations	Degree of Deacetylation (DD)
Crustaceans	- High availability - Established industrial methods - High chitin concentration	- Potential allergens - Presence of heavy metals - Use of harsh chemicals	56–98% (Triunfo *et al*., 2022)
Insects	- Low allergen content - High hydration and solubility capacity	- Requires melanin bleaching step - Limited large-scale production	62–98% (Mohan *et al*., 2020)
Fungi	- Animal protein-free source - More controlled process	- Difficult chitin–glucan separation - Lower yield -	70–93% (Huq *et al*.,

- Lower toxicity	Higher processing costs	2022)

3.4.2 pH, biodegradability, cell adhesion, and immunogenicity

a. pH and Solubility: Chitosan is soluble in acidic solutions (pH < 6.5) due to the protonation of its amino groups. It has a pKa of approximately 6.3, making it ideal for applications in slightly acidic biological environments such as wounds or inflammatory microenvironments. For applications in neutral pH settings (e.g., physiological bone tissue, pH ≈ 7.4), chemical modifications are required to enhance its solubility (Nguyen *et al*., 2023).
b. Biodegradability: Chitosan is degraded in the body by enzymes such as lysozyme, which cleaves the β-(1→4) glycosidic bonds. The degradation rate depends on the degree of deacetylation, molecular weight, and the extent of hydrogel crosslinking. This is advantageous for tissue engineering, as it allows the scaffold to be gradually resorbed as the regenerated tissue replaces it (Sawaguchi *et al*., 2015).
c. Cell Adhesion and Biointeractivity: Chitosan can promote cell adhesion due to electrostatic interactions with extracellular matrix glycoproteins and its compatibility with cellular receptors. The presence of amino groups enhances the adsorption of adhesion proteins (e.g., fibronectin, vitronectin), which in turn mediate the anchoring of osteoblasts and mesenchymal stem cells (Freier *et al*., 2005).
d. Immunogenicity: Numerous studies have shown that chitosan is biocompatible and non-immunogenic under normal conditions. However, it can modulate the immune response by activating antigen-presenting cells and promoting the production of cytokines that are beneficial for bone regeneration. Its effects on the Th1/Th2 axis have been explored as a potential adjuvant in immunotherapy (Li *et al*., 2021).

3.4.3 Mechanical properties

The mechanical properties of pure chitosan are relatively low compared to ceramic or metallic composites, but sufficient for soft tissue applications and, when reinforced, for bone tissue engineering.

The strength and stiffness of chitosan hydrogels can be modulated through:

- Polymer concentration
- Type of crosslinking (physical vs. chemical)
- Addition of nanofillers, such as hydroxyapatite or nanocellulose

Tensile Strength and Elastic Modulus:

- Chitosan films with 75–90% DD exhibit tensile strengths of 50–80 MPa (Chandra *et al*., 2023).
- Chitosan fibers show lower tensile strength, ranging from 11–20 MPa, depending on mechanical treatment and chain alignment.
- Pure chitosan hydrogels have an elastic modulus of approximately 0.29 ± 0.06 MPa, which can increase significantly with reinforcement using nano-hydroxyapatite (Kumar *et al*., 2019).

Porosity and Apparent Density: Structural porosity is critical for enabling cell migration and the formation of vascularized bone tissue. Chitosan hydrogels commonly exhibit porosity values greater than 90%, with pore diameters that can be tuned using techniques such as freeze-drying or electrospinning (Putri & Elsheikh, 2022).

Structural Flexibility: Zhang *et al.* (2021) demonstrated that chitosan hydrogels can exhibit sufficient flexibility to be knotted without breaking, while also supporting weights of up to 475 grams—highlighting their potential for use under moderate mechanical conditions (Zhang *et al*., 2021).

3.5 Chitosan hydrogel fabrication techniques

The biological performance of a hydrogel does not depend solely on the chemical composition of chitosan. The resulting microarchitecture from the fabrication process plays a crucial role in cell migration, nutrient diffusion, and integration with host bone. Below, the three most established processing strategies and their next-generation variants are described, highlighting how each technique modulates the scaffold's morphology, mechanics, and bioactivity.

3.5.1 Electrospinning: biomimetic nanofibers

Electrospinning generates fibers with diameters ranging from 50 nm to 2 µm that mimic the morphology of type I collagen, the main component of the bone matrix. Under a high-voltage electric field, the chitosan solution (often blended with PEO, PCL, or gelatin to adjust viscosity and conductivity) is stretched to form a Taylor cone and deposited as a nonwoven mesh on a collector (Subbiah *et al*., 2005).

Recent advances:

- Chitosan-hydroxyapatite blends have been shown to enhance mineralization and compressive strength of nanofibers, thanks to *in situ* apatite nucleation along the polymer-ceramic network (Purohit *et al*., 2024).
- The use of hydroxypropyl chitosan has enabled better wettability control and accelerated osteoblastic differentiation in *in vitro* models

(Wang *et al*., 2025a).
- Bibliometric studies report a >30% increase in publications on electrospinning-bone in the last two years, indicating rapid clinical adoption (Ma *et al*., 2025).

Mechanical and biological implications:

Electrospun mats exhibit moduli up to 10 MPa and submicron pores that support guided cell migration; being stackable, they enable porosity gradients for complex bone defects (Mazoochi & Jabbari, 2011; Saber *et al*., 2025). However, post-crosslinking (e.g., HCl vapors, genipin) is required to maintain integrity in aqueous environments.

3.5.2 Freeze-drying and freeze-casting: directional macroporosity

Freeze-drying starts with an acidic chitosan solution that is frozen and then subjected to sublimation under vacuum, leaving a spongy network with >90% porosity (Madihally & Matthew, 1999). Variants such as freeze-casting control the thermal gradient to orient ice crystals, generating axial channels that improve vascularization.

Recent advances

- Xylem-inspired structures with centripetal channels have doubled vascular infiltration rates in critical tibial defects (Wang *et al*., 2025b). Freeze-dried chitosan foams show significant bone regeneration in rat calvarial defects, comparable to autografts (Fathy *et al*., 2025).
- 2025 reviews highlight freeze-drying's relevance for achieving compressive strengths >0.5 MPa while maintaining interconnected porosity (Angraini *et al*., 2025).

Limitations and solutions:

The intrinsic fragility can be mitigated by incorporating β-tricalcium phosphate or bioactive glass nanoparticles, increasing the elastic modulus up to 1.2 MPa without compromising porosity (Putri & Elsheikh, 2022; Lourenço *et al*., 2024).

3.5.3 3D Printing and bioprinting: customization and geometric complexity

3D printing of chitosan pastes or inks allows the fabrication of anatomically precise scaffolds with defined porous architectures. Success depends on rheological adjustment: the ink must exhibit shear-thinning behavior and rapid gelation post-extrusion (Lazaridou *et al*., 2022).

Recent advances:

- Hybrid chitosan-bioactive glass inks have achieved resolutions of 200 µm and compressive strengths of 2 MPa, suitable for partial-load defects (Lourenço *et al*., 2024).
- 2024 reviews document the integration of microencapsulated growth factors, achieving controlled BMP-2 release for up to 28 days (Khan *et al*., 2024).
- Bibliometric analyses show that bioprinting with chitosan hydrogels is the fastest-growing research line (>25% annual growth) in bone regeneration (Zhang *et al*., 2025).

Clinical advantages:

- Customization: allows scaffold design based on patient CT/CBCT scans.
- Minimally invasive: thermoresponsive hydrogels can be printed *in situ* through endoscopic cannulas (Patois *et al*., 2009).
- Cell co-encapsulation: chitosan's moderate viscosity preserves >85% viability of MSCs during extrusion, supporting combined therapies.

Current challenges

- Reproducibility at industrial scale.
- Need for fast and cytocompatible crosslinking systems (e.g., visible light + riboflavin).
- Control of mineralization gradients to mimic the bone-cartilage interface.

3.6 Biomedical applications of chitosan hydrogels

The physicochemical versatility of chitosan and its hydrogels has enabled a wide range of biomedical applications, particularly in tissue engineering, targeted drug delivery, and wound healing. Below is a summary of the most relevant advances, emphasizing the relationship between "structure–process–property–function" from a comprehensive biomedical engineering perspective.

3.6.1 Osteochondral tissue engineering

Chitosan hydrogels (CHs) provide a hydrated three-dimensional microenvironment that supports the adhesion, proliferation, and differentiation of mesenchymal stem cells (MSCs), osteoblasts, and chondrocytes. This behavior is attributed to their cationic charge, which promotes the adsorption of extracellular matrix proteins (Freier *et al*., 2005; Kim *et al*., 2023).

- Osteogenesis *in vitro* and *in vivo*: CHs loaded with BMP-2 and hydroxyapatite nanoparticles have shown significant increases in the expression of ALP, Runx2, and osteocalcin, as well as lamellar

bone formation in critical tibial defects in rabbits (Oliveira *et al*., 2021; Li *et al*., 2023).

- Complex interfaces: Using multimaterial 3D bioprinting, CH/bioactive glass nanoparticle gradients have been created to replicate the osteochondral transition, achieving simultaneous integration of hyaline cartilage and subchondral bone in ovine models (Lazaridou *et al*., 2022).
- Neuro-osteogenesis: Recent studies describe CHs doped with gallium ions capable of simultaneously stimulating bone regeneration and peripheral reinnervation, demonstrating the potential for bifunctional platforms (De León-Oliva *et al*., 2023).

3.6.2 Controlled drug delivery systems

The polycationic nature of chitosan (Table 3) enables the formation of ionic complexes with anionic molecules and modulation of release kinetics via pH or temperature changes (Nguyen *et al*., 2023).

These formulations have been explored for both local chemotherapy—avoiding systemic toxicity—and sustained antibiotic delivery in bone grafts, reducing recurrence of osteomyelitis (Aguilar *et al*., 2019).

3.6.3 Wound healing

Although the main focus of this article is bone regeneration, it is worth noting that CHs were initially recognized for their wound healing potential. Their hemostatic capacity, antimicrobial activity, and angiogenesis stimulation accelerate the classical four phases of tissue repair (Azad *et al*., 2004; Ansari, 2019). Self-healing hydrogels made from oxidized chitosan and gelatin achieved complete closure of diabetic wounds in 10 days, compared to 16 days in standard gauze-treated controls (Li *et al*., 2023).

Table 3. Stimulus-responsive mechanisms for drug release with chitosan.

Strategy	Control Principle	Examples and Results
Thermosensitive (CS-β-GP)	Gelation at 37 °C	Sustained doxycycline release for 14 days, reducing peri-implant inflammation (Patois *et al*., 2009).
pH-responsive	$–NH_3^+$ deprotonation (pH > 6.5)	CS/alg–Ca^{2+} microgels with accelerated release in acidic necrotic regions (Sangnim *et al*., 2023).
Redox-sensitive	Disulfide bridges with cystamine	Pulsatile paclitaxel delivery in the presence of tumor GSH (Yanat & Schroën, 2021).

3.7 Current challenges and future perspectives

Despite significant progress in the development of chitosan hydrogels (CHs) for biomedical applications, structural, technological, and regulatory challenges remain that hinder their large-scale clinical translation. The following discussion outlines the main technical obstacles in the field, as well as scientific projections toward a new generation of bioactive scaffolds and personalized regenerative therapies.

3.7.1 Limited solubility of chitosan

One of the main challenges in handling CHs is their low solubility in neutral or basic media, due to the pH-dependent protonation of chitosan's primary amine groups ($–NH_2$). This property restricts their direct application in physiological environments and necessitates the use of weak acids (such as acetic, lactic, or citric acid) for initial dissolution (Aranaz *et al*., 2021; Huq *et al*., 2022).

To address this issue, several strategies have been developed:

- Chemical modifications: Quaternization and sulfonation improve solubility at neutral pH, enhancing the polymer's dispersion in biological fluids (Li *et al*., 2021).
- Formulation with soluble polymers: Combinations with PEG, PVA, or hyaluronic acid increase the miscibility of CHs in physiological solutions without compromising biofunctionality (Nguyen *et al*., 2023).
- Use of green solvents and deep eutectic systems (DES): Recent technologies have demonstrated the effectiveness of solvents like choline–oxalic acid for dissolving chitin and obtaining safer CHs (Pellis *et al*., 2022; Tahir *et al*., 2024).

3.7.2 Need for standardization of degree of deacetylation (DD)

The degree of deacetylation (DD) is one of the most critical structural parameters influencing chitosan's bioactivity and degradability. A high DD (>85%) promotes cell adhesion and interaction with negative charges, while a lower DD (<70%) enables enhanced enzymatic degradation (Freier *et al*., 2005; Ioelovich, 2014). However, the lack of standardized methods for its measurement and reporting hinders reproducibility across studies.

Current efforts include:

- Advanced metrology: Use of NMR spectroscopy, quantitative FTIR, and chromatography to reliably characterize DD (Novikov *et al*., 2023).
- Harmonized international protocols: Regulatory agencies (FDA, EMA) now require precise

specifications of DD and molecular weight in medical applications, promoting polymer traceability from source to final product (Mohan *et al*., 2020; Hahn *et al*., 2020).
- Development of CH databases: Libraries of well-characterized chitosans are being compiled to facilitate their selection according to the intended application (De Alvarenga, 2011; Aranaz *et al*., 2021).

3.7.3 Personalized bioprinting and advanced therapies

With the rise of personalized medicine, CHs are emerging as key bioinks in 3D bioprinting, where their viscoelasticity, biocompatibility, and water retention capacity enable the creation of anatomically precise structures for bone, cartilage, and vascular regeneration (Lazaridou *et al*., 2022; Kim *et al*., 2023).

Ongoing challenges:

- Precise tuning of bioink rheology to maintain structural fidelity and post-printing cell viability.
- Integration with active biomolecules (e.g., growth factors, messenger RNA) to enable spatiotemporally controlled release.
- Multimaterial fabrication: Combination with ceramics such as β-TCP or conductive polymers to generate osteoinductive and even electrostimulative environments.

Future perspectives:

- CHs functionalized with specific ligands will enable the development of smart scaffolds capable of responding to bone microenvironment stimuli such as pH or reactive oxygen species (Zhang *et al*., 2021).
- Combined HQ–stem cell–CRISPR therapies could transform the treatment of congenital or degenerative bone diseases (Rondón *et al*., 2023; De León-Oliva *et al*., 2023).

4 Conclusion

From a biomedical-engineering standpoint, chitosan is firmly established as a natural polymer with high potential for developing hydrogels aimed at regenerative therapies. Its structural versatility, biocompatibility, gelling ability, and tunable physicochemical properties make it a multifaceted platform for advanced medical treatments—especially for bone-tissue regeneration.

Recap of chitosan's benefits in hydrogels

Chitosan hydrogels (CHs) possess a highly hydrated, porous architecture that mimics the bone extracellular microenvironment, promoting cell adhesion, nutrient transport, and osteoblastic proliferation. Key advantages include:

- Controlled biodegradability, adjustable through structural modifications of the polymer.
- Chemical or physical cross-linking capability, enabling injectable, self-supporting, or thermally stable systems.
- High affinity for biomolecules such as morphogenetic proteins (BMPs), antibiotics, and growth factors.

These features position CHs as optimal vehicles for targeted drug delivery, 3-D scaffolds for tissue engineering, and smart systems responsive to physiological stimuli.

Importance of origin and synthesis method

A critical determinant of CH performance is the chitosan's origin and extraction technique. Alternative sources—such as insects and fungi—and modern methods like microwave-assisted deacetylation yield chitosans with more consistent, sustainable molecular profiles suited to biomedical use.

Equally essential is standardizing the degree of deacetylation and molecular weight to ensure material reproducibility and safety in clinical settings. This underscores the need for engineering approaches that integrate chemical-process control, advanced biomaterial characterization, and preclinical functional validation.

Potential applications in bone regeneration and beyond

CHs have shown promising results in repairing critical bone defects, acting as bioactive scaffolds that not only provide mechanical support but also enhance mineralization and new bone formation. Functionalization with nanocomposites or bioactive factors broadens their application to:

- Cartilage and skin regeneration.
- Sustained delivery of anti-inflammatories or antibiotics for osteo-articular lesions.
- 3-D bioprinting of patient-specific tissues by integrating stem cells and modular bioinks.

Consequently, chitosan hydrogels stand out as a strategic technology in modern regenerative medicine, where biomedical engineering supplies rational design tools, advanced manufacturing, and comprehensive *in vitro*/*in vivo* evaluation to accelerate the transition toward effective, safe, and accessible clinical therapies.

References

Aguilar, A., Zein, N., Harmouch, E., Hafdi, B., Bornert, F., Offner, D., ... & Hua, G. (2019). Application of

chitosan in bone and dental engineering. *Molecules*, *24*(16), 3009. https://doi.org/10.3390/molecules24163009

Ansari, M. (2019). Bone tissue regeneration: biology, strategies and interface studies. *Progress in Biomaterials*, 8 (4), pp. 223-237. https://doi.org/10.1007/s40204-019-00125-z

Aranaz, I., Alcántara, A. R., Civera, M. C., Arias, C., Elorza, B., Heras Caballero, A., & Acosta, N. (2021). Chitosan: An overview of its properties and applications. *Polymers*, *13*(19), 3256. https://doi.org/10.3390/polym13193256

Azad, A. K., Sermsintham, N., Chandrkrachang, S., & Stevens, W. F. (2004). Chitosan membrane as a wound-healing dressing: characterization and clinical application. *Journal of Biomedical Materials Research Part B: Applied Biomaterials: An Official Journal of The Society for Biomaterials, The Japanese Society for Biomaterials, and The Australian Society for Biomaterials and the Korean Society for Biomaterials*, *69*(2), 216-222. https://doi.org/10.1002/jbm.b.30069

Chandra, D. K., Kumar, A., & Mahapatra, C. (2024). Fabricating chitosan reinforced biodegradable bioplastics from plant extract with nature inspired topology. *Waste and Biomass Valorization*, *15*(4), 2499-2512. https://doi.org/10.1007/s12649-023-02293-3

De Alvarenga, E. S. (2011). Characterization and properties of chitosan. *Biotechnology of biopolymers*, *91*, 48-53. https://doi.org/10.5772/17058

De Leon-Oliva, D., Boaru, D. L., Perez-Exposito, R. E., Fraile-Martinez, O., García-Montero, C., Diaz, R., ... & Ortega, M. A. (2023). Advanced Hydrogel-Based Strategies for Enhanced Bone and Cartilage Regeneration: A Comprehensive Review. *Gels*, *9*(11), 885. https://doi.org/10.3390/gels9110885

Fathy, I. A., Ali, D. M., Elmansy, Y., Abd El-Sattar, N. E., & Elsayed, S. (2025). Bone-Regenerating Capacity of Chitosan Membrane and Chitosan Foam Scaffolds in Critical Size Defects: *In Vitro* and *In Vivo* Study. *Dentistry Journal*, *13*(4), 153. https://doi.org/10.3390/dj13040153

Freier, T., Koh, H. S., Kazazian, K., & Shoichet, M. S. (2005). Controlling cell adhesion and degradation of chitosan films by N-acetylation. *Biomaterials*, *26*(29), 5872-5878. https://doi.org/10.1016/j.biomaterials.2005.02.033

Hahn, T., Tafi, E., Paul, A., Salvia, R., Falabella, P., & Zibek, S. (2020). Current state of chitin purification and chitosan production from insects. *Journal of Chemical Technology & Biotechnology*, *95*(11), 2775-2795. https://doi.org/10.1002/jctb.6533

Harmsen, R. A., Tuveng, T. R., Antonsen, S. G., Eijsink, V. G., & Sørlie, M. (2019). Can we make chitosan by enzymatic deacetylation of chitin?. *Molecules*, *24*(21), 3862. https://doi.org/10.3390/molecules24213862

Henry, J. P. & Bordoni, B. (2023). Histology, osteoblasts. En: *StatPearls* [Internet]. Treasure Island (FL): StatPearls Publishing. Disponible en: https://www.ncbi.nlm.nih.gov/books/NBK532912

Huq, T., Khan, A., Brown, D., Dhayagude, N., He, Z., & Ni, Y. (2022). Sources, production and commercial applications of fungal chitosan: A review. *Journal of Bioresources and Bioproducts*, *7*(2), 85-98. https://doi.org/10.1016/j.jobab.2022.01.002

Ioelovich, M. (2014). Crystallinity and hydrophility of chitin and chitosan. *Journal of Chemistry*, 3 (3), pp. 7-14. https://www.rroij.com/open-access/crystallinity-and-hydrophility-of-chitin-and-chitosan-.php?aid=33938

Khan, A. R., Grewal, N. S., Jun, Z. y otros (2024). Raising the bar: progress in 3D-printed hybrid bone scaffolds for clinical applications: a review. *Cell Transplantation*, 33, pp. 09636897241273562. https://doi.org/10.1177/09636897241273562

Kim, Y., Zharkinbekov, Z., Raziyeva, K., Tabyldiyeva, L., Berikova, K., Zhumagul, D., ... & Saparov, A. (2023). Chitosan-based biomaterials for tissue regeneration. *Pharmaceutics*, *15*(3), 807. https://doi.org/10.3390/pharmaceutics15030807

Kumar, B. S., Isloor, A. M., Kumar, G. M., Inamuddin, & Asiri, A. M. (2019). Nanohydroxyapatite reinforced chitosan composite hydrogel with tunable mechanical and biological properties for cartilage regeneration. *Scientific reports*, *9*(1), 15957. https://doi.org/10.1038/s41598-019-52042-7

Lazaridou, M., Bikiaris, D. N., & Lamprou, D. A. (2022). 3D bioprinted chitosan-based hydrogel scaffolds in tissue engineering and localised drug delivery. *Pharmaceutics*, *14*(9), 1978. https://doi.org/10.3390/pharmaceutics14091978

Li, W., Wu, Y., Zhang, X., Wu, T., Huang, K., Wang, B., & Liao, J. (2023). Self-healing hydrogels for bone defect repair. *RSC advances*, *13*(25), 16773-16788. https://doi.org/10.1039/d3ra01700a

Li, X., Xing, R., Xu, C., Liu, S., Qin, Y., Li, K., ... & Li, P. (2021). Immunostimulatory effect of chitosan and quaternary chitosan: A review of potential vaccine adjuvants. *Carbohydrate polymers*, *264*, 118050. https://doi.org/10.1016/j.carbpol.2021.118050

Lourenço, L. R., Borges, R., Carastan, D., Mathor, M. B., & Marchi, J. (2024). Precision 3D printing of chitosan-bioactive glass inks: Rheological optimization for enhanced shape fidelity in tissue engineering scaffolds. *Bioprinting*, *43*, e00359. https://doi.org/10.1016/j.bprint.2024.e00359

Ma, Y., Zhou, R., Yang, M. y otros (2025). Electrospinning-based bone-tissue scaffold construction: progress and trends. *Materials & Design*, pp. 113792. https://doi.org/10.1016/j.matdes.2025.113792

Madihally, S. V., & Matthew, H. W. (1999). Porous chitosan scaffolds for tissue engineering. *Biomaterials*, *20*(12), 1133-1142. https://doi.org/10.1016/S0142-9612(99)00011-3

Mazoochi, T., & Jabbari, V. (2011). Chitosan nanofibrous scaffold fabricated via electrospinning: The effect of processing parameters on the nanofiber morphology. *International Journal of Polymer Analysis and Characterization*, *16*(5), 277-289. https://doi.org/10.1080/1023666X.2010.550229

Mohan, K., Ganesan, A. R., Muralisankar, T., Jayakumar, R., Sathishkumar, P., Uthayakumar, V., ... & Revathi, N. (2020). Recent insights into the extraction, characterization, and bioactivities of chitin and chitosan from insects. *Trends in food science & technology*, *105*, 17-42. https://doi.org/10.1016/j.tifs.2020.08.016

Moher, D., Liberati, A., Tetzlaff, J., & Altman, D. G. (2009). Preferred reporting items for systematic reviews and meta-analyses: the PRISMA statement. *Bmj*, *339*. https://doi.org/10.1371/journal.pmed.1000097

Nallusamy, J., & Das, R. K. (2021). Hydrogels and their role in bone tissue engineering: An overview. *Journal of Pharmacy and BioAllied Sciences*, *13*(Suppl 2), S908-S912. https://doi.org/10.4103/jpbs.jpbs_237_21

Nahian, A., & AlEssa, A. M. (2023). Histology, Osteocytes. In *StatPearls [Internet]*. StatPearls Publishing. https://www.ncbi.nlm.nih.gov/books/NBK558990/

Nguyen, H. T., Do, N. H., Lac, H. D., Nguyen, P. L., & Le, P. K. (2023). Synthesis, properties, and applications of chitosan hydrogels as anti-inflammatory drug delivery system. *Journal of Porous Materials*, *30*(2), 655-670. https://doi.org/10.1007/s10934-022-01371-6

Novikov, V. Y., Derkach, S. R., Konovalova, I. N., Dolgopyatova, N. V., & Kuchina, Y. A. (2023). Mechanism of heterogeneous alkaline deacetylation of chitin: A review. *Polymers*, *15*(7), 1729. https://doi.org/10.3390/polym15071729

Oliveira, É. R., Nie, L., Podstawczyk, D., Allahbakhsh, A., Ratnayake, J., Brasil, D. L., & Shavandi, A. (2021). Advances in growth factor delivery for bone tissue engineering. *International journal of molecular sciences*, *22*(2), 903. https://doi.org/10.3390/ijms22020903

Page, M. J., McKenzie, J. E., Bossuyt, P. M., Boutron, I., Hoffmann, T. C., Mulrow, C. D., Shamseer, L., Tetzlaff, J. M., Akl, E. A., Brennan, S. E., Chou, R., Glanville, J., Grimshaw, J. M., Hróbjartsson, A., Lalu, M. M., Li, T., Loder, E. W., Mayo-Wilson, E., McDonald, S., McGuinness, L. A., Stewart, L. A., Thomas, J., Tricco, A. C., Welch, V. A., Whiting, P. & Moher, D. (2021). The PRISMA 2020 statement: an updated guideline for reporting systematic reviews. *BMJ*, 372, pp. n71. https://doi.org/10.1136/bmj.n71

Patois, E., Cruz, S. O. D., Tille, J. C., Walpoth, B., Gurny, R., & Jordan, O. (2009). Novel thermosensitive chitosan hydrogels: *In vivo* evaluation. *Journal of Biomedical Materials Research Part A: An Official Journal of The Society for Biomaterials, The Japanese Society for Biomaterials, and The Australian Society for Biomaterials and the Korean Society for Biomaterials*, *91*(2), 324-330. https://doi.org/10.1002/jbm.a.32211

Pellis, A., Guebitz, G. M., & Nyanhongo, G. S. (2022). Chitosan: sources, processing and modification techniques. *Gels*, *8*(7), 393. https://doi.org/10.3390/gels8070393

Purohit, S. D., Bhaskar, R., Singh, H., Priyadarshi, R., Kim, H., Son, Y., ... & Han, S. S. (2024). Chitosan-based electrospun fibers for bone-tissue engineering: Recent research advancements. *International Journal of Biological Macromolecules*, 136530. https://doi.org/10.1016/j.ijbiomac.2024.136530

Putri, T. S., & Elsheikh, M. (2022). Flexural Strength Evaluation of Chitosan-Gelatin-B-Tricalcium Phosphate-Based Composite Scaffold. *Journal of International Dental and Medical Research*, *15*(1), 31-34. https://www.jidmr.com/journal/wp-content/uploads/2022/03/6-D21_1649_Tansza_Setiana_Putri_Indonesia.pdf

Rondón, J., Sánchez-Martínez, V., Lugo, C., & Gonzalez-Lizardo, A. (2025). Tissue engineering: Advancements, challenges and future perspectives. *Revista Ciencia e Ingeniería. Vol*, *46*(1). http://erevistas.saber.ula.ve/index.php/cienciaeingenieria/article/view/20607/21921932297

Rondón, J., Vázquez, J. y Lugo, C. (2023). Biomaterials used in tissue engineering for the manufacture of scaffolds. *Ciencia e Ingeniería*, 44 (3). http://erevistas.saber.ula.ve/index.php/cienciaeingenieria/article/view/19221

Saber, M., Shaabani, A., Sedghi, R., Motasadizadeh, H., Salimiyan, N., Gholami, M., ... & Haramshahi, S. M. A. (2025). Biguanidylated chitosan nanofiber scaffold: A green approach to promote osteogenesis in calvarial bone regeneration. *Carbohydrate Polymers*, 123736. https://doi.org/10.1016/j.carbpol.2025.123736

Sangnim, T., Dheer, D., Jangra, N., Huanbutta, K., Puri, V., & Sharma, A. (2023). Chitosan in oral drug delivery formulations: A review. *Pharmaceutics*, *15*(9), 2361. https://doi.org/10.3390/pharmaceutics15092361

Sawaguchi, A., Ono, S., Oomura, M., Inami, K., Kumeta, Y., Honda, K., ... & Saito, A. (2015). Chitosan degradation and associated changes in bacterial community structures in two contrasting soils. *Soil Science and Plant Nutrition*, *61*(3), 471-480. https://doi.org/10.1080/00380768.2014.1003965

Subbiah, T., Bhat, G. S., Tock, R. W. y Parameswaran, S. (2005). Electrospinning of nanofibers. *Journal of Applied Polymer Science*, 96 (2), pp. 557-569. https://doi.org/10.1002/app.21549

Sugiyanti, D., Anggrahini, S., Pranoto, Y., Anwar, C., & Santoso, U. (2019). Low Molecular Weight Chitosan from Shrimp Shell Waste using Steam-Explosion Process Under Catalyst of Phosphotungstic Acid. *Oriental Journal of Chemistry*, *35*(1). https://doi.org/10.13005/ojc/350122

Szymańska, E., & Winnicka, K. (2015). Stability of chitosan—a challenge for pharmaceutical and biomedical applications. *Marine drugs*, *13*(4), 1819-1846. https://doi.org/10.3390/md13041819

Tahir, I., Wijaya, K., Krismayanti, D., Saviola, A. J., Wahab, R. A., Amin, A. K., ... & Pratika, R. A. (2024). Microwave radiation-assisted chitin deacetylation: Optimization by response surface methodology (RSM). Korean Journal of Materials Research, 34(2), 85-94. https://doi.org/10.3740/mrsk.2024.34.2.85

Triunfo, M., Tafi, E., Guarnieri, A., Salvia, R., Scieuzo, C., Hahn, T., ... & Falabella, P. (2022). Characterization of chitin and chitosan derived from Hermetia illucens, a further step in a circular economy process. *Scientific reports*, *12*(1), 6613. https://doi.org/10.1038/s41598-022-10423-5

Wang, J., Xiong, J., Li, G., Zhou, Z., Yang, Y., & He, L. (2025a). Electrospinning of hydroxypropyl chitosan nanofibers for bone regeneration application. *bioRxiv*, 2025-01. https://doi.org/10.1101/2025.01.05.631378

Wang, C., Wang, B., Ji, X., Tang, X., Li, Y., Huang, Y., & Ma, X. (2025b). Plant xylem-inspired chitosan-gelatin scaffolds reinforced with graphene oxide with a superior mechanical strength and hydrophilicity for bone tissue engineering. *International Journal of Biological Macromolecules*, 145488 https://doi.org/10.1016/j.ijbiomac.2025.145488

Yanat, M., & Schroën, K. (2021). Preparation methods and applications of chitosan nanoparticles; with an outlook toward reinforcement of biodegradable packaging. *Reactive and Functional Polymers*, *161*, 104849. https://doi.org/10.1016/j.reactfunctpolym.2021.104849

Yue, S., He, H., Li, B., & Hou, T. (2020). Hydrogel as a biomaterial for bone tissue engineering: A review. *Nanomaterials*, *10*(8), 1511. https://doi.org/10.3390/nano10081511

Zhang, Q., Chen, Y., Wei, P., Zhong, Y., Chen, C., & Cai, J. (2021). Extremely strong and tough chitosan films mediated by unique hydrated chitosan crystal structures. *Materials Today*, *51*, 27-38. https://doi.org/10.1016/j.mattod.2021.10.030

Received: *April 28th, 2025*

Accepted: *July 15th, 2025*

Rondón Contreras, Jairo*: Ph.D. in Applied Chemistry, mention: Materials Study, 2015, Universidad de Los Andes. Professor of Biomedical & Chemical Engineering Departments, at the Polytechnic University of Puerto Rico. San Juan, PR-USA. E-mail: jrondon@pupr.edu* *https://orcid.org/0000-0002-9738-966X*

Ramirez-Vargas, Kimberly: *BSc. in Biomedical Engineering, 2024, Polytechnic University of Puerto Rico. San Juan, PR-USA.* *https://orcid.org/0009-0008-5610-0912*

Saucedo-Vazquez, Juan Pablo: *Doctor in Chemistry Sciences, 2012, Universidad Nacional Autónoma de México. Professor at CATS Research Group, School of Chemical Sciences and Engineering, Yachay Tech, Urcuqui, Ecuador. Email: jsaucedo@yachaytech.edu.ec* *https://orcid.org/0000-0002-4314-6363*

Ávila, Edward E.: *Doctor in Chemistry in Applied Chemistry, Materials Study, 2011, Universidad de Los Andes. Professor at GIAMP, School of Chemical Sciences and Engineering, Yachay Tech, Urcuqui, Ecuador. Email: eavila@yachaytech.edu.ec* *https://orcid.org/0000-0002-6910-5826*

Artículo de Investigación. Revista Ciencia e Ingeniería. Vol. 46, No. 3 pp. 265-278, agosto-noviembre, 2025.
ISSN 1316-7081. ISSN Elect. 2244-8780 Universidad de los Andes (ULA)

Artificial liver: Perspective of biomedical engineering

Hígado artificial: Perspectiva de ingeniería biomédica

Rondón, Jairo[1,2*]; García, Andrea[1]; Lugo, Claudio[3]; Gonzalez-Lizardo, Angel[4]
[1]Biomedical Engineering Department, Universidad Politécnica de Puerto Rico, PR 00918 USA.
[2]Chemical Engineering Department, Universidad Politécnica de Puerto Rico, PR 00918 USA.
[3]Laboratorio de Cinética y Catálisis, Universidad de Los Andes Mérida, Venezuela.
[4]Department of Electrical and Computer Engineering and Computer Science,
Universidad Politécnica de Puerto Rico, PR 00918 USA.

* jrondon@pupr.edu

Abstract

Liver failure remains a critical condition with limited therapeutic options beyond transplantation. The growing demand for alternatives has driven the development of artificial liver support systems (ALS), aimed at emulating essential liver functions. This review addresses the main technological approaches: artificial, bioartificial, and hybrid devices, highlighting their detoxification and metabolic support mechanisms. Key aspects of engineering design are analyzed, such as bioreactor architecture, selection of biocompatible biomaterials, microfluidic dynamics, and 3D bioprinting. Furthermore, the integration of artificial intelligence for real-time monitoring, anatomical modeling, and predictive control is examined. Stem cell-derived liver organoids are presented as emerging platforms for regenerative applications. From a critical perspective, the clinical role of ALS in acute and chronic liver failure is evaluated, as well as its use as a bridge to transplantation. Finally, pending challenges in immunocompatibility, vascularization, and scalability are identified. The future of liver support points to a convergence of engineering, regenerative biology, and artificial intelligence, with the potential to transform personalized liver medicine.

Keywords: artificial liver; bioartificial liver; liver organoids; 3D bioprinting; tissue engineering.

Resumen

La insuficiencia hepática continúa siendo una condición crítica con opciones terapéuticas limitadas más allá del trasplante. La creciente demanda de alternativas ha impulsado el desarrollo de sistemas artificiales de soporte hepático (SAHE), orientados a emular funciones esenciales del hígado. Esta revisión aborda los principales enfoques tecnológicos: dispositivos artificiales, bioartificiales e híbridos, destacando sus mecanismos de desintoxicación y soporte metabólico. Se analizan aspectos clave del diseño ingenieril, como la arquitectura del biorreactor, la selección de biomateriales biocompatibles, la dinámica microfluídica y la bioimpresión 3D. Además, se examina la integración de inteligencia artificial para el monitoreo en tiempo real, modelado anatómico y control predictivo. Los organoides hepáticos derivados de células madre se presentan como plataformas emergentes para aplicaciones regenerativas. Desde una perspectiva crítica, se evalúa el papel clínico de los SAHE en insuficiencia hepática aguda y crónica, así como su uso como puente al trasplante. Finalmente, se identifican desafíos pendientes en inmunocompatibilidad, vascularización y escalabilidad. El futuro del soporte hepático apunta hacia una convergencia entre ingeniería, biología regenerativa e inteligencia artificial, con potencial para transformar la medicina hepática personalizada.

Palabras clave: hígado artificial; hígado bioartificial; organoides hepáticos; bioimpresión 3D; ingeniería de tejidos.

1 Introduction

Liver failure remains one of the principal causes of morbidity and mortality at the global level, contributing to over two million deaths annually, primarily as a result of the increasing incidence of both acute and chronic hepatic diseases such as viral hepatitis, alcoholic liver disease, and nonalcoholic fatty liver disease (NAFLD). These conditions are strongly associated with lifestyle modifications, exposure to hepatotoxic agents, and persistent viral infections (Gong *et al*., 2025; He *et al*., 2019). Despite the

liver's remarkable regenerative capacity, this ability becomes insufficient when extensive or repeated injury leads to structural collapse and functional compromise, particularly in advanced stages of hepatic failure (Li *et al*., 2019).

Currently, liver transplantation remains the gold standard for the treatment of irreversible hepatic failure. However, this intervention is severely constrained by a global shortage of organ donors, high financial costs, the risk of immune rejection, and the requirement for lifelong immunosuppression (Jasirwan *et al*., 2023). These limitations have prompted the search for alternative strategies, including the development of Artificial Liver Support Systems (ALSS), which are designed to provide temporary or adjunctive hepatic function until either native liver recovery or transplantation becomes viable.

ALSS technologies are generally classified into artificial, bioartificial, and hybrid systems. Artificial systems rely on physicochemical processes for detoxification, employing filters, adsorbents, and dialysis techniques to remove metabolic waste. In contrast, bioartificial systems integrate biological elements—typically primary hepatocytes or stem cell-derived hepatic cells—with synthetic scaffolds or bioreactors to emulate the metabolic and synthetic functions of the liver (Gadour, 2025; Ramli *et al*., 2020). Hybrid configurations combine these elements to enhance detoxification, protein synthesis, and immunoregulatory capabilities under dynamic, flow-controlled conditions (Rondón *et al*., 2025).

Advances have profoundly influenced the evolution of ALSS in biomedical engineering. Innovations in material science, microscale fluid dynamics, and bioreactor engineering have enabled the development of implantable hepatic devices, patient-specific hepatic constructs fabricated via 3D printing, and organ-on-chip platforms that emulate hepatic microenvironments with high fidelity (Bhardwaj *et al*., 2024). Additionally, integrating artificial intelligence (AI) into liver support systems has allowed for predictive modeling of hepatic function, real-time monitoring of disease progression, and adaptive optimization of system performance (Jumaah *et al*., 2025).

Recent breakthroughs in hepatic tissue engineering have highlighted the utility of liver organoids derived from human pluripotent stem cells. These self-organizing microstructures reproduce essential aspects of hepatic architecture and function *in vitro* and are increasingly applied in high-throughput pharmacological testing and pathophysiological modeling. Moreover, they show promise as bioactive modules in future bioartificial liver systems (Akhtar, 2024).

In light of the liver's multifaceted physiological roles and the urgent need for therapeutic alternatives to transplantation, ALSS development represents both a technological challenge and a translational opportunity. This article comprehensively overviews current and emerging technologies in artificial liver engineering. It emphasizes engineering approaches, regenerative platforms, integration with AI systems, and persisting translational barriers. The objective is to delineate current research gaps and propose strategic directions to enhance clinical applicability and improve patient outcomes.

2 Methodology

- *Search and data compilation:* A comprehensive literature search was conducted using databases including PubMed, ScienceDirect, IEEE Xplore, Springer, MDPI, ResearchGate, and Frontiers. Search terms included "artificial liver", "bioartificial liver", "liver organoids", "3D bioprinting", "hepatocyte bioreactor", "AI in regenerative medicine", and "tissue engineering for hepatic systems". The search covered peer-reviewed publications from 1995 to 2025.
- *Information selection and refinement:* Retrieved articles were screened for relevance, focusing on works that provide experimental, clinical, or technological insights into the development and application of ALSS. Mendeley was used for reference organization. Key selection criteria included novelty, translational potential, and scientific rigor (see Figure 1).
- *Thematic structuring:* Selected works were classified into core thematic areas: (a) classification of ALSS, (b) engineering design and materials, (c) computational and AI modeling, (d) organoids and regenerative liver systems, and (e) clinical trials and implementation barriers.

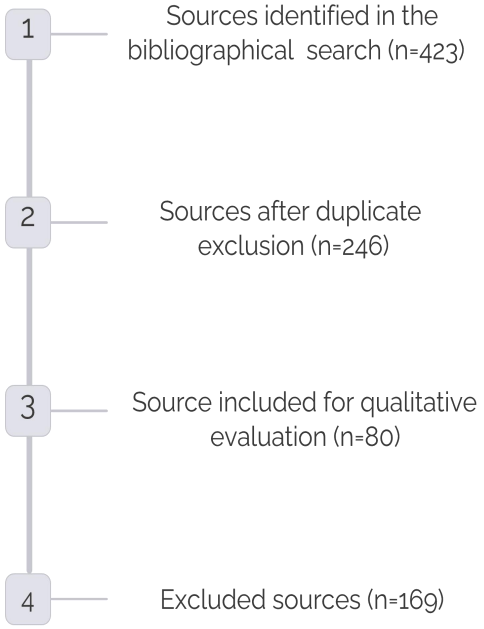

Figure 1. Flowchart of the study selection methodology for this research.

- *Critical analysis:* Cross-comparative analyses were performed to identify technological gaps, converging trends, and future research directions. Emphasis was placed on evidence-based evaluation of functionality, cell compatibility, and scalability for clinical translation (Jumaah *et al*., 2025; Akhtar, 2024; Rondón *et al*., 2024).

3 Results and discussion

3.1 Classification of artificial liver systems

Artificial Liver Support Systems (ALSS) are generally classified into three main categories based on their mechanism of action, biological integration, and clinical purpose: (1) purely artificial systems, (2) bioartificial systems, and (3) hybrid systems and Emerging Strategies (He *et al*., 2019; Jasirwan *et al*., 2023; Ocskay *et al*., 2021). This classification is fundamental for understanding the technological evolution of hepatic support strategies and their functional differentiation (Table 1).

1. *Artificial systems* rely on non-biological methods such as filtration, adsorption, and dialysis to eliminate endogenous and exogenous toxins from the bloodstream. The most prominent examples include the Molecular Adsorbent Recirculating System (MARS), Single-Pass Albumin Dialysis (SPAD), and Prometheus.

MARS combines albumin dialysis with conventional renal replacement therapy to eliminate protein-bound toxins and cytokines (Jasirwan *et al*., 2023; Sen *et al*., 2005; Papamichalis *et al*., 2023). However, these systems do not replicate hepatic metabolic or synthetic functions and are limited to providing temporary detoxification support.

Their clinical use is generally restricted to bridging patients with acute liver failure to transplantation or spontaneous recovery (Stange *et al*., 1999; Feng *et al*., 2024).

2. *Bioartificial systems* combine synthetic membranes with functional biological components, primarily hepatocytes, to perform metabolic and synthetic activities. Notable examples include HepatAssist, ELAD, and the Spheroid Reservoir Bioartificial Liver (SRBAL).

HepatAssist incorporates porcine hepatocytes within a hollow-fiber bioreactor, mimicking key hepatic functions such as ammonia detoxification, gluconeogenesis, and protein synthesis (Li *et al*., 2019; Ellis *et al*., 1996; Heydari *et al*., 2020).

ELAD, developed by Vital Therapies, uses human C3A hepatoblastoma cells to provide metabolic support in a similar extracorporeal configuration (Rondón e*t al*., 2025). While preclinical results have been promising, clinical trials have yielded mixed outcomes regarding efficacy and patient survival (Akhtar, 2024; Sánchez *et al*., 2014).

Although ALSS technologies represent a promising alternative for patients with liver failure, numerous clinical, logistical, and ethical barriers must still be addressed to ensure their safe, effective, and equitable integration into modern healthcare systems.

Ultimately, ALSS are poised to revolutionize the therapeutic landscape of hepatology. As these technologies evolve from extracorporeal support toward complete organ replacement, they hold the potential to extend life and restore both liver function and quality of life for patients worldwide.

Their clinical success would mark a transformative milestone in the era of personalized and regenerative hepatic medicine (Bhardwaj *et al*., 2024; Sommerfeld *et al*., 2023).

Table 1. Classification of artificial liver support systems

System	Description	Advantages	Limitations
Artificial	Mechanical/chemical filtration is used to remove toxins. E.g., MARS, SPAD, Prometheus.	Rapid toxin clearance; well-established technology.	Does not replicate metabolic functions; it provides only temporary support.
Bioartificial	Combines synthetic components with living hepatocytes. E.g., HepatAssist, ELAD, SRBAL.	Offers metabolic and synthetic support; better functional mimicry.	Cell compatibility issues; variable clinical outcomes.
Hybrid	Integrates artificial detoxification modules (e.g., MARS) with cell-based bioreactors.	Synergistic detoxification + metabolism; broader clinical potential.	Technological complexity, challenges in immunocompatibility, and scalability.

3. Hybrid Systems and Emerging Strategies. Hybrid systems incorporate advanced structural and functional approaches, such as cell encapsulation and immune-isolated scaffolds, to minimize host immune responses and improve long-term performance (Bhatt *et al*., 2024; García & Bendjelid, 2018). In parallel, emerging research is focusing on the use of hepatocyte-like cells derived from induced pluripotent stem cells (iPSCs), which offer a renewable and less immunogenic cellular source (Gong *et al*., 2025; Akhtar, 2024; Gao *et al*., 2020; Cerneckis *et al*., 2024)

In this context, computational modeling and artificial intelligence (AI) algorithms are increasingly used to simulate device performance and optimize detoxification rates, shear stress, and nutrient flow dynamics in real time (Jumaah *et al*., 2025).

3.1.1 Limitations and translational challenges

Despite their potential, current systems face critical limitations related to scalability, immunocompatibility, and the long-term viability of hepatocytes. Standardizing protocols and implementing multicenter clinical trials are essential steps for validating clinical efficacy and establishing regulatory pathways for approval (Ocskay *et al*., 2021; Sánchez *et al*., 2014; Joo *et al*., 2025).

3.2 Engineering considerations and biomaterials

Artificial Liver Support Systems (ALSS) 's successful development depends on applying engineering principles that ensure functional mimicry, biocompatibility, mechanical integrity, and effective cellular integration (Table 2). Key design parameters include bioreactor architecture, material properties, fluid dynamics, nutrient transport, and hepatocyte viability (Jasirwan *et al*., 2023; Gadour, 2025; Zhidu *et al*., 2024; Chehelgerdi *et al*., 2023).

3.2.1 Bioreactor and device design

Bioreactors in bioartificial liver systems are engineered to emulate hepatic perfusion and mass transport characteristics. Hollow fiber membrane bioreactors (HFMBs) remain the gold standard due to their high surface area-to-volume ratio, facilitating efficient exchange of oxygen, nutrients, and metabolic waste (Li *et al*., 2019; Lanza *et al*., 2020). Nonetheless, limitations such as shear stress-induced cellular damage and heterogeneous nutrient distribution persist. To address these issues, next-generation dynamic flow systems and microfluidic devices are being actively investigated (Barbosa *et al*., 2025; Gimondi *et al*., 2023).

3.2.2 Biomaterial selection

Biomaterials function as scaffolds and structural supports for hepatocyte adhesion and activity. Ideal materials must exhibit biocompatibility, non-immunogenicity, mechanical robustness, and support for cell proliferation and functionality (Rondón *et al*., 2025). Natural polymers such as alginate, gelatin, collagen, and chitosan offer inherent bioactivity and cell-binding motifs, although they often lack sufficient mechanical strength (Mogoşanu & Grumezescu, 2014). In contrast, synthetic polymers like polyethylene glycol (PEG), polylactic acid (PLA), and polycaprolactone (PCL) offer tunable mechanical properties and degradation rates, though surface modifications are often required to enhance cell compatibility (Trimukhe *et al*., 2017; Rondón *et al*., 2023).

3.2.3 Surface modification techniques

Surface modification techniques such as plasma surface modification (PSM) and chemical grafting are commonly employed to improve surface wettability and increase the availability of functional groups that promote protein adsorption and cell interaction (Karthik *et al*., 2023). Plasma-treated materials have enhanced hepatocyte attachment, spreading, and metabolic activity, especially when modified with amine or hydroxyl groups (Ma *et al*., 2018).

Table 2. Biomaterials used in artificial liver support systems (ALSS)

Type of Material	Examples	Characteristics
Natural Polymers	Alginate, collagen, chitosan	High bioactivity, but limited mechanical strength.
Synthetic Polymers	PLA, PEG, PCL	Tunable mechanical properties and degradation rates often require surface functionalization.
Surface-Modified Materials	Plasma-treated surfaces, chemical grafting	Improve cell adhesion and hepatic activity through enhanced surface functionality.

3.2.4 Scaffold fabrication and 3D bioprinting

The advent of three-dimensional bioprinting has enabled the fabrication of liver-mimetic architectures featuring vascular channels and controlled porosity, thereby improving oxygen diffusion and hepatocyte organization (Bhardwaj *et al*., 2024). Bioprinted constructs using bioinks derived from decellularized liver extracellular matrix (dECM) or stem cell-based formulations have improved liver-specific function and *in vitro* viability (Gong *et al*., 2025; Pruinelli *et al*., 2025).

3.2.5 Cell source and compatibility

Primary human hepatocytes remain the gold standard for replicating hepatic function. However, their limited availability and short *in vitro* lifespan pose significant challenges (He *et al*., 2019). As alternative sources, hepatocyte-like cells derived from induced pluripotent stem cells (iPSCs) or mesenchymal stem cells are being explored, as they can be expanded and differentiated under controlled conditions. Nevertheless, their long-term functionality remains under investigation (Akhtar, 2024; Rawashdeh, 2024).

Finally, the engineering of liver-on-chip platforms and implantable ALSS devices demands a multidisciplinary integration of materials science, tissue engineering, microfluidics, and biomedical computing. This convergence is essential to optimize functionality, ensure clinical safety, and enable scalable production.

3.3 Artificial intelligence and anatomical modeling

Each day, it becomes increasingly evident that artificial intelligence (AI) and computational modeling have become essential tools in developing next-generation artificial liver support systems. These technologies are crucial in device design, functional optimization, anatomical simulation, real-time control, and predictive diagnostics (Jumaah *et al*., 2025; Son *et al*., 2020) (Table 3).

Table 3. Applications of artificial intelligence (AI) in artificial liver support systems (ALSS)

AI Application	Description
Functional Optimization	Adjustment of flow rates, cell metabolism, and toxin clearance using machine learning algorithms.
Predictive Modeling & Digital Twin	Personalized simulation of hepatic physiology and therapeutic response.
Medical Image Segmentation	Automatic reconstruction of liver geometries for surgical planning or 3D printing.
Support in Biofabrication	Automated design of bioprinted structures, including cell, bioink, and vascular channel placement.
Real-Time Control	Dynamic regulation of biochemical parameters via sensors and adaptive feedback systems.

3.3.1 AI-assisted functional optimization

Machine learning algorithms have successfully enhanced key operational parameters in ALSS, including toxin elimination rates, flow dynamics, and cell viability. A representative example of this trend is the *Artificial Liver Classifier* (ALC), a bioinspired model that simulates hepatic detoxification logic using a feed-forward neural network architecture, achieving high classification accuracy and minimal overfitting (Jumaah *et al*., 2025). This approach demonstrates the potential of AI to replicate complex liver functions through *in silico* simulation and its efficient integration with hardware systems via adaptive feedback control.

3.3.2 Predictive modeling and digital twin

AI-enabled simulations have led to the development of liver digital twin models—virtual replicas that integrate patient-specific anatomical and physiological data. These models allow for simulation of disease progression, prediction of treatment response, and support for preoperative planning in bioartificial liver system integration (Wang *et al*., 2021; Tuerxun *et al*., 2022). Their utility is particularly relevant in intensive care units, where real-time physiological monitoring can guide immediate adjustments in ALSS therapy.

3.3.3 Medical image segmentation and anatomical design

Deep learning algorithms, such as convolutional neural networks (CNNs), are applied to medical imaging (MRI, CT) for the automated segmentation of hepatic structures (Ouchi & Koike, 2023; Liu *et al*., 2024). These procedures are fundamental for reconstructing personalized liver geometries used in surgical planning, scaffold design, or

organ-on-chip platforms. AI-assisted segmentation reduces manual workload and enhances the spatial resolution and accuracy of the resulting anatomical models.

3.3.4 Integration with advanced biofabrication

AI models have also been implemented to automate bioprinted design by predicting optimal deposition patterns for cells, bioinks, and vascular channels. When combined with computer-aided design (CAD) tools, these systems rapidly create hepatic constructs with spatially controlled architectures (Bhardwaj *et al*., 2024; Pruinelli *et al*., 2025). This integration represents a critical bridge between virtual modeling and physical biofabrication.

3.3.5 Real-time feedback through biosensors

It is important to highlight that the most advanced ALSS prototypes incorporate biosensors capable of monitoring key biochemical parameters—such as ammonia, urea, albumin, and glucose—in real time. AI algorithms analyze this data to dynamically regulate media flow, nutrient delivery, and cellular metabolism, creating a closed-loop control system (Takebe *et al*., 2013; Takebe *et al*., 2017). These adaptive platforms open new perspectives for developing next-generation wearable or implantable liver support devices.

3.4 Bioactive additives

Incorporating bioactive additives into injectable hydrogels has significantly improved their regenerative potential, particularly in applications targeting joint repair. These additives enhance the system's biological performance and confer therapeutic functions beyond mere structural support. In this context, hydrogels function as platforms for the controlled, localized, and sustained release of bioactive agents such as growth factors, anti-inflammatory compounds, and stem cells (Nguyen *et al*., 2024; Nguyen *et al*., 2017).

Among the most relevant signaling molecules are transforming growth factor-beta (TGF-β), bone morphogenetic protein-7 (BMP-7), and insulin-like growth factor-1 (IGF-1), all of which play fundamental roles in cartilage regeneration. These factors promote chondrocyte proliferation, extracellular matrix synthesis, and lineage-specific differentiation. When encapsulated within hydrogel matrices, they induce targeted therapeutic responses while minimizing systemic side effects. Preclinical models have shown that TGF-β-loaded hydrogels enhance the chondrogenic differentiation of mesenchymal stem cells (MSCs) and accelerate the deposition of cartilaginous matrix (Qin *et al*., 2023; Peng *et al*., 2019; Du *et al*., 2023; Mariani *et al*., 2014).

MSCs, widely used as cellular bioactive components, exhibit dual functionality in immunomodulation and differentiation. When integrated into biocompatible hydrogel matrices, these cells release trophic factors that attenuate inflammation, stimulate endogenous repair mechanisms, and integrate functionally into the surrounding cartilage matrix (Han *et al*., 2022; Zhang *et al*., 2022).

Recent advances have also led to the design of hydrogels with time-controlled or stimulus-responsive release properties. These innovative delivery systems use internal or external triggers—such as pH changes, temperature variations, or enzymatic activity—to activate the release of encapsulated agents, thereby optimizing therapeutic windows by the stages of tissue healing (Lu *et al*., 2024; Municoy *et al*., 2020; Ribeiro *et al*., 2024). In addition, dual-delivery hydrogels have been developed to mimic the spatial and temporal complexity of biochemical signaling involved in cartilage repair (Hashemi-Afzal *et al*., 2025).

Moreover, hydrogels have been engineered to deliver anti-inflammatory agents such as dexamethasone, curcumin, and interleukin-1 receptor antagonists (IL-1Ra) to modulate the inflammatory microenvironment characteristic of osteoarthritic joints. These compounds maintain tissue homeostasis and protect the regenerating cartilage from immune-mediated degradation (Nguyen *et al*., 2024; Nguyen *et al*., 2017).

In parallel, state-of-the-art bioactive hydrogels incorporate nanoscale design elements and extracellular matrix-mimetic components to enhance cell adhesion, retention, and viability. Specifically, the incorporation of matrix metalloproteinase (MMP)-sensitive linkers allows for degradation synchronized with local tissue remodeling processes, supporting adaptive, patient-specific therapies (Lu *et al*., 2024; Cabral-Pacheco *et al*., 2020; Gonzalez-Avila *et al*., 2019).

Nevertheless, several translational hurdles remain. Significant challenges include achieving uniform spatial distribution of bioactive additives, preventing premature system degradation, ensuring production scalability, and standardizing release profiles across diverse patient populations. Overcoming these limitations will require close collaboration among biomedical engineers, materials scientists, and clinical professionals focused on refining hydrogel architecture and enhancing the precision of therapeutic delivery.

3.5 Organoids and regenerative medicine

Today, the emergence of liver organoids has redefined the landscape of regenerative medicine by enabling the development of three-dimensional biomimetic microstructures capable of reproducing liver-specific functions under *in vitro* conditions (Gong *et al*., 2025). These organoids, derived from pluripotent stem cells (PSCs), adult stem cells (ASCs), or hepatic progenitors, possess the ability to self-organize into spheroidal or lobule-like structures that emulate key features of liver architecture

and function, including drug metabolism, protein synthesis, and bile secretion (Luo *et al*., 2023).

3.5.1 Development and culture of liver organoids

Liver organoids are commonly generated from embryonic stem cells (ESCs) and human-induced pluripotent stem cells (hiPSCs), typically cultured in three-dimensional matrices such as Matrigel, gelatin-methacrylate (GelMA), or decellularized extracellular matrix (dECM), which provide essential structural and biochemical cues (Ouchi & Koike, 2023; Hu *et al*., 2024).

Differentiation protocols involve the sequential administration of growth factors such as activin A, fibroblast growth factor (FGF), and hepatocyte growth factor (HGF), which promote the acquisition of functional hepatic phenotypes (Yang *et al*., 2022; Baddal & Mammadov, 2024).

3.5.2 Applications in drug testing and disease modeling

Liver organoids represent a versatile platform for high-throughput hepatotoxicity testing and disease modeling. They have been successfully employed in the study of inherited liver diseases, viral hepatitis, and hepatic fibrosis, allowing for precise evaluation of drug–gene interactions in personalized contexts (Sorrentino *et al*., 2020; Nuciforo & Heim, 2021; Liu *et al*., 2024).

3.5.3 Integration into bioartificial systems

Recent advances have focused on the integration of liver organoids with microfluidic systems and perfusable scaffolds, giving rise to "liver-on-a-chip" platforms that optimize nutrient exchange, prolong cell viability, and replicate mechanical stimuli present *in vivo* (Arroyo *et al*., 2020; Girish *et al*., 2025). When incorporated into Artificial Liver Support Systems (ALSS), organoids can function as active living units within bioreactors, enhancing synthetic performance and reducing reliance on animal-derived hepatocytes.

3.5.4 Current limitations

Despite the progress achieved, significant technical challenges persist. These include batch-to-batch variability, incomplete hepatic zonation, absence of functional vascularization, and immune incompatibility in allogeneic applications (Xu *et al*., 2020; Kim *et al*., 2024). Additionally, derived hepatocytes frequently exhibit embryonic rather than adult phenotypes, limiting their metabolic capacity and reliability as functional models (Gong *et al*., 2025; Liu *et al*., 2024).

A critical limitation is the lack of a functional vascular network, which restricts efficient oxygen and nutrient diffusion, compromising tissue viability and long-term *in vitro* performance (Ouchi & Koike, 2023; Luo *et al*., 2023). This issue becomes particularly relevant when considering system scalability and translational applicability. Moreover, in allogeneic or xenogeneic contexts, immunogenicity remains a substantial barrier, necessitating the development of complementary strategies such as cell encapsulation, immune-isolated microenvironments, or targeted immunosuppressive protocols (Kim *et al*., 2024; Xu *et al*., 2020).

3.5.5 Future perspectives

The clinical consolidation of liver organoids will require overcoming these limitations through advanced co-culture strategies involving endothelial, immune, or stromal cells, as well as the implementation of vascularized scaffolds and *in vivo* conditioning protocols that more accurately replicate physiological hepatic architecture and function (Gong *et al*., 2025; Liu *et al*., 2024).

From a biomedical engineering perspective, implementing liver organoids as bioactive platforms within hybrid liver support systems will demand the precise integration of biotechnological strategies, adaptive biomaterials, and intelligent bioelectronic interfaces. It is possible only through this convergence to achieve the compatibility, stability, and therapeutic efficacy required in real clinical scenarios.

3.6 Clinical applications and challenges

Artificial Liver Support Systems (ALSS) have made significant progress from preclinical research, with clinical applications ranging from managing acute liver failure (ALF) to bridging therapy for liver transplantation.

However, transitioning from experimental prototypes to standardized clinical devices faces substantial regulatory, biological, and technological challenges (Jasirwan *et al*., 2023; Gadour, 2025; Brown *et al*., 2025).

3.6.1 Management of acute liver failure (ALF)

In this critical condition, ALSS devices such as MARS and Prometheus have proven effective in stabilizing patients by removing neurotoxic substances like ammonia and bilirubin, thereby reducing hepatic encephalopathy and supporting hemodynamic stability (Sen *et al*., 2005; Papamichalis *et al*., 2023; Stange *et al*., 1999; Feng *et al*., 2024).

For instance, in a cohort of 113 ALF patients, MARS treatment achieved a one-year survival rate of 74%, which increased to 91% when liver transplantation was included (Sakiyama *et al*., 2017).

Nevertheless, their long-term impact on liver regeneration remains limited, and outcomes often depend on early intervention and appropriate patient selection (Thorgersen *et al*., 2019).

3.6.2. Bridge to liver transplantation

Bioartificial systems such as ELAD and HepatAssist have been used to prolong survival in patients on the transplant waiting list, improving their clinical status before transplantation. Despite the promise shown, randomized clinical trials have yielded mixed results, and definitive data on long-term efficacy are still lacking (Ellis *et al*., 1996; Heydari *et al*., 2020; Sánchez *et al*., 2014; Liu *et al*., 2022; Pless, 2007; Gerth *et al*., 2017).

3.6.3. Chronic liver disease and acute-on-chronic liver failure (ACLF).

Emerging evidence suggests that ALSS may also be beneficial in episodes of acute decompensation of chronic liver disease, reducing short-term mortality. MARS-based studies have shown significant mortality reductions in ACLF patients, although the benefit appears transient (Pless, 2007; Gerth *et al*., 2017). Advances in personalized device design may broaden their use in cirrhotic patients experiencing sudden deterioration (Yarrarapu & Sanghavi, 2025; Mielnicki *et al*., 2019).

3.6.4. Regulation and safety

One of the most critical challenges is the lack of unified regulatory standards. Issues such as immune compatibility, endotoxin leakage, thrombogenicity, and long-term biocompatibility remain unresolved. Furthermore, the heterogeneity in cell sources and device configurations hinders cross-study comparisons and delays regulatory approval by agencies such as the Food and Drug Administration (FDA) and European Medicines Agency (EMA) (Gadour, 2025; Rondón *et al*., 2025; Joo *et al*., 2025).

3.6.5. Cost, infrastructure, and accessibility

High costs, complex technical requirements, and the need for multidisciplinary teams hinder the routine implementation of ALSS. In resource-limited settings, the infrastructure needed to sustain continuous extracorporeal support poses a significant barrier (Bañares *et al*., 2013; Saliba *et al*., 2022).

3.6.6. Ethical and logistical challenges in organ replacement therapies

With advances in hepatic organoids and implantable systems, ethical debates surrounding stem cell sourcing, genetic manipulation, and equitable access to advanced therapies are intensifying. It is imperative to develop global guidelines to govern these aspects for responsible implementation (Ballester *et al*., 2025; Riva *et al*., 2024; Hassanein *et al*., 2011).

5 Conclusion

Artificial Liver Support Systems (ALSS) represent a strategic convergence of biomedical engineering, tissue regeneration, stem cell biotechnology, and computational intelligence to address the growing global burden of liver failure. With over two million deaths annually attributed to hepatic dysfunction, the pursuit of viable alternatives to transplantation has driven the development of extracorporeal detoxification platforms, hepatocyte-based bioreactors, and regenerative technologies such as liver organoids.

This review has provided an integrative synthesis of ALSS technologies, highlighting their classification into artificial, bioartificial, and hybrid modalities, and analyzing the engineering principles, biological interfaces, and computational tools that support their development. Advancements in bioreactor design, microfluidic integration, and biomaterial functionalization have progressively enhanced cell viability and *in vitro* metabolic performance. Simultaneously, the rise of stem cell-derived liver organoids and 3D bioprinting has expanded the scope of regenerative hepatology, enabling disease modeling, pharmacological testing, and the potential creation of personalized autologous grafts.

Equally relevant has been the incorporation of artificial intelligence into real-time biosensor monitoring, the generation of digital twin models, and the adaptive control of hepatic devices, laying the foundation for predictive and personalized liver support. These emerging systems respond dynamically to physiological changes and can be algorithmically optimized according to individual patient needs.

Nevertheless, critical barriers remain. Limitations in immunocompatibility, reliability of cell sources, vascularization, and large-scale implementation continue to delay clinical translation. In addition, the absence of standardized regulatory frameworks and the ethical complexities associated with cellular manipulation and equitable access must be proactively addressed. Future success in this field will depend on the development of fully

vascularized, immunoprotected, and AI-integrated implantable liver constructs. Strategic alliances between academic institutions, biotechnology companies, and regulatory bodies such as the U.S. Food and Drug Administration (FDA) and the European Medicines Agency (EMA) will be essential to validate these systems at scale and ensure their bioethical deployment.

Thus, ALSS has transcended theoretical concepts to become active biomedical platforms with the potential to redefine hepatology. As they evolve from extracorporeal support systems to functional organ replacements, they hold unprecedented capacity to prolong life, restore liver function, and improve the quality of life for patients worldwide. Their successful integration will mark a pivotal transition toward personalized and regenerative hepatic medicine.

6 Recommendations

To consolidate the development and clinical implementation of Artificial Liver Support Systems (ALSS), it is essential to establish standardized international regulatory frameworks incorporating technical, biological, and ethical criteria. Such frameworks would enable cross-platform comparisons and facilitate approval by agencies like the FDA and EMA. Likewise, it is recommended to intensify research into hybrid systems that integrate detoxification modules with immunoisolated cellular components, thereby minimizing adverse responses in clinical applications. Engineering hepatic organoids requires clear prioritization of functional vascularization, a sine qua non condition for their integration into implantable devices or microfluidic platforms such as liver-on-a-chip. At the engineering design level, it is imperative to systematically apply artificial intelligence and computational modeling to develop bioreactors, optimizing critical parameters such as shear stress, nutrient diffusion, and toxin clearance kinetics.

In the field of biofabrication, it is essential to consolidate smart bioinks functionalized with growth factors and stimuli-responsive materials that enable stable and functionally active three-dimensional personalized bioprinting. In parallel, developing predictive models and hepatic digital twins that integrate anatomical, physiological, and molecular variables will allow for data-driven, real-time personalized support medicine. This entire technological ecosystem must be supported by multidisciplinary consortia composed of universities, research centers, biotech startups, and regulatory agencies to ensure the scalability, clinical validation, and global accessibility of ALSS.

Additionally, it is recommended that multicenter clinical trials be designed with an adaptive approach, considering the etiological heterogeneity of liver failure and incorporating biomarkers and genetic profiles as predictive variables. Finally, in light of the emerging use of stem cells, gene editing, and implantable devices, there is an urgent need to establish global bioethical guidelines that regulate their application, ensure patient privacy, and promote equitable access to these disruptive technologies.

References

Akhtar, Z. B. (2024). *Exploring biomedical engineering (BME): Advances within accelerated computing and regenerative medicine for a computational and medical science perspective exploration analysis*. J. Emerg. Med. OA, 2, 1–23.

Arroyo, V., Moreau, R., & Jalan, R. (2020). *Acute-on-chronic liver failure*. New England Journal of Medicine, 382(22), 2137–2145. https://doi.org/10.1056/nejmra1914900

Baddal, B., & Mammadov, E. (2024). *Design, manufacture, and characterization of a liver-chip model: A platform for disease modeling and toxicity screening*. https://doi.org/10.4274/cjms.2023.2023-94

Ballester, M. P., Elshabrawi, A., & Jalan, R. (2025). *Extracorporeal liver support and liver transplantation for acute-on-chronic liver failure*. Liver International, 45(3), e15647. https://doi.org/10.1111/liv.15647

Barbosa, F., Coutinho, P., Ribeiro, M. P., Moreira, A. F., Lourenço, L. M., & Miguel, S. P. (2025). *Advancements and challenges in SLA-based microfluidic devices for organ-on-chip applications*. Materials & Design, 114254. https://doi.org/10.1016/j.matdes.2025.114254

Bañares, R., Nevens, F., Larsen, F. S., Jalan, R., Albillos, A., Dollinger, M., ... & RELIEF Study Group. (2013). *Extracorporeal albumin dialysis with the molecular adsorbent recirculating system in acute-on-chronic liver failure: The RELIEF trial*. Hepatology, 57(3), 1153–1162. https://doi.org/10.1002/hep.26185

Bhardwaj, N., Sood, M., & Gill, S. S. (2024). *3D-bioprinting and AI-empowered anatomical structure designing: A review*. Current Medical Imaging, 20, 1–15. https://doi.org/10.2174/0115734056259274231019061329

Bhatt, S. S., Krishna Kumar, J., Laya, S., Thakur, G., & Nune, M. (2024). *Scaffold-mediated liver regeneration: A comprehensive exploration of current advances*. Journal of Tissue Engineering, 15, 20417314241286092. https://doi.org/10.1177/20417314241286092

Brown Jr, R. S., Fisher, R. A., Subramanian, R. M., Griesemer, A., Fernandes, M., Thatcher, W. H., ... & Curtis, M. (2025). *Artificial liver support systems in acute liver failure and acute-on-chronic liver failure: Systematic review and meta-analysis*. Critical Care Explorations, 7(1), e1199.

https://doi.org/10.1097/cce.0000000000001199

Cabral-Pacheco, G. A., Garza-Veloz, I., Castruita-De la Rosa, C., Ramirez-Acuña, J. M., Perez-Romero, B. A., Guerrero-Rodriguez, J. F., ... & Martinez-Fierro, M. L. (2020). The roles of matrix metalloproteinases and their inhibitors in human diseases. *International journal of molecular sciences*, *21*(24), 9739. https://doi.org/10.3390/ijms21249739

Cerneckis, J., Cai, H., & Shi, Y. (2024). *Induced pluripotent stem cells (iPSCs): Molecular mechanisms of induction and applications*. Signal Transduction and Targeted Therapy, 9(1), 112. https://doi.org/10.1038/s41392-024-01809-0

Chehelgerdi, M., Behdarvand Dehkordi, F., Chehelgerdi, M., Kabiri, H., Salehian-Dehkordi, H., Abdolvand, M., ... & Ranjbarnejad, T. (2023). *Exploring the promising potential of induced pluripotent stem cells in cancer research and therapy*. Molecular Cancer, 22(1), 189. https://doi.org/10.1186/s12943-023-01873-0

Du, X., Cai, L., Xie, J., & Zhou, X. (2023). The role of TGF-beta3 in cartilage development and osteoarthritis. *Bone research*, *11*(1), 2. https://doi.org/10.1038/s41413-022-00239-4

Ellis, A. J., Hughes, R. D., Wendon, J. A., Dunne, J., Langley, P. G., Kelly, J. H., ... & Williams, R. (1996). *A pilot-controlled trial of the extracorporeal liver assist device was conducted in acute liver failure*. Hepatology, 24(6), 1443–1448. https://doi.org/10.1002/hep.510240621

Feng, S., Roll, G. R., Rouhani, F. J., & Fueyo, A. S. (2024). *The future of liver transplantation*. Hepatology, 80(3), 674–697. https://doi.org/10.1097/HEP.0000000000000873

Gadour, E. (2025). *Lesson learnt from 60 years of liver transplantation: Advancements, challenges, and future directions*. World Journal of Transplantation, 15(1), 93253. https://doi.org/10.5500/wjt.v15.i1.93253

Gao, X., Li, R., Cahan, P., Zhao, Y., Yourick, J. J., & Sprando, R. L. (2020). *Hepatocyte-like cells derived from human induced pluripotent stem cells using small molecules: Implications of a transcriptomic study*. Stem Cell Research & Therapy, 11, 1–21. https://doi.org/10.1186/s13287-020-01914-1

García Martínez, J. J., & Bendjelid, K. (2018). *Artificial liver support systems: What is new over the last decade?* Annals of Intensive Care, 8, 1–14. https://doi.org/10.1186/s13613-018-0453-z

Gerth, H. U., Pohlen, M., Thölking, G., Pavenstädt, H., Brand, M., Hüsing-Kabar, A., ... & Schmidt, H. H. (2017). Molecular adsorbent recirculating system can reduce short-term mortality among patients with acute-on-chronic liver failure—a retrospective analysis. *Critical care medicine*, *45*(10), 1616-1624. *DOI:* 10.1097/CCM.0000000000002562

Gimondi, S., Ferreira, H., Reis, R. L., & Neves, N. M. (2023). *Microfluidic devices: A tool for nanoparticle synthesis and performance evaluation*. ACS Nano, 17(15), 14205–14228. https://doi.org/10.1021/acsnano.3c01117

Girish, V., Mousa, O. Y., Syed, K., & StatPearls contributors. (2025). *Acute on chronic liver failure*. In StatPearls. StatPearls Publishing. https://www.ncbi.nlm.nih.gov/books/NBK499902/

Gong, D., Song, J., & Zhang, Y. (2025). *Advances, challenges, and future applications of liver organoids in experimental regenerative medicine*. Frontiers in Medicine, 11, 1521851. https://doi.org/10.3389/fmed.2024.1521851

Gonzalez-Avila, G., Sommer, B., Mendoza-Posada, D. A., Ramos, C., Garcia-Hernandez, A. A., & Falfan-Valencia, R. (2019). Matrix metalloproteinases participation in the metastatic process and their diagnostic and therapeutic applications in cancer. *Critical reviews in oncology/hematology*, *137*, 57-83. https://doi.org/10.1016/j.critrevonc.2019.02.010

Han, Y., Yang, J., Fang, J., Zhou, Y., Candi, E., Wang, J., ... & Shi, Y. (2022). The secretion profile of mesenchymal stem cells and potential applications in treating human diseases. *Signal transduction and targeted therapy*, *7*(1), 92. https://doi.org/10.1038/s41392-022-00932-0

Hashemi-Afzal, F., Fallahi, H., Bagheri, F., Collins, M. N., Eslaminejad, M. B., & Seitz, H. (2025). Advancements in hydrogel design for articular cartilage regeneration: A comprehensive review. *Bioactive Materials*, *43*, 1-31. https://doi.org/10.1016/j.bioactmat.2024.09.005

Hassanein, T. I., Schade, R. R., & Hepburn, I. S. (2011). *Acute-on-chronic liver failure: Extracorporeal liver assist devices*. Current Opinion in Critical Care, 17(2), 195–203. https://doi.org/10.1097/mcc.0b013e328344b3aa

He, Y. T., Qi, Y. N., Zhang, B. Q., Li, J. B., & Bao, J. (2019). *Bioartificial liver support systems for acute liver failure: A systematic review and meta-analysis*. World Journal of Gastroenterology, 25(27), 3634–3648. https://doi.org/10.3748/wjg.v25.i27.3634

Heydari, Z., Najimi, M., Mirzaei, H., Shpichka, A., Ruoss, M., Farzaneh, Z., ... & Vosough, M. (2020). *Tissue engineering in liver regenerative medicine: Insights into novel translational technologies*. Cells, 9(2), 304. https://doi.org/10.3390/cells9020304

Hu, Y., Geng, Q., Wang, L., Wang, Y., Huang, C., Fan, Z., & Kong, D. (2024). *Research progress and*

application of liver organoids for disease modeling and regenerative therapy. Journal of Molecular Medicine, 102(7), 859–874. https://doi.org/10.1007/s00109-024-02455-3

Jasirwan, C. O. M., Muradi, A., & Antarianto, R. D. (2023). *Bio-artificial liver support system: A prospective future therapy*. Livers, 3(1), 65–75. https://doi.org/10.3390/livers3010006

Joo, D. J., Nelson, E., Chen, H., Amiot, B., & Nyberg, S. (2025). *Bioartificial liver support for acute liver failure*. Annals of Liver Transplantation, 5(1), 31–39. https://doi.org/10.52604/alt.25.0004

Jumaah, M. A., Ali, Y. H., & Rashid, T. A. (2025). *Artificial liver classifier: A new alternative to conventional machine learning models*. arXiv preprint arXiv:2501.08074. https://doi.org/10.48550/arXiv.2501.08074

Karthik, C., Rajalakshmi, S., Thomas, S., & Thomas, V. (2023). *Intelligent polymeric biomaterials surface driven by plasma processing*. Current Opinion in Biomedical Engineering, 26, 100440. https://doi.org/10.1016/j.cobme.2022.100440

Kim, Y., Kang, M., Mamo, M. G., Adisasmita, M., Huch, M., & Choi, D. (2024). *Liver organoids: Current advances and future applications for hepatology*. Clinical and Molecular Hepatology, 31(Suppl), S327. https://doi.org/10.3350/cmh.2024.1040

Lanza, R., Langer, R., Vacanti, J. P., & Atala, A. (Eds.). (2020). *Principles of tissue engineering*. Academic Press. ISBN: 9780128184226

Li, Y., Chen, H. S., Shaheen, M., Joo, D. J., Amiot, B. P., Rinaldo, P., & Nyberg, S. L. (2019). *Cold storage of porcine hepatocyte spheroids for spheroid bioartificial liver*. Xenotransplantation, 26(4), e12512. https://doi.org/10.1111/xen.12512

Liu, M., Xiang, Y., Yang, Y., Long, X., Xiao, Z., Nan, Y., ... & Ai, K. (2022). *State-of-the-art advancements in liver-on-a-chip (LOC): Integrated biosensors for LOC*. Biosensors and Bioelectronics, 218, 114758. https://doi.org/10.1016/j.bios.2022.114758

Liu, S., Cheng, C., Zhu, L., Zhao, T., Wang, Z., Yi, X., ... & Yang, B. (2024). *Liver organoids: Updates on generation strategies and biomedical applications*. Stem Cell Research & Therapy, 15(1), 244. https://doi.org/10.1186/s13287-024-03865-3

Lu, P., Ruan, D., Huang, M., Tian, M., Zhu, K., Gan, Z., & Xiao, Z. (2024). Harnessing the potential of hydrogels for advanced therapeutic applications: Current achievements and future directions. *Signal transduction and targeted therapy*, *9*(1), 166. https://doi.org/10.1038/s41392-024-01852-x

Luo, Q., Wang, N., Que, H., Mai, E., Hu, Y., Tan, R., ... & Gong, P. (2023). *Pluripotent stem cell-derived hepatocyte-like cells: Induction methods and applications*. International Journal of Molecular Sciences, 24(14), 11592. https://doi.org/10.3390/ijms241411592

Ma, X., Liu, J., Zhu, W., Tang, M., Lawrence, N., Yu, C., ... & Chen, S. (2018). *3D bioprinting of functional tissue models for personalized drug screening and in vitro disease modeling*. Advanced Drug Delivery Reviews, 132, 235–251. https://doi.org/10.1016/j.addr.2018.06.011

Mariani, E., Pulsatelli, L., & Facchini, A. (2014). Signaling pathways in cartilage repair. *International journal of molecular sciences*, *15*(5), 8667-8698. https://doi.org/10.3390/ijms15058667

Mielnicki, W., Dyla, A., & Karczewski, M. (2019). *Clinical effectiveness of MARS treatment–Multidirectional analysis of positive clinical response to treatment*. Clinical and Experimental Hepatology, 5(4), 271–278. https://doi.org/10.5114/ceh.2019.89163

Mogoşanu, G. D., & Grumezescu, A. M. (2014). *Natural and synthetic polymers for wounds and burns dressing*. International Journal of Pharmaceutics, 463(2), 127–136. https://doi.org/10.1016/j.ijpharm.2013.12.015

Municoy, S., Alvarez Echazu, M. I., Antezana, P. E., Galdopórpora, J. M., Olivetti, C., Mebert, A. M., ... & Desimone, M. F. (2020). Stimuli-responsive materials for tissue engineering and drug delivery. *International Journal of Molecular Sciences*, *21*(13), 4724. https://doi.org/10.3390/ijms21134724

Nguyen, M., Battistoni, C. M., Babiak, P. M., Liu, J. C., & Panitch, A. (2024). Chondroitin sulfate/hyaluronic acid-blended hydrogels suppress chondrocyte inflammation under pro-inflammatory conditions. *ACS Biomaterials Science & Engineering*, *10*(5), 3242-3254. https://doi.org/10.1021/acsbiomaterials.4c00200

Nguyen, Q. T., Jacobsen, T. D., & Chahine, N. O. (2017). Effects of inflammation on multiscale biomechanical properties of cartilaginous cells and tissues. *ACS Biomaterials Science & Engineering*, *3*(11), 2644-2656. https://doi.org/10.1021/acsbiomaterials.6b00671

Nuciforo, S., & Heim, M. H. (2021). *Organoids to model liver disease*. JHEP Reports, 3(1), 100198. https://doi.org/10.1016/j.jhepr.2020.100198

Ocskay, K., Kanjo, A., Gede, N., Szakács, Z., Pár, G., Erőss, B., ... & Molnár, Z. (2021). *Uncertainty in the impact of liver support systems in acute-on-chronic liver failure: A systematic review and network meta-analysis*. Annals of Intensive Care, 11, 1–17. https://doi.org/10.1186/s13613-020-00795-0

Ouchi, R., & Koike, H. (2023). *Modeling human liver*

organ development and diseases with pluripotent stem cell-derived organoids. Frontiers in Cell and Developmental Biology, 11, 1133534. https://doi.org/10.3389/fcell.2023.1133534

Papamichalis, P., Oikonomou, K. G., Valsamaki, A., Xanthoudaki, M., Katsiafylloudis, P., Papapostolou, E., ... & Papadopoulos, D. (2023). *Liver replacement therapy with extracorporeal blood purification techniques: Current knowledge and future directions*. World Journal of Clinical Cases, 11(17), 3932. https://doi.org/10.12998/wjcc.v11.i17.3932

Peng, X. B., Zhang, Y., Wang, Y. Q., He, Q., & Yu, Q. (2019). IGF-1 and BMP-7 synergistically stimulate articular cartilage repairing in the rabbit knees by improving chondrogenic differentiation of bone-marrow mesenchymal stem cells. *Journal of Cellular Biochemistry*, *120*(4), 5570-5582. https://doi.org/10.1002/jcb.27841

Pless, G. (2007). Artificial and bioartificial liver support. *Organogenesis*, *3*(1), 20-24. https://doi.org/10.4161/org.3.1.3635

Pruinelli, L., Balakrishnan, K., Ma, S., Li, Z., Wall, A., Lai, J. C., ... & Simon, G. (2025). *Transforming liver transplant allocation with artificial intelligence and machine learning: A systematic review*. BMC Medical Informatics and Decision Making, 25(1), 98. https://doi.org/10.1186/s12911-025-02890-3

Qin, S., Zhu, J., Zhang, G., Sui, Q., Niu, Y., Ye, W., ... & Liu, H. (2023). Research progress of functional motifs based on growth factors in cartilage tissue engineering: a review. *Frontiers in Bioengineering and Biotechnology*, *11*, 1127949. https://doi.org/10.3389/fbioe.2023.1127949

Ramli, M. N. B., Lim, Y. S., Koe, C. T., Demircioglu, D., Tng, W., Gonzales, K. A. U., ... & Chan, Y. S. (2020). *Human pluripotent stem cell-derived organoids as models of liver disease*. Gastroenterology, 159(4), 1471–1486. https://doi.org/10.1053/j.gastro.2020.06.010

Rawashdeh, B. (2024). *Artificial intelligence in organ transplantation: Surveying current applications, addressing challenges and exploring frontiers*. Artificial Intelligence in Medicine and Surgery: An Exploration of Current Trends, Potential Opportunities, and Evolving Threats – Volume 2, 75. https://doi.org/10.5772/intechopen.114356

Ribeiro, C., Silván, U., & Lanceros-Mendez, S. (Eds.). (2024). *Stimuli-Responsive Materials for Tissue Engineering*. John Wiley & Sons.

Riva, I., Marino, A., Valetti, T. M., Marchesi, G., & Fabretti, F. (2024). *Extracorporeal liver support techniques: A comparison*. Journal of Artificial Organs, 27(3), 261–268. https://doi.org/10.1007/s10047-023-01409-9

Rondón, J., Muñiz, C., Lugo, C., Farinas-Coronado, W., & Gonzalez-Lizardo, A. (2024). *Bioethics in biomedical engineering*. Ciencia e Ingeniería, 45(2), 159–168. http://erevistas.saber.ula.ve/index.php/cienciaeingenieria/article/view/19768/

Rondón, J., Sánchez-Martínez, V. M., Lugo, C., & Gonzalez-Lizardo, A. (2025). *Tissue engineering: Advancements, challenges, and future perspectives*. Revista Ciencia e Ingeniería, 46(1), 19–28. http://erevistas.saber.ula.ve/index.php/cienciaeingenieria/article/view/20607/21921932297

Rondón, J., Vázquez, J., & Lugo, C. (2023). *Biomaterials used in tissue engineering for the manufacture of scaffolds*. Ciencia e Ingeniería, 44(3), 297–308. http://erevistas.saber.ula.ve/index.php/cienciaeingenieria/article/view/19221

Sakiyama, R., Blau, B. J., & Miki, T. (2017). Clinical translation of bioartificial liver support systems with human pluripotent stem cell-derived hepatic cells. *World journal of gastroenterology*, *23*(11), 1974. http://dx.doi.org/10.3748/wjg.v23.i11.1974

Saliba, F., Bañares, R., Larsen, F. S., Wilmer, A., Parés, A., Mitzner, S., ... & Jaber, S. (2022). *Artificial liver support in patients with liver failure: A modified DELPHI consensus of international experts*. Intensive Care Medicine, 48(10), 1352–1367. https://doi.org/10.1007/s00134-022-06802-1

Sánchez, C. L., Len, O., Gavalda, J., Bilbao, I., Castells, L., Gelabert, M. A., ... & Pahissa, A. (2014). *Liver biopsy–related infection in liver transplant recipients: A current matter of concern?* Liver Transplantation, 20(5), 552–556. https://doi.org/10.1002/lt.23817

Sen, S., Mookerjee, R. P., Cheshire, L. M., Davies, N. A., Williams, R., & Jalan, R. (2005). *Albumin dialysis reduces portal pressure acutely in patients with severe alcoholic hepatitis*. Journal of Hepatology, 43(1), 142–148. https://doi.org/10.1016/j.jhep.2005.01.032

Son, H. H., Phuong, P. C., van Walsum, T., & Ha, L. M. (2020). *Liver segmentation on a variety of computed tomography (CT) images based on convolutional neural networks combined with connected components*. VNU Journal of Science: Computer Science and Communication Engineering, 36(1). https://doi.org/10.25073/2588-1086/vnucsce.241

Sommerfeld, O., Neumann, C., Becker, J., von Loeffelholz, C., Roth, J., Kortgen, A., ... & Sponholz, C. (2023). *Extracorporeal albumin dialysis in critically ill patients with liver failure: Comparison of four different devices—A retrospective analysis*. The International Journal of Artificial Organs, 46(8–9), 481–491.

https://doi.org/10.1177/0391398823119195
Sorrentino, G., Rezakhani, S., Yildiz, E., Nuciforo, S., Heim, M. H., Lutolf, M. P., & Schoonjans, K. (2020). *Mechano-modulatory synthetic niches for liver organoid derivation*. Nature Communications, 11(1), 3416. https://doi.org/10.1038/s41467-020-17161-0
Stange, T., Mitzner, S., Risler, T., Erley, C., Lauchart, W., Goehl, H., ... & Hopt, U. (1999). *Molecular adsorbent recycling system (MARS): Clinical results of a new membrane-based blood purification system for bioartificial liver support*. Artificial Organs, 23(4), 319–330. https://doi.org/10.1046/j.1525-1594.1999.06122.x
Takebe, T., Sekine, K., Enomura, M., Koike, H., Kimura, M., Ogaeri, T., ... & Taniguchi, H. (2013). *Vascularized and functional human liver from an iPSC-derived organ bud transplant*. Nature, 499(7459), 481–484. https://doi.org/10.1038/nature12271
Takebe, T., Sekine, K., Kimura, M., Yoshizawa, E., Ayano, S., Koido, M., ... & Taniguchi, H. (2017). *Massive and reproducible production of liver buds entirely from human pluripotent stem cells*. Cell Reports, 21(10), 2661–2670. https://doi.org/10.1016/j.celrep.2017.11.005
Thorgersen, E. B., Barratt-Due, A., Haugaa, H., Harboe, M., Pischke, S. E., Nilsson, P. H., & Mollnes, T. E. (2019). The role of complement in liver injury, regeneration, and transplantation. *Hepatology*, *70*(2), 725-736. https://onlinelibrary.wiley.com/doi/pdf/10.1002/hep.30508
Trimukhe, A. M., Pandiyaraj, K. N., Tripathi, A., Melo, J. S., & Deshmukh, R. R. (2017). *Plasma surface modification of biomaterials for biomedical applications*. In Tripathi, A., & Melo, J. (Eds.), *Advances in biomaterials for biomedical applications* (Vol. 66). Springer. https://doi.org/10.1007/978-981-10-3328-5_3
Tuerxun, K., He, J., Ibrahim, I., Yusupu, Z., Yasheng, A., Xu, Q., ... & Xu, T. (2022). *Bioartificial livers: A review of their design and manufacture*. Biofabrication, 14(3), 032003. https://doi.org/10.1088/1758-5090/ac6e86
Wang, J., Ren, H., Liu, Y., Sun, L., Zhang, Z., Zhao, Y., & Shi, X. (2021). *Bioinspired artificial liver system with hiPSC-derived hepatocytes for acute liver failure treatment*. Advanced Healthcare Materials, 10(23), 2101580. https://doi.org/10.1002/adhm.202101580
Xu, T., Li, L., Liu, Y. C., Cao, W., Chen, J. S., Hu, S., ... & Zhou, H. (2020). *CRISPR/Cas9-related technologies in liver diseases: From feasibility to future diversity*. International Journal of Biological Sciences,16(13), 2283. https://doi.org/10.7150/ijbs.33481
Yang, Z., Liu, X., Cribbin, E. M., Kim, A. M., Li, J. J., & Yong, K. T. (2022). *Liver-on-a-chip: Considerations, advances, and beyond*. Biomicrofluidics, 16(6). https://doi.org/10.1063/5.0106855
Yarrarapu, S. N. S., & Sanghavi, D. K. (2025). *Molecular absorbent recirculating system*. StatPearls Publishing. http://europepmc.org/books/NBK555939
Zhang, Y., Dong, N., Hong, H., Qi, J., Zhang, S., & Wang, J. (2022). Mesenchymal stem cells: therapeutic mechanisms for stroke. *International Journal of Molecular Sciences*, *23*(5), 2550. https://doi.org/10.1016/j.tice.2024.102380
Zhidu, S., Ying, T., Rui, J., & Chao, Z. (2024). *Translational potential of mesenchymal stem cells in regenerative therapies for human diseases: Challenges and opportunities*. Stem Cell Research & Therapy, 15(1), 266. https://doi.org/10.1186/s13287-024-03885-z

Received: *April 29th, 2025*

Accepted: *July 16th, 2025*

Rondón Contreras, Jairo: *Ph.D. in Applied Chemistry, mention: Materials Study, 2015, Universidad de Los Andes. Professor of Biomedical & Chemical Engineering Departments at the Polytechnic University of Puerto Rico. San Juan, PR-USA.* *https://orcid.org/0000-0002-9738-966X*

García, Andrea: *BSc. in Biomedical Engineering, 2025, Polytechnic University of Puerto Rico. San Juan, PR-USA. Email: garcia_128860@students.pupr.edu*
https://orcid.org/0009-0000-7023-3692

Lugo Claudio, *Doctor in Chemistry in Applied Chemistry, Materials Study, 2017. (ULA). Professor at the University of the Andes, Faculty of Sciences, Kinetics and Catalysis Laboratory. Email: claudiolugo@ula.ve*
https://orcid.org/ 0000-0001-8003-0354

Gonzalez-Lizardo, Angel: *Ph.D. Engineering, 2003, University of Dayton, Dayton, OH. Professor, Director, Plasma Engineering Laboratory and Sponsored Research Office at the Polytechnic University of Puerto Rico, San Juan, Puerto Rico, USA. Email: agonzalez@pupr.edu*
https://orcid.org/0000-0002-0722-1426

Artículo de Investigación. Revista Ciencia e Ingeniería. Vol. 46, No. 1 pp. 279-294, agosto-noviembre,2025.
ISSN 1316-7081. ISSN Elect. 2244-8780 Universidad de los Andes (ULA)

Efecto antibacteriano y cambios de calidad en piña (*Ananas comosus*) fresca cortada tratada con luz ultravioleta

Antibacterial effect and quality changes in fresh cut pineapple (*Ananas comosus*) treated with ultraviolet light

Ramos-Villarroel, Ana[1,2*]; Maftei, Nicoleta-Maricica[3]
[1]Instituto Venezolano de Investigaciones Científicas (IVIC), Caracas, Venezuela.
[2]Universidad de Oriente, Nucleo de Monagas, Venezuela.
[3]Departamento de Ciencias Farmacéuticas, Universidad de Galati "Dunarea de Jos", Galati, Romanía.
*ay2170@gmail.com

Resumen

El objetivo de esta investigación fue evaluar el efecto antibacteriano y cambios de calidad en piña fresca cortada tratada con luz ultravioleta. Para ello, la piña fue seleccionada, lavada, cortada en triángulos y envasada para someterse al análisis microbiológico, donde se inocularon 100 µL (10^7 y 10^9 UFC/mL) de un cultivo de *Escherichia coli* y *Listeria innocua* por separado, en la superficie de los trozos de piña. Posteriormente fueron tratados durante 5 min con luz UV a distancias de 15 y 8 cm con dosis de 1,479 y 2,064 kJ/cm^2, respectivamente. Para el análisis fisicoquímico (pH, color y firmeza) las muestras se procesaron y trataron de la misma manera, pero sin inocular. Finalmente se sellaron las bandejas y se almacenaron a 5 °C. Los análisis microbiológicos y fisicoquímicos fueron realizados cada 3 días durante 15 días de almacenamiento. En los resultados de los análisis microbiológicos se registraron reducciones de 4,50 y 3,51 log UFC/g para *E. coli* y *L. innocua* respectivamente. Mostrándose *E. coli* más sensible a la luz UV. En cuanto a los parámetros fisicoquímicos el pH aumentó gradualmente (2,39 - 3,66). El color de la coordenada a* aumentó en función del tiempo dirigiéndose hacia las tonalidades rojas (pardeamiento). El parámetro b* no resultó afectado por el tratamiento con luz ultravioleta, pero si lo afectó el tiempo de almacenamiento, con un valor inicial y final de 23,81 y 14,64, respectivamente. La firmeza disminuyó a lo largo de todo el estudio (12,77 – 9,11 N). La luz ultravioleta como método alternativo es efectivo para la inactivación de *E. coli* y *L. innocua* además mejoró la calidad fisicoquímica de la piña fresca cortada.

Palabras clave: piña, luz ultravioleta, inactivación bacteriana, fruta fresca cortada.

Abstract

The objective of this research was to evaluate the antibacterial effect and quality changes in fresh cut pineapple treated with ultraviolet light. For this, the pineapple was selected, washed, cut into triangles and packaged to undergo microbiological analysis, where 100 µL (107 and 109 CFU/mL) of a culture of *Escherichia coli* and *Listeria innocua* were inoculated separately, on the surface of the pineapple pieces. Subsequently, they were treated for 5 min with UV light at distances of 15 and 8 cm with doses of 1,479 and 2,064 kJ/cm2, respectively. For the physicochemical analysis (pH, color and firmness) the samples were processed and treated in the same way, but without inoculation. Finally, the trays were sealed and stored at 5 °C. Microbiological and physicochemical analyzes were carried out every 3 days during 15 days of storage. In the results of the microbiological analyses, reductions of 4.50 and 3.51 log CFU/g were recorded for *E. coli* and *L. innocua* respectively. *E. coli* showing itself to be more sensitive to UV light. Regarding the physicochemical parameters, the pH gradually increased (2.39 - 3.66). The color in the a* coordination increased as a function of time, moving towards red tones (browning). The b* parameter was not affected by the treatment with ultraviolet light but was affected by the storage time, with an initial and final value of 23.81 and 14.64, respectively. Firmness decreased throughout the study (12.77 – 9.11 N). Ultraviolet light as an alternative method was effective for the inactivation of *E. coli* and *L. innocua* and improved the physicochemical quality of fresh cut pineapple.

Keywords: pineapple, ultraviolet light, bacterial inactivation, fresh-cut fruits.

1 Introducción

El ser humano reconoce la importancia de incorporar frutas y hortalizas frescas en la dieta diaria por su alto contenido de vitaminas, antioxidantes, minerales, fibra, carbohidratos y agua, así como de sustancias fitoquímicas que mejoran el bienestar humano y reducen el riesgo de varias enfermedades (Montero, 2010).

Dentro de las frutas tropicales más consumidas en Venezuela se encuentra la piña (*Ananas comosus*) que, además de ser una fruta sabrosa y refrescante, trae consigo múltiples propiedades medicinales que brindan beneficios para la salud: estimula la digestión y la actividad del intestino delgado por su alto contenido en agua y bromelina, es diurética, desintoxicante, normaliza la flora microbiana del colon, desinflama las hemorroides, tiene acción expectorante, previene y corrige el estreñimiento, además ejerce una acción normalizadora sobre la secreción y superficie alterada de las mucosas inflamadas (Morales, 2011). Estos son algunos de los beneficios que aporta, por ello su consumo se ha incrementado en las últimas décadas en todo el mundo.

El actual ritmo de vida, con escaso tiempo para preparar comidas equilibradas, ha provocado la demanda de productos vegetales naturales, frescos, saludables y dispuestos para consumir, como son los mínimamente procesados en fresco (MPF), denominados comercialmente "Cuarta gama" (Artés y col., 2009), que corresponden a frutas y hortalizas frescas, limpias, trozadas y envasadas para su consumo, las cuales mantienen gran parte de sus propiedades naturales (Aranceta y Pérez, 2006).

Los productos mínimamente procesados no son sometidos a ningún tratamiento térmico para la destrucción de microorganismos, sino que sus tejidos mantienen sus funciones metabólicas activas hasta que llegan al consumidor final (Montero, 2010). Estos productos frescos cortados, al tener una mayor superficie expuesta, son mucho más sensibles al ataque microbiano.

En vista de lo anterior, la industria alimentaria al tratar de satisfacer las exigencias de inocuidad ha impulsado el desarrollo y diseño de nuevas tecnologías, equipos, procesos y metodologías que permitan obtener productos con características semejantes a los alimentos frescos y con una vida útil equiparable a los productos procesados. Según López-Malo y Palou (2005), figuran como tecnologías no térmicas la aplicación de atmósferas modificadas, ozono, recubrimientos comestibles, radiación gamma, pulsos de luz intensa y luz ultravioleta (UV), entre otros.

La luz UV como tecnología emergente ha demostrado reducir el número de microorganismos en la superficie de las frutas frescas cortadas, sin un impacto significativo sobre sus propiedades fisicoquímicas y sensoriales (Rivera-Pastrana y col., 2007; Gómez y col., 2010).

La luz ultravioleta es una radiación no ionizante (tratamiento físico que no deja residuos) que daña el ADN microbiano, llegando a causar la muerte celular, sin alterar la estructura de las células vegetales (Artés-Hernández y col., 2009). La luz UV se utiliza ampliamente como una alternativa a la esterilización química y en la reducción microbiana de productos alimenticios. Su uso ha sido aprobado como desinfectante en el tratamiento superficial de alimentos (USFDA, 2002).

El uso de la luz UV con fines de desinfección involucra a la región ultravioleta del espectro electromagnético, con un rango de longitud de onda entre 100 y 400 nm. La radiación UV produce cambios fotoquímicos, cuyos efectos pueden variar según la especie de microorganismo que se trate. El mecanismo de acción letal depende de su absorción por el ADN, pudiendo detener el crecimiento celular y provocar la muerte (Domínguez y Parzanese, 2011).

Se han realizado estudios utilizando este método de conservación en una gran variedad de sustratos de origen vegetal, dentro de los que se pueden mencionar frutos de fresa (*Fragaria vesca* Coville), manzana (*Pyrus malus* Borkh), mango (*Mangifera indica* L.), durazno (*Prunus persica* L.), limón (*Citrus limon* L.), uva de mesa (*Vitis vinifera* L.), tomate (*Lycopersicum esculentum* Mill.) y otros (Rivera-Pastrana, 2007). El crecimiento de bacterias tales como *Salmonella* spp., *Escherichia coli*, y *Listeria monocytogenes* en frutas frescas cortadas, ha sido reportado en investigaciones sobre inocuidad alimentaria (López-Malo y Palou, 2005). Estos microorganismos son comúnmente estudiados porque usualmente están involucrados en toxiinfecciones alimentarias que afectan la salud del consumidor (Salgado 2024).

Por otro lado, los atributos sensoriales están dados por el aroma, sabor, color y textura, por lo que éstos, deben examinarse cuidadosamente cuando se determina la vida útil de las frutas (Inicente-Quiroz y col., 2021). El procesamiento mínimo de frutas y hortalizas presenta un gran reto que es el poder combinar adecuadamente distintos factores de preservación a fin de generar productos inocuos, pero que al mismo tiempo garanticen las características sensoriales de frescura que desea el consumidor (Trujillo y col., 2001). Sin embargo, hay poca información disponible sobre la eficacia de este tratamiento sobre la calidad de la piña fresca cortada. El objetivo de esta investigación fue evaluar el efecto antibacteriano y cambios de calidad en piña fresca cortada tratada con luz ultravioleta.

2 Materiales y Métodos

2.1 Preparación de la muestra

Se utilizó piña de la variedad Cayena Lisa, con un estado de madurez 3 según García y col. (2011) (ver Figura 1), obtenida de un Supermercado del municipio Maturín, estado Monagas. El proceso se realizó bajo condiciones asépticas donde la fruta entera, los materiales (cuchillos, tablas) y área de trabajo se desinfectaron con 200 µL/L de Hipoclorito de Sodio (pH 7) siguiendo la metodología reportada por Ramos-Villarroel y col. (2012). Posteriormente se cortó la fruta con un cuchillo afilado de acero inoxidable con el fin de retirar la corteza de la piña y obtener de la pulpa con un molde triangular trozos de 2 cm de cada lado y 1,5 cm de espesor, los cuales tuvieron un peso de aproximadamente 10 g cada uno (ver Figura 2).

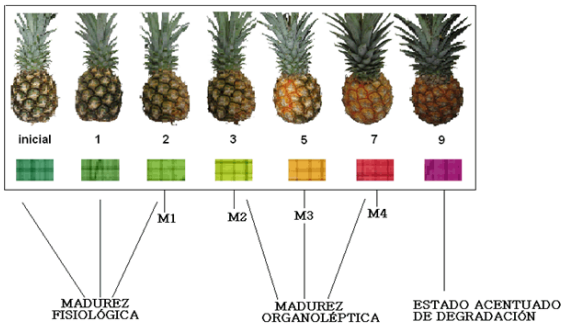

Fig 1. Escala de madurez y carta de colores de la variedad en estudio (García y col., 2011).

2.2 Análisis microbiológico

2.2.1 Preparación del inóculo

La cepa de *Escherichia coli* se obtuvo del Laboratorio de Microbiología del Departamento de Biología y Sanidad Animal de la Escuela de Zootecnia de la Universidad de Oriente, Campus Los Guaritos, Municipio Maturín Monagas, Venezuela, la cual será utilizada como sustituta de la cepa patógena *E. coli* 0157:H7. La cepa de *Listeria innocua* CVCM 448 se obtuvo del Laboratorio de Microbiología del Instituto de Ciencia y Tecnología de Alimentos (ICTA) de la Universidad Central de Venezuela, Caracas, Venezuela, y será empleada como sustituta de la cepa patógena *Listeria monocytogenes* en este estudio.

Las cepas originales de *E. coli* y *L. innocua* se mantuvieron en tubos con Agar Tripticasa de Soya (HIMEDIA) inclinado a una temperatura de 5 °C hasta su uso. Los inóculos se obtuvieron reactivando las cepas. *L. innocua* se cultivó en Caldo Tripticasa de Soya + 0,6 % de extracto de levadura (HIMEDIA) a 35 °C durante 15 horas (Ramos-Villarroel y col., 2012), para obtener cepas cercanas a la fase estacionaria de crecimiento al momento de llevar a cabo la inoculación. El cultivo de *E. coli* se realizó en caldo nutritivo (HIMEDIA) a 37°C durante 24 horas (fase estacionaria).

2.2.2 Inoculación de la muestra

Dos (2) trozos de piña con un peso de aproximadamente 10 g cada uno, se colocaron en las bandejas plásticas y posteriormente fueron inoculados con 100 µL de una población cercana a 10^8 UFC/mL de *E. coli* o *L. innocua* para cada estudio. El inóculo se dispersó en la superficie de los trozos utilizando una micropipeta estéril. Luego de dos horas aproximadamente, las muestras se trataron con luz ultravioleta.

Fig 2. Preparación de la muestra y trozos de piña triangular.

2.3 Tratamiento con luz UV

El tratamiento con luz ultravioleta se llevó a cabo con una lámpara Modelo N° BGN18 de 115 V- 60 ciclo Philips, Holanda (ver Figura 3a). El espectro emitido fue desde 200 a 400 nm con una duración de 5 minutos a una distancia de 8 y 15 cm, las cuales son las variables del estudio. La lámpara estuvo ubicada en la parte superior del soporte de la muestra.

2.3.1 Dosis

Para determinar la intensidad de la luz UV (mW/cm^2) se utilizó un radiómetro digital marca LUTRON modelo UV 340, Taiwan (ver Figura 3b). La intensidad aplicada se midió como la media de cuatro (4) repeticiones a cada lado de la lámpara y en el centro de la misma. Se comprobó que todos los puntos recibieran la misma intensidad que permitió calcular la dosis de aplicación de 1,479 y 2,064 kJ/cm^2 correspondiente a las distancias de 15 y 8 cm respectivaamente. La ecuación (López-Rubira, 2007) utilizada fue la siguiente:

$$D = \frac{I \,.\, t}{1000^2}$$

D: dosis de irradiación aplicada (kJ/m^2)
I: intensidad de irradiación bajo el área de emisión de luz UV-C (W/m^2)
t: tiempo de exposición (s)

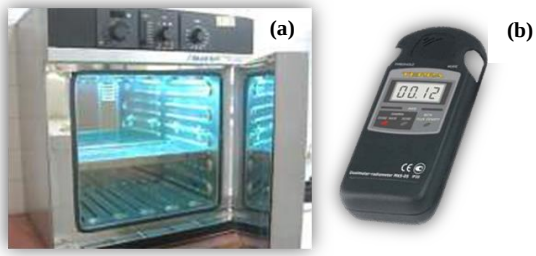

Fig 3. Lámpara UV Modelo N° BGN18 e 115 V- 60 ciclo (a) y radiómetro digital marca LUTRON modelo UV 340 (b).

2.4 Empacado y condiciones de almacenamiento

Una vez inoculados e irradiados los dos (2) trozos de piña, inmediatamente fueron selladas las bandejas de Tereftalato de polietileno (PET) de 750 cc (Plásticos Guayana, Venezuela). Las muestras fueron almacenadas a 5 °C, para su posterior análisis cada 3 días durante 15 días, iniciando desde el día 0.

2.5 Recuento microbiano

Un (1) trozo de piña se retiró asépticamente de la bandeja y se transfirió a una bolsa plástica estéril (Ziploc ®). Se colocaron 90 mL de agua peptonada (0,1 % de peptona + 0,85% cloruro de sodio, marca HIMEDIA) para frotar la muestra durante 5 minutos para posteriormente realizar las diluciones seriadas desde 10^{-1} hasta 10^{-6}. La siembra se realizó en superficie a razón de 0,1 mL distribuyéndola con una espátula de Drigalsky en placas por duplicado con agar EMB-eosina-azul de metileno- (HIMEDIA) y agar Palcam (Merck) para determinar *E. coli* y *L. innocua*, respectivamente. Las placas se incubaron durante 24 horas a 37°C. Las colonias características de los microorganismos *E. coli* (verde tornasol) y *L. innocua* (negro brillante con halo) se contaron y reportaron en $\log_{10}$ UFC/g. El análisis se realizó por duplicado cada 3 días durante los 15 días de almacenamiento (Ramos-Villarroel y col. 2012).

2.6 Determinación de parámetros físicos y químicos

Las muestras utilizadas para los análisis fisicoquímicos se trataron con luz UV sin inocular.

2.6.1 Determinación de pH

La determinación de pH se realizó con un potenciómetro modelo 420 marca ORION bajo la metodología de la norma COVENIN (1317-79). Se pesaron 10 g de la muestra, se colocaron con 90 mL de agua destilada, luego se homogeneizó y filtró la mezcla en un beaker para determinar el pH. Se evaluaron un total de seis trozos de piña por duplicado para cada tratamiento.

2.6.2 Medición del color

El color de las muestras se determinó utilizando un colorímetro COLOR TEC PCM/PSM midiendo las coordenadas L*, a*, b*. Se evaluaron un total de seis trozos por duplicado para cada tratamiento de acuerdo a la metodología empleada por Ramos-Villarroel y col. (2012).

2.6.3 Evaluación de firmeza

La firmeza se midió con un texturómetro Modelo Lloyd 500 con una capacidad de 50 N. Se utilizó una sonda de 6,2 mm de diámetro para penetrar los trozos de piña en forma triangular, a una tasa de velocidad de 5mm/s y un trigger de 0,05 kgf. Los resultados se expresaron en Newton (kg.m/s), que fue el esfuerzo realizado por el equipo para penetrar la muestra en cada tratamiento de acuerdo a la metodología empleada por Ramos-Villarroel y col. (2012).

2.7 Diseño experimental

Se utilizó un diseño completamente aleatorizado con arreglo factorial 3 x 6, donde el factor A: son los tratamientos con luz ultravioleta (sin luz UV, luz UV a 8 cm y luz UV a 15 cm) y el factor B: es el tiempo de medición (0, 3, 6, 9, 12 y 15). Para estudiar las variables microbiológicas, los análisis se realizaron por duplicado para cada tratamiento con dos (2) réplicas, haciendo un total de 72 observaciones. Por otra parte, para el estudio de las variables fisicoquímicas (pH, color y textura), los análisis se realizaron por duplicado con seis (6) réplicas para un total de 216 observaciones.

2.8 Análisis estadístico

Los resultados de las mediciones instrumentales de las propiedades fisicoquímicas y microbiológicas se analizaron por separado mediante un ANAVA de dos factores (factores: irradiación con luz ultravioleta y tiempo de medición). En todos los casos, las diferencias significativas entre medias se establecieron aplicando el test de Duncan con un nivel de confianza del 95%. Los resultados serán expresados como la media ± la desviación estándar de los promedios.

3 Resultados y Discusión

Determinación de la efectividad del tratamiento por luz ultravioleta sobre la inactivación bacteriana

Para determinar la efectividad de la luz ultravioleta sobre microorganismos como *Escherichia coli* y *Listeria innocua* inoculados a un nivel de 10^9 y 10^7 UFC/100g, respectivamente en la piña fresca cortada, las piezas fueron tratadas con luz ultravioleta durante 5 min a una distancia de 15 y 8 cm (dosis de 1.479 y 2.064 kJ/m2 para cada tratamiento).

La Figura 4 muestra la inactivación de *E. coli* en trozos de piña fresca cortada tratada con luz ultravioleta y almacenados a 5 °C durante 15 días. En dicha figura se evidenció que a medida que transcurrió el tiempo de almacenamiento los recuentos del microorganismo disminuyeron notablemente. Las pruebas de media indicaron que hubo diferencias significativas ($p< 0,05$) entre todos los tratamientos justo el primer día del análisis. Por otra parte, las muestras tratadas con luz ultravioleta a una distancia de 8 y 15 cm no presentaron diferencias significativas ($p < 0,05$) entre ellas durante los días 6 y 12 de su almacenamiento.

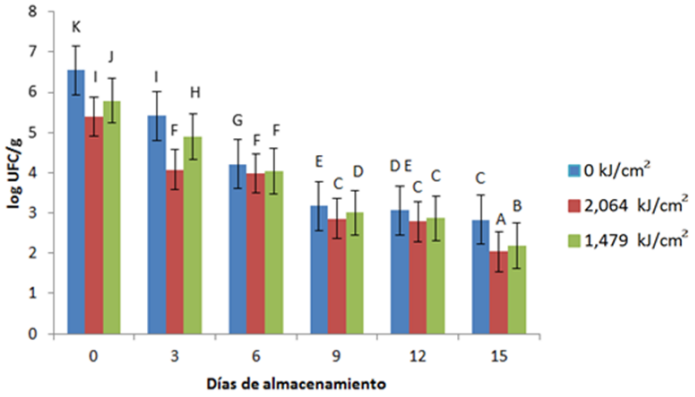

Fig 4 Inactivación de *Escherichia coli* en trozos de piña fresca cortada tratada con luz ultravioleta a dosis de exposición de 0; 2,064 y 1,479 kJ/m2 almacenadas a 5 °C durante 15 días.

El recuento inicial de *E. coli* para las muestras control fue superior a los registrados por los trozos tratados con luz UV, se observó la acción bactericida de este tratamiento físico, donde el recuento disminuyó con el incremento de la dosis de irradiación. Al inicio del estudio la muestra control presentó un recuento de 6,54 log UFC/g que fue mucho mayor, en comparación con las muestras irradiadas que mostraron recuentos de 5,79 y 5,40 log UFC/g para distancias de 15 cm (1,479 kJ/cm^2) y 8 cm (2,064 kJ/cm^2), respectivamente. En el caso de los recuentos al final del almacenamiento, la muestra sin tratar presentó el mayor conteo (2,83 log UFC/g), a diferencia de las muestras irradiadas que mostraron valores de 2,18 y 2,04 log UFC/g a distancias de 15 y 8 cm respectivamente.

Durante todo el almacenamiento se observó una disminución de los recuentos bacterianos por efecto del tratamiento con luz UV, notándose que las muestras tratadas siempre fueron menores en comparación a las muestras sin tratar. Al inicio del almacenamiento se logró una reducción en las muestras irradiadas de 0,75 y 1,148 log UFC/g (a distancias de 15 y 8 cm, respectivamente), siendo esta última la mayor inactivación que se obtuvo al inicio del estudio. Por otro lado, al final del almacenamiento en las muestras tratadas a dosis de 1,479 y 2,064 kJ/cm^2 se alcanzó una reducción logarítmica de 4,36 y 4,50 log UFC/g, respectivamente.

Los niveles de inactivación ocasionados por la luz UV pueden ser explicados por el mecanismo de acción de este tratamiento. Según Márquez y col. (2013) esta tecnología inactiva los microorganismos principalmente debido a la inducción de la formación de dímeros de pirimidina que alteran las hélices de ADN y los bloques de replicación de las células microbianas, que destruyen la capacidad de reproducción y otras funciones de la célula.

En este sentido, los distintos microorganismos requieren de una dosis específica para ser inactivados, esta variación dependerá de la estructura de la pared celular, del espesor y composición de la misma, de proteínas que absorban la luz UV o de las diferencias en la estructura de los ácidos nucleicos (Chang y col., 1985). Con respecto a la pared celular, las bacterias Gram-negativas a pesar de ser multilaminares poseen una pequeña capa de peptidoglicano que va de 1 a 2 nm, esta delgada capa posiblemente permitió que la luz UV ocasionara más daño a nivel celular. Ahora bien, otro factor que quizá influyó en la inactivación bacterial fue el hábitat natural de este microorganismo, el cual se encuentra confinado en el tracto intestinal tanto del hombre como de los animales haciendo que *E. coli* sea más sensible a la luz ultravioleta (Rowan y col., 1999).

Cabe destacar que, al final del tiempo de almacenamiento la disminución en el recuento bacteriano en las muestras sin tratar pudo deberse además al agotamiento de nutrientes y desechos tóxicos presentes como consecuencia del metabolismo microbiano (producción de CO_2 y otros compuestos).

Los resultados concuerdan con lo reportado por Calderón-Gabaldón y col. (2012), donde evaluaron el efecto de diferentes dosis de luz UV-C y ácido málico sobre *Rhodotorula glutinis* (flora deteriorativa predominante) en trozos de papaya frescas cortadas, inoculadas sobre su superficie con un cultivo puro de *R. glutinis* (10^7 UFC/mL) y después tratadas con luz UV-C (0; 0,96; 2,88; 5,76 y 8,64

kJ/m^2). Estos autores observaron diferencias significativas ($p < 0,05$) entre los recuentos de *R. glutinis* en los trozos de papaya, encontrándose que dosis de luz UV-C de 8,64 kJ/m^2 ejercieron la mayor inactivación de la población (6,3 log UFC/g).

Listeria innocua

La Figura 5 muestra la influencia de *L. innocua* sobre los trozos de piña fresca cortada tratada con luz ultravioleta almacenada a 5 °C durante 15 días. En dicha figura se evidenció claramente como disminuyeron los recuentos de *L. innocua* desde el día inicial del análisis hasta el día final del almacenamiento Las pruebas de medias indicaron que no hubo diferencias significativas ($p< 0,05$) el primer día del análisis entre la muestra control y la muestra tratada a 15 cm de distancia. Por otra parte, las muestras irradiadas a 8 cm presentaron diferencias significativas ($p < 0,05$) con respecto a las no tratadas y a las irradiadas a 15 cm.

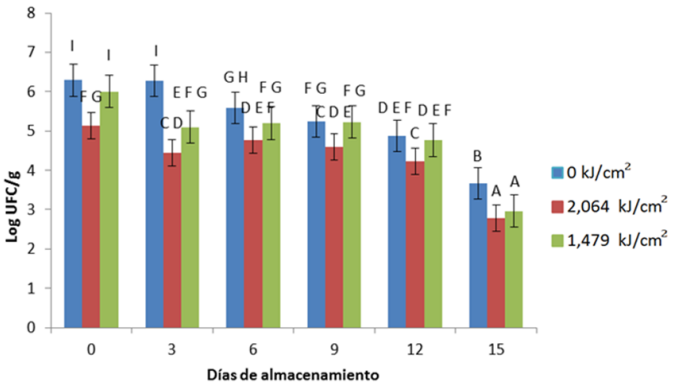

Fig 5. Inactivación de *Listeria innocua* en trozos de piña fresca cortada tratada con luz ultravioleta a dosis de exposición de 0; 2,064 y 1,479 kJ/m^2 almacenadas a 5 °C durante 15 días.

La muestra control al inicio del estudio presentó un recuento de 6,29 log UFC/g que fue mucho mayor, en comparación con las muestras irradiadas que mostraron recuentos de 6,01 y 5,14 log UFC/g para dosis de 1,479 y 2,064 kJ/cm^2, respectivamente. El día 6 y 9 del análisis se observó un incremento en el recuento de las muestras irradiadas, esto se puede atribuir al tejido fibroso de la fruta, donde el inóculo pudo no ser alcanzado por la luz UV y por lo tanto esa población sobreviviente o lesionada se multiplicó. Al final de la investigación la muestra sin tratar presentó un valor de 3,66 log UFC/g, en comparación con las muestras tratadas que mostraron recuentos de 2,96 y 2,78 log UFC/g para 15 y 8 cm, respectivamente.

Al inicio del almacenamiento en las muestras irradiadas a 15 y 8 cm de distancia, se logró una reducción de 0,28 y 1,15 log UFC/g. Por otro lado, al final del almacenamiento en las muestras tratadas a dosis de 1,479 y 2,064 kJ/cm^2 se alcanzó una reducción logarítmica de 3,33 y 3,51 log UFC/g, respectivamente.

Estos niveles de inactivación pueden ser causados principalmente por el mecanismo de inactivación de la luz ultravioleta, el cual ocurre directamente sobre el ADN microbiano. Por otro lado, *L. innocua* al encontrarse ampliamente distribuida en el medio ambiente (suelo, agua, vegetales, entre otras) y estar expuesta a la luz solar mostró más resistencia a la luz UV que *E. coli*. En este caso *E. coli* como se mencionó anteriormente, está confinada al tracto intestinal de seres humanos y animales siendo más sensible a la luz solar y por consiguiente a la luz UV. Otro factor importante es el grosor de la pared celular de *Listera* que es una bacteria Gram-positiva y tiene una capa más gruesa de peptidoglicano (estructura rígida de 20 a 80 nm) lo cual fue quizás una de las causas en la resistencia en comparación con *E. coli*.

Los resultados son comparables a lo reportado por Birmpa y col. (2013), quienes estudiaron la eficacia de la luz UV inoculando *L. innocua* en fresas frescas cortadas. Ellos lograron una reducción de 1 – 1,7 log UFC/g utilizando un tiempo de 10 min y una dosis de exposición 7,2 J/cm^2. Schenk y col. (2008), mostraron la respuesta de *L. innocua* y *L. monocytogenes*, a la luz UV en rebanadas de pera fresca mínimamente procesada, utilizando una dosis de exposición de 87 kJ/m^2 y un tiempo de 20 min, dando como resultado reducciones logarítmicas de 2,6 y 3,4 respectivamente, para los microorganismos inoculados en el sustrato. Estos resultados son similares a los obtenidos en la presente investigación, siendo el tratamiento con luz UV eficiente para inactivar este tipo de bacteria.

Determinación del efecto del tratamiento por luz ultravioleta sobre los parámetros físicoquímicos

pH

En la Figura 6 se muestra el pH de los trozos de piña fresca cortada tratada con luz ultravioleta. Las pruebas de medias no arrojaron diferencias significativas ($p < 0,05$) entre la muestra irradiada a 15 cm y la muestra control el día inicial del análisis, pero sí al final del período de almacenamiento

El pH de la muestra sin tratar, al inicio del estudio, presentó un valor de 2,39, aumentando a lo largo del almacenamiento hasta alcanzar un valor de 3,43 el día final del mismo. Por otro lado, los valores de las muestras irradiadas a dosis de 2,064 y 1,479 kJ/cm^2 presentaron la misma tendencia que las muestras sin irradiar, obteniendo valores iniciales de 2,50 y 2,42 respectivamente, para cada tratamiento. Al final del almacenamiento, el valor de ambas muestras tratadas fue de 3,66.

El pH de las frutas aumenta según el grado de maduración que éstas presenten, en el caso de la piña, los frutos con la

base ligeramente amarilla a mitad amarilla (grado 3), tienen mejor vida de mostrador que aquellas con la superficie más coloreada, puesto que los frutos que no muestran nada de amarillo pueden no estar lo suficientemente maduros para dar una calidad óptima (González**,** 1999).

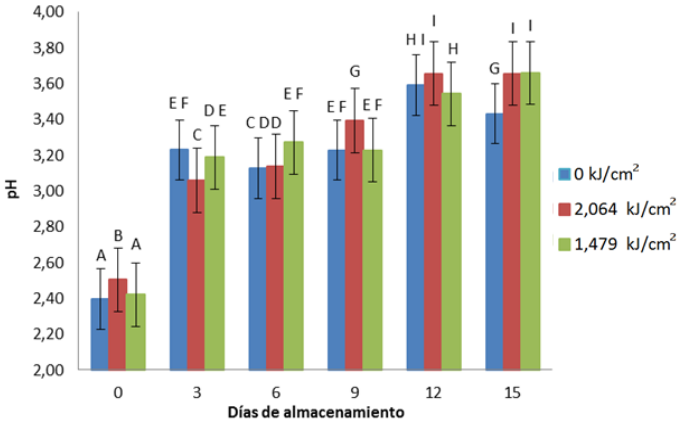

Fig 6. pH de trozos de piña fresca cortada tratada con luz ultravioleta a dosis de exposición de 0; 2,064 y 1,479 kJ/m^2 almacenadas a 5 °C durante 15 días.

Quizás el grado de maduración 3 que se escogió, influyó en el aumento del pH a lo largo del almacenamiento. Según Wills y col. (1984) durante la maduración, los ácidos orgánicos son oxidados en el metabolismo respiratorio y convertidos en carbohidratos, dichos ácidos pueden ser considerados como una reserva más de la fruta, debido a que durante el curso de la maduración su contenido desciende en el período de máxima actividad metabólica y el valor de pH aumenta. Este valor representa la presencia de grupos acídicos incluyendo ácidos orgánicos, fenoles y aminoácidos. Sin embargo, en las frutas, normalmente se considera que los ácidos orgánicos proporcionan la mayor parte de los iones hidrógeno y generalmente durante la maduración, a medida que desciende la acidez, el pH aumenta (Hulme, 1971).

El grado de maduración escogido corresponde a un color de la base ligeramente amarilla (ver Figura 4), lo cual según los autores mencionados anteriormente se traduce en una gran cantidad de ácidos que aún no se degradan para formar los compuestos responsables del ablandamiento y posteriores cambios químicos y físicos que ocurren en la fruta después del procesado y durante el tiempo de almacenamiento. Es por esa cantidad de ácidos que el pH fue bajo en el primer día y luego aumentó los siguientes días del análisis.

Según Alférez y col. (2003), es el resultado de los cambios bioquímicos que sufre la piña durante el período de maduración luego de su cosecha, planteándose conceptualmente que a medida que la piña se madura, el pH aumenta, tiende a básico, por ello en los primeros días se encuentra dentro de los rangos de acidez, debido a que la maduración se ha provocado en primera instancia por el estrés de la recolección, y a partir de los días sucesivos tiende a acelerarse el proceso de maduración y la futura senescencia del fruto como proceso natural.

Este incremento del pH en la mayoría de los casos en comparación con las muestras sin tratar, puede ser debido a lo señalado por Manzocco y col. (2011), quienes indicaron que la exposición a la luz UV promueve la modificación de la estructura celular de la fruta, lo cual dependiendo de la dosis de exposición conduce a la ruptura de las membranas de las células y favorece la deshidratación progresiva de la muestra. La salida de ácidos y compuestos intracelulares pudieron producir un incremento del pH en los trozos de piña fresca cortada, aunado al proceso natural de maduración del fruto.

Color

La evaluación del color se realizó a través de los parámetros L* que representa la luminosidad, a* que indica el color rojo-verde y b* que es el responsable de la cromaticidad amarillo-azul.

*Coordenada L**

En el caso del parámetro L*, existió diferencia significativa ($p < 0,05$) por efecto del tiempo de almacenamiento y la irradiación sobre los trozos de piña fresca cortada almacenados durante 15 días a 5 °C.

La Figura 7 muestra el efecto del tiempo sobre la luminosidad (L*) de los trozos de piña fresca cortada almacenada durante 15 días a 5 °C. En dicha figura se puede evidenciar que los trozos de piña con un valor promedio inicial de 68,99 presentó diferencia significativa ($p < 0,05$) con respecto a los demás días según las pruebas de medias, disminuyendo levemente su tendencia para los días 3 y 6. En el caso de los últimos días (9, 12 y 15) del almacenamiento no hubo diferencias significativas ($p < 0,05$) entre ellos, registrándose un valor de 59,25; 57,86, y 58,11 respectivamente.

La Figura 8 muestra el efecto de los tratamientos (con luz UV y sin luz UV) sobre el parámetro L* en piña fresca cortada almacenada durante 15 días a 5 °C. Las pruebas de medias arrojaron que hubo diferencias significativas ($p<0,05$) entre todos los tratamientos, las muestras irradiadas con luz UV presentaron un valor promedio de 60,12 y 62,32 para distancias de 8 y 15 cm respectivamente, la muestra sin tratar por otra parte mostró un valor de 63,90.

La disminución de la coordenada L* es producto del proceso de maduración de la fruta donde va perdiendo

luminosidad a medida que se sintetizan muchos compuestos y posteriormente se da el proceso degradativo.

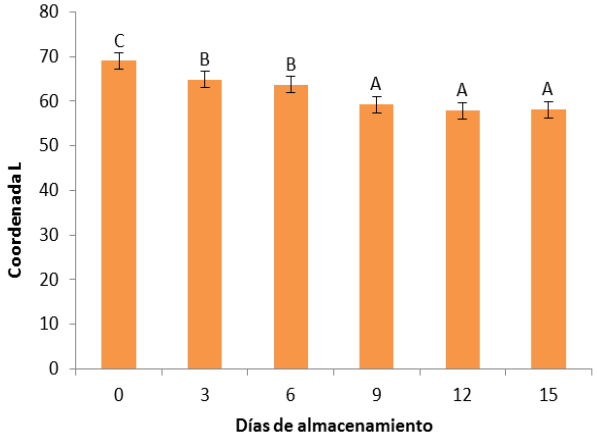

Fig 7. Efecto del tiempo sobre las muestras tratadas con luz UV y aquellas sin tratar sobre el parámetro L* en piña fresca cortada almacenada durante 15 días a 5 °C.

La pérdida de luminosidad es usada como indicador de pardeamiento (González-Aguilar y col., 2008; Djioua y col., 2010). El cual ocurre durante el procesamiento de las frutas donde las células se rompen y provoca que las enzimas se descompartamentalicen y entren en contacto con sus sustratos (Manzocco y col., 2011).

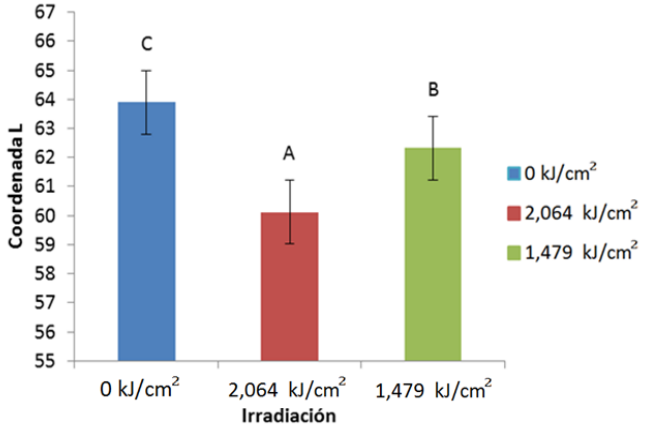

Fig 8. Cambios en los valores del parámetro L* en trozos de piña fresca cortada tratada con luz ultravioleta a dosis de 0; 2,064 y 1,479 kJ/m^2 almacenadas a 5 °C durante 15 días.

Al igual que la luz UV (UV-A, UV-B y UV-C) afecta al tejido de la fruta, también ocurre con el color de la misma, puesto que se ve reflejado que las muestras irradiadas presentaron valores de L* menores que los de las muestras control, lo que difiere de lo reportado por Márquez y Pretell (2013) que aplicaron dosis de 7 y 14 kJ/m^2 y obtuvieron valores de L* mayores que las muestras control sobre el color de las rebanadas de piña, esto puede atribuirse a que las dosis aplicadas eran mucho mayores que las del presente estudio, ocasionando tal vez que la luminosidad de la piña fuera mayor en las muestras irradiadas.

La incidencia de la luz UV puede repercutir de otra manera en los sustratos. Manzocco y col. (2011) utilizaron dos irradiaciones UV-C (1,2–24,0 kJ/m^2) y un tiempo de almacenamiento de 15 días a 6 °C para posteriormente evaluar el parámetro L* en rodajas de manzana mínimamente procesada, las cuales al final del almacenamiento presentaron claramente un mayor pardeamiento superficial incrementado con el aumento de la dosis de radiación UV-C. Estos resultados concuerdan con los del presente estudio, donde el parámetro L* también se vio afectado.

*Coordenada a**

La Figura 9 muestra el efecto del tiempo de almacenamiento sobre el parámetro a* de las muestras de piña fresca cortada, donde esta coordenada varió conforme avanzaron los días de almacenamiento. Las pruebas de medias indicaron que hubo diferencia significativa ($p < 0,05$) entre el día inicial del análisis con respecto al resto de los días de almacenamiento, que no presentaron diferencias entre ellos hasta el día 12.

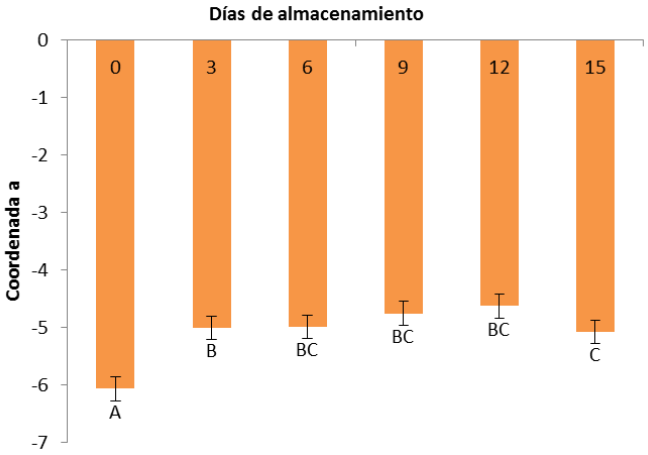

Fig 9. Efecto del tiempo sobre el parámetro a* en trozos de piña fresca cortada tratada con luz ultravioleta en función del almacenamiento a 5 °C durante 15 días.

La coordenada a* el primer día presentó en los trozos de piña un valor negativo de -6,07 que fue en aumento hasta el día 12 del análisis con un valor de -4,63. Esto se debe a que el color se dirige hacia las tonalidades rojas, es decir, hacia el lado positivo de la coordenada. Dicha tendencia corresponde al oscurecimiento de la fruta, lo cual, se puede relacionar con la formación de compuestos poliméricos coloreados y el avance del pardeamiento en la fruta después

del procesamiento (Bhat y col., 2011).

El pardeamiento enzimático resulta de la acción de un grupo de enzimas denominadas polifenoloxidasas (PPO), las cuales se encuentran en todas las plantas. Estas enzimas catalizan la reacción de oxidación de los compuestos fenólicos a quininas. La posterior oxidación y polimerización de las quininas dan lugar a la formación de compuestos pardos (García y Barrett, 2002).

Numerosos autores han reportado que un decrecimiento en el valor de L* y un incremento en el valor de a* son indicativos de pardeamiento (Monsalve-González y col., 1993; Goupy y col., 1995; Rocha y Morais, 2003), tal como se evidenció en este estudio, donde los valores de L* disminuyeron y los de a* aumentaron.

La luz UV afecta tanto al tejido de las frutas como al color de las mismas, viéndose el parámetro a* influenciado por la incidencia de ésta. En la figura 10 se observa que las muestras irradiadas a 15 y 8 cm presentaron mayores valores (-4,95 y -4,86, respectivamente) que los de la muestra control (-5,46) encontrándose diferencias significativas ($p < 0,05$) en las pruebas de medias. Así, Márquez y Pretell (2013) obtuvieron la misma tendencia que en el presente estudio aplicando dosis de 7 y 14 kJ/m^2, donde la coordenada a* se dirigía hacia el lado positivo, sin embargo, registraron valores menores en las muestras irradiadas comparadas con las muestras control sobre este parámetro de color en rebanadas de piña.

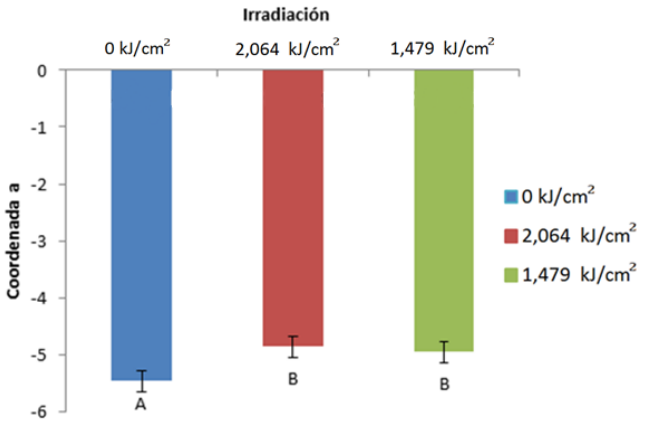

Fig 10. Cambios en los valores del parámetro a* en trozos de piña fresca cortada tratada con luz ultravioleta a dosis de exposición de 0; 2,064 y 1,479 kJ/m^2 almacenadas a 5 °C durante 15 días.

Manzocco y col. (2016), estudiaron el efecto de la luz UV-C en palitos de piña fresca cortada empacados en bandejas (PET, EVOH y PE) y almacenados a 6 °C. Estos investigadores emplearon una dosis de irradiación de 200 J/m^2 y obtuvieron resultados similares presente estudio en cuanto al parámetro a* (-4,3) de color. Concluyeron que los cambios en la apariencia de la piña fresca cortada se atribuyen a la variabilidad intrínseca de los frutos en lugar de la aplicación de luz UV-C.

Por lo tanto, los tratamientos de luz UV pueden afectar el parámetro a* en la piña cortada según lo observado en comparación con las muestras sin tratar.

*Coordenada b**

En la Figura 11 se aprecia el efecto del tiempo sobre el parámetro b* en trozos de piña fresca cortada almacenada a 5 °C durante 15 días. Se observó que al inicio del análisis la coordenada b* tuvo un valor de 23,81 y a medida que transcurrió el almacenamiento fue disminuyendo gradualmente hasta llegar al día 15 con un valor de 14,64, lo cual concordó con la tendencia a la pérdida de tonalidades amarillentas iniciales en la pulpa de esta fruta hacia su oscurecimiento. La prueba de Duncan indicó que no hubo diferencia significativa entre los días 3, 6, y 9 del almacenamiento, más sí entre estos días y los días 0, 12 y 15.

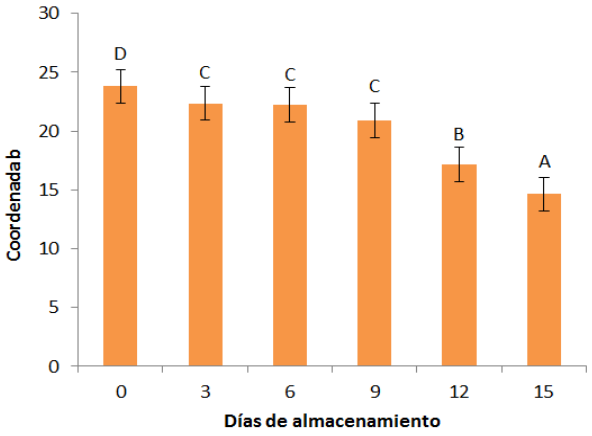

Fig 11. Efecto del tiempo sobre el parámetro b* en trozos de piña fresca cortada tratada con luz ultravioleta en función del almacenamiento a 5 °C durante 15 días.

Márquez y Pretell (2013) aplicaron dosis de 7 y 14 kJ/m^2 a rebanadas de piña y obtuvieron valores de b* mayores que las muestras control, no fue así el caso del presente estudio donde las dosis aplicadas fueron diferentes y los resultados también. Según Jay (1997), la disminución de los parámetros de a* y b* por efecto de la luz UV indica que el tratamiento induce a una disminución de las concentraciones de carotenoides afectando la concentración de algunos compuestos y además cataliza cambios oxidativos, lo que lleva a la decoloración.

El color de las frutas se debe fundamentalmente a la presencia de tres familias de pigmentos: clorofilas, carotenoides y antocianinas. En algunas variedades el color verde disminuye en el curso de la maduración pues los cloroplastos, organelos que contienen la clorofila y donde se

realiza la fotosíntesis, son reemplazados progresivamente por pequeños organelos con pigmentos naranjas y amarillos (carotenos y xantofilas). Los cambios de color pueden utilizarse como indicadores del avance del proceso de maduración (Báez y Bringas, 1995).

La estructura de estos pigmentos puede verse afectada en cierto grado durante el desarrollo, la maduración y los tratamientos poscosecha. Factores tales como la luz, el pH, la humedad relativa, la composición de gas y sistemas enzimáticos estarían involucrados en el deterioro del color (Artés y col., 2002). Los otros aspectos de la apariencia que reducen la calidad son la pérdida de frescura, como el marchitamiento, la pérdida de brillo en la superficie o arrugamiento de la piel, y el desarrollo de defectos externos e internos, causados por la senescencia natural, desórdenes fisiológicos y el desarrollo de organismos causantes de enfermedades (Aked, 2002).

Por otro lado, cabe destacar el trabajo de Manzocco y col. (2011), quienes utilizaron dos irradiaciones UV-C (1,2–24,0 kJ/m^2) y un tiempo de almacenamiento de 15 días a 6 °C para posteriormente evaluar los parámetros de color b* en rodajas de manzana mínimamente procesada, las cuales al final del almacenamiento presentaron claramente un mayor pardeamiento superficial incrementado con el aumento de la dosis de radiación UV-C. Los valores de b* coincidieron con los reportados por estos autores, donde la luz UV incidió de manera diferente en el color superficial de la fruta.

Firmeza

La Figura 12 muestra el efecto del tiempo sobre la firmeza de los trozos de piña fresca cortada almacenada a 5 °C durante 15 días. La firmeza, medida como la fuerza de penetración, disminuyó a medida que transcurrió el tiempo de almacenamiento. Según la prueba de medias, existió diferencia significativa ($p < 0,05$) entre todos los días del análisis, mientras que entre el día 3 y 9; el día 6 y 9; y los días 6 y 12 del almacenamiento, no se presentaron diferencias significativas ($p < 0,05$).

Al inicio del almacenamiento los trozos de fruta presentaron un valor de 12,77 N, que fue la fuerza requerida por el equipo para penetrar el tejido. Para los últimos días del estudio, la piña disminuyó los niveles de firmeza donde la fuerza que necesitó el equipo fue en promedio de 9,11 N.

Esta disminución gradual coincidió con el proceso de maduración descrito por la fruta y el comienzo de la senescencia en la cual su dermis se encuentra envejecida, lo que provoca una menor resistencia a la penetración de la sonda del texturómetro, puesto que durante la maduración, la velocidad de degradación de las sustancias pécticas está relacionada con el ablandamiento de la fruta (Aguilera *y* Stanley, 1999), lo que explica que durante dicho proceso las sustancias pépticas se despolimerizan y solubilizan, perdiendo humedad las células por causa de la transpiración, disminuyendo con ello la presión de turgencia y debilitando la estructura y consistencia de la fruta (Rao *y* Steffe, 1992).

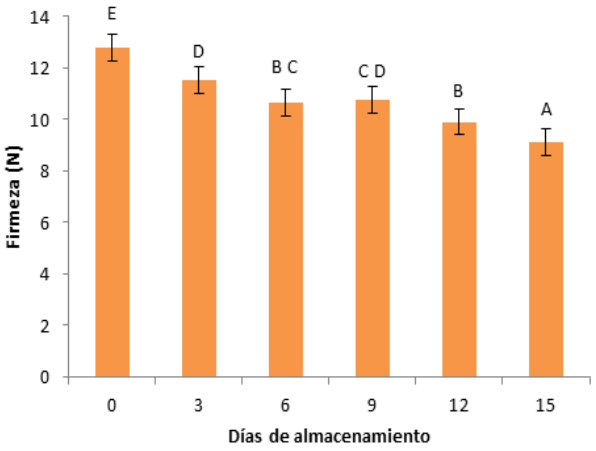

Fig 12. Efecto del tiempo sobre la firmeza en trozos de piña fresca cortada almacenada a 5 °C durante 15 días.

La firmeza es una cualidad sensorial, con un rol muy relevante en la aceptabilidad por parte de los consumidores, en las frutas, este parámetro de calidad está influenciado por factores estructurales químicos: los constituyentes bioquímicos de los organelos celulares, el contenido de agua y la composición de la pared celular. Por lo tanto, cualquier agente externo que afecte a uno o varios de estos factores puede modificar la firmeza e inducir cambios que modifiquen la calidad final del producto (Martínez-Romero y col., 2007).

La pared y membrana celular son organelos blanco de la irradiación UV, debido a que los componentes de la membrana (fosfolípidos y glicolípidos) y de la pared (proteína y ligninas), absorben energía en el rango ultravioleta; al mismo tiempo la luz UV genera especies reactivas de oxígeno que causan estrés oxidativo afectando la estabilidad de la pared y de la membrana celular (Foyer y col., 1994).

En este sentido, los trozos de piña fueron sometidos a bajas dosis pero expuestos a todo el rango de luz UV (UV-A, UV-B y UV-C), por lo tanto, las muestras irradiadas presentaron una menor resistencia que la muestra control al análisis de firmeza como se muestra en la Figura 13. Se atribuye que este comportamiento es resultado del cambio ocurrido por efecto de la luz UV en el tejido de las muestras irradiadas, aunado además al proceso de maduración y posterior senescencia luego del procesado y tiempo de almacenamiento de la fruta.

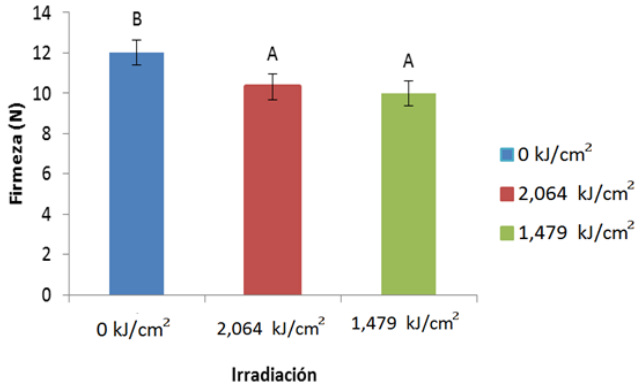

Figura 13. Valores de firmeza en trozos de piña fresca cortada tratada con luz ultravioleta a dosis de 0; 2,064 y 1,479 kJ/m^2 almacenadas a 5 °C durante 15 días.

Pan y Zu (2012) reportaron que las rebanadas de piña tratadas durante 90 s con dosis de irradiación UV-C a 4,5 kJ/m^2 durante su almacenamiento por 12 días a 10 °C retuvieron mejor la firmeza, en comparación con la muestra control y Márquez y col. (2013) encontraron una mayor retención de la firmeza en rebanadas de carambola tratadas con 7 y 14 kJ/m^2 de irradiación UV-C, almacenadas a 5 °C durante 16 días, en comparación con la muestra control.

Estos investigadores utilizaron dosis más altas y emplearon la luz UV-C en el pico más alto de la acción germicida (254 nm), lo cual no concuerda con los resultados obtenidos en este estudio debido principalmente a las dosis aplicadas, siendo en este caso la muestra control la que presentó una mayor resistencia en sus tejidos que las muestras irradiadas.

3 Conclusiones

La luz ultravioleta logró reducir el primer día del procesado 3,61 y 3,36 ciclos logarítmicos de una población de *E. coli* tratada a dosis de 1,479 y 2,064 kJ/cm^2 respectivamente, en la piña cortada. La luz UV redujo una población de *L. innocua* hasta 2,96 y 2,78 ciclos logarítmicos utilizando dosis de 2,064 y 1,479 kJ/cm^2, respectivamente al inicio del estudio. A mayores dosis de energía en los tratamientos con luz ultravioleta, mayor será la inactivación bacteriana en el sustrato. Por otro lado, el pH aumentó gradualmente en todos los tratamientos en función del tiempo. El pH de las muestras tratadas (3,66) fue mayor que en las muestras sin tratar (3,43) al final del estudio. La luminosidad disminuyó a lo largo del almacenamiento en todos los tratamientos. A mayor dosis de luz UV menor luminosidad en el sustrato. La coordenada a* aumentó hasta el valor más alto (-4,86) registrado, a la dosis más alta de irradiación (2,064 kJ/cm^2). El parámetro b* de color no resultó afectado por el tratamiento con luz ultravioleta pero si lo afectó el tiempo de almacenamiento, con un valor inicial de 23,81 y final de 14,64. La firmeza disminuyó a lo largo del almacenamiento, los trozos de piña tratados presentaron menor resistencia que las muestras no tratadas. Finalmente se puede decir que la luz ultravioleta como método alternativo de conservación resultó ser un tratamiento efectivo para la inactivación de *E. coli* y *L. innocua* en piña fresca cortada.

Referencia

Aguilera, J., Stanley, D., (1999). *Microestructural principles of food processing and engineering.* (Second edition). Maryland: ASPEN publication.

Aked, J., (2002). Maintaining the postharvest quality of fruits and vegetables. En: Jongen, W. (Ed.), Fruit and vegetable processing. Improving quality, Woodhead Publishing Limited and CRC Press, England. Alférez, F., Agusti, M., Zacarías, L., (2003). Postharvest rind staining in Navel oranges is aggravated by changes in storage relative humidity: effect on respiration, ethylene production and water potential Postharvest Biology and Technology. 28: 143-152. https://www.sciencedirect.com/science/article/abs/pii/S0925521402001205

Alvis, A., Pérez, L., Arrazola, G., (2011). Estudio de Propiedades Físicas y Viscoelásticas de Panes Elaborados con Mezclas de Harinas de Trigo y de Arroz Integral. Inf. Tecnológica. 22(4): 107-116. https://www.scielo.cl/scielo.php?pid=S0718-07642011000400012&script=sci_abstract

Alzamora, S., Guerrero, S., Lopez-Malo, A., Palou, E., Char, C., Raffelini, S., (2010). "Models for microorganism inactivation:application in food preservation design". En: Processing effects on safety and quality of foods. Ortega-Rivas, E. CRC Press. Londres, Inglaterra.

Aranceta, J., Pérez, C., (2006). *Frutas, verduras y salud*. Barcelona: Elsevier Masson.

Artés, F., Minguez, M. I., Hornero, D., (2002). Analysing changes in fruits pigments. En: Mac Dougall, D.B. (Ed.), Colour in food. Improving quality, Woodhead Publishing Limited and CRC Press, England. Cap. 10.

Artés-Hernández, F., Aguayo, E., Gómez, P., (2009). Innovaciones tecnológicas para preservar la calidad de los productos vegetales mínimamente procesados o de la "cuarta gama". Horticultura Internacional. 69:52-57. https://bibdigital.epn.edu.ec/bitstream/15000/11903/1/CD-6580.pdf

Báez, S., Bringas, E., (1995). Elaboración de la norma mexicana de calidad para el mango fresco y su aplicación. Proc. Interamerican Soc. Trop. Hort. 39:127-141. https://www.redalyc.org/pdf/610/61025405.pdf

Barahona, M., Sancho, E., (1991). *Fruticultura especial*

.
Fascículo II. Piña y Papaya. Universidad Estatal a Distancia. San José, Costa Rica.

Bhat, R., Ameran, S., Voon, H., Karim, A., Tze, L., (2011). Quality attributes of star fruit (*Averroha carambola* L.) juice treated with ultraviolet radiation. Food Chemistry. 127:641-644. https://pubmed.ncbi.nlm.nih.gov/23140712/

Birmpa, A., Sfika, V., Vantarakis, A., (2013). Ultraviolet light and ultrasound as non-thermal treatments for the inactivation of microorganisms in fresh ready-to-eat foods. International Journal of Food Microbiology.167:96–102 https://pubmed.ncbi.nlm.nih.gov/23827815/

Borja, E., (2010). Estudio de la conservación de fresas (*Fragaria vesca*) mediante tratamientos térmicos. Tesis Doctoral. Facultad de Ciencia e Ingeniería en Alimentos, Universidad Técnica de Ambato, Ecuador.

Brennan, M., Le Port, G., Gormley, R., (2000). Post-harvest treatment with citric acid or hidrogen peroxide to extend the shelf life of fresh sliced mushrooms. Lebensmittel-Wissenschaft und Technologie. 33(4):283-289. https://www.researchgate.net/publication/222351166_Postharvest_Treatment_with_Citric_Acid_or_Hydrogen_Peroxide_to_Extend_the_Shelf_Life_of_Fresh_Sliced_Mushrooms

Calderón-Gabaldón, M., Raybaudi-massilia, R., Mosqueda-Melgar, J. y Tapia, M., (2012). Efecto de la luz UV-C y ácido málico sobre poblaciones de *Rhodotorula glutinis* y vida útil de rebanadas de papaya 'maradol'. Bioagro. 24(2):103-114. https://www.redalyc.org/pdf/857/85723473004.pdf

Cerrato, I., (2013). Manual de producción de piña. Programa Nacional de Desarrollo Agroalimentario (PRONAGRO). Honduras.

CFSPH (Center for Food Security & Public Health), (2009). *E. coli* enterohemorrhagic. Iowa State University. Iowa, USA.

Chang, J., Ossoff, S., Lobe, D., Dorfman, M., Dumais, C., Qualls, R., Johnson, J. (1985). UV inactivation of pathogenic and indicator microorganisms. Applied and Environmental Microbiology. 49(6):1361-1365. https://pmc.ncbi.nlm.nih.gov/articles/PMC241729/

COVENIN (Comisión Venezolana de Normas Industriales). 1979. Alimentos. Determinación del pH (acidez iónica) (1315).

Chuchuca, G., Dick, A., Peñafiel, J., (2012). Implementación y validación de una metodología económica para la medición de color aplicada en alimentos. Tesis de grado. Escuela Superior Politécnica del Litoral. Guayaquil, Ecuador.

Djioua, T., Charles, F., Freire, M., FilgueiraS, H., Ducamp-Collin, M., Sallanon, H., (2010). Combined effects of postharvest heat treatment and chitosan coating on quality of fresh-cut mangoes (*Mangifera indica L.*) International Journal of Food Science and Technology. 45: 849–855. https://ifst.onlinelibrary.wiley.com/doi/abs/10.1111/j.1365-2621.2010.02209.x

Domínguez, L., Parzanese, M. (2011). Luz ultravioleta en la conservación de alimentos. Alimentos Argentinos, 52:70-76. https://alimentosargentinos.magyp.gob.ar/contenido/rvista/ediciones/52/articulos/r52_13_LuzUltravioleta.pdf

Ewing, W., (1985). *Edwards and Ewing´s Identification of Enterobacteriaceae.* 4th Edition. Elsevier Science Publishing. New York. EE.UU.

FAOSTAT, (2013). *Índices nacionales de producción* (Dataset). Disponible en: http://data.fao.org/ref/e130bfe5-289a-4072-9a5b-1df9d42176f.html?ver sion=1.0

Foyer, C., Descourviéres, P. y Kunert, K., (1994). Protection against oxygen radicals: an important defense mechanism studied in transgenic plant. Plant Cell Env. 17:507-523. https://onlinelibrary.wiley.com/doi/10.1111/j.1365-3040.1994.tb00146.x

Garcia, E. y Barrett, D., (2002). Preservative treatments for fresh-cut fruits and vegetables. En: O. Lamikanra (Ed.), Fresh-cut Fruits and Vegetables. Science, Technology and Market. Boca Raton, Florida: CRC Press LLC.

Gómez, P., Alzamora, S., Castro, M. y Salvatori, D., (2010). Effect of ultraviolet-C light dose and storage on color changes of fresh-cut apple. Journal of Food Engineering. 98 (1): 60–70. https://bibliotecadigital.exactas.uba.ar/collection/paper/document/paper_02608774_v98_n1_p60_Gomez

González-Aguilar, G., Celis, J., Sotelo-Mundo, R., De La Rosa, L., Rodrigo-García, J., Álvarez-Parrilla, E. (2008). Physiological and biochemical changes of different fresh-cut mango cultivars stored at 5 ºC. International Journal of Food Science and Technology. 43: 91–101. https://ifst.onlinelibrary.wiley.com/doi/abs/10.1111/j.1365-2621.2006.01394.x

González, I., (2010). Caracterización química del color de diferentes variedades de guayaba (*Psidium guajava* l.) colombiana. Tesis de Magister. Universidad Nacional de Colombia. Facultad de Química. Bogotá, Colombia.

González, G., (1999). Viabilidad de la piña colombiana variedad Cayena lisa para su industrialización combinando las operaciones de deshidratación osmótica, impregnación a vacío y secado por aire caliente. Universidad Politécnica de Valencia, Departamento de Tecnología de Alimentos. Valencia, España.

Goupy, P., Amiot, M., Richard-Forget, F., Duprat, F.,

Aubert, S., Nicolas, J., (1995). Enzymatic browning of model solutions and apple phenolic substrates by apple polyphenoloxidase. Journal of Food Science. 60(3): 497. https://ift.onlinelibrary.wiley.com/doi/abs/10.1111/j.1365-2621.1995.tb09811.x

Hulme, A., (1971). *The mango. In the biochemistry of fruit and ther products*. London y New York: Ed. Hulme, A. C. Academic Press.

Jay, J., (1997). Radiation preservation of foods and nature of microbial radiation and resistance. In: (Ed). Modern Food Microbiology Chapman and Hall. New York. pp. 304-323. https://ouci.dntb.gov.ua/en/works/9Z6Vdow9/

Kraemer, M., Eliana, L., (2011). Evaluación de distintas técnicas de postcosecha para prolongar la vida útil de peras mínimamente procesadas. Trabajo para optar al grado de Magister en Ciencias Agropecuarias. Universidad de Chile, Chile.

Kulkarni, S., Karadbhajne, S., (2015). Influence of uv light exposure on shelf life extension of fresh-cut fruits. International Journal of Advanced Research. 3(5): 1296-1306. https://www.journalijar.com/article/4792/influence-of-uv-light-exposure-on-shelf-life-extension-of-fresh-cut-fruits/

López-Malo, A., Palou, E., (2005). Ultraviolet Light and Food Preservation. En: Novel Food Processing Technologies. Barbosa-Cánovas, G., Tapia, M. y Cano, M. (eds). Marcel Dekker Inc, New York. EE. UU.

López-Rubira, V., Artés-Hernández, F., Artés, F., (2007). Evaluación de la calidad de granadas tratadas con UV-C y almacenadas en atmósfera controlada. V Congreso Iberoamericano de Tecnología Postcosecha y Agroexportaciones. https://repositorio.upct.es/entities/publication/09fe1555-ca6e-42d7-ab81-0e5737beacec

Manzocco, L., Da pieve, S., Bartolomeoli, I. y Maifreni M., (2011). Shelf life extension of fresh-cut fruit by UV-light exposure. In: 11th International Congress on Engineering and Food. Atenas, Grecia. https://es.scribd.com/document/365316868/Food-procces-engineering-vol-3-pdf

Manzocco, L., Plazzotta, S., Maifreni, M., Calligaris, S., Anese, M. y Nicoli, M., (2016). Impact of UV-C light on storage quality of fresh cut pineapple in two different packages. Food Science and Technology. 65:1138-1143 https://www.sciencedirect.com/science/article/abs/pii/S0023643815302255

Martín-Belloso, O., (2010). Tecnologías emergentes en la conservación de alimentos. Institució Catalana de Recerca i Estudis Avançasts (ICREA). Universidad de Lleida, España. https://www.benasque.org/2010fronterastalim/talks_contr/061Olga_Martin_Belloso.pdf

Martínez-Romero, D., Guillén, F., Valverde, J., Serrano, M., Zapata, P., Bailen, G., Valero, D., Castillo, S., (2007). *Aloe vera* gel como recubrimiento comestible en frutas y hortalizas. Universidad Miguel Hernández, España. https://www.horticom.com/revistasonline/horticultura/rh195/42_45.pdf

Márquez, L., PretelL C., (2013). Irradiación UV-C en frutas tropicales mínimamente procesadas. Sci. Agropecu. 4(3):147-161. https://www.redalyc.org/pdf/3576/357633706001.pdf

Márquez, L., PretelL C. y Minchón, C, (2013). Efecto de la dosis de irradiación UV-C y tiempo de almacenamiento sobre las características fisicoquímicas, microbiológicas, y antioxidantes en rebanadas de carambola (*Averrhoa carambola* L.) variedad Golden Star mínimamente procesada. Pueblo Cont. 23(2):353-369. https://www.semanticscholar.org/paper/EFECTO-DE-LA-DOSIS-DE-IRRADIACI%C3%93N-UV-C-Y-TIEMPO-DE-Villacorta-V%C3%A1squez/3dada79e00d164683d08d93471c9bbbec71dab9f

Monsalve-González, A., Barbosa-Canovas, G., Cavalieri, R., Mcevily, A., y Iyengar, R., (1993). Control of browning during storage of apple slices preserved by combined methods, 4-hexyl resorcinol as antibrowning agent. Journal of Food Science. 58: 797-800. https://ift.onlinelibrary.wiley.com/doi/10.1111/j.1365-2621.1993.tb09361.x

Montero, M., (2010). Internal quality profile and influence of packaging conditions on fresh-cut pineapple. Tesis Doctoral. Universidad de Lleida. Lleida, España.

Montilla de Bravo, I., Fernández, S., Alcalá de Marcano, D., Gallardo, M., (1997). El cultivo de la piña en Venezuela. Fondo Nacional de Investigaciones Agropecuarias. Centro de Investigaciones Agropecuarias del Estado Lara, Venezuela. https://repositorio.iica.int/items/1256ca4d-2684-4167-b68e-ebc801c22680

Morales, A., (2011). Frutoterapia: La fruta, el oro de mil colores. EDAF. https://www.ecoediciones.com/wp-content/uploads/2015/07/Las-frutas-oro-de-mil-colores-Vista-preliminar-del-libro.pdf?srsltid=AfmBOorq3AoPJsMsCZfZx6uR5Aa7OdhX5au6n3B28x5HexqPDPZOoEvl

Neidhardt, F., (1999). *Escherichia coli* and *Salmonella*: cellular and molecular Biology. 2nd edition. Washington:ASM Press. https://www.researchgate.net/publication/313647867_Escherichia_coli_and_Salmonella_Cellular_and_m

olecular_biology_2nd_edition

Pan, Y., Zu, H., (2012). Effect of UV-C radiation on the quality of fresh-cut pineapples. Procedia Engineering 37:113-119. https://www.sciencedirect.com/science/article/pii/S1877705812018619

Parzanese, M., (2012). Vegetales mínimamente procesados. Revista Alimentos Argentinos, 55:30-39. https://alimentosargentinos.magyp.gob.ar/contenido/revista/ediciones/55/productos/R55_vegetales.pdf

Paula, A., Conti-Silva, A., (2014). Texture profile and correlation between sensory and instrumental analyses on extruded snacks. Journal of Food Engineering. 121: 9-14. https://www.sciencedirect.com/science/article/pii/S0260877413004111

Pérez, M., Laskowski, L., Zambrano, J., Piña, H., (1997). Comportamiento postcosecha de frutos de piña (*Ananas comosus*) tratados con retardantes de la maduración almacenados a diferentes temperaturas. Universidad del Zulia, Venezuela. Revista de la Facultad de Agronomía. 14(4):393-398. https://www.revfacagronluz.org.ve/v14_4/v144z002.html

Pérez, L., (2003). Aplicación de métodos combinados para el control del desarrollo del pardeamiento enzimático en pera (variedad Blanquilla) mínimamente procesada. Tesis Doctoral. Universidad Politécnica de Valencia. Departamente de Tecnología de Alimentos. Valencia, España.
https://www.academia.edu/47614779/Aplicaci%C3%B3n_de_m%C3%A9todos_combinados_para_el_control_del_desarrollo_del_pardeamiento_enzim%C3%A1tico_en_pera_variedad_Blanquilla_m%C3%ADnimamente_procesada

Pisabarro, A., (2009). Microbiología clínica. En: 1er curso de Diplomatura en Enfermería. Tema 2: Crecimiento y muerte de microorganismos. Universidad Pública de Navarra. Departamento de Producción Agraria. Navarra, España.

Pizzocaro, F., Torreggiani, D. y Gilardi, G., (1993). Inhibition of apple polyfhenoloxidase (PPO) by ascorbic acid, citric acid and sodium chloride. Journal of Food Processing and Preservation. 17:21-30. https://www.researchgate.net/publication/229448660_Inhibition_of_apple_polyphenoloxidase_PPO_by_ascorbic_acid_citric_acid_and_sodium_chloride

Purizaga, Z., (2008). Control predictivo no lineal basado en modelos Hammerstein y Wiener para pH. Tesis de Grado. Universidad de Piura. Perú.

Ramos-Villarroel, A., Aron-Maftei, N., Martín-Belloso, O., Soliva-Fortuny, R., (2012). Influencia de la distribución espectral de inactivación y de calidad cambios bacterianos de sandía fresca cortada tratados con pulsos de luz intensa. Postharvest Biology and Technology. 69:32–39. https://www.sciencedirect.com/science/article/abs/pii/S0925521412000518

Rao, M., Steffe, J., (1992). Viscoelastic properties of foods. Elsevier Applied Science. New York, USA.

Rivera-Pastrana, D., Gardea-Béjar, A., Martínez-Téllez, M., Rivera-Domínguez, M., González-Aguilar, G., (2007). Efectos bioquímicos postcosecha de la irradiación UV-C en frutas y hortalizas. Revista Fitotécnia de Mexicana. 30(4):361-372. https://www.redalyc.org/pdf/610/61030403.pdf

Rocha, A., Morais, A., (2003). Shelf life of minimally processed apple (cv. Jonagored) determined by colour changes. Food Control. 14:13-20. https://www.sciencedirect.com/science/article/abs/pii/S0956713502000464

Rowan, N., Macgregor, S., Anderson, J.M., Fouracre, R., Cllvaney, L., Farish, O., (1999). Pulsed-ligh inactivation of food-relate microorganims. Applied and Envirenmental Microbiology. 65:1312-1315. https://pubmed.ncbi.nlm.nih.gov/10049899/

Soloman, D., Razali, Z., Santhirasegaram, V., Somasundram, C., (2015). Effects of ultaviolet light (UV-C) and heat treatment on the quality of fresh-cut 'Chokanan' mango and 'Josephine' pineapple. Journal of Food Science. 80(2): S426-S434. https://pubmed.ncbi.nlm.nih.gov/25586772/

Schenk, M., Guerrero, S., Alzamora, S., (2008). Response of some microorganisms to ultraviolet treatment on fresh-cut pear. Food and Bioprocess Technology. 1(4):384–392.
https://bibliotecadigital.exactas.uba.ar/collection/paper/document/paper_19355130_v1_n4_p384_Schenk

Siddiq, M., Ahmed, J., Lobo, M., Ozadali, F., (2012). Tropical and Subtropical Fruits. Postharvest Physiology, Processing and Packaging. New Delhi: Wiley-Blackwell.

SIOVM, [Mayo, 2011]. *Sistema de Información de OrganismosVivos Modificados*. Proyecto GEF - CI-BIOGEM/CONABIO. México, D.F. Disponible en: http://www.conabio.gob.mx/conocimiento/bioseguridad/doctos/consutaSIOVM.html

Thompson, A., (1998). *Tecnología post-cosecha de frutas y hortalizas*. Convenio SENA-Reino Unido. Colombia: Editorial Kinesis.

Trepat, M., (2002). Incidencia y comportamiento de *Salmonella* y *Listeria* en pechugas de pavo curadas. Tesis Doctoral. Facultad de Veterinaria, Universidad Autónoma de Barcelona. España.

Torres, K., Sierra, S., Poutou, R., Carrascal, A. Mercado, M., (2005). Patogénesis de *Listeria monocytogenes*, microorganismo zoonótico emergente. Universidad de Córdoba, Colombia. Revista de la Facultad de Medicina Veterinaria y Zootecnia. 10(1): 511-543 https://revistamvz.unicordoba.edu.co/article/view/47

5/543

Trujillo, F., López, S., Tavera, V., Tapia, M., Cava, R., (2001). Estudio de la estabilidad microbiológica de melón mínimamente procesado por impregnación a vacío. Archivos Latinoamericanos de Nutrición. 51:173-179. https://ve.scielo.org/scielo.php?script=sci_arttext&pid=S0004-06222001000200009

USFDA (United States Food and Drug Administration), (2002). Ultraviolet radiation for the processing and treatment of food. Code of Federal Regulations (CFR) Volumen 3. Título 21. Sección 179.39. https://www.ecfr.gov/current/title-21/chapter-I/subchapter-B/part-179/subpart-B/section-179.39

USDA (United States Department of Agriculture). Agricultural Research Service, (2014). USDA National Nutrient Database for Standard Reference. Release 27.

Wills, R., Lee, T., Grahm, D., Mcglason, W., Hall, E., (1984). *Fisiología y manipulación de frutas y hortalizas poscosecha*. Zaragoza: Editorial Acribia.

Received: *January 12th, 2025*

Accepted: *May 22th, 2025*

Ana Ramos, *PhD en Ciencias y Tecnologia Agraria y Alimentaria por la Universidad de Lleida, Lleida, España. Investigador del Centro de Oceanología y Estudios Antárticos. Instituto Venezolano de Investigaciones Científicas.*
https://orcid.org/0000-0003-4587-7327

Nicoleta Maftei, *PhD en Ingeniería Industrial. Profesor titulado en Farmacia. Universidad de Galati "Dunarea de Jos", Galati, Romanía. Correo electrónico: nicoleta.aron@ugal.ro*
https://orcid.org/0000-0003-0918-5534

Artículo de Investigación. Revista Ciencia e Ingeniería. Vol. 46, No. 3, pp. 295-302, agosto-noviembre, 2025.
ISSN 1316-7081. ISSN Elect. 2244-8780 Universidad de los Andes (ULA)

Sintonización por reubicación de polos de los cuatro parámetros de un controlador PID para plantas FOPTD

Four parameters PID controller sintonization using poles placement for FOPTD plants

Teppa-Garran, Pedro[1*]; Caraballo, Luis[2]
[1]Departamento de Gestión de Proyectos y Sistemas, Universidad Metropolitana, Caracas, Venezuela.
[2]Escuela de Ingeniería Eléctrica, Universidad Metropolitana, Caracas, Venezuela.
[*]pteppa@unimet.edu.ve

Resumen

La mayoría de los métodos de sintonización de controladores PID permiten el diseño de tres constantes del controlador. Sin embargo, dado que el término derivativo no puede aplicarse en forma pura se requiere incluir un cuarto parámetro en el filtro de derivación que posteriormente suele ajustarse a través de relaciones empíricas predefinidas. Estos procedimientos que combinan la sintonización de tres parámetros y el ajuste posterior del cuarto, muchas veces producen controladores PID pobremente sintonizados. En este trabajo se propone un método de sintonización directo de los cuatro parámetros del controlador PID basado en la reubicación de polos para un modelo de la planta de primer orden con retardo de transporte.

Palabras clave: Controlador PID, Patada del derivador, Reubicación de polos, Sistemas con retardo, Sistema FOPTD, Naciones Unidas ODS 9.

Abstract

Most PID controller tuning methods allow for the design of three controller constants. However, since the derivative term cannot be applied in its pure form, a fourth parameter must be included in the derivative filter, which is then typically tuned using predefined empirical relationships. These procedures, which combine tuning of three parameters and subsequent adjustment of the fourth, often produce poorly tuned PID controllers. This paper proposes a four-parameter PID controller tuning method based on pole placement for a first-order plant model with transport delay.

Keywords: PID controller, Derivative kick, Pole placement, Delay systems, FOPTD System, United Nations SDG 9.

1 Introducción

El controlador Proporcional-Integral-Derivativo (PID) es una de las primeras estrategias de control que se empleó en la práctica, su implementación inicial fue a través de dispositivos neumáticos, seguido por el uso de tubos de vacío y circuitos electrónicos analógicos, hasta la implementación digital actual mediante microprocesadores (Bennett, 1993). Hoy en día, y a pesar de los significativos avances alcanzados en la teoría de control, es la estrategia más utilizada en el control de procesos industriales porque proporciona estabilidad y respuestas rápidas para un rango amplio de condiciones de operación. Según Åström y Hagglund (1995) más del 90 % de los sistemas industriales de control, contienen algún tipo de controlador PID. Un estudio posterior, llevado a cabo por Desbourough y Miller (2002) consideró alrededor de 11.000 controladores en refinerías, industrias químicas y fábricas de papel, concluyendo que alrededor del 97 % de los controladores poseía una estructura PID. Una arquitectura típica del controlador PID se muestra en la Fig. 1, donde se aprecia que la señal de error $e(t)$ se utiliza para generar las acciones proporcional, integral y derivativa, que luego se ponderan y suman para formar la señal de control $u(t)$. Un modelo matemático del controlador PID es

$$u(t) = K_p e(t) + K_i \int_0^t e(\tau)\, d\tau + K_d \frac{d}{dt} e(t) \qquad (1)$$

O equivalentemente, usando la transformada de Laplace

$$U(s) = \left(K_p + \frac{K_i}{s} + K_d s\right) E(s) \qquad (2)$$

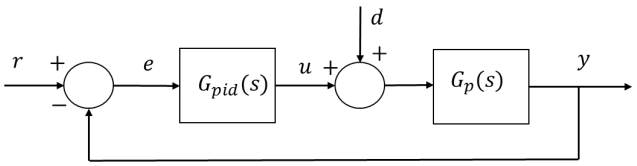

Fig. 1. Arquitectura típica de un controlador PID.
(*A typical PID control structure*)

Como se aprecia en (1) o (2), los parámetros del controlador PID son tres: la constante proporcional K_p, la constante integral K_i y la constante derivativa K_d. Estas constantes deben sintonizarse para responder a los requerimientos de diseño y a ese fin se han formulado diversas reglas de sintonización, muchas de ellas utilizados comúnmente en la práctica, pueden mencionarse: la regla de Ziegler y Nichols (1942), la de Chien, Hrones y Reswick (1952), la de Cohen y Coon (1953), la regla complementaria (Mantz y Taconi, 1989), las reglas de algo de sobrepico y sin sobrepico (Seborg, Edgar y Mellichamp, 1989), la regla modificada de Ziegler y Nichols (Hang, Åström y Ho, 1991), la regla de la integral del error cuadrático multiplicado por el tiempo (Zhuang y Atherton, 1993), la de la integral del error absoluto (Pessen, 1994), la fórmula de Wang, Juang y Chan (1995) y el rechazo activo de perturbaciones (Teppa-Garrán y García, 2017). Estas reglas, muchas de ellas fáciles de implementar, aportan métodos de sintonización de los parámetros del controlador PID que en muchos casos no suministran los mejores ajustes de las constantes (Lee y col, 2014). Por tal razón, se han propuesto métodos de sintonización óptima: basados en algoritmos genéticos (El-Deen y col, 2015; Gunawan y col, 2018), asistidos por computadora (Teppa-Garran y col, 2021; Teppa-Garran y El Gharib, 2024) o basados en el regulador lineal cuadrático (Teppa-Garran y col, 2025a).

Ahora bien, en aplicaciones prácticas, la acción derivativa pura en (1) nunca se emplea, debido al fenómeno de "la patada del derivador" (*derivative kick*) producido en la señal de control para entradas tipo escalón y a la amplificación del ruido de medición (Atherton y Majhi, 1999; Zhu, 2009). Por tal razón, el término derivativo se coloca en cascada con un filtro pasa-bajo de primer orden, resultando que la ecuación (2) toma la forma

$$U(s) = \left(K_p + \frac{K_i}{s} + \frac{K_d s}{\tau_d s + 1}\right) E(s) \qquad (3)$$

Todas las reglas (tradicionales y óptimas) citadas previamente consideran únicamente la sintonización de las tres constantes K_p, K_i y K_d pero no el término τ_d. Para fijar este último se suelen emplear simulaciones posteriores a partir de rangos predefinidos. Por ejemplo: (Goodwin y col, 2001).

$$0.1\left(K_d/K_p\right) \le \tau_d \le 0.2\left(K_d/K_p\right) \qquad (4)$$

O resultados que buscan mitigar el efecto de la patada del derivador pero usando controladores PID difusos (Kumar, y Rana, 2016) o controladores PID de orden fraccional (Lendek y Tan, 2021).

Los sistemas de control con retardo temporal se encuentran presentes en numerosas aplicaciones industriales, como la ingeniería química, la bioquímica, la industria aeroespacial y la generación de energía, por nombrar solo algunas (Gu y col, 2003). Aunque no sean un componente natural del proceso controlado, los actuadores y sensores de un sistema de control introducen retardos en su funcionamiento (Richard, 2003). La principal causa de estos retardos en los procesos industriales es el transporte de materiales o energía en tuberías de gran longitud (Bresch y col, 2014) o el tráfico de datos en redes de comunicación (Ariba y col, 2009). Se sabe que el retardo temporal degrada el rendimiento del proceso, llegando incluso a desestabilizarlo. Como caso especial de sistemas con retardo temporal, muchos procesos industriales de lazo abierto de interés práctico pueden modelarse eficazmente mediante una cascada de funciones de transferencia de orden bajo con un retardo temporal. Los sistemas de primer orden con retardo temporal (FOPTD) son el modelo de proceso más utilizado en el diseño de control (O'Dwyer, 2009).

En este trabajo se propone un método de sintonización de los cuatro parámetros del controlador PID decrito por (3) para una planta representada mediante un modelo FOPTD empleando un enfoque algebraico de reubicación de polos. Varios ejemplos muestran la eficacia del procedimiento propuesto. Finalmente, los resultados de este trabajo fomentan la innovación en el control de procesos industriales y de esta manera contribuir con el ODS 9 de las Naciones Unidas.

2 Método

En el sistema de control a lazo cerrado de la Fig. 1 ya se mencionaron las señales de control $u(t)$ y de error $e(t)$ que aparecen en el controlador PID. La señal $r(t)\colon \mathbb{R}^+ \to \mathbb{R}$ es la entrada de referencia, $d(t)\colon \mathbb{R}^+ \to \mathbb{R}$ es una señal de perturbación, $y(t)\colon \mathbb{R}^+ \to \mathbb{R}$ es la salida controlada y t es la variable independiente del tiempo. La señal de error se define como $e(t) = r(t) - y(t)$. La función de transferencia a lazo cerrado de r a y viene dada por la ecuación

$$G_{yr}(s) = \frac{Y(s)}{R(s)} = \frac{G_{pid}(s)G_p(s)}{1 + G_{pid}(s)G_p(s)} \qquad (5)$$

Donde la función de transferencia del controlador PID es la expresión de cuatro parámetros dada por

$$G_{pid}(s) = K_p + \frac{K_i}{s} + \frac{K_d s}{\tau_d s + 1} \qquad (6)$$

Y la planta se modela mediante un sistema de primer orden con retardo de transporte θ_d (FOPTD).

$$\frac{Y(s)}{U(s)} = \frac{K}{Ts+1} e^{-\theta_d s} \tag{7}$$

Empleando un modelo de Padé de primer orden para aproximar el retardo de transporte en (7) $(e^{-\theta_d s} \approx (2-\theta_d s)/(2+\theta_d s))$ (Hanta y Procházka, 2009) permite obtener la siguiente función de transferencia de la planta

$$G_p(s) = \frac{-b_1 s + b_0}{s^2 + a_1 s + a_0} \tag{8}$$

Donde

$$b_1 = K/T,\ b_0 = 2K/T\theta_d,\ a_1 = (2T+\theta_d)/T\theta_d,\ a_0 = 2/T\theta_d$$

La ecuación (8) será empleada para diseñar el controlador (6) de la Fig. 1. Sin embargo, para representar el controlador PID se usará una forma alternativa que se presenta en el siguiente teorema.

Teorema 1: Cualquier controlador PID modelado por la función de transferencia

$$G_{pid}(s) = \frac{n_2 s^2 + n_1 s + n_0}{d_2 s^2 + d_1 s} \tag{9}$$

Es idéntico al controlador PID modelado por (6) donde

$$\begin{aligned} K_p &= \frac{n_1 d_1 - n_0 d_2}{d_1^2} \\ K_i &= \frac{n_0}{d_1} \\ K_d &= \frac{n_2 d_1^2 - n_1 d_1 d_2 + n_0 d_2^2}{d_1^2} \\ \tau_d &= \frac{d_2}{d_1} \end{aligned} \tag{10}$$

Prueba: La ecuación (6) se reescribe como

$$\frac{\left(K_d + K_p\tau_d\right)s^2 + \left(K_p + K_i\tau_d\right)s + K_i}{\tau_d s^2 + s}$$

Y la ecuación (9) en la forma

$$\frac{\frac{n_2}{d_1}s^2 + \frac{n_1}{d_1}s + \frac{n_0}{d_1}}{\frac{d_2}{d_1}s^2 + s}$$

Al igualar las dos ecuaciones previas queda establecido el teorema.

A continuación se va a desarrollar un método para determinar los cuatro parámetros del controlador PID en (6) mediante un procedimiento de reubicación de polos pero usando la forma de representación (9) y luego se emplea el Teorema 1 para efectuar la conexión con la forma (6).

A partir de la ecuación característica $1 + G_{pid}(s)G_p(s) = 0$ del sistema de control a lazo cerrado (5) haciendo uso de (8) y (9) se obtiene el polinomio característico

$$\begin{aligned} d_2 s^4 + (a_1 d_2 + d_1 - b_1 n_2)s^3 \\ + (a_0 d_2 + a_1 d_1 + b_0 n_2 \\ - b_1 n_1)s^2 + (a_0 d_1 + b_0 n_1 \\ - b_1 n_0)s + b_0 n_0 \end{aligned} \tag{11}$$

Mediante unos requerimientos de diseño pueden definirse un conjunto de polos deseados $\{p_1, p_2, p_3, p_4\}$ y de esta manera formar el polinomio a lazo cerrado deseado

$$T(s) = t_4 s^4 + t_3 s^3 + t_2 s^2 + t_1 s + t_0 \tag{12}$$

Con parámetros $t_i > 0$ conocidos.

Comentario 1: No hay pérdida de generalidad si el polinomio en (12) se define como mónico ($t_4 = 1$).

En este trabajo los polos a lazo cerrado se van a seleccionar a través de un procedimiento de garantía de polos dominantes propuesto inicialmente por (Persson y Åström, 1992) y empleado en varias aplicaciones de control. Por ejemplo, en el control de sistemas de dos grados de libertad (Teppa-Garran y col, 2023), en el control robusto a través de la optimización lineal (Teppa-Garran y Leizaola, 2024) y en el control de sistemas quasi-LPV (Teppa-Garran y col, 2025b).

Las especificaciones de desempeño en el tiempo de la salida controlada se convierten en un par de polos conjugados $s_{1,2} = -\alpha \pm j\beta$. Su dominancia requiere que el cociente entre la parte real de los otros polos y $-\alpha$ exceda un término λ. De esta manera, todos los otros polos se encuentran a la izquierda de la línea vertical $s = -\lambda\alpha$. En nuestro caso, el polinomio $T(s)$ se puede escribir como

$$T(s) = (s^2 + 2\zeta\omega_n s + {\omega_n}^2)(s + \lambda\zeta\omega_n)^2 \tag{13}$$

El coeficiente de amortiguación ζ y la frecuencia natural ω_n de los polos dominantes se computan en términos del sobrepico (M_p) y del tiempo de establecimiento (T_s) deseados a través de las ecuaciones (Dorf y Bishop, 2017).

$$\begin{aligned} M_p = e^{\left(-\zeta\pi/\sqrt{1-\zeta^2}\right)} \Longrightarrow \\ \zeta = 1\Bigg/\sqrt{1+\left(\frac{\pi}{ln(M_p)}\right)^2} \\ T_s = 4/(\zeta\omega_n) \Longrightarrow \omega_n = 4/\zeta T_s \end{aligned} \tag{14}$$

Teorema 2: Si los coeficientes de los polinomios (11) y (12) son iguales, entonces lo parámetros del controlador (6) se computan a través de las ecuaciones

$$K_i = \frac{t_0 A_1}{A_2}$$

$$\tau_d = b_0 t_4 K_{i_1}$$

$$K_p = \left(\frac{b_0 A_1}{A_2}\right)^2 \left[\frac{A_2 A_3}{(b_0 A_1)^2} - \frac{t_0 t_4}{b_0}\right] \quad (15)$$

$$K_d = \left(\frac{b_0 A_1}{A_2}\right)^2 \left[\frac{t_0 {t_4}^2}{b_0} + \frac{{A_2}^2 A_4}{(b_0 A_1)^3} - \frac{t_4 A_2 A_3}{(b_0 A_1)^2}\right]$$

Con

$$A_1 = {b_0}^2 + a_1 b_0 b_1 + a_0 {b_1}^2$$

$$A_2 = {b_1}^3 t_0 + {b_0}^3 t_3 - a_1 {b_0}^3 t_4 + b_0 {b_1}^2 t_1 + {b_0}^2 b_1 t_2 - a_0 {b_0}^2 b_1 t_4$$

$$A_3 = {b_0}^2 t_1 + b_0 b_1 t_0 + a_1 {b_1}^2 t_0 - a_0 {b_0}^2 t_3 + a_0 a_1 {b_0}^2 t_4 + {a_0}^2 b_0 b_1 t_4 - a_0 b_0 b_1 t_2 + a_1 b_0 b_1 t_1$$

$$A_4 = {b_1}^2 t_0 + {b_0}^2 t_2 + a_1 {}^2 {b_0}^2 t_4 + b_0 b_1 t_1 - a_0 {b_0}^2 t_4 - a_1 {b_0}^2 t_3 - a_0 b_0 b_1 t_3 + a_0 a_1 b_0 b_1 t_4$$

Prueba: Igualando los coeficientes de los polinomios (11) y (12) resulta en el sistema de ecuaciones

$$\begin{bmatrix} 1 & 0 & 0 & 0 & 0 \\ a_1 & 1 & -b_1 & 0 & 0 \\ a_0 & a_1 & b_0 & -b_1 & 0 \\ 0 & a_0 & 0 & b_0 & -b_1 \\ 0 & 0 & 0 & 0 & b_0 \end{bmatrix} \begin{bmatrix} d_2 \\ d_1 \\ n_2 \\ n_1 \\ n_0 \end{bmatrix} = \begin{bmatrix} t_4 \\ t_3 \\ t_2 \\ t_1 \\ t_0 \end{bmatrix} \quad (16)$$

El teorema queda establecido resolviendo (16) y empleando (10).

Comentario 2: Una pregunta legítima es por qué la ecuación (6) del controlador PID se representa en la forma (9). La razón es que si la forma (6) se usa directamente para construir el polinomio característico (11). El sistema de ecuaciones es no lineal y sobredeterminado en lugar de lineal como se tiene en (16).

Comentario 3: El determinante de la matriz de coeficientes en (16) es igual a $b_0\left({b_0}^2 + a_1 b_0 b_1 + a_0 {b_1}^2\right)$. Para que sea nulo debe cumplirse que $b_0 = 0$. Pero esto es imposible que ocurra dado que la ganancia K en (7) también debería ser cero. Por lo tanto, el sistema de ecuaciones (16) tiene solución única y siempre pueden encontrarse valores de las constantes del controlador PID empleando (15) en el teorema 2.

Comentario 4: Para calcular las constantes del controlador no se emplean las ecuaciones (15). El teorema 2 es un resultado teórico para justificar el procedimiento y que siempre es posible computar las constantes del controlador. La manera de determinar las constantes del controlador PID (6) es a través de la resolución de (16) para obtener los valores de d_2, d_1, n_2, n_1 y n_0 y posteriormente computar las constantes del controlador PID a través de (10).

3 Resultados

En esta sección se desarrollan varios ejemplos que muestran como aplicar el método de sintonización de los cuatro parámetros del controlador PID descrito en la forma (6) para plantas FOPTD. El ejemplo 1 considera un proceso de flujo de calor donde el retardo de transporte no es significativo en relación a la constante de tiempo del sistema. El segundo ejemplo trata el caso donde el retardo de transporte si es importante. Finalmente, el ejemplo 3, un sistema de tanques acoplados, muestra que el método puede extenderse para tratar otro tipo de sistemas diferentes al modelo FOPTD.

En todos los ejemplos los requerimientos de diseño para la salida controlada se definen a través de un sobrepico M_p y un tiempo de establecimiento T_s deseados y se implementan mediante un criterio de garantía de polos dominantes.

3.1 Ejemplo 1

Se considera un proceso de flujo de calor (Teppa-Garran y Leizaola, 2024) que consiste en un ducto de fibra de vidrio con un calentador y un soplador localizados en un extremo y tres sensores de temperatura a lo largo del ducto. La salida controlada corresponde a la temperatura y la señal de control es el voltaje aplicado al elemento calentador (el voltaje del soplador se mantiene constante). El modelo de temperatura en el tercer sensor (más alejado) viene dado por la función de transferencia

$$\frac{Y(s)}{U(s)} = \frac{6.1}{28s + 1} e^{-0.85s} \quad (17)$$

La ecuación (8) toma la forma

$$G_p(s) = \frac{-0.2179s + 0.5126}{s^2 + 2.3887s + 0.0840} \quad (18)$$

Empleando el criterio de garantía de polos dominantes para que la salida controlada tenga un sobrepico $M_p \leq 10\%$ y un tiempo de establecimiento $T_s = 40$ s resulta en el polinomio a lazo cerrado deseado

$$T(s) = s^4 + 2.6s^3 + 1.941s^2 + 0.3384s + 0.032 \quad (19)$$

Utilizando el procedimiento de diseño propuesto, los parámetros del controlador PID en (6) vienen dados por los valores $K_p = 0.9288, K_i = 0.1126, K_d = 0.5065$ y $\tau_d = 1.9082$.

En la Fig. 2 se muestra la evolución de la temperatura en el tercer sensor cuando el perfil de temperatura de la entrada de referencia cambia en forma escalonada. La Fig. 3 ilustra la señal de control que debe aplicarse. En la simulación se

emplea para representar a la planta el modelo FOPTD dado por (17).

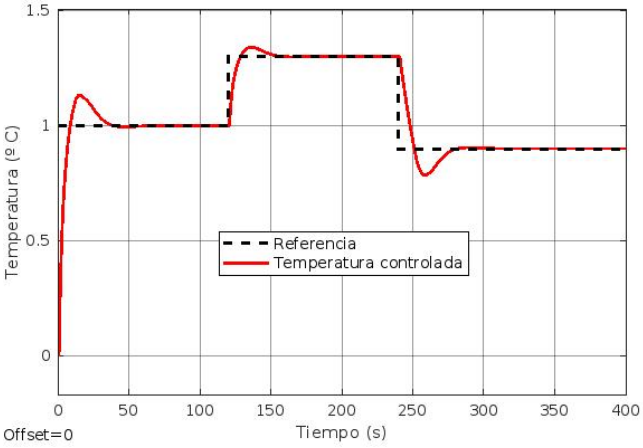

Fig. 2. Control de la temperatura del tercer sensor en el proceso de flujo de calor.
(*Temperature control of the third sensor in the heat flow process)*

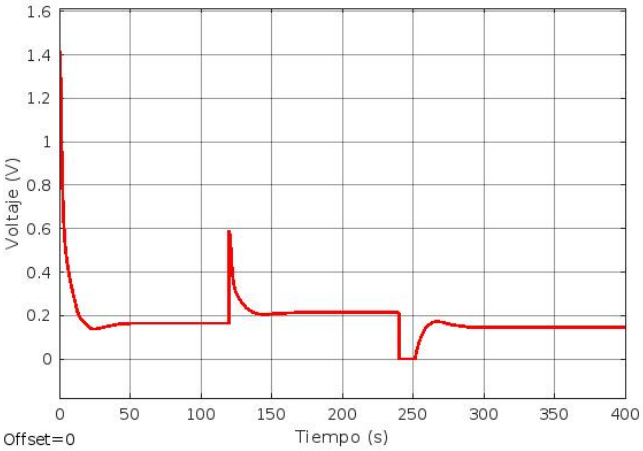

Fig. 3. Señal de control aplicada al proceso de flujo de calor.
(*Input control signal applied to the heat flow process)*

3.2 Ejemplo 2

En el ejemplo anterior se cumplía la relación $\theta_d/T < 1$. En este ejemplo se va a tratar la situación más exigente donde $\theta_d/T > 1$. A ese fin se considera un proceso de orden elevado descrito por el modelo

$$\frac{Y(s)}{U(s)} = \frac{1}{(s+1)^{10}} \tag{20}$$

Empleando el método de ajustes de mínimos cuadrados entre el proceso y la respuesta frecuencial del modelo descrito en (Hang y Bi, 1997) se obtiene la función de transferencia

$$\frac{Y(s)}{U(s)} = \frac{1}{2.72s+1} e^{-7.69s} \tag{21}$$

Y en este caso la ecuación (8) toma la forma

$$G_p(s) = \frac{-0.3676s + 0.0956}{s^2 + 0.6277s + 0.0956} \tag{22}$$

La Tabla 1 muestra los valores calculados, con el método de sintonización propuesto, de los cuatro parámetros del controlador PID utilizando el mismo tiempo de establecimiento $T_s = 60$ s y tres valores de sobrepico (5 % , 10% y 20 %).

Tabla 1. Valores de las constantes del controlador PID para diferentes condiciones de sobrepico en el ejemplo 2.
(*PID controller constant values for different overshoot conditions in Example 2*)

	$T_s = 60$ s		
	$M_p = 5$ %	$M_p = 10$ %	$M_p = 20$ %
K_p	0.0165	0.0815	0.2321
K_i	0.0513	0.0674	0.1039
K_d	0.2877	0.3445	0.5056
τ_d	0.8214	0.7923	0.7263

La Tabla 2 muestra las constantes calculadas para el controlador PID para tres valores de tiempo de establecimiento (40 s, 50 s y 60 s) manteniendo el sobrepico en 10 %.

Tabla 2. Valores de las constantes del controlador PID para diferentes condiciones de tiempo de establecimiento en el ejemplo 2.
(*PID controller constant values for different settling time conditions in Example 2*)

	$M_p = 10$ %		
	$T_s = 40$ s	$T_s = 50$ s	$T_s = 60$ s
K_p	0.5201	0.2648	0.0815
K_i	0.1245	0.0893	0.0674
K_d	3.5324	1.1600	0.3445
τ_d	0.2888	0.5060	0.7923

La Fig. 4 presenta la evolución de la salida controlada para los tres valores de sobrepico considerados en la Tabla 1 y la Fig. 5 cuando se varía el requerimiento de tiempo de establecimiento según aparece en la Tabla 2. En ambos casos se aprecia que las respuestas son influenciadas por las especificaciones de diseño. La Fig. 6 exhibe el comportamiento de la salida controlada para un controlador PID de cuatro parámetros sintonizados por el método propuesto y un controlador PID con las constantes proporcional, integral y derivativa sintonizadas conforme a la popular regla de Ziegler-Nichols y luego el parámetro τ_d ajustado según la relación empírica (4). Puede apreciarse que este último resultado no es satisfactorio. Esto no es algo inusual, generalmente este tipo de reglas suministran unos valores preliminares que mediante simulaciones posteriores se van ajustando hasta encontrar un conjunto de costantes adecuado. Sin embargo, resulta evidente que los primeros valores que generó el método propuesto ya son satisfactorios. En la Figura 7, aparecen las señales de

control para los dos esquemas de sintonización. Ambos exhiben niveles de amplitud adecuados.

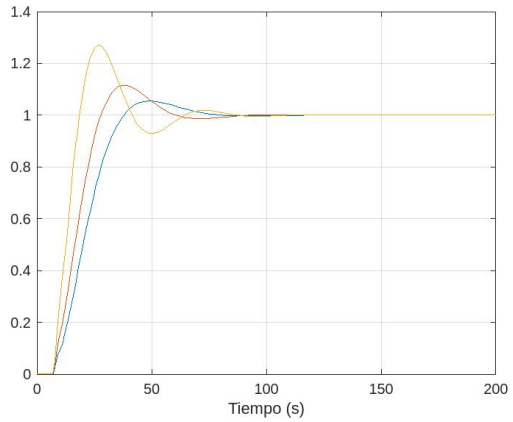

Fig.4. Salida controlada en el Ejemplo 2 para diferentes requerimientos de sobrepico considerados en la Tabla 1.
(*Controlled output in Example 2 for different overshoot requirements considered in Table 1*)

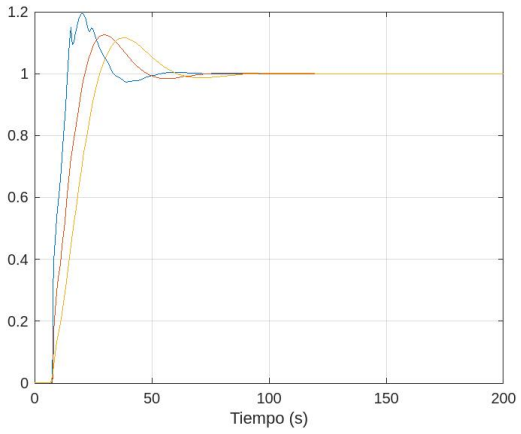

Fig. 5. Salida controlada en el Ejemplo 2 para diferentes requerimientos de tiempo de establecimiento considerados en la Tabla 2.
(*Controlled output in Example 2 for different settling time requirements considered in Table 2*)

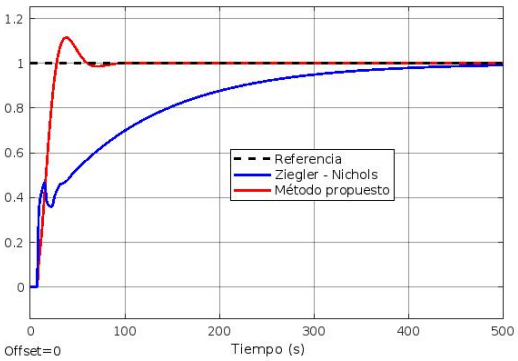

Fig. 6. Salida controlada en el Ejemplo 2 para controladores PID sintonizados por el método propuesto y por la regla de Ziegler-Nichols.
(*Controlled output in Example 2 for PID controllers tuned by the proposed method and by the Ziegler-Nichols rule*)

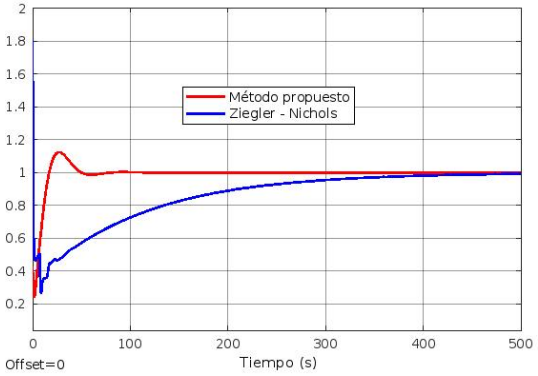

Fig. 7. Señal de control en el Ejemplo 2 para controladores PID sintonizados por el método propuesto y por la regla de Ziegler-Nichols.
(*Control signal in Example 2 for PID controllers tuned by the proposed method and by the Ziegler-Nichols rule*)

3.3 Ejemplo 3

Un modelo no lineal de espacio de estados de un sistema de dos tanques acoplados se presenta en la ecuación (23) (Teppa-Garran y col, 2025b). El vector de estados $[x_1(t) \quad x_2(t)]^T$ es igual a los niveles de los tanques, la señal de control $u(t)$ corresponde al voltaje de entrada aplicado a una bomba y la salida $y(t)$ se selecciona como el nivel del segundo tanque. Los niveles de los tanques se encuentran en el intervalo $[0, 30]$ cm y el voltaje de la bomba en $[0, 22]$ V.

$$\begin{aligned} \dot{x}_1(t) &= -0.904\sqrt{x_1(t)} + 0.258u(t) \\ \dot{x}_2(t) &= 0.904\sqrt{x_1(t)} - 0.508\sqrt{x_2(t)} \\ y(t) &= x_2(t) \end{aligned} \tag{23}$$

Linealizando (23) en el punto de operación (15, 15) cm se obtiene la función de transferencia

$$\frac{Y(s)}{U(s)} = \frac{0.0302}{s^2 + 0.183s + 0.0077} \tag{24}$$

Puede apreciarse que es de la forma (8) con $b_1 = 0, b_0 = 0.0302, a_1 = 0.183$ y $a_0 = 0.0077$. Por lo que puede implementarse un PID de la forma (6) para controlar el sistema de tanques acoplados y sintonizar sus constantes utilizando el método propuesto.

Para $M_p = 5\,\%$ y $T_s = 80$ s resultan las constantes del controlador $K_p = 0.5528, K_i = 0.0261, K_d = 0.7299$ y $\tau_d = 2.3981$.

La Fig. 8 muestra el seguimiento del nivel en el segundo tanque cuando se aplica una entrada de referencia que cambia el punto de ajuste del nivel en los instantes $t = 150$ s y $t = 300$ s. Se aprecia que el seguimiento es satisfactorio y debe destacarse que en la simulación se utiliza el modelo no lineal del sistema de tanques acoplados dado por la ecuación (23). La Fig. 9 ilustra la evolución de

la señal de control y puede apreciarse que se encuentra dentro de los límites de actuación del voltaje de la bomba.

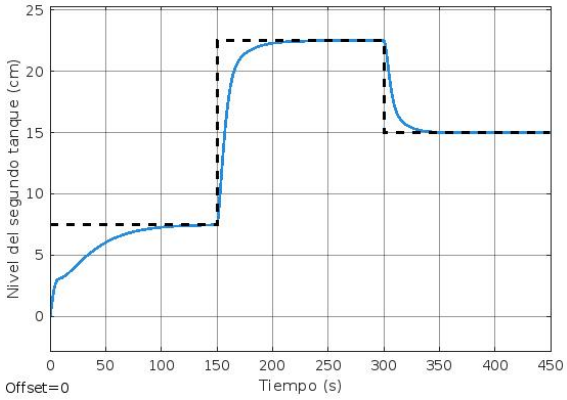

Fig. 8. Seguimiento del nivel del segundo tanque para varios cambios en el punto de ajuste.
(*Tracking the second tank level for different setpoint changes*)

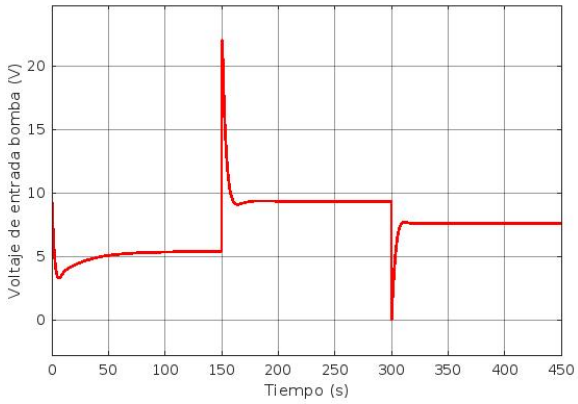

Fig. 9. Voltaje de entrada aplicado a la bomba en el sistema de tanques acoplados.
(*Input voltage applied to the pump in the coupled tank system*)

Conclusiones

En este trabajo se propone un método de sintonización de los cuatro parámetros de un controlador PID expresado en la forma paralela dada por la ecuación (6). El método aplica para un modelo de la planta de primer orden con retardo de transporte. Las especificaciones de desempeño se definen a través de un criterio de garantía de polos dominantes mediante la selección de un sobrepico y un tiempo de establecimiento deseados en la salida controlada del sistema. Se consideraron ejemplos donde el retardo de transporte era menor y mayor que la constante de tiempo del sistema y en ambos casos se obtuvieron resultados satisfactorios. También se muestra que el método puede extenderse a otro tipo de plantas como fue el caso de un sistema de tanques acoplados cuya dinámica es no lineal.

En uno de los ejemplos se observa que los procedimientos actuales de sintonización que se concentran inicialmente en la sintonización de las constantes proporcional, integral y derivativa mediante el empleo de concocidas reglas y el posterior ajuste del parámetro del filtro de derivación utilizando relaciones predefinidas puede resultar en un desempeño inadecuado.

Agradecimientos

Los autores agradecen el apoyo brindado por el Programa de Investigación de la Universidad Metropolitana en Caracas, Venezuela a través del proyecto número PI-A-01-23-24.

Referencias

Ariba, Y., Gouaisbaut, F., y Labit, Y. (2009). Feedback control for router management and TCP/IP network stability. *IEEE Transactions on Network and Service Management*, *6*(4), 255-266.

Åström, K. y Hagglund, T. (1995). *PID controllers: Theory, design and tuning*. NC: Instrument Society of America, Research Triangle Park.

Atherton, D. P., y Majhi, S. (1999, June). Limitations of PID controllers. In *Proceedings of the 1999 American Control Conference (Cat. No. 99CH36251)* (Vol. 6, pp. 3843-3847). IEEE.

Bennett, S. (1993). Development of the PID controllers. *IEEE Control System Magazine*, 13(2), pp. 58 – 65.

Bresch-Pietri, D., Chauvin, J., y Petit, N. (2014). Prediction-based stabilization of linear systems subject to input-dependent input delay of integral-type. *IEEE Transactions on Automatic Control*, 59(9), pp. 2385-2399.

Chien, K., Hrones, J. y Reswick, J. (1952). On the automatic control of generalised passive systems. *Transactions of the ASME*, pp. 175 -185.

Cohen, G. y Coon, G. (1953). Theoretical considerations of retarded control. *Transactions of the ASM*E, pp. 827 - 834.

Desbourough, L. y Miller, R. (2002). Increasing customer value of industrial control performance monitoring: Honeywell's experience, In *6th International Conference on Chemical Process Control*, AIChE Symposium Series, Vol. 98(326).

Dorf, R., Bishop, R., (2017). *Modern control systems*. Pearson Prentice Hall.

El-Deen, A. T., Mahmoud, A. H., y El-Sawi, A. R. (2015). Optimal PID tuning for DC motor speed controller based on genetic algorithm. *Int. Rev. Autom. Control*, *8*(1), pp. 80-85.

Goodwin, G. C., Graebe, S. F., y Salgado, M. E. (2001). *Control system design* (Vol. 240). Upper Saddle River: Prentice Hall.

Gu, K., Chen, J., y Kharitonov, V. L. (2003). *Stability of time-delay systems*. Springer Science & Business Media.

Gunawan, S. A., Yuwono, Y. C. H., Pratama, G. N. P., Cahyadi, A. I., & Winduratna, B. (2018, August).

Optimal fractional-order PID for DC motor: Comparison study. In *2018, the 4th International Conference on Science and Technology (ICST)* (pp. 1-6). IEEE.

Hang, C., Åström, K. y Ho, W. (1991). Refinements of the Ziegler–Nichols tuning formula. *IEE Proceedings-D*, 138(2), pp. 111 – 118.

Hang, C. C. y Bi, Q. (1997). A frequency domain controller design method. *Chemical Engineering Research and Design*, *75*(1), pp. 64-72.

Hanta, V., y Procházka, A. (2009). Rational approximation of time delay. *Institute of Chemical Technology in Prague. Department of computing and control engineering. Technická*, *5*(166), p. 28.

Kumar, V., y Rana, K. P. S. (2016). Some investigations on hybrid fuzzy IPD controllers for proportional and derivative kick suppression. *International Journal of Automation and Computing*, *13*, pp. 516-528.

Lendek, A., y Tan, L. (2021). Mitigation of derivative kick using time-varying fractional-order PID control. *IEEE Access*, *9*, 55974-55987.

Lee, J., Cho, W., y Edgar, T. F. (2014). Simple analytic PID controller tuning rules revisited. *Industrial & Engineering Chemistry Research*, *53*(13), pp. 5038-5047.

Mantz, R. y Taconi, E. (1989). Complementary rules to Ziegler-Nichols: rules for a regulating and tracking controller. *International Journal of Control*, 49(5), pp. 1465 – 1471.

O'Dwyer, A. Handbook of PI and PID Controller Tuning Rules, 3rd ed.; Imperial College Press: London, UK, 2009.

Persson, P. y Åström, K. (1992). Dominant pole design a unified view of PID controller tuning, IFAC Proceedings Volumes, 25(14), pp. 377-382.

Pessen, D. (1994). A new look at PID controller tuning. *Journal of Dynamic Systems, Measures and Control*, 116, pp. 53 – 557.

Richard, J. P. (2003). Time-delay systems: an overview of some recent advances and open problems. *Automatica*, 39(10), pp. 1667-1694.

Seborg, D., Edgar, T. y Mellichamp, D. (1989). *Process Dynamics and Control*. New York: Wiley.

Teppa-Garran, P. y Garcia, G. (2017). Design of an Optimal PID controller for a coupled tanks system employing ADRC, *IEEE Latin America Transactions*, 15(2), pp. 189-192.

Teppa-Garran, P., Arzola, F., y Elyas, E. (2021). Ajuste óptimo de controladores PID mediante Matlab/Simulink. *Anales De Ciencias Básicas, Físicas Y Naturales*, (37), pp. 15–32.

Teppa-Garran, P., Faggioni, M y Garcia, G. (2023). Optimal tracking in two-degree-of-freedom control systems: Coupled tank system. *Journal of Applied Research and Technology*, 21(4), pp. 560-570.

Teppa-Garran, P. y El Gharib, G. (2024). Sintonización óptima asistida por computadora de controladores PI para sistemas no lineales con restricciones de amplitud en el actuador. *Ciencia e Ingeniería,* 45(1), pp. 1-10.

Teppa-Garran, P. y Leizaola I. (2024). Control robusto de un proceso de flujo de calor empleando la optimización lineal. *Ciencia e Ingeniería*, 45(3), pp.289-294.

Teppa-Garran, P., Bohórquez, G., y Garcia, G. (2025). Optimal tuning of PID-type controllers. *Journal of Applied Research and Technology*, *23*(2), pp. 145–154.

Teppa-Garrán, P., Muñoz-de Escalona, D., y Zambrano, J. (2025). Liquid level tracking for a coupled tank system using quasi–LPV control. *Ingenius*, (33), pp. 15-26.

Wang, F. S., Juang, W. S., y Chan, C. T. (1995). Optimal tuning of PID controllers for single and cascade control loops. *Chemical Engineering Communications*, *132*(1), pp. 15-34.

Zhu, X. (2009). Practical PID controller implementation and the theory behind it. In *2009, Second International Conference on Intelligent Networks and Intelligent Systems* (pp. 58-61). IEEE.

Zhuang, M. y Atherton, D. (1993). Automatic tuning of optimum PID controllers. *IEE Proceedings-D*. 140(3), pp. 216 – 224.

Ziegler, J. y Nichols, N. (1942). Optimum settings for automatic controllers. *Transactions of the ASME*, 64, pp. 759 -768.

Recibido: *14 de febrero de 2025*

Aceptado: *20 de junio de 2025*

Pedro Teppa-Garrán*; Ingeniero Electricista UNIMET, MSc Ingeniería Electrónica, USB. MSc Matemáticas, USB. PhD Sistemas de Control, Université Paul Sabatier, Francia. Postdoctorado en Sistemas de Control, LAAS – CNRS, Francia. Profesor Titular UNIMET.*
https://orcid.org/ 0000-0001-6384-3185

Luis Caraballo*: Ingeniero Electricista UNIMET.*
Correo electronico:c.luis@correo.unimet.edu.ve
https://orcid.org/0009-0004-5507-272X

Artículo de Investigación. Revista Ciencia e Ingeniería. Vol. 46, No. 3 pp. 313-320, agosto-noviembre, 2025.
ISSN 1316-7081. ISSN Elect. 2244-8780 Universidad de los Andes (ULA)

Estudio espectrofotométrico de la actividad antioxidante de extractos metanólicos de corteza y frutos de *Vismia baccifera* var. *dealbata* aplicando el sistema radicalario DPPH•

Spectrophotometric study of the antioxidant activity of methanolic extracts of *Vismia baccifera* var. *dealbata* bark and fruit using the DPPH• radical system

Vizcaya, Marietta[1]; Pérez, Patricia[1]; Rodríguez, Pedro[2]; Lugo, Claudio[3]; Plaza, Claudia[4];
[1]Laboratorio de Polímeros, Departamento de Química, Facultad de Ciencias, Universidad de Los Andes, Venezuela.
[2]Facultad de Ciencias Químicas, Universidad de Concepción, Edmundo Larenas 129, Casilla 160C, Chile.
[3]Laboratorio de Cinética y Catálisis, Departamento de Química, Facultad de Ciencias, Universidad de Los Andes, Venezuela.
[4]Instituto de Investigaciones Científicas, Facultad de Farmacia y Bioanálisis, Universidad de Los Andes, Venezuela.
*marietta@ula.ve

Resumen

Se evaluó la capacidad antioxidante de extractos metanólicos de corteza (EMC) y frutos (EMF) de *Vismia baccifera* var. *dealbata* mediante el método espectrofotométrico de captura del radical libre DPPH•. Los extractos fueron obtenidos por maceración del material vegetal seco y triturado. La actividad antioxidante fue determinada a partir de la disminución de la absorbancia del DPPH• a 517 nm, utilizando ácido ascórbico como control positivo. Los resultados mostraron una inhibición dependiente de la concentración, obteniéndose valores de IC_{50} de $998{,}18 \pm 187\,\mu g/mL$ para EMC y $827{,}61 \pm 187\,\mu g/mL$ para EMF. Ambos extractos demostraron capacidad moderada de neutralización de radicales libres, siendo más activa la fracción del fruto. La actividad observada sugiere la presencia de compuestos fenólicos o flavonoides, lo que respalda el potencial bioactivo de esta especie y justifica futuras investigaciones fitoquímicas orientadas a su aplicación en el desarrollo de productos terapéuticos o nutracéuticos.

Palabras clave: *Vismia*, DPPH•, radical libre, antioxidante.

Abstract

The antioxidant capacity of methanolic extracts of *Vismia baccifera* var. *dealbata* bark (EMC) and fruit (EMF) was evaluated using the spectrophotometric method of free radical capture DPPH•. The extracts were obtained by maceration of the dried and crushed plant material. The antioxidant activity was determined from the decrease in DPPH• absorbance at 517 nm, using ascorbic acid as a positive control. The results showed a concentration-dependent inhibition, obtaining IC_{50} values of $998.18 \pm 187 \mu g/mL$ for EMC and $827.61 \pm 187 \mu g/mL$ for EMF. Both extracts demonstrated moderate free radical neutralization capacity, the fruit fraction being more active. The observed activity suggests the presence of phenolic compounds or flavonoids, which supports the bioactive potential of this species and justifies future phytochemical research aimed at its application in the development of therapeutic or nutraceutical products.

Keywords: *Vismia,* DPPH•*, free radical, antioxidant.*

1 Introducción

Existen múltiples reacciones bioquímicas que se llevan a cabo en organismos vivos, generando especies reactivas como los radicales libres, los cuales son capaces de dañar biomoléculas cruciales; estas especies son captadas por constituyentes celulares, pudiendo ocasionar diferentes patologías. No obstante, la acción de los radicales libres puede ser bloqueada por sustancias antioxidantes, las cuales depuran el organismo previniéndolo de enfermedades neurodegenerativas (Gerber y col., 2002), cardiovasculares (Kris-Etherton y col., 2002) y cancerígenas (Serafini y col., 2002).

Una de las áreas más relevantes en las ciencias de la salud es la búsqueda de nuevos antioxidantes naturales para el control de enfermedades que implican daño oxidativo; en este sentido, las sustancias provenientes de plantas

medicinales han demostrado ser una fuente importante de compuestos con marcada actividad antioxidante, permitiendo el crecimiento acelerado de investigaciones en esta área (Bergman y col., 2001).

El género *Vismia* no se escapa de ser objeto de estudio de posibles fuentes con poder antioxidante, ya que, se han reportado publicaciones acerca del tema, como lo fue la investigación sobre los frutos de *Vismia baccifera* var. *ferruginea* y *Vismia guiannesis* extraídos mediante percolación sucesiva con éter de petróleo, acetato de etilo y metanol, mostrando capacidad captadora de radicales frente al DPPH•, observándose la mayor actividad en el extracto de acetato de etilo seguido por el de éter de petróleo; estableciendo claramente a estos extractos como potenciales antioxidantes. Los extractos mostraron IC_{50} comprendidas entre 3,72 y 7,04 µg/mL. Esta actividad posiblemente esté asociada con las propiedades químicas de los metabolitos aislados, ya reportados en publicaciones anteriores, como los antranoides prenilados ferruginina A, γ-hidroxiferruginina y la antraquinona vismiaquinona A (Álvarez y col., 2008).

Así mismo, los extractos de las hojas *Vismia magnoliifolia* fueron probados frente a la especie radicalaria DPPH•, sustancia muy conveniente para el cribado de un gran número de muestras de diferente polaridad a causa de su alto rendimiento. La especie de *Vismia* en este ensayo no mostró la capacidad de los antioxidantes para secuestrar los radicales libres probablemente porque dentro de los metabolitos presentes en el extracto no existían especies capaces de donar hidrógeno a los radicales libres. (Elita y col., 2012).

En esta misma línea argumental, una investigación realizada por autores venezolanos en 2016, comparó extractos metanólicos de *Vismia baccifera* recolectada en Mérida y *Vismia macrophylla* del estado Táchira, evidenciando una alta presencia de antraquinonas en ambas especies, así como una fuerte actividad antioxidante particularmente en *V. macrophylla*, que alcanzó un valor de CI_{50} de 5,50 $\mu g/mL$ frente al radical DPPH•. Adicionalmente, se estableció una correlación directa entre el contenido total de fenoles y flavonoides y la capacidad de inhibición radicalaria, lo que refuerza la importancia del género como fuente potencial de antioxidantes naturales (Buitrago y col., 2016).

Además, estos investigadores evaluaron el posible efecto protector para extractos metanólicos de *Vismia baccifera* y *Vismia macrophylla* estableciendo un factor de protección solar medio de FPS 25,3 para *Vismia baccifera* y 20,7 para *Vismia macrophylla*, lo cual refuerza la relevancia de este género como fuente de metabolitos bioactivos de interés, tanto cosmético como farmacológico. (Buitrago y col., 2022).

En continuidad con estos estudios, uno de los más recientes en otras especies menos exploradas del género, es la *Vismia cayennensis*, cuyas frutas también han demostrado poseer un perfil fitoquímico complejo y bioactivo. En 2023, se reportó que los extractos crudos de fruta de *V. cayennensis* mostraron una significativa capacidad antioxidante frente al radical DPPH•, siendo el extracto de diclorometano (EDVcFr) el más activo y con mayor contenido de compuestos fenólicos totales. Estas contribuciones constituyen antecedentes fundamentales que sustentan la continuidad de estudios dirigidos a explorar nuevas especies y variedades del género *Vismia* (Lopes y col., 2023).

La presente investigación tiene como finalidad evaluar la capacidad antioxidante de extractos de corteza y frutos obtenidos de *Vismia baccifera* var. *dealbata* mediante el método de captura del radical libre DPPH•, utilizando el ácido ascórbico como control positivo. Estos resultados no solo permitirán establecer cuál de los extractos vegetales evaluados presenta mayor eficiencia antioxidante, sino que además aportará una orientación de futuras estrategias para el desarrollo de posibles fármacos antioxidantes.

2. Marco Teórico

2.1 Descripción botánica de la especie Vismia baccifera var. Dealbata

La especie *Vismia baccifera* es la más polimórfica del género. Las plantas características de esta especie, son árboles que se identifican por tener un tamaño comprendido entre 5 a 8 m de altura y de 5 a 10 cm de diámetro.

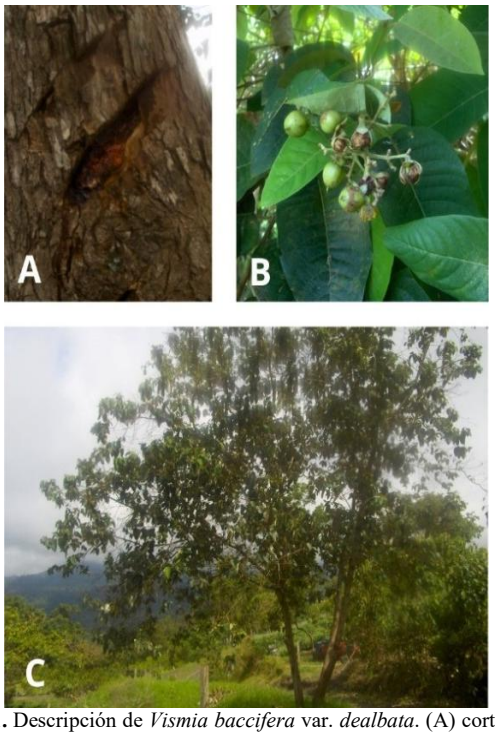

Figura 1. Descripción de *Vismia baccifera* var. *dealbata*. (A) corteza, (B) fruto y (C) árbol.
Description of *Vismia baccifera* var. *dealbata*. (A) bark, (B) fruit, and (C) tree.

El árbol típico de Latinoamérica es ampliamente de hoja ovalada y de peciolo largo, no es tan bifacial, con un color amarillo pálido o ceniza en la superficie inferior, una panícula difusa, cuyas ramas se extienden en ángulo recto con el raquis (Ewan, 1962).

La corteza externa es de color marrón-rojizo, los troncos están ramificados a baja altura y las ramas terminales son cilíndricas. Se observa un exudado anaranjado al desprenderse cualquier parte de la planta. El fruto es una cápsula globosa verde, que se torna marrón al madurar, exhibiendo restos del cáliz en la base y los remanentes de los estigmas en la punta. (Ewan, 1962); los mismos son pesados y de gran tamaño (12-13 mm de diámetro, 15-17 mm de largo). La subespecie *dealbata* posee una hoja llamativa, blanquecina en su superficie, ubicada al Norte de Venezuela y Colombia con las hojas fuertemente bicolor (Ewan, 1962) (Figura 1).

2.2.- Importancia de la actividad

El radical libre 2,2-difenil-1-picrilhidrazil (DPPH•) constituye una sonda espectrofotométrica altamente eficiente para la evaluación de la capacidad antioxidante de compuestos bioactivos. Su estructura paramagnética confiere un intenso color violeta, el cual se desvanece a medida que ocurre la reducción estequiométrica por especies donadoras de hidrógenos o electrones, principalmente fenoles y flavonoides, permitiendo cuantificar la actividad antirradicalaria mediante la disminución de la absorbancia a 517 nm. Este ensayo, ampliamente empleado en química de productos naturales, farmacognosia y ciencia de alimentos, permite estimar parámetros como el IC_{50} para comparar cuantitativamente la potencia antioxidante de diferentes sistemas.

Desde una perspectiva fisicoquímica, el método DPPH• es valorado por su simplicidad, bajo costo y elevada reproducibilidad, consolidándose como una herramienta preliminar robusta en la caracterización de matrices complejas. Si bien se trata de un modelo químico in vitro que no contempla todas las rutas mecanísticas involucradas en el estrés oxidativo *in vivo*, su uso sistemático permite inferir el potencial protector de sustancias frente a especies reactivas de oxígeno, siendo un paso inicial esencial en la validación de compuestos con posibles aplicaciones farmacológicas, nutracéuticas o cosméticas (Brand-Williams y col., 1995).

3. Procedimiento Experimental

3.1 Recolección del material biológico

El material botánico fue recolectado, la aldea San Juanito, parroquia Chiguará, municipio Sucre, altitud 1250 m.s.n.m. en Mérida, Venezuela. Una muestra fue depositada en el herbario de la Facultad de Farmacia y Bioanálisis de la Universidad de Los Andes (ULA), N° de voucher JR-21.

3.2 Obtención de extractos

El material botánico recolectado (frutos y corteza) se colocó en un horno con una rampa de calentamiento de 5 °C por minuto hasta 40 ºC para ser secado durante dos días. Posteriormente, se trituró y se colocó en una malla de nylon para realizar la extracción por maceración en metanol, durante cinco días para cada solvente, a temperatura ambiente. Los extractos obtenidos se concentraron en un rotavapor bajo presión reducida a una temperatura máxima de 50 ºC.

3.3 Evaluación antioxidante

3.3.1 Materiales y métodos

Tanto en el análisis cualitativo como en el cuantitativo se midió la capacidad secuestrante de radicales libres utilizando el test de 1,1-difenil-2-picrilhidrazil (DPPH•) en donde se aprovechan las propiedades cromáticas del radical, según el protocolo propuesto por Goupy y colaboradores en 1999 (Goupy y col., 1999). El equipo para medir la absorbancia de la mezcla de reacción fue un espectrofotómetro Genesys 5 Milton Roy® y celdas de vidrio Fisher Scientific®, así como un agitador de Vórtice Whirlimixer® y Micropipetas de 200 μL y 5 mL DiamondTM.

3.3.2 Sustancias a ensayar

En el ensayo cualitativo se evaluaron dos (02) concentrados, un extracto metanólico de corteza (EMC) y un extracto metanólico de fruto (EMF), ambos procedentes de la especie *Vismia baccifera* var. *dealbata*, junto con el testigo. El reactivo empleado fue 1,1-difenil-2-picrilhidrazil (DPPH•) perteneciente a la casa comercial Sigma®; se utilizó ácido ascórbico (Bayer®) como testigo y el solvente para todas las sustancias fue metanol grado analítico al 98% (Merck®).

3.3.3 Ensayo experimental

Tanto para la evaluación cualitativa como para la cuantitativa, se preparó una solución patrón de 0,6 *mM* del radical libre 1,1-difenil-2-picril-hidrazilo (DPPH•) en metanol grado analítico, la cual se almacenó a 0 ºC, en recipiente ámbar recubierto con papel aluminio para mayor protección contra la luz. Para efectos de esta evaluación se prepararon soluciones de 1 *mg/mL* de cada una de las sustancias a ensayar y la solución de trabajo de DPPH• se preparó diariamente a partir de la solución patrón almacenada con el volumen a usar a una concentración de 0,06 *mM* tal como lo establece el protocolo, así como la solución de ácido ascórbico a una concentración de 1 *mM*.

A los tubos de ensayo previamente estériles y rotulados se les añadió 200 μL de la solución a ensayar, luego a cada tubo se le adicionó 2,8 mL de la solución de DPPH$^{\bullet}$ incluyendo al testigo y el tubo de grupo control (tubo sólo con DPPH$^{\bullet}$); posteriormente, se agitaron en vórtice y se colocaron en la oscuridad por treinta (30) minutos.

Para la medición de las absorbancias a una longitud máxima de 517 nm, se ajustó el blanco de metanol a cero, luego se midió la absorbancia del DPPH$^{\bullet}$ que se encuentra reportada a 0,600 para esa concentración y luego la del ácido ascórbico que se localiza según el protocolo alrededor de 0,018; por último, se realizan las mediciones de todas las sustancias.

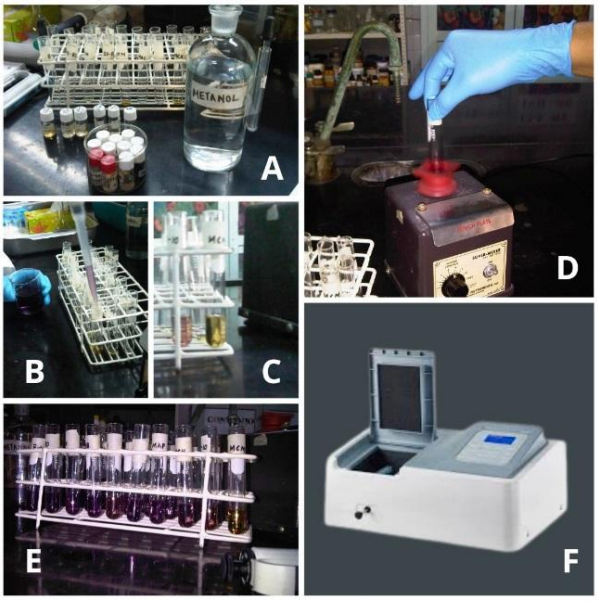

Figura 2. Descripción del proceso experimental de la actividad antioxidante. (A) rotulado, (B) muestra, (C) DPPH$^{\bullet}$, (D) agitación, (E) tiempo de reacción y (F) equipo de medición.
Description of the experimental process for antioxidant activity. (A) labeling, (B) sample, (C) DPPH•, (D) stirring, (E) reaction time, and (F) measuring equipment.

La evaluación cuantitativa se realizó a diferentes concentraciones (1200, 1100, 1000, 900, 800, 700, $\mu g/mL$) con el objetivo de calcular los porcentajes de inhibición para cada una de las concentraciones, y determinar el índice de inhibición medio (IC_{50}) o la concentración en la cual el porcentaje de reducción del radical es del 50 %; las determinaciones se llevaron a cabo por triplicado. El esquema de este ensayo se resume en la Figura 2.

4. Discusión y Resultados

El método utilizado en este ensayo se basó en la reducción de la absorbancia de la solución en metanol de DPPH$^{\bullet}$ en presencia de las sustancias extraídas de *Vismia baccifera* var. *dealbata*, quienes de ser o poseer sustancias capaces de donar hidrógeno y generar la forma no radicalaria DPPH-H, se considerarían sustancias con actividad antioxidante. La Tabla 1 muestra los cambios en absorbancia por triplicado, de cada una de las sustancias evaluadas a 1000 $\mu g/mL$, así como también el porcentaje de capacidad secuestrante de radicales libres promedio, junto con su desviación estándar.

Tal como muestra la Tabla 1, las sustancias que corresponden a los extractos metanólicos de corteza y fruto, exhiben actividad antioxidante difícil de predecir, debido a que la misma podría estar constituida por las actividades individuales de cada uno de los compuestos presentes en dicho extracto o inhibida bajo el mismo concepto. Los compuestos proporcionan sus efectos antioxidantes, a través de diferentes mecanismos tales como la captación de radicales, la actividad quelante de metales, la inhibición de lípidos, peroxidación o enfriamiento rápido de oxígeno singlete (Bergman y col., 2001).

Tabla 1. Determinación de la CSRL para las sustancias obtenidas de *Vismia baccifera* var. *dealbata* a 1000 $\mu g/mL$.
Determination of the CSRL for substances obtained from *Vismia baccifera* var. *dealbata* at 1000 $\mu g/mL$.

Determinación de la Capacidad Secuestrante de Radicales Libres, CSRL			
Muestra	**Absorbancia (a 30 minutos)**	**CSRL (%)**	**($CSRL_{Promedio}\pm\sigma$) %**
EMC	0,161	67,54	67,74 ± 0,20
	0,159	67,94	
	0,160	67,74	
EMF	0,247	50,20	51,07 ± 0,81
	0,239	51,81	
	0,242	51,20	
Ácido Ascórbico ®	0,018	96,37	96,37 ± 0
	0,018	96,37	
	0,018	96,37	
DPPH$^{\bullet}$	0,496	-	-

Extracto Metanólico de Corteza (EMC)
Extracto Metanólico de Frutos (EMF)
1,1-difenil-2-picrilhidrazil (DPPH$^{\bullet}$)

Los resultados usando este ensayo, mostraron una propiedad antioxidante en los extractos metanólicos tanto de corteza como de frutos a la concentración bajo estudio, cerca del 50 %, por lo que se procedió a medir la absorbancia a concentraciones superiores e inferiores a 1000 $\mu g/mL$, para realizar un estudio de porcentaje de reducción de la especie DPPH$^{\bullet}$ en función de la concentración de ambos extractos obtenidos de la especie de *Vismia* y así determinar gráficamente la concentración en $\mu g/mL$ de la muestra requerida para inhibir la formación de radicales DPPH$^{\bullet}$ en un 50 %. En la Tabla 2, se registran las absorbancias por triplicado de los extractos metanólicos a diferentes concentraciones, así como también, el porcentaje de capacidad secuestrante de radicales libres promedio junto con su desviación estándar para los mencionados extractos.

Los compuestos presentes en los extractos estudiados fueron buenos donantes de electrones, y según lo expuesto por el protocolo, son capaces de terminar la reacción en

cadena por radicales mediante la conversión en productos más estables. De la Tabla 02 se deduce que mientras la concentración va en aumento el porcentaje de reducción es mayor. La Figura 3 muestra los porcentajes de reducción del radical DPPH• a diferentes concentraciones donde los puntos describen una trayectoria lineal con pendiente positiva y donde se consiguió determinar gráficamente la concentración a la cual los extractos inhiben la formación de radicales en un 50 %.

La Tabla 3 reúne los datos obtenidos del análisis de regresión lineal del estudio de las rectas visualizadas en la Figura 3 en donde se determinó a través de una extrapolación al eje X de concentraciones, que la magnitud a la cual el extracto metanólico de corteza y el extracto metanólico de frutos es capaz de inhibir el 50 % de los radicales DPPH• es (998,18±187) *µg/mL* y (827,61±187) *µg/mL* respectivamente, concentraciones superiores a las reportadas para el extracto metanólico de *Vismia guianensis*. (Álvarez y col., 2008) las cuales superan considerablemente al testigo, Ácido ascórbico®.

Tabla 2. Determinación de la CSRL para EMC y EMF de *Vismia baccifera* var. *dealbata* a diferentes concentraciones (*µg/mL*).
Determination of CSRL for EMC and EMF of *Vismia baccifera* var. *dealbata* at different concentrations (*µg/mL*).

Cantidad (*µg/mL*)	Absorbancia EMF	Absorbancia EMC	CSRL % EMF	CSRL % EMC	($CSRL_{Promed}$±σ) % EMF	($CSRL_{Promed}$±σ) % EMC
1200	0,199	0,091	59,87	81,65	61,09±1,22	82,53±1,18
	0,187	0,089	62,30	82,06		
	0,193	0,080	61,09	83,87		
1100	0,201	0,117	59,47	76,41	58,33±1,03	77,21±0,92
	0,211	0,114	57,46	77,01		
	0,208	0,108	58,06	78,22		
1000	0,251	0,162	49,40	67,34	49,73±0,38	67,74±0,40
	0,250	0,158	49,60	68,15		
	0,247	0,160	50,20	67,74		
900	0,291	0,199	41,33	59,87	42,27±1,02	61,09±1,21
	0,287	0,187	42,14	62,30		
	0,281	0,193	43,35	61,09		
800	0,309	0,241	37,70	51,41	39,96±0,95	50,26±2,2
	0,311	0,259	37,30	47,78		
	0,318	0,249	35,89	51,61		
700	0,352	0,311	29,03	37,30	27,75±1,22	37,03±1,22
	0,364	0,307	26,61	38,10		
	0,359	0,319	27,62	35,69		
Ácido Ascórbico ®	0,018		96,37		96,37±0	
	0,018		96,37			
	0,018		96,37			
DPPH•	0,496		-		-	

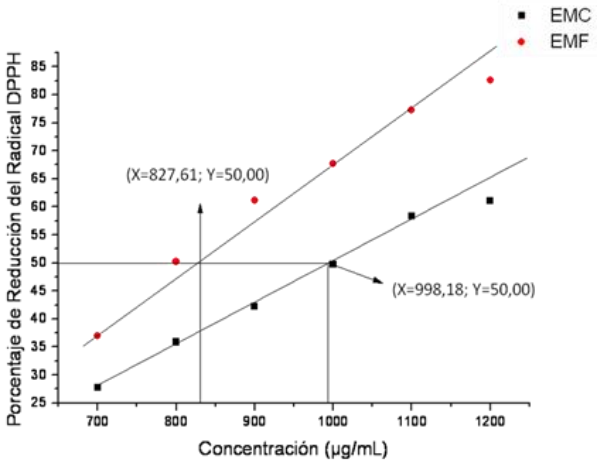

Figura 3. Determinación del porcentaje de reducción medio del DPPH• (IC50) para EMC y EMF.
Determination of the average percentage reduction of DPPH• (IC50) for EMC and EMF.

Las plantas que poseen propiedades antioxidantes y otras propiedades farmacológicas, comúnmente se les relaciona con la presencia de compuestos fenólicos, especialmente ácidos fenólicos y flavonoides (Fabri y col., 2009). Aunque dentro del género *Vismia* aún no se han reportado ácidos fenólicos, si se han reportado compuestos polifenólicos como gutiferonas, antranoides prenilados, algunas antraquinonas e incluso flavonoides (Vizcaya y col., 2012).

La actividad antioxidante de los polifenoles fue atribuida a sus propiedades redox, que les permiten actuar como agentes reductores, donadores de hidrógeno y oxígeno singlete, así como sus capacidades de metales quelantes (Vladimir-Knezevic y col., 2011). La mayoría de los investigadores en el área de la fitoquímica asociada al campo de reacciones con radicales libre, manifiestan que, si una muestra exhibe una elevada actividad con un método, probablemente no muestre resultados similares con métodos desiguales; por lo que es esencial evaluar muestras con precisión por varios procedimientos que incluyan diferentes especies radicalarias. (Goupy y col., 1999).

Tabla 3. Datos obtenidos del análisis de regresión lineal en la determinación gráfica del porcentaje de reducción medio del DPPH• (IC_{50}) para EMC y EMF.
Data obtained from the linear regression analysis in the graphical determination of the average percentage reduction of DPPH• (IC50) for EMC and EMF.

Regresión Lineal	EMC	EMF
Punto de Corte	-22,86 %	-15,71 %
Pendiente	0,09 (%/$\mu g x mL^{-1}$)	0,07 (%/$\mu g x mL^{-1}$)
Dispersión	0,99	0,98
(σ x)	187 (%/$\mu g x mL^{-1}$)	187 (%/$\mu g x mL^{-1}$)
(σ y)	17 %	12,45 %
Ec. de Línea Recta	Y= -22,86+0,09X	Y= -15,71+0,07X
IC_{50}	998,18	827,61
(IC_{50} ± σ) *µg/mL*	998,18±187	827,61±187

(σ X) = Desviación estándar para valores de X en µg/mL
(σ Y)= Desviación estándar para valores de Y en %.

Cabe destacar que la evaluación realizada, establece una contribución importante en la búsqueda de metabolitos secundarios para retardar o prevenir la oxidación de otras moléculas, inhibiendo la producción de radicales libres que comienzan reacciones en cadenas, ya que para la fecha se han reportado escasas investigaciones de actividad antioxidante de la especie bajo estudio, por lo que representa un aporte significativo tanto en fitoquímica, como en el área de la salud y de prevención de enfermedades.

5. Conclusiones

Los extractos metanólicos obtenidos de la corteza y los frutos de *Vismia baccifera* var. *dealbata* demostraron actividad antioxidante frente al radical libre DPPH•, con valores de IC_{50} de 998,18±187 *µg/mL* y 827,61 ±187 *µg/mL*, respectivamente. Estos resultados indican que ambas fracciones poseen capacidad de neutralización de radicales libres, siendo más pronunciada en el extracto proveniente del fruto.

Aunque la potencia antioxidante observada es moderada en comparación con estándares de referencia como el ácido ascórbico, los hallazgos respaldan el potencial bioactivo de esta variedad vegetal, y sugieren la presencia de compuestos fenólicos o flavonoides con efecto antioxidante.

Este estudio aporta evidencia inicial sobre la bioactividad de *Vismia baccifera* var. *dealbata*, abriendo nuevas posibilidades para su caracterización fitoquímica detallada y su eventual aplicación en formulaciones fitoterapéuticas, nutracéuticas o cosméticas orientadas a la mitigación del estrés oxidativo.

Agradecimientos

Los autores expresan su agradecimiento por la colaboración a la Dra. Claudia Plaza del Instituto de Investigaciones de la Facultad de Farmacia y Bioanálisis de la Universidad de Los Andes por su apoyo en el suministro de los reactivos necesarios para la evaluación antioxidante. Así como también, a la Dra. Lorena Díaz de Torres, profesora de Química Medicinal de la Facultad de Farmacia y Bioanálisis de la Universidad de Los Andes, por la supervisión del análisis cualitativo de este trabajo. Y, por último, se agradece de manera especial a la MSc. Tibisay Ramírez especialista en gestión ambiental y profesora Asistente de la cátedra de Química ambiental, por su colaboración en la evaluación cuantitativa realizada en el Laboratorio de Fitoquímica del decanato de Investigación de la Universidad Nacional Experimental del Táchira (UNET).

Referencias

Álvarez, E., Jiménez, O., Posada, C., Rojano, B., Gil, J., García, C., Durango, D. (2008). Actividad Antioxidante y contenido fenólico de los extractos provenientes de las bayas de dos especies del género Vismia (Guttiferae). VITAE. Revista de la Facultad de química farmacéutica de la Universidad de Antioquía Medellín- Colombia, Vol. 15, pp. 165-172.

Bergman, M., Varshavsky, L., Gottlieb, HE., Grossman, S., (2001). The antioxidant activity of total anthocyanins from Perilla pankinensis decne. Journal of Etnopharmacology. Vol. 58, pp. 143-152.

Brand-Williams, W., Cuvelier, M.E., Berset, C., (1995), Use of a free radical method to evaluate antioxidant activity, LWT - Food Science and Technology, Vol. 28(1), pp. 25-30.

Buitrago, A., Rojas-Vera, J., Peñaloza, Y., (2016). *In vitro* antioxidant activity and qualitative phytochemical analysis of two *Vismia* (Hypericaceae) species collected in Los Andes, Venezuela, Revista de Biología Tropical, Vol. 64(4), pp. 1431-1439.

Buitrago-Díaz, A., Rojas-Vera, J., Torres-Barajas, L., (2022). Antioxidant activity and solar protection factor of two *Vismia* species colleted from Venezuelan Andes, Revista Ciencia e Ingeniería, Vol. 43(1), pp. 33-40.

Elita, S., Renata, F., Mendes, E., Motta, P., Bellozi, D., Aragão, J., Rodrigo, L., Jussara, R., Isabel, V., Bouzada, M. (2012). Antimicrobial and Antioxidant Activities of Some Plant Extracts. Phytochemicals as Nutraceuticals Global Approaches to Their Role in Nutrition and Health. Chapter 2. Editorial Venketeshwer Rao, pp. 22-42.

Ewan, J. (1962). The South American Species of *Vismia* (Guttiferae). U.S. Nat. Museum, Contribution from de National Herbarium Vol. 35, pp. 293-361.

Fabri, R., Nogueira, M., Braga, F., Coimbra, E., Scio E., (2009). Mitracarpus frigidus Aerial Parts Exhibited potent Antimicrobial, Antileismanial and Antioxidant Effects. Bioresource Technology, Vol. 100(1), pp. 428-433.

Gerber, M., Boutron-Ruault, M., Hercberg, S., Riboli, E., Scalbert, A., Siess, M., (2002). Food Cancer: State of the art about the protective effect of fruits and vegetables. Bulletin du Cancer, Vol. 89, pp. 293-312.

Goupy, P., Hugues, M., Boivin, P., Amiot, M.J., (1999). Antioxidant composition and activity of barley (Hordeumvulgare) and malt extracts and of isolated phenoliccompounds. Journal of the science of food and agriculture, Vol. 79, pp. 1625-1634.

Kris-Etherton, P., Hecker, K., Bonanome, A., Coval, S., Binkoski, A., Hilpert, K., Griel, A., Etherton, T., (2002). Bioactive Compounds in Foods: Their Role in the Prevention of Cardiovascular Disease and Cancer. The American Journal of Medicine, Vol. 113(9), pp. 71-88.

Lopes, A., Paes, W., De Araujo Becerra, J., Mar, J., Sanches, E., Maia, P., Corrêa, G., Carmo, D., (**2023**), Chemical constituents and antioxidant capacity of fruit extracts from Vismia cayennensis, Revista Observatorio de la Economia Latinoamericana, Vol. 21(3), pp. 1482-1500.

Serafini, M., Belloco, R., Wolk, A., Ekstrom, AM., (2002). Total antioxidant potential of fruit and vegetables and risk of gastric cancer. Gastroenterology, Vol. 123, pp. 985-991.

Vizcaya, M., Morales, A., Rojas, J., Nuñez, R., (2012). Revisión bibliográfica sobre la composición química y actividades farmacológicas del género *Vismia* (Guttiferae). Boletín Latinoamericano y del Caribe de Plantas Medicinales y Aromáticas, Vol. 11(1), pp. 12-34.

Vladimir-Knezević, S., Blazeković, B., Stefan, M.B., Alegro, A., Koszegi, T., Petrik, J., (2011). Antioxidant Activities and Polyphenolic Contents of Three Selected Micromeria Species from Croatia. Molecules, Vol. 16(2), pp. 1454-1470.

Received: *March 15th,2025*

Accepted: *July 22th, 2025*

Vizcaya, Marietta: *Ph.D. en Química de Medicamentos 2014, Instituto de Investigaciones Científicas, Facultad de Farmacia y Bioanálisis, ULA. Profesora del Lab. de Polímeros, Facultad de Ciencias ULA. Mérida-Venezuela.*
https://orcid.org/ 0000-0002-2064-4175

Pérez, Patricia: *Ph.D. en Química de Medicamentos 2017, Instituto de Investigaciones Científicas, Facultad de Farmacia y Bioanálisis, ULA. Profesora del Lab. de Polímeros, Facultad de Ciencias ULA. Mérida-Venezuela. Correo electrónico: patriciap@ula.ve*
https://orcid.org/ 0000-0003-0591-2351

Rodríguez Sulbarán, Pedro: *Ph.D. en Química Aplicada, mención Estudio de Materiales, 2016, Universidad de los Andes. Estudiante de Doctorado en la Universidad de Concepción, Facultad de Ciencias Químicas, Edmundo Larenas 129, Casilla 160C, Chile. Correo electrónico: pedrojrs@gmail.com*
https://orcid.org/0000-0002-1309-8532

Lugo González, Claudio Antonio: *Ph.D. en Química Aplicada, mención Estudio de Materiales, 2017, Universidad de los Andes. Profesor del Departamento de Química (Laboratorio de Cinética y Catálisis) de la Facultad de Ciencias, ULA. Mérida, Venezuela. Correo electrónico: claudiolugo@ula.ve*
https://orcid.org/0000-0001-8003-0354

Plaza, Claudia: *Ph.D. en Química de Medicamentos 2015, Instituto de Investigaciones Científicas, Facultad de Farmacia y Bioanálisis, ULA. Investigadora del Instituto de Investigaciones Científicas, Facultad de Farmacia y Bioanálisis. Mérida-Venezuela.*
https://orcid.org/ 0009-0007-8887-9388

Artículo de Investigación. Revista Ciencia e Ingeniería. Vol. 46, No. 3 pp. 303-312, agosto-noviembre, 2025.
ISSN 1316-7081. ISSN Elect. 2244-8780 Universidad de los Andes (ULA)

Syngas production and greenhouse gas mitigation using Fe/Ni bimetallic perovskite catalysts in methane dry reforming

Producción de gas de síntesis y mitigación de gases de efecto invernadero mediante catalizadores tipo perovskita Fe/Ni en el reformado seco de metano

Lugo, Claudio[1]*; Guerrero, Maryuri[1]; Fereira, Carla[1]; Petit, Eliel[1]; Torres, Ruben[1]; Vizcaya, Marietta[2]; Pérez, Patricia[2]; Rondón, Jairo[3]

[1]Laboratorio de Cinética y Catálisis, Departamento de Química, Facultad de Ciencias, Universidad de Los Andes, Mérida, Venezuela.
[2]Laboratorio de Polímeros, Departamento de Química, Facultad de Ciencias, Universidad de Los Andes, Mérida, Venezuela.
[3]Biomedical & Chemical Engineering Departments, Universidad Politécnica de Puerto Rico, San Juan, Puerto Rico, USA.

**claudiolugo@ula.ve*

Abstract

In this investigation, mixed oxides of the perovskite type with formula $Ba_{0,3}Sr_{0,7}Ni_{1-x}Fe_xO_3$ (x = 0,0-0,3-0,5-0,7-1,0) were synthesized via solution combustion, SCS, in the presence of microwave radiation. The oxides were characterized by Fourier transform infrared spectroscopy, FTIR, and X-ray diffraction, XRD. The spectroscopic study shows distinctive signals of M-O interactions at low wavelengths. X-ray diffraction allowed the identification of the primary phase present, an orthorhombic perovskite (space group: Pnma) of the $LaFe_{0.6}Ni_{0.4}O_3$ type, formed during the combustion of glycine; this technique allowed the calculation of the size of the crystalline domain, with values below 20 nm for all perovskites. The catalytic performance for the dry reforming reaction of methane with perovskites as catalysts shows good thermal stability and resistance to sintering and deactivation by carbon deposition. The perovskites with the highest average methane conversion were NiFe-MG3 and NiFe-MG4 with 87,54 and 61,14 % hydrocarbon conversion, respectively.

Keywords: *Perovskites, mixed oxides, methane reforming, greenhouse gases.*

Resumen

En esta investigación se sintetizaron óxidos mixtos tipo perovskitas de fórmula $Ba_{0,3}Sr_{0,7}Ni_{1-x}Fe_xO_3$ (x = 0,0-0,3-0,5-0,7-1,0) vía combustión en solución, SCS, en presencia de radiación microondas. Los óxidos se caracterizaron a partir de la espectroscopia infrarroja con transformada de Fourier, FTIR y la difracción de rayos x, DRX. El estudio espectroscópico muestra señales distintivas de las interacciones M-O a longitudes de onda bajas. La difracción de rayos x permitió identificar como fase principal presente, una perovskita ortorrómbica (grupo espacial: Pnma) tipo $LaFe_{0,6}Ni_{0,4}O_3$, formada durante la combustión de la glicina; esta técnica permitió calcular el tamaño del dominio cristalino, con valores por debajo de los 20 nm para todas las perovskitas. El performance catalítico para la reacción de reformado seco de metano con las perovskitas como catalizadores de la reacción, muestra buena estabilidad térmica y resistencia a la sinterización y desactivación por deposición de carbono. Las Perovskitas con mayor conversión promedio de metano fueron NiFe-MG3 y NiFe-MG4 con un 87,54 y 61,14 % de conversión del hidrocarburo respectivamente.

Palabras clave*: Perovskitas, óxidos mixtos, reformado de metano, gases de invernadero.*

1 Introduction

Since the Industrial Revolution in the mid-18th century, humanity has undergone profound transformations in economic, social, cultural, and technological spheres, leading to changes in the number, type, and distribution of living species. This is mainly due to the exploitation of natural resources, indiscriminate soil plowing, and pollution of the atmosphere, seas, and oceans, all contributing to the progressive deterioration of planet Earth (Kammer et al., 2001; Arevalo, 2019).

In recent years, mixed oxides have been studied for use as heterogeneous catalysts in industrial processes. Their popularity is growing due to significant advantages over other types of catalysts, such as lower energy consumption and reduced harmful environmental effects. Various methods have been developed for their preparation based on their crystallographic (surface-to-volume ratio) and

electronic properties relevant to catalysis. Among them, solution combustion synthesis (SCS) stands out as a rapid technique that does not require expensive equipment and starts from metal precursor salts (Civera et al., 2003; Specchia et al., 2004; Wang et al., 2009; García et al., 2010; Pérez et al., 2015; Lugo et al., 2010-2022-2024.a).

Certain mixed oxides, such as perovskites, exhibit ideal properties for use as catalysts in heterogeneous processes like methane reforming. SCS enables the synthesis of nanoparticles with unique properties compared to their bulk counterparts. These materials also promote the formation of synthesis gas (a mixture of CO and H_2) while minimizing coke deposition, one of the leading causes of active site deactivation in catalysts (Lugo et al., 2010).

Part of the produced synthesis gas (syngas) is used for electricity generation, particularly through Integrated Gasification Combined Cycle (IGCC) technology. Although syngas can be derived from almost any carbon-rich source, such as oil, coal, biomass, or organic waste, natural gas is the primary feedstock for syngas production. Moreover, the abundance of this raw material makes methane reforming a feasible process for obtaining syngas (Edwards et al., 1995; Cabrera et al., 2012).

Natural gas (an abundant resource in Venezuela) is primarily a mixture of gases, with methane accounting for 75% to 95% of the total volume. Other components include ethane, propane, butane, nitrogen, carbon dioxide, hydrogen sulfide, helium, and argon (Wang et al., 2009). Venezuela holds the tenth-largest proven natural gas reserves globally (~5.67 trillion cubic meters), much of which is associated gas (C.I.A., 2021).

The average composition of Venezuelan natural gas is approximately 82% methane (CH_4), 10% ethane (C_2H_6), 3.7% propane (C_3H_8), and 0.2% carbon dioxide (CO_2). The final product is mainly methane, with a small fraction of ethane. Much of this methane is flared and released into the atmosphere, leading to economic losses for the nation and negative environmental impacts (García, 2012).

Supported catalysts based on transition metals as the active phase (metal oxide or metal) can form a dispersed phase on a high-surface-area support, which enhances catalytic activity and stability. Metals, metal oxides, metal sulfides, organometallic complexes, and enzymes can be supported on inorganic solids such as metal oxides, zeolites (aluminosilicates), or clays. In these catalysts, the active phase typically appears as nanometer-sized crystals (10^{-9} m = 1 *nm*). Additionally, a wide range of metal oxide-based catalysts is available for various commercial processes (Martín et al., 2021).

This work prepared bimetallic perovskites (Fe/Ni) using solution combustion synthesis (SCS). The solids were characterized by Fourier-transform infrared spectroscopy (FTIR) and X-ray diffraction (XRD). Catalytic testing was performed by coupling a gas chromatograph (GC) to the reaction system. The perovskites were used as catalysts for the dry reforming of methane (DRM), and the results demonstrate that these materials (perovskite oxides) are suitable for this type of reaction due to their high thermal stability and hydrocarbon activation capability.

2 Experimental procedure

2.1 Synthesis of perovskites

The mixed oxides were prepared using solution combustion synthesis (SCS), as described by Patil (Patil et al., 1997–2002), Mukasyan (Mukasyan et al., 2001–2007), and Varma (Varma et al., 2003), and verified at the Kinetics and Catalysis Laboratory of the Universidad de Los Andes by Pérez (Pérez et al., 2015), Briceño (Briceño et al., 2020), and Lugo (Lugo et al., 2010–2017–2022–2024a–2024b).

2.1.1 Synthesis methodology

Once the precursor mixture was prepared, it was placed in a modified porcelain crucible with a lid to allow the release of gases produced during fuel combustion. The crucible was then placed in a domestic microwave oven (Premium brand, model PM7078, 700W power), and radiation was applied at 80% of maximum power (Zhao et al., 2004).

Combustion of the precursor mixture occurred after 35 seconds of irradiation. It continued for approximately 15 more seconds, during which violent flames and a large amount of gas were generated due to the ionization of gases accumulated inside the ceramic trap, further increasing the temperature inside the crucible. The total irradiation time of the precursor mixture was approximately 95 seconds. At the end of the process, a fine grayish powder was obtained, corresponding to the perovskite-type mixed oxide.

2.1.2 Stoichiometry

The different perovskites synthesized via SCS are shown in Table 1. Additionally, the starting material, gel formation, and the solid synthesized with and without maceration-obtained after the combustion of the precursor mixture-can be observed in Figure 1.

Table 1. Perovskite-type compounds $Ba_{0,3}Sr_{0,7}Ni_{1-x}Fe_xO_3$ (x= 0,0-0,3-0,5-0,7-1,0) synthesized via SCS.

Formula (ABO_3)	Ignition	Code
$Ba_{0,3}Sr_{0,7}FeO_3$	Microwave	Fe-MG-1
$Ba_{0,3}Sr_{0,7}Ni_{0,3}Fe_{0,7}O_3$		NiFe-MG-2
$Ba_{0,3}Sr_{0,7}Ni_{0,5}Fe_{0,5}O_3$		NiFe-MG-3
$Ba_{0,3}Sr_{0,7}Ni_{0,7}Fe_{0,3}O_3$		NiFe-MG-4
$Ba_{0,3}Sr_{0,7}NiO_3$		Ni-MG-5

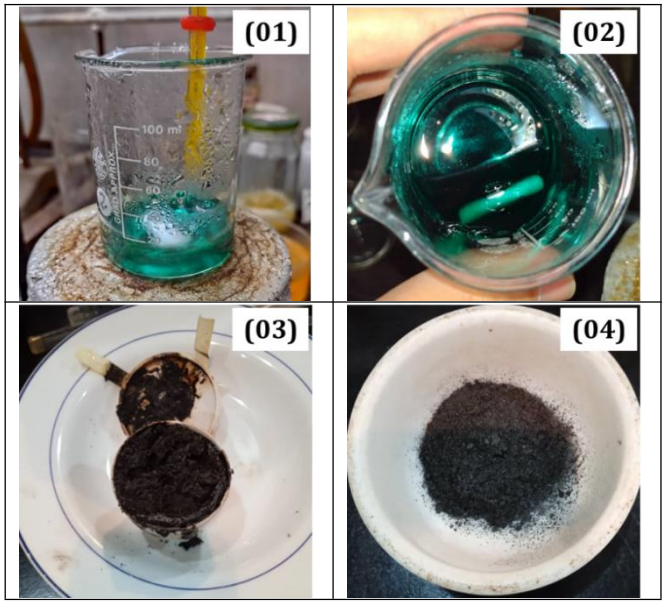

Figure 1. SCS synthesis of *Perovskites*: 1.- Start of SCS, 2.- Gel formation (before irradiation), 3.- Product after microwave irradiation, MO, and 4.- Maceration.

2.2 Characterization

The synthesized materials were characterized by:

1. Fourier-transform infrared spectroscopy (FTIR), using a Perkin Elmer Frontier FTIR Spectrophotometer, and

2. X-ray diffraction (XRD) in powder form, using a Bruker D8 Advance diffractometer with Cu Kα radiation (wavelength 1.5406 Å), operating at 40 kV and 40 mA. Data were recorded in the 2θ range of 2°–70°, with a step time of 0.6 s and a step size of 0.02035°.

3. Results and discussion

3.1 Fourier-transform infrared spectroscopy (FTIR)

The infrared spectra of the perovskites of the type $Ba_{0,3}Sr_{0,7}Ni_{1-x}Fe_xO_3$ (x = 0,0-0,3-0,5-0,7-1,0), synthesized via SCS, are shown in Figure 2. Table 2 presents the band assignments of the infrared spectrum for the synthesized solids. The band at 3401.5 cm^{-1} corresponds to symmetric and asymmetric stretching vibrations of the O–H group, related to water molecules coordinated in the solids, originating from the synthesis process (Ramos et al., 2015; Neira et al., 2016). At 2925 and 2854 cm^{-1}, two low-intensity peaks are observed, attributed to the $–CH_2–C=O$ stretching vibrations with sp^3 hybridization, resulting from excess fuel during synthesis (Wade, 2004). The signal around 1625.7 cm^{-1} is due to an asymmetric deformation of the carboxylate ion (COO^-), a species formed during synthesis (Hernández et al., 2006). A band near 1450.8 cm^{-1} is associated with asymmetric stretching vibrations of nitrate groups (NO_3^-) from the synthesis and/or atmospheric carbonate (CO_3^{2-}) absorption (Darroudia et al., 2016; Song et al., 2016).

The peak at approximately 1384 cm^{-1} corresponds to symmetric stretching vibration of the N–O bond (NO_2 type species), associated with bidentate coordination compounds (Rendón et al., 2006). The signal at 1091.6 cm^{-1} is attributed to in-plane bending modes of the C–O bond, associated with acetals and saturated primary aliphatic alcohols. The band at 1024.5 cm^{-1} results from out-of-plane bending of the C–H bond, present in all precursors, and provides information about the NH_4OH added during synthesis to adjust the pH (Gómez, 2010).

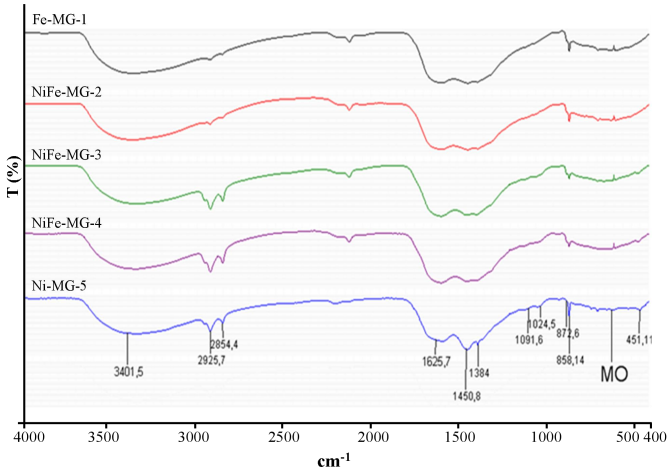

Figure 2. FTIR spectra of the synthesized perovskite-type (Fe/Ni) oxides.

There is a region known as the *fingerprint region* of metal–oxygen (M–O) interactions (at lower wavelengths), where characteristic signals of the vibrational modes permitted for metals and non-metals (Fe^{2+}, Ni^{2+}, Sr^{2+}, and Ba^{2+}) can be observed, involving OH groups and oxygen atoms bonded to these metals (O–M–O) (Anacona et al., 2013).

At 872.6 cm^{-1}, a peak appears corresponding to the bending vibration of the Sr–O bond in an octahedral site (Sithole et al., 2017; Briceño et al., 2020). Near 858.14 cm^{-1}, a band is associated with stretching vibrations of the Ba–O bond (Villaquirán et al., 2015). The signal at 640 cm^{-1} is attributed to the characteristic stretching vibration of the Sr–O bond (Harish et al., 2017). The peak around 630 cm^{-1} may be associated with vibrations of the face-centered cubic Ni–O phase (Liu et al., 2013).

Near 600 cm^{-1}, bending vibrations of the Fe–O bond are observed, corresponding to the MO_6 octahedral structure. The intensity of this signal decreases as the degree of iron substitution increases (Haye et al., 2017).

Table 2. Band assignments of FTIR spectra for (Fe/Ni) perovskites.

ν (Ref.) cm^{-1}	ν (cm^{-1})	Bond	Assignment
3440	3401,5	O–H	Symmetric and asymmetric stretching vibrations of the O–H group.
3050-2870	2925-2854	CH_2–C=O	–CH_2–C=O stretching vibrations.
1650-30	1625,7	COO–M	Asymmetric deformation of the carboxylate ion (COO^-–M).
1470-40	1450,8	N–O/C–O	Asymmetric stretching vibrations of nitrate (NO_3^-) and/or carbonate (CO_3^{2-}) groups.
1384	1384	N–O	Symmetric stretching of NO_2 (N–O bond).
1040	1091,6	C–O	In-plane bending modes of the C–O bond.
1025	1024,5	C–H	Out-of-plane bending of the C–H bond.
Metal–Oxygen Interactions			
862	872,6	Sr–O	Bending vibrations of the Sr–O bond in an octahedral site.
864	858,14	Ba–O	Stretching vibration of the Ba–O bond.
660	~640	Sr–O	Stretching vibration of the Sr–O bond.
660	~630	Ni–O	Ni–O bond vibrations in a face-centered cubic structure.
558	~600	Fe–O	Bending vibrations of the Fe–O bond in the MO_6 octahedral structure.
470	~451	Ni–O	Ni–O bond vibration.

Finally, the peak at 451 cm^{-1}, located at a low wavenumber, is attributed to asymmetric vibrations of the Ni–O bond (Rahdar et al., 2015).

3.2 X-ray diffraction (XRD)

Figure 3 shows the XRD patterns of the perovskites $Ba_{0,3}Sr_{0,7}Ni_{1-x}Fe_xO_3$ (x = 0,0 - 0,3 - 0,5 - 0,7 - 1,0). Phase identification of the synthesized materials was carried out using the X'Pert HighScore Plus 2.1 software with the PDF2-2004 database from the ICDD.

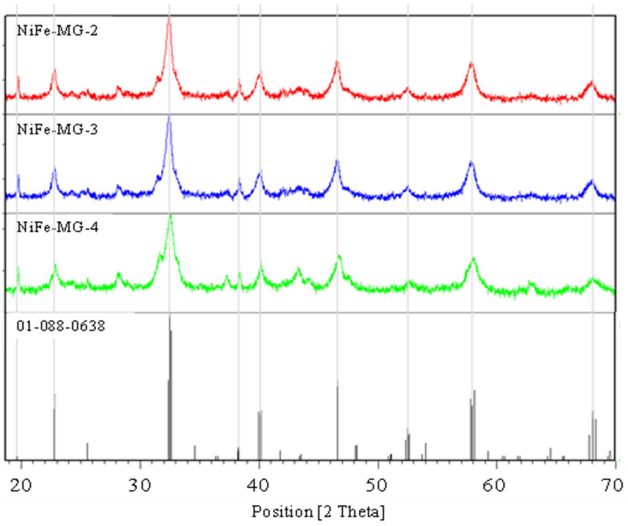

Figure 3. X-ray diffraction patterns of the $Ba_{0,3}Sr_{0,7}Ni_{1-x}Fe_xO_3$.perovskites. Reference: 01-070-1333 (perovskite La_2NiO_4).

The presence of an orthorhombic perovskite-type phase (space group: Pnma), specifically lanthanum iron-nickel oxide, $LaFe_{0,6}Ni_{0,4}O_3$, was identified, matching the reference card 01-088-0638 (Falcon et al., 1990).

The formation of the perovskite phase is favored in the prepared solids due to the extremely high temperatures reached during the combustion process, which promotes the crystallization of the perovskite phase (Pérez et al., 2015).

3.2.1 Crystallite size calculation

The crystallite size of the synthesized oxides was calculated using the Scherrer equation (Eq. 01) (Langford et al., 1978).

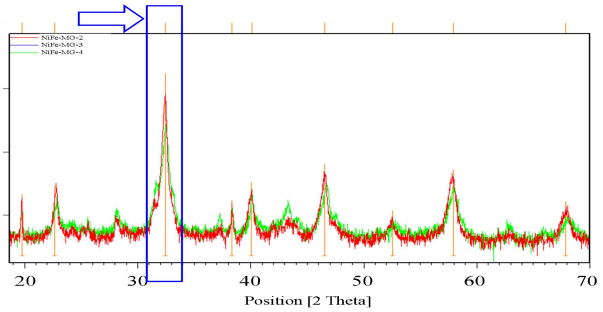

Figure 4. Diffraction pattern showing the hkl (103) line used to calculate the crystallite domain size of the perovskite.

$$\beta = \frac{(0.89).\lambda}{FWHM_{(S)}.(cos\,2\theta)} \qquad \text{(Eq. 01)}$$

β = crystallite domain size.
λ = wavelength of the radiation used (λ_Cu) in nm.
FWHM(S) = full width at half maximum of the diffraction peak at angle θ.

$$FWHM(S) = \frac{SF\ x\ A}{l} \qquad \text{(Eq. 02)}$$

SF = shape factor constant, approximately 0.85.
A = sum of the net intensity of all points forming the diffraction peak.
l = height of the diffraction peak at angle θ.

In all cases, the (103) diffraction line was selected, corresponding to the most intense peak of the dominant phase in the synthesized oxides (Fig. 4).

Table 3 presents the crystallite domain sizes determined using the Scherrer equation (Eq. 01–02). It can be observed that the prepared solids exhibit average crystallite domain sizes below the threshold commonly used to classify them as nanoparticles—that is, diameters smaller than 20 *nm*.

Table 3. Parameters used and diameters of the crystalline domain of *Perovskites*.

Código	SF	Área	Altura	k	λ (Cu)	2θ	cos2θ	FWHM(S)	*d(nm)*
NiFe-MG-2	0,85	352,7	1017,9	1,00	1,54	32,46	0.5027	0,51980	**5,89**
				0,89		32,46	0.5027	0,29455	**9,26**
NiFe-MG-3	0,85	190,3	1023,1	1,00	1,54	32,43	0.5263	0,27910	**10,48**
				0,89		32,43	0.5263	0,15815	**16,47**
NiFe-MG-4	0,85	335,1	666,6	1,00	1,54	32,53	0.4365	0,75420	**4,68**
				0,89		32,53	0.4365	0,42737	**7,35**

3.3 Catalytic test: Dry reforming of methane

3.3.1 Instrumental response (gas chromatograph – GC)

For the gas chromatograph, the thermal conductivity detector's (TCD) response factor was calculated using argon as the carrier gas, flowing at a rate of 30 *mL/min* through the internal column system.

Table 4. TCD response factors for each gas.

Gaseous compound	TCD Response Factor
Hydrogen	8.29
Methane	3.76
Carbon dioxide	1.26
Carbon monoxide	1.00

**All values relative to CO.*

The GC oven was operated under isothermal conditions at approximately 150°*C*. A distinct response factor was verified for each compound (Table 4).

3.3.2 Pretreatment

The synthesized (Fe/Ni) perovskites were pretreated with hydrogen at a 30 *mL/min* flow rate, using a heating ramp programmed to increase at 10 °*C/min* from room temperature to 700 °*C*. The temperature was held at 700 °*C* for approximately 15 minutes (Fig. 5).

3.3.3 Calibration (gas chromatograph – GC)

Parameters such as mass, reactant flow rate, temperature range, and space velocity were calibrated to ensure kinetic regime conditions during the reaction. The ideal conditions for kinetic studies using perovskites in the DRM (Dry Reforming of Methane) system are summarized in Table 5.

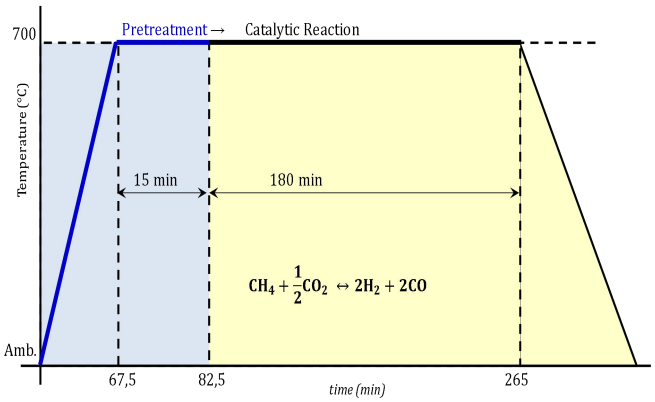

Figure 5. Thermal cycle (pretreatment/catalytic reaction) in DRM using perovskites as catalysts.

Table 5. Actual conditions used for GC analysis.

Parameter	Value
Total flow rate (*mL/min*)	≥ 50
Temperature range (°*C*)	700
Catalyst mass (mg)	≥ 0.030
Space velocity range ×10^{-3} (*mL/g*h*)	120–240

3.3.4 Reaction conditions

Approximately 30 *mg* of perovskite catalyst was weighed and placed into a U-shaped quartz reactor. The reaction temperature was set to 700 °*C*. The molar feed ratio of the reactants CH_4/CO_2 was 1:1, with a total volumetric flow rate of 40 *mL* and a space velocity of 120.000 *mL/g*h*.

3.3.5 Catalytic test (methane reforming)

The conversions of methane and carbon dioxide, the selectivity towards synthesis gas, and the H_2/CO molar ratio for the DRM reaction using $Ba_{0,3}Sr_{0,7}Ni_{1-x}Fe_xO_3$ perovskites as heterogeneous catalysts at 700 °C are shown in Figure 6. It was found that the partial substitution of iron with nickel

enhances both the activity and selectivity of the dry reforming of methane to synthesis gas. All perovskite catalysts tested in the DRM reaction exhibited good thermal stability over a reaction time of approximately 200 minutes, indicating resistance to sintering and minimal deactivation due to carbon deposition.

The stability observed in the DRM reaction may be related to: 1) the small size of the metallic particles, particularly the average size of nickel, and 2) The strong interaction of the metallic sites with the support structure at high temperatures (Sierra et al., 2009; García et al., 2010).

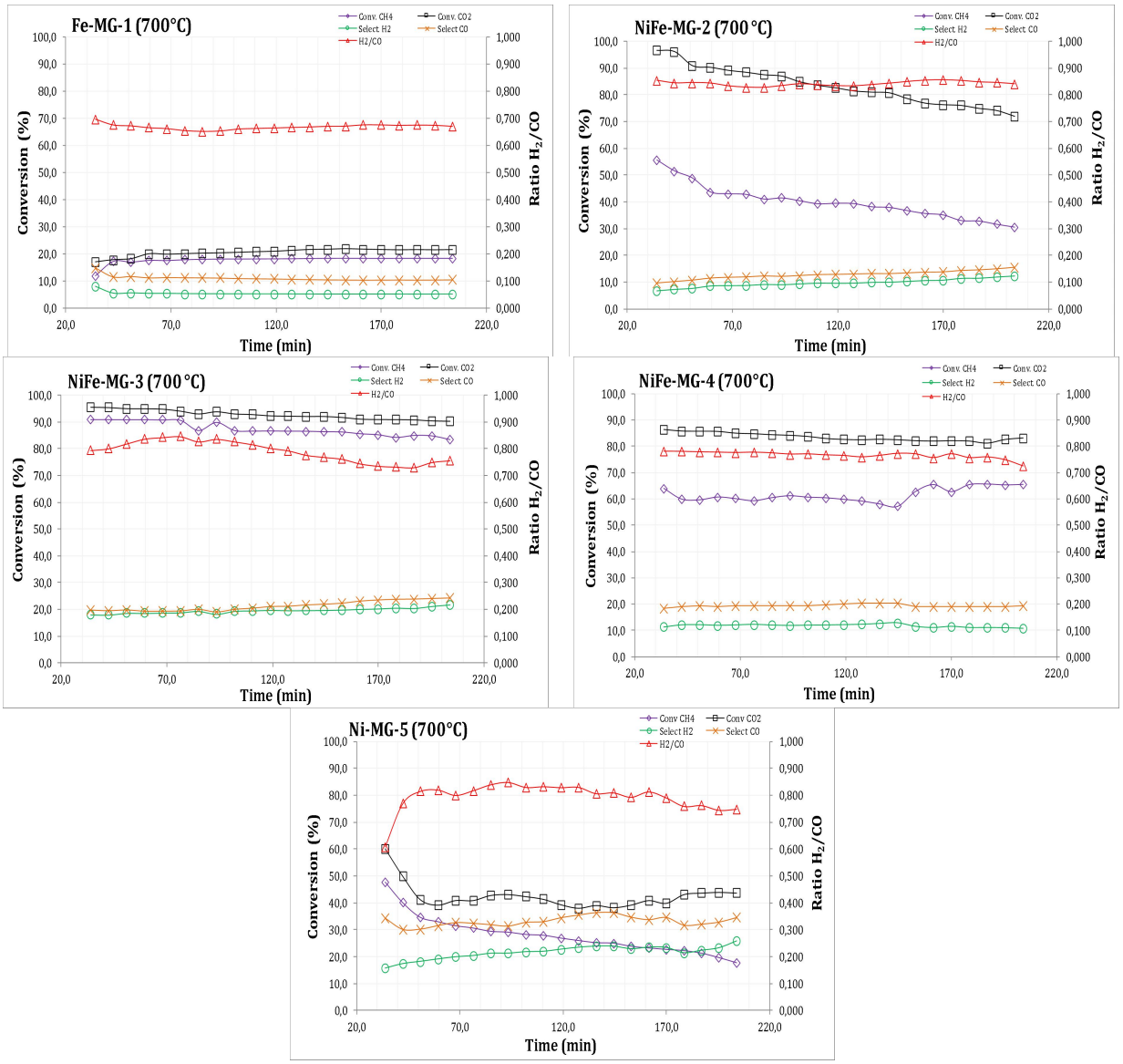

Figure 6. CH_4 and CO_2 conversions, *Syngas* selectivity, and H_2/CO ratio for $Ba_{0,3}Sr_{0,7}Ni_{1-x}Fe_xO_3$ perovskites in the DRM reaction.

Table 6. Average conversions (%) of CH_4 and CO_2, H_2/CO ratio, and selectivity towards syngas for the perovskites at 700 °C.

Measured Parameter	Fe-MG-1	NiFe-MG-2	NiFe-MG-3	NiFe-MG-4	Ni-MG-5
CH_4 Conversion (%)	17,78	39,97	87,54	61,14	27,93
CO_2 Conversion (%)	20,56	83,28	92,70	83,63	42,45
H_2/CO Ratio	0,67	0,84	0,79	0,77	0,79
H_2 Selectivity (%)	5,28	9,66	19,39	11,93	21,56
CO Selectivity (%)	11,01	12,69	21,15	19,52	33,20
Σ Selectivity (H_2 + CO) (%)	16,28	22,35	40,54	31,45	54,76

The conversion of carbon dioxide is favored over methane in all solids of the P-NiCo-RT series, due to the presence of simultaneous competitive reactions such as the reverse water–gas shift reaction (RWGS), where CO_2 reacts with H_2 to produce CO and water vapor (Haghighi et al., 2007) (Eq. 03).

$$CO + H_2O \leftrightarrows CO_2 + H_2 \qquad \Delta H^\circ \; +9{,}8 \; Kcal/mol \qquad \text{(Eq. 03)}$$

The H_2/CO molar ratio showed values below 1, which is likely due to side reactions such as the reverse water–gas shift reaction (Eq. 03), resulting in increased CO and consequently a lower final H_2/CO ratio, deviating from the stoichiometry of the DRM reaction (Lugo et al., 2010). The relatively low selectivity percentages may be attributed to the extreme operating conditions and secondary reactions competing for the active metal sites.

Among the $Ba_{0,3}Sr_{0,7}Ni_{1-x}Fe_xO_3$ perovskite catalysts tested at 700 °*C*, the highest CH_4 conversions were observed for:

(NiFe-MG-3)		(NiFe-MG-4)
87,37 %	>	61,62 %

The observed catalytic pathway is attributed to a **synergistic effect** between iron and nickel, which appears to enhance the properties of the metallic active sites.

4 Conclusions

Mixed oxide perovskite-type materials were successfully synthesized via solution combustion synthesis (SCS)—a rapid, efficient, and cost-effective method for obtaining nanomaterials.

FTIR spectroscopy confirmed the presence of characteristic vibrational modes of metal–oxygen interactions at low wavenumbers (<1000 cm^{-1}), revealing overlapping bands indicative of the presence of these metals in the synthesized heterogeneous catalyst.

XRD patterns of the bimetallic samples (NiFe-MG2, NiFe-MG3, NiFe-MG4) revealed the formation of a dominant orthorhombic perovskite-type phase (space group: *Pnma*) corresponding to lanthanum iron-nickel oxide, $LaFe_{0.6}Ni_{0.4}O_3$, identified using reference card 01-088-0638 from the ICDD PDF2-2004 database.

Crystallite domain size estimation using the Scherrer equation indicated particle sizes below 20 *nm*, confirming the presence of nanoparticles in the material structure.

Catalytic tests for DRM demonstrated that partial iron substitution with nickel enhances activity and selectivity toward synthesis gas. Most perovskites exhibited good thermal stability over the reaction duration, indicating resistance to sintering and minimal deactivation from carbon deposition.

Average methane conversions in DRM for the synthesized perovskites were as follows:

NiFe-MG-3	>	NiFe-MG-4	>	NiFe-MG-2
(87,54 %)		(61,14 %)		(39,97 %)

This supports a synergistic effect between Ni and Fe that improves active site performance, resulting in higher hydrocarbon conversions.

CO_2 conversion was favored in the reaction system, likely due to competitive secondary reactions such as the reverse water–gas shift reaction, where CO_2 reacts with H_2 to form CO and water.

All H_2/CO molar ratios in the DRM reaction were below unity, confirming the presence of the RWGS reaction, which increases CO production and thus decreases the final H_2/CO ratio in the syngas mixture.

Acknowledgments

We thank the X-ray Laboratory of the Universidad Industrial de Santander and its director, Professor José Antonio Henao Martínez, for his invaluable support in the powder X-ray diffraction analyses of the synthesized samples in this study.

References

Anacona, O., García, D., Kiminami, R. y Raigoza, C., (**2013**). Efecto de la temperatura en la estructura cristalina de polvos cerámicos de $K_{0.5}Na_{0.5}NbO_3$ obtenidos por el método de reacción por combustión, Revista latinoamericana de Metalurgia y Materiales, Vol. 33 (1), pp. 108-115.

Arévalo, R., (**2019**). La Industria y sus efectos en el cambio climático Global. RECIAMUC, Vol. 2 (2), pp. 595-611.

Briceño, J., Lugo, C., García, E., Rondón, J., Pérez, P., Rodríguez, P., Del Castillo, H. y Imbert, F., (**2020**). Síntesis de perovskitas basadas en Ni y Fe vía SCS con radiación microondas y su empleo en el reformado seco de metano. Revista Ciencia e Ingeniería, Vol. 41 (2), pp. 205-216.

Cabrera, G., Madriñan, S., Muñoz, D., (**2012**). Caracterización del gas de síntesis obtenido a partir de algarrobo y bagazo de caña. Biotecnología en el Sector Agropecuario y Agroindustria, Vol. 10 (1), pp. 166-172.

C.I.A., (**2021**). Natural gas - proved reserves. The World Factbook. https://www.cia.gov/the-world-factbook/static/3a6e5fc200e47bc5cf68bd3a5d57481b/Energy_World.pdf

Civera, A., Pavese, M., Saracco, G. y Specchia, V., (**2003**). Combustion synthesis of perovskite-type catalysts for

natural gas combustion. Catalysis Today, Vol. 83, pp. 199-211.

Darroudia, M., Bagherpour, M., Hosseini, H. y Ebrahimic, M., (**2016**). Biopolymer-assisted green synthesis and characterization of calcium hydroxide nanoparticles. Ceramics International, Vol. 42 (3), pp. 3816-3819.

Edwards, J. y Maitra, A., (**1995**). The chemistry of methane reforming with carbon dioxide and its current and potential applications. Fuel Processing Technology, Vol. 42 (2-3), pp. 269-289.

Falcon, H., Goeta, A., Punte, G., Carbonio, R., (**1997**). Crystal structure refinement and stability of $LaFe_xNi_{1-x}O_3$ solid solutions, Journal of Solid State Chemistry, Vol. 133(2), pp. 379-385.

García, F., (**2012**). Estimación técnico económica de la separación de los compuestos de gas licuado de petróleo a partir de gases de quema y/o venteo. Trabajo Especial de Grado, Facultad de Ingeniería, Universidad Central de Venezuela, pp. 10-24.

García, E., Rondón, J., Belandria, L., Meléndez, H., Lugo, C. y Imbert F., (**2010**). Dry methane reforming over Ni-Co supported by impregnation on MgO nanoparticles, Revista Ciencia e Ingeniería, Vol. 31 (2), pp. 77-82.

Gómez, J., (**2010**). Síntesis y caracterización del sistema $LaSrCrFeO_3$ soportado sobre óxidos de cerio dopados con elementos de transición interna. Tesis Doctoral en Ciencias Química, Departamento de Química, Facultad de Ciencias, Universidad Nacional de Colombia, Bogotá, Colombia, pp. 156-158.

Haghighi M., Sun Z., Wu J., Bromly J., Wee H.L., Ng E., Wang Y., Zhang D., (**2007**). On the reaction mechanism of CO_2 reforming of methane over a bed of coal char, Proceedings of the Combustion Institute, Vol. 31 (2), pp. 1983-1990.

Harish, S., Sabarinathan, M., Archana, J., Navaneethan, M., Nisha, K., Ponnusamy, S., Gupta, V., Muthamizhchelvan, C., Aswal, D., Ikeda, H., Hayakawa, Y., (**2017**). Synthesis of ZnO/SrO nanocomposites for enhanced photocatalytic activity under visible light irradiation, Applied Surface Science, Vol. 418(A), pp. 147-155.

Haye, E., Bruyere, S., André, E., Boulet, P., Barrat, S., Capon, F., Miska, P., Migot, S., Carteret, C., Coustel, R., Gendarme, C., Diliberto, S., Munnik, F., (**2017**). $LaFeO_xN_y$ perovskite thin films: Nitrogen location and its effect on morphological, optical and structural properties. Journal of Alloys and Compounds, Vol. 724, pp. 74-83.

Hernández, J., Castillo, S., Esparza, H., Téllez, E. y Duarte, J., (**2006**). Síntesis y caracterización de nano-monocristales de Glicina-Nitrato de Sodio, GSN, con propiedades ópticas no-lineales. Tecnura, Vol. 9 (18), pp. 4-9.

Kammer, K., Skou, E., Christensen, H., Turek, T., (**2001**). Perovskites as Catalysts for the Selective Catalytic GaoReduction of Nitric Oxide with Propene: Relationship between Solid State Properties and Catalytic Activity. Journal of Catalysis, Vol. 199 (1), pp. 32-140.

Langford, J. y Wilson, A., (**1978**). Scherrer after sixty years: A survey and new results in determining crystallite size. Journal of Applied Crystallography, Vol. 11, pp. 102-113.

Liu, L., Guo, Y., Wang, Y., Guo, H., (**2013**). Hollow NiO nanotubes synthesized by bio-templates as the high-performance anode materials of lithium-ion batteries. Electrochimica Acta, Vol. 114, pp. 42-47

Lugo, C., García, E., Rondón, J., Meléndez, H., Pérez, P. y Del Castillo, H., (**2010**). Síntesis de óxidos mixtos de Co, Ni y Cu sobre MgO por el método de combustión con urea y estudio en la reacción de reformado seco de metano con CO_2. Revista Ciencia e Ingeniería, Vol. 31 (1), pp. 53-60.

Lugo, C., Pérez, M., Quintero, M., Rondón, J., Pérez, P., D´Angelo, R., Meléndez, H., Villarroel, M., Rodríguez, P., Imbert, F. y Del Castillo, H., (**2017**). Study of the reaction of dry reforming of methane using mixed oxide perovskites type $La_xSr_{1-x}Ni_yAl_{1-y}O_3$. Revista Ciencia e Ingeniería, Vol. 38 (1), pp. 17-30.

Lugo, C., Rosal, H., Hidalgo, J., Rondón, J., Pérez, P., Rodríguez, P., Del Castillo, H. y Imbert, F., (**2022**). Preparation of single and layered Perovskites (A= La and Sr/Ca; B = Ni/Co and Ni/Al) from solution combustion synthesis, SCS, via microwave radiation. Revista Ciencia e Ingeniería, Vol. 43 (3), pp. 245-256.

Lugo C., Fereira C., Petit E., Guerrero M., Torres R., Pérez P., Rodríguez P., Rondón J., (**2024.a**). Estudio catalítico sobre RSM empleando óxidos mixtos Perovskitas $Sr_{0.7}Mg_{0.3}Ni_xCo_{1-x}O_3$, obtenidas vía combustión en solución, SCS. Revista Ciencia e Ingeniería, Vol. 45 (2), pp. 169-178.

Lugo C., Petit E., Guerrero M., Torres R., Fereira C., Pérez P., Rondón J., (**2024.b**). Síntesis de perovskitas en capas tipo $A_{n+1}B_nX_{3n+1}$ (A=Sr/Mg; B=Ni/Fe; X=O) vía SCS con Actividad Catalítica en el Reformado seco de metano. Revista Ciencia e Ingeniería, Vol. 45 (3), pp. 265-274.

Martín, N., Viniegra, M., Vargas, R., Garza, J., (**2021**). Óxidos nanoestructurados de metales de transición con aplicaciones en Catálisis. Mundo Nano, Vol. 14 (26), pp. 35-46.

Mukasyan, A., Costello, C., Sherlock, K., Lafarga, D., y Varma, A., (**2001**). Perovskite Membranes by Aqueous Combustion Synthesis: Synthesis and Properties. Separation and Purification Technology, Vol. 25 (1-3), pp. 117-126.

Mukasyan, A., Epstein, P. y Dinka, P., (**2007**). Solution combustion synthesis of nanomaterials. Proceedings of the Combustion Institute, Vol. 31 (2), pp. 1789-1795.

Neira, A., Gómez, J. y Vera, E., (**2016**). Synthesis and characterization of a simple $La_{0.8}Sr_{0.2}CrO_3$ perovskite

(Universidad del Valle). Revista de Ciencias, Vol. 20 (1), pp. 79-94.

Patil, K., Aruna, S. y Ekambaram, S., (**1997**). Combustion synthesis. Current Opinion in Solid State and Materials Science, Vol. 2 (2), pp. 158-165.

Patil, K., Aruna, S. y Mimani, T., (**2002**). Combustion synthesis: an update. Current Opinion in Solid State and Materials Science, Vol. 6 (6), pp. 507-512.

Pérez, M., Lugo, C., Quintero, M., Pérez, P., Villarroel, M., Rodríguez, P., Imbert, F. y Del Castillo, H., (**2015**). Síntesis de óxidos mixtos tipo perovskitas de $La_xSr_{1-x}Ni_yAl_{1-y}O_3$ preparados vía combustión en solución (SCS). Revista Ciencia e Ingeniería, Vol. 36 (2), pp. 93-104.

Rahdar, A., Aliahmad M., Azizi Y., (**2015**). NiO Nanoparticles: Synthesis and Characterization, Journal of Nanostructures, JNS, Vol. 5, 145-151.

Ramos, K., Jiménez, Y. y Linares C., (**2015**). Síntesis y caracterización de óxidos MgAl, MgFe, FeAl y MgFeAl para la degradación de fenol con foto-fenton solar. Revista latinoamericana de Metalurgia y Materiales, Vol. 35 (2), pp. 315-325.

Rendón, J., Moreno, L. y Valencia, J., (**2006**). Síntesis y caracterización de perovskitas de $LaCoO_3$ por el método citrato. Revista colombiana de Física, Vol. 38 (2), pp. 906-909.

Sierra, G., Gallego, J., Batiot-Dupeyrat, C., Barrault, J. y Mondragón, F., (**2009**). Influence of Pr and Ce in dry methane reforming catalysts produced from $La_{1-x}A_xNiO_{3-\delta}$ (A= Pr, Ce). Applied Catalysis A: General, Vol. 369, (1-2), pp. 97-103.

Sithole, M., Omondi, B., & Ndungu, P., (**2017**). Synthesis and characterization of $Ce_{0.6}Sr_{0.4}Fe_{0.8}Co_{0.2}O_{3-\delta}$ perovskite material: Potential cathode material for low temperature SOFCs. Journal of Rare Earths, Vol. 35 (4), pp. 389-397.

Song, S., Sheptyakov, D., Korsunsky, A., Duong, H. y Lu L., (**2016**). High Li ion conductivity in a garnet-type solid electrolyte via unusual site occupation of the doping Ca ions. Materials and Design, Vol. 93, pp. 232-237.

Specchia, S., Ciera, A. y Saracco, G., (**2004**). In situ combustion synthesis of perovskite catalysts for efficient and clean methane premixed metal burners. Chemical Engineering Science, Vol. 59 (22-23), pp. 5091-5098.

Varma, A., Mukasyan, A., Deshpande, K., Pranda, P. y Erii, P., (**2003**). Combustion Synthesis of Nanoscale Oxide Powders: Mechanism, Characterization and Properties. Materials Research Society Symposium Proceeding, Vol. 800, pp. 113-125.

Villaquirán, C., Medina, C., & Tirado, L., (**2015**). Effect of cobalt-incorporation on the proper-ties of $Sr_xBa_{1-x}Nb_2O_6$ system. Ingeniería y Desarrollo, Vol. 33 (2), pp. 281-300.

Wade L., (**2004**). Química Orgánica (quinta edición). Madrid-España: Pearson Educación S.A., 500, 505, 1207.

Wang, K., Zhong, P. y Zhu, J., (**2009**). Preparation of Highly Active and Stable Perovskite-like Catalyst by Combustion Method: Effect of Complex. Catalysis Letters, Vol. 131, pp. 672-675.

Zhao, Y., Hong, L., Hong, J. y Zhu, J., (**2004**). Synthesis of lead sulfide nanocrystals via microwave and sonochemical methods. Materials Chemistry and Physics, Vol. 87 (1), pp. 149-153.

Received: *May 22th, 2025*

Accepted: *July 17th, 2025*

Lugo González, Claudio Antonio: *Ph.D. in Applied Chemistry, mention Materials Studies, 2017, Universidad de Los Andes; Professor of Chemistry Department (Kinetics and Catalysis Laboratory), at the Faculty of Sciences, ULA. Merida, Venezuela.*

https://orcid.org/0000-0001-8003-0354

Guerrero Rojas, Maryuri: *Bachelor's Degree in Chemistry, 2023, Chemistry Department (Kinetics and Catalysis Laboratory) at the Faculty of Sciences, Universidad de Los Andes, Mérida, Venezuela. Email: mar94688@gmail.com*

https://orcid.org/0009-0000-8230-7038

Fereira Chacón, Carla Yanosky: *Bachelor's Degree in Chemistry, 2023, Chemistry Department (Kinetics and Catalysis Laboratory) at the Faculty of Sciences, Universidad de Los Andes, Mérida, Venezuela. Email: carlayanosky@gmail.com*

https://orcid.org/0009-0004-2961-7802

Petit Chacón, Eliel José: *Bachelor's Degree in Chemistry, 2023, Chemistry Department (Kinetics and Catalysis Laboratory) at the Faculty of Sciences, Universidad de Los Andes, Mérida, Venezuela. Email: elielpetit4@gmail.com*

https://orcid.org/0009-0004-3623-2732

Torres Ibarra Rubén Darío: *Bachelor's Degree in Chemistry, 2023, Chemistry Department (Kinetics and Catalysis Laboratory) at the Faculty of Sciences, Universidad de Los Andes, Mérida, Venezuela. Email: rubendti.16@gmail.com*

https://orcid.org/0009-0000-3600-8571

Vizcaya, Marietta: *Ph.D. in Drug Chemistry, 2014, Scientific Research Institute, Faculty of Pharmacy and Bioanalysis, Universidad de Los Andes; Professor of Polymer Laboratory at the Faculty of Sciences, ULA.*

Mérida, Venezuela. Email: marietta@ula.ve
https://orcid.org/ 0000-0002-2064-4175

Pérez Dávila, Patricia: *Ph.D. in Drug Chemistry, 2017, Scientific Research Institute, Faculty of Pharmacy and Bioanalysis, Universidad de Los Andes; Professor of Polymer Laboratory at the Faculty of Sciences, ULA. Mérida, Venezuela. Email: perezdpatricia@gmail.com*
https://orcid.org/0000-0003-0591-2351

Rondón Contreras, Jairo: *Ph.D. in Applied Chemistry, mention Materials Study, 2015, Universidad de Los Andes; Professor of Biomedical & Chemical Engineering Departments, at the Polytechnic University of Puerto Rico, San Juan, PR-USA. Email: jrondon@pupr.edu*
https://orcid.org/0000-0002-9738-966X

Artículo de Investigación. Revista Ciencia e Ingeniería. Vol. 46, No. 3 pp. 321-330, agosto-noviembre, 2025.
ISSN 1316-7081. ISSN Elect. 2244-8780 Universidad de los Andes (ULA)

Development of an Android application for rock mass evaluation (RMR, GSI, Q-Barton, SMR) with field validation in Los Guáimaros, Campo Elías, Mérida, Venezuela

Desarrollo de una aplicación Android para la evaluación de macizos rocosos (RMR, GSI, Q-Barton, SMR) con validación práctica en Los Guáimaros, Campo Elías, Mérida, Venezuela.

López, Luis[1*]; Molina, Germán[2]; Cardillo, Juan[3]; Cuevas, Rómulo[4]
[1]Faculty of Engineering. School of Geological Engineering, ULA,
[2]Faculty of Engineering. School of Geological Engineering, ULA,
[3]Faculty of Engineering. School of Systems Engineering, ULA,
[4]Rogii University
[*]luisjoselopezd@gmail.com

Abstract

We present an Android application for evaluating rock mass quality using geomechanical methodologies (RMR, GSI, Q-Barton, and SMR). This tool optimizes the collection and analysis of geological data, facilitating its implementation in geotechnical projects. First, a flowchart defining the application's functionalities was developed. This flowchart was implemented using React Native. To validate the app, two types of tests were conducted: interface and functionality. For this purpose, two datasets were used: historical data from prior evaluations and field data collected during visits to the Los Guáimaros region, Mérida State, where three rock masses were assessed. These in-situ tests enabled evaluation and refinement of the app's performance. The results from both datasets were compared with manual calculations performed in Excel spreadsheets, based on the three cases mentioned.

Keywords: APP, React Native, Rock mechanics, Rock massif, Geomechanical classifications, Geotechnical engineering

Resumen

Presentamos una aplicación Android para la evaluación de la calidad de macizos rocosos mediante metodologías geomecánicas (RMR, GSI, Q-Barton y SMR). Esta herramienta optimiza la recolección y análisis de datos geológicos, facilitando su implementación en proyectos geotécnicos. Primero, se elaboró un diagrama de flujo que define las funcionalidades de la aplicación. Este diagrama de flujo se implementó utilizando el lenguaje React Native. Para validar la aplicación se llevaron a cabo dos tipos de prueba, la de interfase y de funcionamiento. Para ello se usaron dos tipos de datos, el primero, histórico de evaluaciones previas y el segundo, una visita de campo en la región de Los Guáimaros, estado Mérida, donde se evaluaron tres macizos rocosos, estas pruebas in-situ permitieron evaluar y mejorar el funcionamiento de la aplicación. Los resultados obtenidos con ambos conjuntos de datos se compararon con los obtenidos por cálculos realizados manualmente en hojas de Excel, utilizando tres casos mencionados.

Palabras claves: APP, React Native, Mecánica de rocas, Macizos rocosos, Clasificaciones geomecánicas

1 Introduction

Digital technologies are revolutionizing the field of geology by providing tools and techniques that improve efficiency and accuracy in the study of the Earth, responding to a technological world that demands ubiquity, speed and adaptability. Geological methodologies such as the Mass Rating Index (MRR); the Geological Strength Index (GSI); the Q-Barton system and the Slope Mass Rating (SMR) have been used for decades.

The importance of these methods lies in their ability to relate quality indices with geotechnical parameters crucial for project planning and execution. In order to optimize these processes, we propose the development of an Android application that implements the RMR, GSI, Q-Barton and S.M.R methodologies for the evaluation of the quality of rock massifs. Although the application was validated in the locality of Los Guáimaros, Mérida state, its design allows its implementation in any rock massif, regardless of its geographical location, adapting to the specific characteristics of each formation.

2 Theoretical framework

2.1 Rock mechanics

It is the theoretical and applied science that studies the mercanic behavior of rocks, rock masses and the field of forces acting in their environment (Ramírez and Alejano, 2004).

2.2 The evaluation of rock masses

It is a crucial aspect in geotechnical and mining engineering, RMR, GSI, Q-Barton and SMR methodologies are fundamental for this purpose.

2.2.1 Bieniawski's RMR Classification

The specific parameters considered by this classification are: resistance to simple compression of the rock matrix (RQD), degree of seepage of the rock mass, spacing of discontinuities, hydrogeological conditions and orientation of discontinuities (González de Vallejo, et al., 2002).

To obtain the RMR Index, the values of the first five (5) parameters evaluated are added, resulting in a value called basic RMR. The sixth (6th) parameter, corresponding to the orientation of the discontinuities with respect to the excavation, is not added directly, but is applied as a correction to the basic RMR value. This value varies between 0 and 100.

2.2.2 Geologic Strength Index (GSI), Hoek and Brown

The GSI differs from other classification systems in its qualitative rather than quantitative approach (Sönmez and Ulusay, 2002).

The GSI (Geological Strength Index) values range from 1 to 100, where lower values represent rock masses of lower quality, characterized by a high degree of weathering and fracturing. It is determined by means of a classification table that allows estimating the value based on two visual criteria: on the vertical axis, the type of rock mass structure (SR, Structure Rating) is represented, and on the horizontal axis, the surface quality of the discontinuities (SCR, Surface Condition Rating). This arrangement facilitates a quick and consistent evaluation of the rock mass in the field.

Translated with DeepL.com (free version)

2.2.3 The Q-Barton Index

The Q-Barton Index classifies rock on a scale ranging from exceptionally poor to exceptionally good, based on values ranging from 0.001 to 1000 (Barton, 2002).

The Q-Index is obtained by the following equation

$$Q = \frac{RQD}{\text{Jn}} x \frac{\text{Jr}}{\text{Jr}} x \frac{\text{Jw:}}{SRF}$$

Where the following parameters are entered:

RQD: rock quality index.
Jn: cleavage index indicating the degree of turnover.
Jr: index that contemplates the roughness, filling and continuity of discontinuities.
Ja: Description of joint alteration.
Jw: Reductive coefficient due to the presence of water.
Stress Reduction Factor (SRF): Coefficient that takes into account the influence of the stress state on the rock mass.

The variation index of the parameters is: RQD: between 0 and 100; Jn: between 0.5 and 20; Jr: between 0.5 and 4; Ja: between 0.75 and 20; Jw: between 0.05 and 1; SRF: between 05 and 20.

2.2.4 The Romana SMR Index

The Slope Mass Rating (SMR) for the classification of slopes was proposed by Romana (1985). It is obtained from the RMR index by subtracting an adjustment factor that depends on the orientation of the joints (product of three subfactors) and adding an excavation factor that depends on the method used (cited in Tomás, Delgado and Cuenca, 2005).

According to the following equation:

SMR = Basic SMR + (F1* F2* F3) + F4

The RMR is calculated according to Bieniawski's coefficients.

1. Simple compressive strength of the rock matrix.
2. RQD (measured in boreholes or estimated).
3. Discontinuity spacing.
4. Discontinuity conditions.
5. Discontinuity water flow.

On the other hand:

F1: depends on the parallelism between the direction of the joints and the slope face.

F2: depends on the dip of the plane break.

F3: reflects the relationship between the dip of the joints and the slope.

F4: adjustment factor according to the excavation method.

2.3 Rock slope stability

It is essential to know the modes of rupture that occur in rock whose movement is controlled by geological discontinuities. They are divided into: Flat breakage, wedge breakage and strata overturning breakage (Ramirez and Alejano, 2004).

2.4 Stereographic projection

This type of projection defines an inversion in space that transforms the points of the sphere into points of the plane (Tomás, Delgado and Cuenca, 2005).

2.5 Mobile application development

Mobile applications are relatively simple. Sometimes they interact with the device hardware including camera, storage device, GPS sensor, etc. (Cabrera and Cueva, 2015).

Android is an operating system developed by Goo-gle that offers advantages such as greater market reach, in addition to being used in a wide range of devices from different manufacturers (Cabrera and Cueva, 2015).

2.6 React Native

It is an open-source development framework for building native mobile applications using JavaScript and React (React Native, 2024).

3 Methodology

In order to meet the proposed objectives, the methodological scheme shown in Figure *1*was designed and is described below.

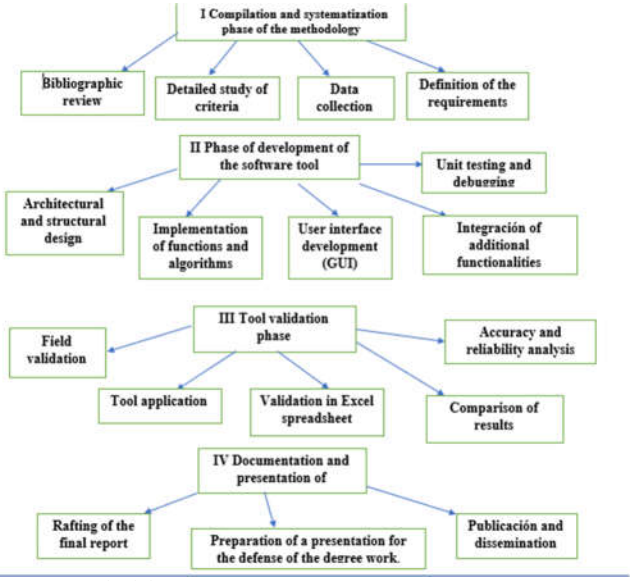

Figure 1. Methodology

3.1 Phase 1: Compilation and systematization of the Methodology.

The information available on the methodologies to be implemented is reviewed and compiled in order to thoroughly understand the criteria involved in them, which allows defining the requirements and specifications of the Application to be developed.

3.2 Phase 2: Application Development

The integral development of the application covers from the design of the software architecture and structure, to the implementation of functions and algorithms for the calculation of rock mass quality indexes, according to RMR, GSI, Q-Barton and SMR methodologies. It also includes the creation of an intuitive user interface, the integration of modules for data management and export, the automated generation of reports, as well as the execution of unit tests and debugging processes, in order to ensure an optimal and reliable operation of the system.

3.3 Phase 3: Application validation

It is carried out in two stages. First, a field validation in the Los Guáimaros region, Mérida state, in-situ data are collected from three rock massifs and the application is used to calculate the indices. The results obtained are compared with traditional rock mass evaluation methods to analyze the accuracy and reliability of the application in real conditions. Second, a validation is performed using Ex-cel spreadsheets, where the same data are entered in the application and in the spreadsheets, and the results obtained are compared to evaluate the consistency and accuracy of the system.

4 Application development

This section shows the technical and methodological aspects of the development of the application.

4.1 Technical aspects to be considered

The development of an Application with the Android operating system was chosen, oriented to the improvement of the necessary records for the evaluation of the quality of rock massifs by means of the technologies mentioned above.

4.2 Data Flow Chart

A Data Flowchart, Figure *2*, is a visual representation that details the process of user interaction with the application, starting from the initial point and culminating with the final results.

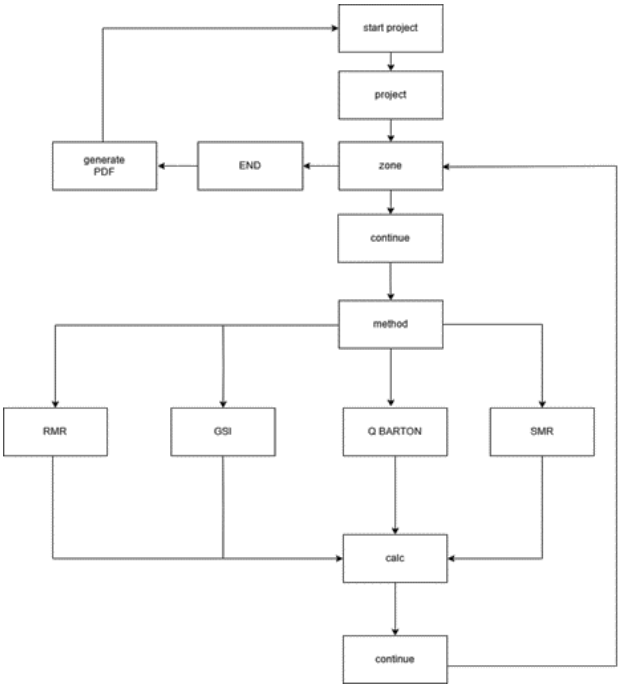

Figure 2. Data flowchart

4.3 Structure in programming language

Based on an object-oriented model where each entity of the system is represented as properties. This approach allows encapsulating both data and related behavior, facilitating the management and manipulation of information.

4.4 URI information

Uniform Resource Identifier (URI), in Spanish, identicador uniforme de recursos. This term is used for all types of names and addresses that refer to objects on the Internet, such as pages, images, videos, etc. A URI is therefore a string of characters that allows interaction between different resources on the Internet and other types of networks.

4.5. User's manual

Based on an object-oriented model where each entity of the system is represented as properties. This approach allows encapsulating both data and related behavior, facilitating the management and manipulation of information.

5 Evaluation and testing of the application.

5.1 Application evaluation and testing

The developed application has been tested so far with 3 different devices with at least 2gb of RAM, which makes it accessible to most geologists and field technicians. The devices tested so far are listed:

- Pixel 7 Android 11, 4 GB de RAM
- Redmi 9a Android 10, 2 GB de RAM
- Redmi 13C Android 14, 8 GB de RAM

5.2 Field Tests

The rock massifs studied in situ are located between the towns of Los Guáimaros and Mesa de Los Indios, in the municipality of Campo Elías, in the state of Mérida.

Figure *3* shows the expanded study area, this addition covers more territory and allows capturing a greater diversity of data from the formations: Aguardien-te, Apon, Rio Negro and Tostos. By evaluating three rock massifs, the following reports were obtained directly from the application. Figures 4, 5 and 6

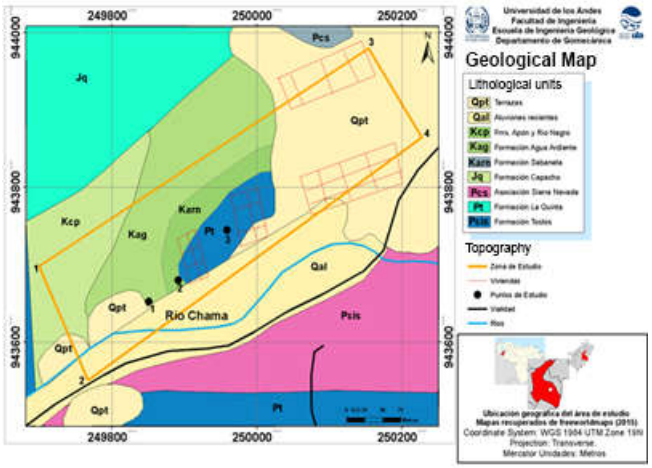

Figure 3. Enlarged study area

Figure 4. Rock mass 1

Figure 5. Rock mass 2

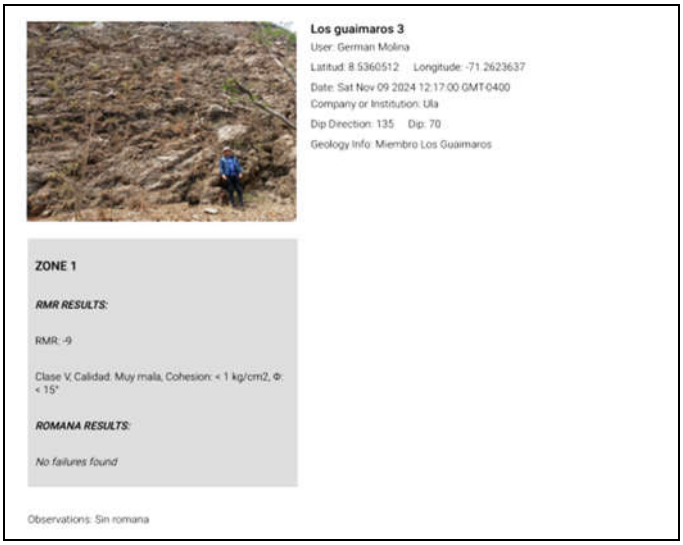

Figure 6. Rock mass 3

6 *Analysis and comparison of results*

6.1. Case 1

In case 1, a comparison was made with the graduate work: "Geomechanical study of rock massifs under the influence of external loads, located in the Los Araques sector, Sucre municipality, Merida state", carried out in November 2019 by Hernandez Yaneidy and Lopez Jesus, under the supervision of Dr. Norly Belandria. In this degree work, three families of discontinuities were evaluated. Table 1

Table 1. Orientation and dip

ORIENTATION AVERAGE	DIP DIP DIRECTION
Family 1	53/246
Family 2	59/143
Family 3	68/360

Table *2* shows the conditions of the aforementioned families

Table 2. Discontinuity family conditions

CONDITIONS	FAMILY 1	FAMILY 2	FAMILY 3
Persistence	>20m	2m	<1m
Opening	0.1-1mm	2-7mm	1cm
Rugosity	Slightly rough	Slightly rough	Rugged
Filling	Unfilled	Unfilled	Unfilled
Alteration	Slightly altered	Slightly altered	Slightly altered

The evaluation of the parameters obtained can be seen in Table *3*, which in turn indicates the basic RMR value.

Table 3. Parameter evaluation

PARAMETER	CHARACTERISTIC	GREATER VALUE	LOWER VALUE
1.α	126 Mpa	12	12
2.RQD	18.01%	3	3
3. Separation	(0.058 -1) m	15	5
4. Conditions: Opening	0.1mm – 1.cm	4	0
Persistence	<1 m - > 20m	6	0
Rugosity	Slightly rough	5	3
Filling	Unfilled	6	6
Alteration	Slightly altered	5	5
5. Water presentation	Dry	15	15
Basic RMR		∑71	∑49

In this research they also calculated the GSI, the results can be seen in Figure 7.

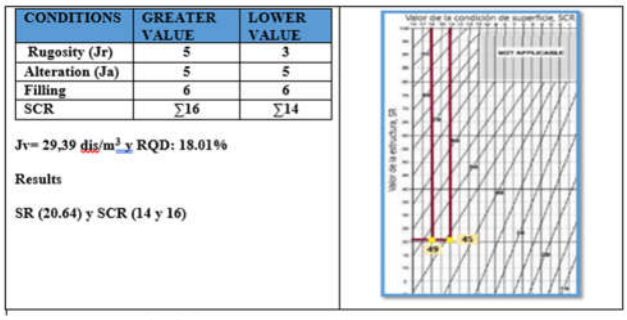

CONDITIONS	GREATER VALUE	LOWER VALUE
Rugosity (Jr)	5	3
Alteration (Ja)	5	5
Filling	6	6
SCR	∑16	∑14

Jv= 29,39 dis/m³ y RQD: 18.01%

Results

SR (20.64) y SCR (14 y 16)

Figure 7. GSI calculations

Using the application, the following results were found, see Figure 8

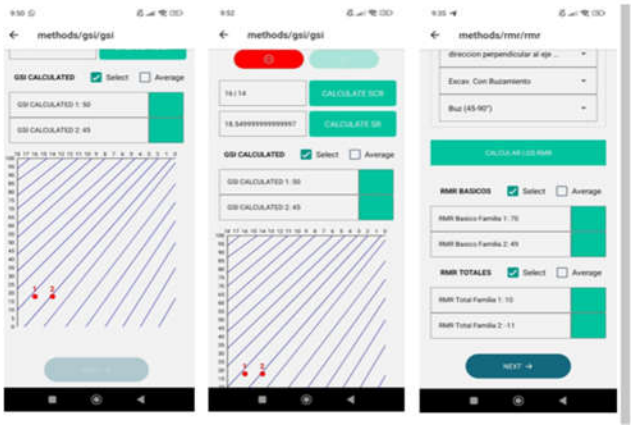

Figure 8. Application results, from left to right: GSI part 1, GSI part 2 and RMR.

Table 4 shows the results of both the research and the application.

Table 4. Results

RESULTS	APP RESULTS
RMR Basics: 71 y 49	**RMR Basics: 70 y 49**
GSI Results: 49 y 45	**GSI Results: 50 y 45**

Finally, to evaluate the performance and accuracy of the application, the same data from the case study were used and the calculations were performed manually in Excel spreadsheets, obtaining the following results. See Table 5.

The results of the case study, the application and the Excel spreadsheet vary by minimum values and suggest a remarkable similarity between them.

Table 5. Calculations using Microsoft Excel

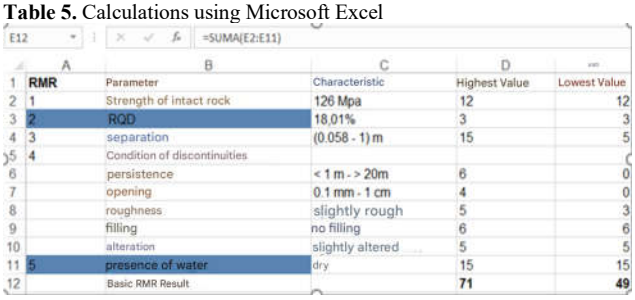

E12 =SUMA(E2:E11)

	A	B	C	D	E
1	RMR	Parameter	Characteristic	Highest Value	Lowest Value
2	1	Strength of intact rock	126 Mpa	12	12
3	2	RQD	18,01%	3	3
4	3	separation	(0.058 - 1) m	15	5
5	4	Condition of discontinuities			
6		persistence	< 1 m - > 20m	6	0
7		opening	0.1 mm - 1 cm	4	0
8		roughness	slightly rough	5	3
9		filling	no filling	6	6
10		alteration	slightly altered	5	5
11	5	presence of water	dry	15	15
12		Basic RMR Result		71	49

6.2 Case 2

In case 2, a comparison was made with the project: Design of Hechicera-La Pedregosa Tunnel, located in Merida state, dated September 2019. Carried out by Bastidas Naila, et al, under the supervision of Dr. Norly Belandria. Table 6 shows the orientation of the discontinuities.

Table 6. Discontinuities orientation

Section	1	2	3
Orientation	Heading/Dipping	Heading/Dipping	Heading/Dipping
Tunnel	N63E / 89SE	N63E / 89SE	N63E / 89SE
Foliation	N45E / 70SE	N45E /83NW	N45E/ 70NW
Discontinuity 1	N61W /45SW	N61W /45SW	N61W /45SW
Discontinuity 2	N80E / 60NW	N80E / 60NW	N80E / 60NW
Entry slope	N30W / 42NE		
Exit slope			N30W / 30SW

Calculation of dip direction: a)70/135; b) 45/209; c) 60/350

On the other hand, the comparison between the results of the stereographic projection of the project and the application is presented. Figure .

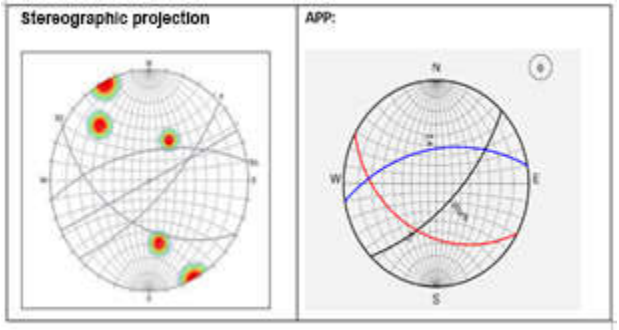

Figure 9. Comparison between project and application results

Although there are similarities, in the application there is a certain difference, the curves are more pronounced. For this reason, a comparison made with Photoshop is added by superimposing the images. Figure .

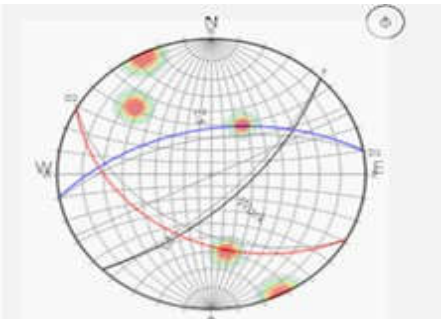

Figure 10. Comparison made with Photoshop overlaying the images

Therefore, adjustments were made to achieve better accuracy, see Figure 11.

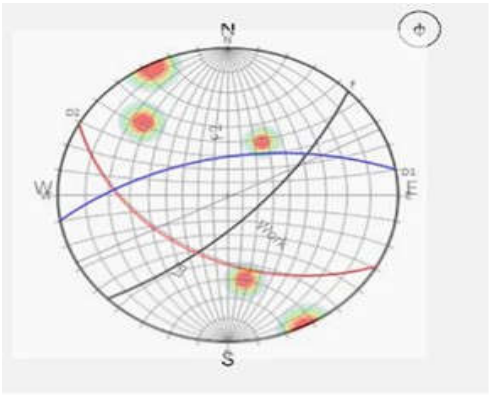

Figure 11. Image made by photoshop superimposing the images after adjustments in the application

It should be noted that the Stereonet program and the Dips program use different grids for the eastographic projection, also Stereonet has more pronounced curves than Dips. The curves of the application were tried to be similar to Dips, even using the same grid; however, both programs were used during these analyses to check results.

Other tests performed with the same case study

Table 7 presents data on tunnel failures, analyzed according to dip and dip direction. Information that is part of this case.

For the realization of the projection, they did not take fault 1, therefore, it was performed in this way. Figure .

Table 7. Failure data

ID	DIP	Dip Direction	Set
1	74	10	
2	89	28	
3	88	35	1
4	82	30	1
5	70	101	2
6	69	110	
7	57	97	
8	68	105	2
9	81	95	
10	71	87	
11	12	135	3
12	21	130	3
13	9	122	3
14	14	137	3
15	21	20	

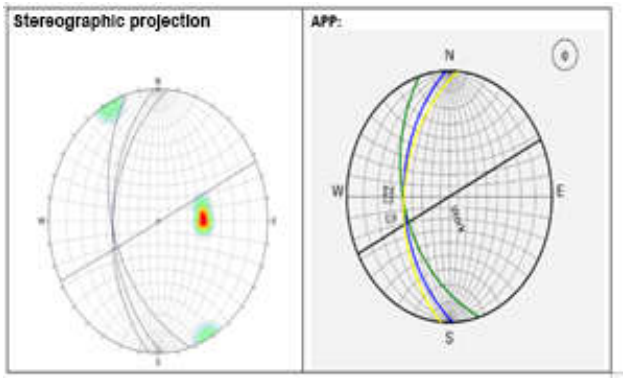

.

Figure 12. Comparison between the project and the application

An overlay image is included to assess accuracy. Figure .

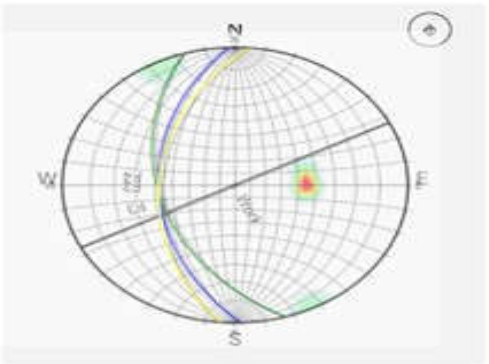

Figure 13. Comparison by superimposing both images, using photoshop

In this research they also performed the Q-Barton Calculation, the data are shown in Table *8*.

Table 8. Data for Q-Barton sections

Section	1	2	3
Quality of rock (RQD)	65,5	65,5	65,5
Diaclasate (Jn)	9	9	9
Rugosity (Jr)	1,5	1	1,5
Alteration (Ja)	2	2	2
Presence of water (Jw)	0,66	0,66	0,66
SRF	1	1	1

This calculation yielded the following result

$$Q = \frac{65,5}{9}\ x\ \frac{1.1,5}{2}\ x\ \frac{0,66}{1} = 2,40 \text{ Poor quality}$$

Using the application, the results presented in Table 9 below were found.

Table 9. Application results

Section 1	Section 2	Section 3
Result APP= 0.715	It was decided not to carry out tranche 2	Same parameters, same results
Very bad rock type		
Attached is a screenshot of the application report.		
ZONE 1 Q BARTON RESULTS Q BARTON: 0.715 Rock Type: Very Bad		

It is clarified that this study has an error in the RQD parameter since they directly used the "65.5" instead of its valuation from the RQD table. It can be affirmed then, that if he correct valuation is used, the result of the application is obtained. Finally, to evaluate the performance and accuracy of the application, the same data from the case study were used and the calculations were made manually in Excel spreadsheets, obtaining the results shown in Table 10.

Table 10. Calculations using Microsoft Excel

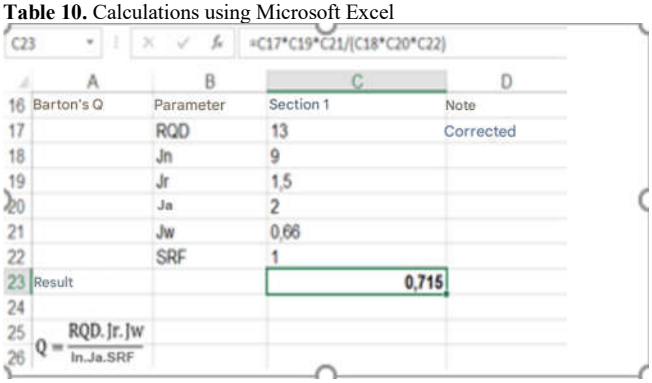

It can be seen that the results of the study, the application and the Excel calculation coincide perfectly.

6.3 Case 3

In case 3, a comparison was made with the graduate work: Evaluation of the geotechnical properties of the outcrops between El Caucho and San José de las Flores Alto, Mérida, Mérida state, carried out in November 2022, by Bravo Jorge and Gatrif Jesús, under the supervision of Professor Germán Molina.

Table 11 shows data from the outcrops evaluated in the research.

Table 11. Outcrop data

ID	DIP	Dip Direction	Set
1	74	10	
2	89	28	
3	88	35	1
4	82	30	1
5	70	101	2
6	69	110	
7	57	97	
8	68	105	2
9	81	95	
10	71	87	
11	12	135	3
12	21	130	3
13	9	122	3
14	14	137	3
15	21	20	

Figure 14 shows the comparison between the results of the stereographic projection of the degree work and the application. They are the same results; however, it should be noted that the image of Bravo & Gatrif's thesis is distorted, it is not a perfect circle.

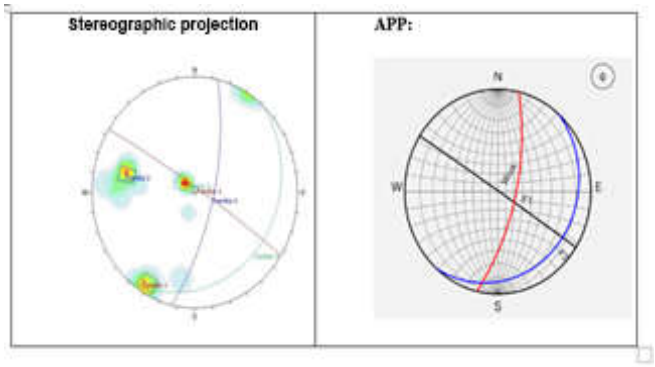

Figure 14. Comparison between thesis and application data.

In this research they also performed the calculation of Q Barton, the data can be found in Table 12.

Table 12. Calculation of Q-Barton

Family 1

Parameters	RQD	Jn	Jr	Ja	Jw	SRF
Description	Regular	3 families	Light Rough	Closed	Slightly Wet	D
Rating	13	9	3	4	1	7,5

Family 2

Parameters	RQD	Jn	Jr	Ja	Jw	SRF
Description	Regular	3 families	Rough	Closed	Slightly Wet	D
Rating	13	9	5	4	1	7,5

Family 3

Parameters	RQD	Jn	Jr	Ja	Jw	SRF
Description	Regular	3 families	Light Rough	Closed	Slightly Wet	D
Rating	13	9	3	4	1	7,5

With these data, the Q value is determined, which has an average of 0.84, indicating that the rock is very bad. The following results were obtained from the application. Table 13.

Table 13. Application results

Family 1	Family 2	Family 3
Result APP: 0.144	In parameter Jr there is no value associated with 5	They have the same parameters as family 1, therefore, the same results are obtained.
Rock type: very bad		
Attached is a screenshot of the application report.		
ZONE 1 Q BARTON RESULTS Q BARTON: 0.144 Rock Type: Very Bad		

In this case it is clear that the thesis students used a nonmenclature different from the tables used in the application, even in the second family they used a value that is not found in the theory; in the same way, a value is obtained that falls within a range close to their results.

To evaluate the performance and accuracy of the application, the same data of the case study were used and the calculations were made manually in Excel spreadsheets, obtaining the results shown in Table 14

Table 14. Calculations using Microsoft Excel

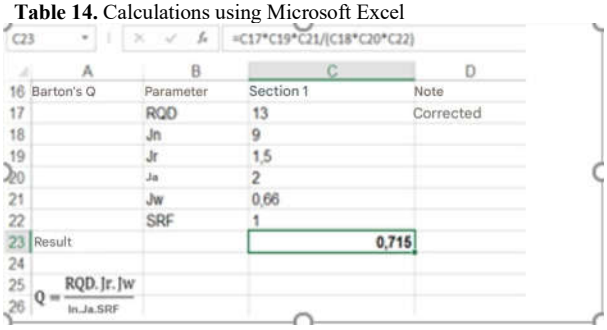

All the results of the case study, the application and the Excel sheet match perfectly.

7. Conclusions

The final validation of the application in terms of its functionality and accuracy were field tests, which allowed for modifications and improvements.

Significant savings in man-hours dedicated to data collection and analysis are evident. On average, a total of 40 minutes was estimated for the RMR method and an average of 10 to 15 minutes for the other methods.

Another no less important validation is the numerical calculation machine used, with respect to those traditionally used. Comparing the results obtained with calculations performed manually on Excel spreadsheets using data from three cases available in the literature, the following results were obtained: in case 1, in case 1, they coincided 99% with the application. Case 2: there was a 100% match. Case 3: There was a 100% match.

Based on the design of the application and the rock mass data collection methodology, it is recommended to create independent projects when there are significant variations in the geometric and geo-logical properties of the study area.

The use of the application favors portability in these processes, since it would not be necessary to carry materials such as notebooks, guides or files; and reports could be sent by messages or mail, i.e., in real time.

The application is a beta version restricted to the use of the University's School.q Currently, it works with quality and accuracy, but ideally it should be further evaluated and improved to implement new functionalities.

References

Barton, N. (2002). *Some new Q-value correlations to assist in site characterization and tunnel design.* International Journal of Rock Mechanics and Mining Sciences, 39(2), 185-216**.**

Bastidas, N, et al. (2019) *Diseño de Túnel Hechicera* – La Pedregosa. (Research project, Los Andes University). Mérida, Venezuela

Bravo, J. & Gatrif, J. (2022). Evaluación de las propiedades de los afloramientos comprendidos entre El Caucho y San José de las Flores Alto. (Degree Project, Los Andes University). Mérida, Venezuela**.**

Cabrera, A. & Cueva, D. (2015). Arquitectura adaptada para el diseño de aplicaciones móviles en Android. (Degree Project, Antenor Orrego Private University). Recovered from https://repositorio.upao.edu.pe/handle/20.500.12759/1221

González de Vallejo, L., Ferrer, M., Ortuño, L., & Oteo, C. (2002). Ingeniería Geológica. Madrid: Pearson Educación.

Hernández, Y. & López, J. (2019) Estudio Geomecánico de macizos rocosos ante la influencia de cargas externas, ubicados en sector Los Araques, municipio Sucre, del estado Mérida (Degree Project, Los Andes University). Mérida, Venezuela

Ramírez, P., & Alejano, L. (2004). Mecánica de Rocas 2: Fundamentos e ingeniería de taludes Recovered from https://oa.upm.es/14183/

React Native. (2024). Get Started with React Native. Recovered from: https://reactnative.dev/docs/getting-started.

Sönmez, H. y Ulusay, R. (2002). A discussion on the Hoek-Brown failure criterion and suggested modifications to the criterion verified by slope stability case studies. Yerbilimleri, 26, 77-99.

Tomás, R, Delgado J. y Cuenca, A. (2005). Procedimiento gráfico para la obtención de los parámetros de corrección del SMR a través de la proyección estereográfica. Alicante University. Recovered from: https://rua.ua.es/dspace/handle/10045

Received: *February 10th, 2025*

Accepted: *July 20th, 2025*

López Delgado, Luis: *Geological Engineer. University of Los Andes (2025).*
https://orcid.org/0009-0006-7492-5390

Molina Becerra, Germán: *Geological Engineer. Assistant Professor at the University of Los Andes (ULA), Venezuela. Master's student in Water Resources Planning and Development student. Director of the School of Geological Engineering at ULA Since 2024.email: gmolinab@ula.ve*
https://orcid.org/0009-0003-7684-5835

Cardillo Albarrán, Juan: *Full Professor at the Control Systems Department, os Andes University Mérida Vemezuela. Doctor in Automation (Université Paul Sabatier Toulouse-France) 2004, Doctor in Applied Sciences (University of Los Andes) 2014. email: ijuan@ula.ve.*
https://orcid.org/0000-0001-8358-677X

Cuevas Hernandez, Rómulo: *Geological engineer graduated from the University of Los Andes in Mérida, Venezuela. More than 10 years of experience in oil and gas geology operations and services. Skilled in planning and executing Geosteering projects in various environments and reservoirs. Currently Senior GEOSTEERING ANALYST working for ROGII. email: Romulo@rogii.com*
https://orcid.org/0009-0002-8932-007X

Artículo de Investigación. Revista Ciencia e Ingeniería. Vol 46, No.3 pp 331-342, agosto- noviembre, 2025
ISSN 1316-7081. ISSN Elect. 2244-8780 Universidad de los Andes (ULA)

Optimizing nutrition in rainbow trout: evaluation of alternative ingredients in feed formulation

Evaluación de materias primas alternativas en la formulación de alimentos para trucha arcoíris (*oncorhynchus mikyss*)

Villegas, Wilmer[1]*; Noboa, Glenda[1]; Izaguirre, César[1]; González, Aura[1]; De Lima, Aida[1]; Prato José [2]; Gómez, Ruben[1] †

[1] Laboratory of Food Science, Engineering and Biotechnology, Faculty of Engineering, School of Chemical Engineering, Universidad de los Andes, Mérida, Venezuela..

[2] Research Group Interdisciplinary Studies, Faculty of Engineering, National University of Chimborazo, Riobamba-Ecuador

*eng.wilmerv@gmail.com

Abstract

*Trout farming is a significant primary sector activity in Mérida, Venezuela; however, it has experienced a notable decline in recent years, largely due to difficulties in accessing suitable and affordable feed. The formulation of balanced diets for Rainbow Trout (Oncorhynchus mykiss) relies heavily on fishmeal and fish oil as essential raw materials. These ingredients are vital because they offer an optimal amino acid profile and contain Polyunsaturated Fatty Acids, which enhance the Feed Conversion Rate for this carnivorous salmonid species. However, the production of fishmeal and fish oil has been increasingly constrained by stringent regulations on trawling, which aim to address its detrimental effects on marine ecosystems and the competition for food resources among human populations. To address these challenges, several feed formulations have been proposed that theoretically fulfill the nutritional requirements of Rainbow Trout while considering the limitations concerning the inclusion of specific raw materials and the physiological factors pertinent to the species. To aid in the formulation calculations, a computer program named Trout **Formulation.exe** has been developed. This tool is designed to optimize feed composition in accordance with these nutritional requirements and constraints. As a result, six formulations are proposed that theoretically fulfill the nutritional requirements of Rainbow Trout, utilizing alternative raw materials instead of the two traditional ingredients. These alternatives include Black Soldier Fly (Hermetia illucens) larvae meal reared on fish industry waste substrate, as well as Amaranth (Amaranthus spp.) and Buckwheat (Fagopyrum esculentum) meal. It was determined that while a complete elimination of fish meal and fish oil from the formulation is not feasible—since they play a critical role in ensuring palatability and maintaining the ω6/ω3 balance essential for the proper development of the trout—the formulation incorporating up to 55% Black Soldier Fly larvae meal achieves a theoretical reduction of only 13% in the inclusion of Super Prime fish meal.*

Keywords: concentrated trout feed, black soldier fly larvae meal, amaranth, buckwheat, formulation.

Resumen

*La Truchicultura, como actividad del sector primario en el estado Mérida-Venezuela, ha decaído fuertemente en los últimos años, principalmente debido a la dificultad para acceder al alimento adecuado y a costos asequibles. La harina y aceite de pescado, son las materias primas clave en las formulaciones de alimento balanceado para Trucha Arcoíris (Oncorhynchus mykiss,) debido a su equilibrio aminoacídico y de Acidos Grasos Poliinsaturados, que aumentan la Tasa de Conversión Alimenticia de este salmónido carnívoro. Sin embargo, su producción está comprometida por las crecientes regulaciones sobre la pesca de arrastre, que afectan negativamente el equilibrio biológico de mares y océanos y compiten con la alimentación humana. En esta investigación, se plantean diversas formulaciones que cumplen teóricamente con los requerimientos nutricionales de la Trucha Arcoíris, considerando las limitaciones de inclusión de ciertas materias primas por razones fisiológicas. Para facilitar los cálculos de formulación, se creó un programa computacional denominado **Formulación Truchas.exe**. Como resultado, se proponen 6 formulaciones que cumplen teóricamente con los requerimientos nutricionales de la Trucha Arcoíris, utilizando materias primas alternativas como la harina de larva de*

Mosca Soldado Negra (Hementia Illucens) criada en substrato de residuos de la industria del pescado, harina de Amaranto (Amaranthus spp.) y harina de Trigo Sarraceno (Fagopyrum esculentum). Aunque no es viable eliminar completamente la harina y el aceite de pescado en la formulación, ya que garantizan la palatabilidad y el equilibrio ω6/ω3 necesario para el desarrollo adecuado de la trucha, se encontró que una formulación con hasta un 55% de harina de larva de Mosca Soldado Negra podría reducir teóricamente hasta un 13% la inclusión de harina de pescado de tipo Súper Prime.

Palabras clave: alimento concentrado para truchas, harina de larva de mosca soldado negra, amaranto, trigo sarraceno, formulación.

1 Introduction

Regarding salmonid feed, the trend has been oriented towards the formulation of concentrated fish feed from raw materials of plant and animal origin as an alternative to fishmeal, in order to achieve sustainable aquaculture over time. It has been reported (Makkar et al., 2014) that insect meal could potentially replace between 25% and 100% of fish meal in fish feed, mainly because the general levels of essential amino acids in insect meals are good for this purpose. In the case of vegetable meals, they provide a good source of starch which is useful for the feed pelleting process (Tacon, 1989) and some also provide an excellent source of amino acids and essential fatty acids which, in the latter case, can reduce the dependence on fish meal and fish oil as the main source of protein and lipids, respectively. Amino acids are the basic components of proteins and the amount of these elements present in the feed is decisive in determining the "quality" of the protein, which constitutes its value as a primary component of the diet (Guerrero-Muñoz, 2012). Of the 20 amino acids found in proteins, fish can metabolize 10 and therefore the others must be supplied in the diet, the latter are known as essential amino acids. For salmonids such as rainbow trout (Oncorhynchus mykiss), an absolute requirement of 10 ami-amino acids has been demonstrated: arginine, histidine, isoleucine, leucine, lysine, methionine, phenylalanine, threonine, tryptophan and valine (National Research Council, 1993).

Nutritional deficiencies caused by low amino acid intake in aquaculture species and animals are very difficult to diagnose due to the general state of alteration that is evident in the animal (Castro and Avilia, n.d.). Faced with a nutritional problem of this type, the main indicators shown by the animal are: a deterioration in conversion efficiency (feed/weight), a reduction in growth rate and a much higher mortality than expected (Guerrero-Muñoz, 2012). However, in certain fish species, such as rainbow trout, a deficiency of methionine or tryptophan also leads to the development of pathologies, because these amino acids not only constitute proteins, but are also used for the synthesis of other essential compounds (National Research Council, 1993).

In the case of dietary lipids, they must be important sources of essential fatty acids (EFAs), which are necessary for proper growth and development and also aid in the absorption of fat-soluble vitamins. Dietary lipids, mainly in the form of triacylglycerols, are hydrolyzed by digestive enzymes to a mixture of free fatty acids and 2-monoglycerides. These compounds are then absorbed and used for the synthesis of various cellular components such as fatty acids with double bonds at the ω6 (linoleic series) and ω3 (linolenic series) positions (Tacon, 1989; or catabolized for energy (National Research Council, 1993). Rainbow trout show an exclusive requirement of fatty acids belonging to the ω3 series in their diet: Linolenic acid (18:3ω3), Eicosapentaenoic acid (EPA) (20:5ω3) and Docosahexaenoic acid (DHA) (22:6ω3) (Tacon, 1989). Although ω6 fatty acids may be essential, their required level in the diet is unknown and evidence indicates that a high ratio of ω6 to ω3 fatty acids in a trout diet may actually be detrimental to the growth of the fish (Takeuchi & Watanabe, 1977). Feeding rainbow trout with experimental diets deficient in EFA has resulted in decreased growth and survival, as well as poor feed conversion efficiency (Tacon, 1989). Other effects of stress include dermal signs (broken fins), shock syndrome, myocarditis and increased mortality.

In order to obtain raw materials that meet the nutritional requirements of trout, these must have a composition that satisfies the needs to achieve their optimum development. In this sense, the required levels of the necessary macro and micronutrients that a concentrated feed must have to achieve a good development of Rainbow Trout, in its juvenile stage, are reported in Table 1.

In their natural habitat, rainbow trout consume insects that fall on aquatic surfaces; it is for this reason that alternatives to fish meal can be found with the use of insect meal. Black soldier fly larvae meal (*Hermetia illucens*) has been successfully implemented in concentrated diets for rainbow trout (Kroeckel et al., 2012), confirming that the good balance of essential amino acids contained in this meal satisfies the nutritional requirements of trout. Thanks to the ease with which this insect can be reared on low-cost substrates such as organic waste, especially those of the fishing industry, and its ability to take advantage of the nitrogen and phosphorus present in such waste, generating a lower environmental impact in this matrix, the meal of the larvae of this fly represents a valid source of protein and fat, with remarkable results mainly in aquaculture (Mancini et al., 2017). In addition to this, the Black Soldier Fly, from the family of the diptera *Stratiomyidae*, can be found in

nature in tropical and subtropical areas. It has not been reported as a transmitter of diseases; on the contrary, it acts as a regulating agent of other pathogenic pests such as the common house fly (*Musca domestica*).

Table 1. Nutritional requirements of a concentrated feed for Rainbow Trout to ensure good development during the ova to fry stage.

Macro or Micronutrient	Percentage required in the diet (%)
Crude Protein [1,2]	≥ 50
Essential Amino Acids [3]	
Arginine	≥1,4
Histidine	(0,6-1)
Isoleucine	≥1,0
Leucine	(1,8-2,5)
Lysine	≥2,1
Cystine + Methionine	≥1,1
Phenylanine	≥1,2
Threonine	≥1,4
Tryptophan	≥0,2
Valine	≥1,2
Lipids [1]	(10-20)
If as α-Linolenic Acid	20
If as EPA and DHA	10
Carbohydrates [3]	≤ 20
Minerales [1]	
Calcium (*)	0-1
Phosphorus	0,7-0,8 (inorganic)
Magnesium	≥0,006
Iron	N. D
Zinc	0,0015-0,003
Iodine	0,6-1,1
Selenium	0,1-0,35

Vitamins [1,2]			
Vitamin A +	≤ 2000	**Thiamine** *	≥10
Vitamin D_3 +	≤ 3000	**Riboflavin** *	≥20
Vitamin K *	≤ 80	**Niacin** *	150
Vitamin E +	≥ 30	**Pantothenic Acid** *	40
Antioxidant *	200	**Pyridoxine** *	10
Moisture (%)	6-10	**Cobalamin (B_{12})** *	≥0,02
Canthaxanthin	190-450	**Folic acid***	≥5
Biotin*	1	**Inositol***	≥400
Ascorbic acid*	≥100	**Colina***	≥3000

Label: +: U.I/Kg food, *: mg/Kg food.
Sources: Hilton and Slinger, 1981 (1); Guerrero-Muñoz, 2012 (2); National Research Council, 1993 (3).

On the other hand, although there has been little success in the substitution of fishmeal with raw materials of vegetable origin, Amaranth (*Amaranthus spp*.) as well as Common Buckwheat Flour (*Fagopyrum esculentum*) have a higher crude protein content than that presented by cereals that are also used in fish feed formulations, presenting one of the best amino acid profiles of all protein-rich vegetable feeds, headed mainly by a high content of lysine and methionine which are deficient in most cereals and which are fundamental in the growth of Rainbow Trout. In addition to its protein content, Amaranth and Buckwheat Flours represent a good source of starch, (Venskutonis & Kraujalis, 2013), which makes it suitable for industrial applications in the elaboration of concentrated feed for Trout.

This research, in addition to determining alternative raw materials that reduce the dependence on fishmeal and fish oil, proposes formulations for the nutrition of Rainbow Trout, considering at the same time the limitations that these raw materials have at a nutritional and economic level, through the development of a computer program.

2 Background

2.1 Black Soldier Fly Larvae Meal in commercial salmonid feed formulas

Makkar et al. (2014) highlight the potential of rearing Black Soldier Fly larvae as an alternative to reduce by 25-100 % the use of soybean meal and fish meal in fish feed formulation, whose production costs are constantly increasing. In particular, in rainbow trout feed, it was demonstrated that dried pre-pupae of black soldier fly, reared on dairy cattle manure enriched with 25-50 % trout offal, can replace up to 50 % of fishmeal-derived protein in diets for a period of 8 weeks. This replacement had no significant impact on fish growth or sensory quality of trout fillets, although a slight (but not statistically significant) reduction in growth was observed.

During a 78-day period, isonitrogenous, isolipidic and isoenergetic diets were evaluated with increasing levels of partially defatted larval meal of Hermetia illucens (HI) as a substitute for fish meal: 0 % (HI0, control diet), 25 % (HI25) and 50 % (HI50). The results indicated that partially defatted larval meal can be included in trout diets up to 40 % without affecting survival, growth performance, feed conversion factor (kg feed supplied/kg weight gain of trout), somatic indices, physical quality parameters of dorsal fillet and intestinal morphology of the fish.

However, Dumas et al. (2018) investigated the impact of partially defatted black soldier fly larval meal (BSFLM) and mechanically extracted black soldier fly larval oil (BSFLO) on growth, body composition, gut histology and

blood plasma biochemistry of rainbow trout during a three-month growth trial. They found that the feed conversion factor increased significantly with each increasing level of BSFLM inclusion ($p < 0.05$) and that there was a negative relationship between blood glu-cosa and BSFLO inclusion level, suggesting a possible antihyperglycemic effect of BSFLO in fasting trout. Based on these results, the authors recommended a maximum inclusion of 13 % for BSFLM in rainbow trout diets, while for BSFLO the inclusion could not exceed 10 %. These limits are associated with a higher digestibility of hydroxyproline in diets containing black soldier fly larvae products, representing potential benefits for trout.

In the study of physicochemical characteristics of rainbow trout fillets, Mancini et al. (2017) and Renna et al. (2017) evaluated three diets with progressive levels of fish meal substitution by *Hermetia illucens* larval meal (Hi): a control diet without Hi inclusion (0 %), Hi25 (25 % Hi inclusion) and Hi50 (50 % Hi inclusion). The results showed an increase in saturated fatty acid content, particularly lauric acid (C12:0), associated with Hi inclusion, at the expense of a decrease in monounsaturated and polyunsaturated fatty acids (including ω3 and ω6). In addition, a reduction in the yellowish coloration of fillets was observed with the Hi50 diet, which negatively impacted the concentration of adenosine monophosphate in fillets. However, no significant differences in the proximal composition or protein profile of the fillet were reported.

Bolton et al. (2021) formulated five diets to evaluate their effects on rainbow trout fillets. These included a basal diet with fish meal (CTRL), two diets with inclusion of 15 % and 30 % black soldier fly (BSF) larvae meal (BSF15 and BSF30, respectively), and two diets with the same levels of BSF but supplemented with a supplemental pro-tease enzyme (BSF15P and BSF30P, respectively), designed to evaluate possible dietary improvement. The results showed an increase in yellow coloration of the muscle as the proportion of BSF in the diet increased ($p = 0.004$). Also, trout fed BSF showed significantly less lipid peroxidation after harvest ($p < 0.001$), with a reduction in malondialdehyde levels proportional to the increase in BSF in the diet, regardless of the addition of protease. In addition, protease treatments increased total protein concentration in trout body content, reflecting potentially improved efficiency of protein utilization. In conclusion, the protease-enriched black soldier fly larvae meal-based diet constitutes a high-energy protein concentrate, viable to replace up to 30% of fish meal in rainbow trout diets, without adverse effects on trout growth.

2.2 Amaranth and Buckwheat as part of a concentrated fish feed formulation

The use of pseudocereals such as amaranth and buckwheat in fish feed formulation presents an underexplored area of study, but with enormous potential for development. Poczyczyński et al. (2014) analyzed the effects of substituting fish oil for amaranth oil in rainbow trout feeds, finding that the highest daily growth rate (3.75%/day) corresponded to the group fed the diet containing the highest level of amaranth oil (7.2% inclusion). Although there is no direct history on the use of amaranth meal as a protein ingredient in rainbow trout diets, Ngugi et al., 2017 evaluated the nutritional properties and feasibility of replacing fish meal with amaranth leaf protein concentrates (ALPC, *Amaranthus hy-bridus*) in the diet of Nile tilapia (*Oreochromis niloticus*). This study compared the effects of substitution in terms of fish growth, nutrient utilization, body composition and apparent digestibility, demonstrating that it is possible to replace up to 80% of fishmeal with ALPC without affecting the performance of *O. niloticus*.

Although at the moment, there is no research linking the use of buckwheat flour in concentrated feed formulations for rainbow trout, it has a crude protein content between 12% and 18.9%, higher than that of cereals that are also commonly used in fish feed formulations (Christa & Soral-Smietana, 2008). More important than the crude protein content, however, is the presence of one of the best amino acid profiles of all protein-rich vegetable feeds, headed mainly by a high lysine content (amounting to about 6 g/100 g of protein) (Bonafaccia et al., 2003), which is fundamental in the growth of Rainbow Trout, and which is deficient in most cereals, which may account for its efficiency in the use of formulations.

3 Methodology

3.1 Design of a computer program named Truchas.exe

In order to develop a formulation that meets the nutritional requirements of rainbow trout, it is essential that it provides a composition that satisfies the biological demands necessary for proper development. In this context, the use of programming methods allows the design of diets with an optimal balance of nutrients, resulting in more efficient and profitable fish rearing (National Research Council, 1993). These programs consider several key factors: the specific nutritional needs of rainbow trout, the nutrient content and bioavailable energy in the ingredients, the minimum and maximum restrictions on the concentrations of various components, and, last but not least, the cost of the raw materials used.

Based on the research on the nutritional requirements for optimal growth of rainbow trout, a program was developed and named Trout Formulation.exe. This software,

designed on the Microsoft Visual Basic platform and programmed in C++, integrates four main modules that are described below.

3.1.1 Main Program Window

The main window appears after logging into the Trout Formulation.exe program (see Figure 1). In this module, the user finds shortcuts to all the functionalities of the software, organized in icons for convenience. In addition, at the bottom of the interface, an information bar shows the name of the active user, as well as the date and time of use.

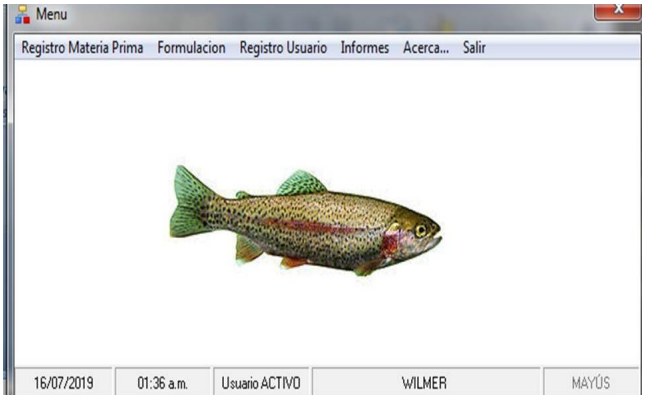

Figure 1. Main screen of the program Trout Formulation.exe

3.1.2 Raw Materials Registration

By selecting the icon located at the top left of the main window, you access the Raw Material Registration module. This module allows recording the nutritional composition of each raw material used in the feed formulation, covering both macronutrients and micronutrients. The information recorded is stored in an internal database designed in Microsoft Office Access®. The nutritional composition of the raw materials is recorded in specific units per 100 g of the ingredient, as follows: macronutrients and minerals, in percentage by mass (% w/w); vitamins A, D3 and E are quantified in Inter-national Units (I.U.); while the rest of the vitamins are entered in milligrams per kilogram of raw material (mg/kg).

3.1.3 Formulation

The Formulation module allows you to perform mass balances to calculate the amounts of macro- and micro-nutrients in the diet, using the units previously described. These calculations are made from the entered proportions of the selected raw materials, applying the following formulas:

$$\%\boldsymbol{Nutrient} = \frac{(\boldsymbol{M_1} * \boldsymbol{Nut_{M1}} + \boldsymbol{M_2} * \boldsymbol{Nut_{M2}} \ldots + \boldsymbol{M_n} * \boldsymbol{Nut_{Mn}})\boldsymbol{g}}{\boldsymbol{1000g\ of\ formulated\ feed}} * \boldsymbol{100}$$

Equation 1. Internal formula of the Program to calculate the nutrients expressed in Percentage (% w/w) where Nut_{Mn}: Nutrient contained in the nth raw material used in the formulation.

$$\boldsymbol{Vitamin} = \frac{\boldsymbol{M_1} * \frac{\boldsymbol{Nut_{M1}}}{\boldsymbol{100g}} + \boldsymbol{M_2} * \frac{\boldsymbol{Nut_{M2}}}{\boldsymbol{100g}} \ldots + \boldsymbol{M_n} * \frac{\boldsymbol{Nut_{Mn}}}{\boldsymbol{100g}}}{\boldsymbol{1000}}$$

Equation 2. Internal formula of the Program to calculate vitamins expressed in miligrams and International Units

The formulator can access the raw materials stored in the program database and assign the corresponding amount of each to formulate 1000 g of feed (ensuring that the total sum of the ingredients is exactly 1000 g). Once the process is completed, it is possible to assign a unique ID or specific record to save the formulation. The program will automatically calculate the resulting nutritional composition, which will be displayed on the screen when the "Print" button is pressed. Figure 2 illustrates an example of the nutritional composition of a random formulation, expressed in the units previously described.

Figure 2. Report shown by the Trout Formulation.exe program, of a random formulation with ID: 4. In blue is denoted crude protein (CP) and essential amino acids, in yellow lipids, in red carbohydrates and in black crude fiber (CF), minerals and other vitamins.

3.2 Multi-level formulation table

The feed formulation process, according to the proposed computer program, is characterized by being iterative and generating an unlimited number of alternatives. However, evaluating all these formulations through calculations, field tests and laboratory trials would take considerable time. Therefore, it is essential to establish specific conditions as a preliminary criterion of feasibility and effectiveness, in order to filter and optimize the formulations before entering them into the program. In this context, and based on the literature review, a multilevel table was designed. This tool allows, in a precise way, to identify those combinations of raw materials that, at a theoretical level, meet the nutritional requirements of rainbow trout in their juvenile stage (given that this phase is critical due to its high caloric demand and sensitivity of

trout to nutritional imbalances), thus facilitating their subsequent entry into the program to generate the final composition of the formulations. The multi-level table optimizes the process by discarding unviable formulations before their evaluation in the program.

buckwheat flour, whose nutritional composition was documented by Bonafaccia et al. (2003), were included.

To cover lipid requirements and balance ω3/ω6 fatty acids, amaranth oil, based on information from

Sources: ([1]): Paucar, 2014; ([2]): Venskutonis y Kraujalis, 2013, Bonafaccia et al., 2003; ([3]): Hilton y Slinger, 1981; ([4]): Spranghers et al., 2017; ([5]): Barroso et al., 2019; ([6]): Bortone, 2007 y ([7]): Conchillo et al., 2006

Figure 3. Multilevel table designed based on the composition and limitations in the use of raw materials.

To design the multilevel table, information was collected on the selected raw materials: a) Fish meal: Three types were included from lower to higher quality (Prime, Super Prime and LT - low temperature), based on the nutritional composition and production costs described by Paucar (2014). b) Black soldier fly larvae meal: Nutritional variants of larvae fed with chicken feed and with waste from the fishing industry were considered, according to the findings of Barroso et al. (2019). c) Starch sources: Amaranth flour, obtained from seeds of species such as A. Dubius, A. Caudatus, A. Cruentus and A. hypochondriacus (studied by Venskutonis & Kraujalis, 2013b), and Poczyczyński et al. (2014), and fish oil, as reported by Conchillo et al. (2006), were incorporated.

In addition, the multilevel table establishes constraints related to the costs of these raw materials. For example, although fishmeal offers an excellent protein and essential amino acid profile, its inclusion as a main ingredient in trout feeds is limited. This is due to the increase in cost, depending on the nutritional quality, which has repercussions on economic formulations. As for amaranth and buckwheat flours, despite their good lysine content, their use is restricted to levels of 20-22% in the formulation, mainly due to their high carbohydrate content, an inherent characteristic of vegetable flours.

When analyzing the limitations of the use of the two types of black soldier fly larvae meal as a pure ingredient, the following is observed: the meal derived from larvae reared on a broiler feed substrate presents a high content of saturated fatty acids, accompanied by a reduced level of ω3 fatty acids, which could lead to growth deficiencies in trout. On the other hand, in the meal obtained from larvae fed with a substrate coming from fishery waste, doubts arise about its palatability from an inclusion level of 50%. Figure 3 illustrates the multilevel formulation table developed.

To complement the multilevel table, the diets proposed by Hilton and Slinger, (1981), have made it possible to determine the appropriate limits for the inclusion of meals, oils, premixes, pigments and antioxidants (see Table 2), with the purpose of reaching the optimum levels of proteins, lipids, carbohydrates, minerals and vitamins necessary for the healthy development of rainbow trout.

Table 2. Ideal ratios of raw materials for the formulation of balanced diets for rainbow trout.

Flours (%)	84
Oils (%)	10
Premix Vitamins (%)	1
Premix Minerals (%)	1
Pigmenters (mg/Kg feed)	190
Antioxidants (mg/Kg incorporated flours)	200-500
Water (%)	8

Source: Hilton and Slinger (1981).

4 Results and Discussion

After entering various formulations in the *Trout Formulation.exe* program, six theoretical formulations were selected for in situ testing of a concentrated feed for Rainbow Trout in the fry stage. The proportions of raw materials used in these formulations are presented in Table 3.

Table 3. Proportion of raw materials in proposed formulations.

Formulation	**1**	**2**	**3**	**4**	**5**	**6**
%						
Fishmeal SP	60	60	57	31	13	-
Amaranth Flour	-	25	22	22	20	21
Buckwheat Flour	25	-	6	-	-	-
Black Soldier Fly Larvae meal [+]	-	-	-	38	55	67
Fish Oil	10	10	10	4	8,5	7
Amaranth Oil	-	-	-	2	-	1
Premix Vitamins*	1	1	1	1	1	1
Premix Minerals*	1	1	1	1	1	1
Water	3	3	3	1	1,5	2

Label: SP: Super Prime, +: Black soldier fly larvae meal reared on fish substrate described by Barroso et al. (2019). * With the conditions described by Hilton and Slinger (1981).

On the other hand, tables 4 and 5 show the results of the nutritional composition generated by the program, based on the mass balances of the proposed formulations. Based on these data, the theoretical feasibility of using black soldier fly larvae meal, fed with substrates from fishery waste, as well as amaranth flour and oil and buckwheat flour, was evaluated. These ingredients were considered as possible substitutes for fish meal and fish oil in concentrate feed formulations designed for rainbow trout.

In formulations 1 (which includes up to 60% Super Prime fishmeal) and 3 (with up to 28% vegetable meals), a protein level slightly lower than that reported as optimal for rainbow trout during the fingerling phase (≤45%) was observed (Hilton and Slinger, 1981; Orna, 2010). However, both formulations present a higher balance than required in all essential amino acids for rainbow trout proposed by Halver (1972), highlighting the level of lysine (≥2.1%), which could favor an adequate development of this salmonid.

In formulation 6 (which totally excludes fishmeal), although the protein requirement is met, the lysine level is close to the lower limit necessary for trout feeding. Therefore, the extent to which it is feasible to eliminate the inclusion of fishmeal in optimal formulations should be carefully evaluated.

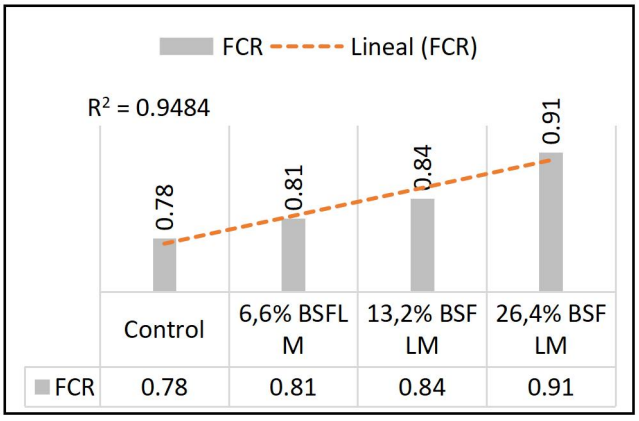

Source: (Dumas et al., 2018).
Label: BSFLM: Black soldier fly larvae meal.

Figure 4. Increase in Feed Conversion Factor (FCR) with respect to the increase of black soldier fly larvae meal in the formulation.

According to Dumas et al. (2018), an inclusion of up to 26.4% of black soldier fly larvae meal as seen in Figure 4 could increase the Feed Conversion Factor (FCR) (feed administered in g/fish mass gain in g) by 15% in trout, resulting in trout reaching marketable size at least one month later than those fed the control formulation.

However, Renna et al. (2017) reported that a partially defatted black soldier fly larvae meal can be used in rainbow trout diets with inclusion levels up to 40%, without compromising survival, growth, somatic indices, or dorsal fillet quality. Both studies agree on the need for further studies to design feeding strategies and dietary formulations that mitigate the adverse effects of insect meal on the fatty acid profile of trout, which are largely dependent on the substrates used for rearing black soldier fly larvae.

Table 4. Theoretical nutritional composition in macronutrients of the formulated diets.

Nutrient	Formulations					
	(1)	(2)	(3)	(4)	(5)	(6)
Protein (%)	43,81	45,25	43,29	48,48	45,48	45,14
Arginine (%)	2,50	2,87	2,73	2,58	2,48	2,06
Histidine (%)	1,05	1,07	1,02	1,15	1,12	1,08
Leucine (%)	3,27	3,34	3,20	3,06	2,71	2,41
Lisina (%)	5,00	5,10	4,87	3,78	2,25	2,07
Methionine (%)	4,09	4,13	3,78	2,48	2,36	1,78
Phenylalanine (%)	1,73	1,86	1,77	1,68	1,48	1,32
Threonine (%)	1,64	1,76	1,68	1,64	1,52	1,33
Tryptophane (%)	0,45	0,37	0,37	0,40	0,41	0,37
Valine (%)	1,95	1,97	1,89	2,06	2,06	1,87
Lipids (%)	16,78	16,80	16,55	16,72	20,51	20,87
C18:3ω3 (%) *	0,38	0,38	0,37	0,34	0,40	0,39
C20:5ω3 (%) *	5,37	5,38	5,18	4,04	6,48	6,01
C22:6ω3 (%) *	4,27	4,27	4,11	4,47	7,37	7,54
∑ω3 (g/100 g Lip) *	54,08	54,07	53,07	33,47	46,55	40,12
∑ω6 (g/100 g Lip) *	5,056	5,86	6,09	16,29	7,79	13,15
ω6/ω3	0,09	0,11	0,11	0,486	0,17	0,33
Carbohydrates (%)	20,05	15,42	18,34	13,57	12,34	12,96
Fiber (%)	14,44	9,07	10,09	7,29	6,39	4,86

Label: *: Balances performed manually

In relation to the level of polyunsaturated fatty acids (HUFA) type ω3, which constitute the main source of energy for the vital functions of Rainbow Trout, formulations 1, 2 and 3, where Amaranth Flour and Buckwheat Flour are used as a partial substitute for Fish Meal, present a balanced content of these fatty acids. This is mainly due to the inclusion of a higher percentage of fish oil, known for its high content of ω3 fatty acids. In spite of having a lower lipid level than other formulations, they reach a value close to 10% w/w in the sum of eicosapentaenoic acid (EPA) and docosahexaenoic acid (DHA). This characteristic allows the trout to optimize the use of essential amino acids for the synthesis of "body protein", while using EPA and DHA in energetic functions, such as homeo-viscous regulation, a process by which fish adjust the composition of the phospholipids of their bio-membranes in response to changes in environmental temperature (National Research Council, 1993).

Table 5. Theoretical nutritional composition in micronutrients of the formulated diets.

Nutrient	Formulations					
	(1)	(2)	(3)	(4)	(5)	(6)
Phosphorus (%)	8,76	0,13	0,14	0,36	0,74	0,52
Calcium (%)	0,12	0,16	0,15	1,19	2,28	2,08
Magnesium (%)	3,08	0,07	0,06	0,36	0,51	0,58
Iron (%)	1,13	0,008	0,008	0,02	0,04	0,04
Zinc (%)	7,58	0,01	0,02	0,02	0,02	0,03
Iodine (%)	0	0,001	0,001	0,03	0,04	0,05
Selenium (%)	0	0	0	0,004	0,005	0,007
Thiamine (mg)	25,7	25,25	25,39	25,22	25,2	25,21
Riboflavin (mg)	75,35	76,23	76,16	76,08	75,98	76,03
Niacin (mg)	142,55	127,25	131,19	126,98	126,8	126,89
Pant. Ac (mg)	75,00	78,75	78,30	78,30	78	78,15
Pyridoxine (mg)	15,38	16,9	16,76	16,67	16,52	16,60
B_{12} (mg)	15	15	15	15	15	15
Folic Ac. (mg)	5	5	5	5	5	5
Biotin (mg)	0,25	0,25	0,25	0,25	0,51	0,25
Ascorbic Ac. (mg)	200	218,75	216,50	78,30	215	215,75
Inositol (mg)	0	1,1	0,97	0,97	0,88	0,924
Choline (mg)	0	0	0	0	0	0
Vitamin K (mg)	13,50	13,50	13,50	13,50	13,50	13,50
Vitamin A (U.I)	4000	4005	4004	4004	4004	4004
Vitamin D_3 (U.I)	250	250	250	250	250	250
Vitamin E (U.I)	75	75	75	75	75	75

Label: Pant Ac: Pantothenic Acid; Folic Ac: Folic Acid; Ascorbic Ac: Ascorbic Acid

On the other hand, formulations 4, 5 and 6, which integrate Black Soldier Fly larvae meal reared on fishery waste substrates, maintain lipid and protein percentages above the recommended minimum. However, formulation 4 presents a ω6/ω3 ratio higher than the optimum range established for Rainbow Trout feeding (0.08-0.2) (National Research Council, 1993), due to its higher inclusion percentage of Amaranth Oil, rich in ω6 type fatty acids.

Although to a lesser extent, formulation 6 also exhibits such a characteristic; however, it shows a difference of more than 10% in the summation of EPA (C20:5) and DHA (C22:6), which, as mentioned above, are structurally fundamental to the physiological functions of fish. The use of Amaranth Oil as part of the formulation is feasible, as a preliminary study by Poczyczyński et al. (2014) showed that, even with higher levels of Amaranth Oil inclusion than those proposed in these formulations (5.0% and 7.2%), no significant differences were found between the experimental groups and the control group. In addition, the highest specific growth rate (SGR) (3.75%/day) was observed in fish fed with the formulation containing the highest percentage of Amaranth Oil. In this group, there was also a higher content of crude protein and fat in the fish flesh (16.3% and 10.5% of body weight, respectively). Although the fatty acid composition was similar, a higher content of Amaranth Oil in the diet resulted in a marked decrease of EPA and DHA in the lipid profile of the fish.

Formulation 5, which includes only 13% Super Prime Fishmeal, stands out as the most nutritionally adequate formulation to ensure effective and sustainable feeding of Rainbow Trout. This formulation incorporates Black Soldier Fly Larvae Meal, a raw material that can significantly reduce the dependence on fish meal in traditional diets for this salmonid. Modifications in the rearing substrate of this larva further increase the flexibility of its use, since rearing larvae in a medium rich in ω3 fatty acids, as evidenced by Barroso et al. (2019) and Segura-Cazorla (2014), considerably improves their nutritional profile in relation to these compounds.

It is important to note that one factor that could influence the efficacy of substituting fish meal for black soldier fly larvae meal is the presence of chitin in the exoskeleton of the larvae at the prepupal stage. This polysaccharide, which constitutes approximately 87.0 g/kg dry mass (Kroeckel et al., 2012), can affect digestibility and nutrient absorption in Rainbow Trout. Although chitinase activity has been identified in the blood, plasma, and intestinal tract of some fish, it has not been conclusively demonstrated that this enzyme efficiently breaks down chitin in this species. Therefore, diets containing chitin or cellulose may significantly interfere with gastric lysozyme function, as noted by Lindsay (1984). The possible loss of gastric lysozyme could increase the susceptibility of trout to bacterial diseases sensitive to this enzyme, although this hypothesis still requires experimental validation. Since cellulose is a common ingredient in commercial salmonid feeds and is frequently used as a binding agent in experimental diets (starch), this aspect deserves further study.

5 Conclusions

Black Soldier fly larvae meal is presented as a promising alternative to replace fish meal in the formulation of concentrated feed for rainbow trout. Its nutritional profile is significantly optimized by using fish waste from the fishing industry as feed substrate. Likewise, the incorporation of Amaranth and Buckwheat flour, thanks to its excellent profile of essential amino acids, would efficiently complement this substitution, enhancing the quality of the formulated feed.

The ratio of ω6/ω3 fatty acids is a determining factor in ensuring that Rainbow Trout meet their energy requirements. To achieve an optimal value (0.08-0.2), the inclusion of fish oil is key. However, validation of the use of amaranth oil as a substitute in formulations requires additional studies to specifically evaluate its impact on the feed conversion ratio (FCR) of rainbow trout.

Based on the analyses carried out, it is concluded that formulation 5, composed of 13% Super Prime fishmeal, 20% Amaranth meal, 55% Black Soldier Fly larvae meal and 8.5% fish oil, stands out as the most adequate from both a nutritional and economic perspective. This formulation satisfies the parameters established in this research, guaranteeing an efficient and sustainable feed for rainbow trout, and constitutes an important step towards the reduction of fishmeal dependence in aquaculture.

The development of a computer program integrated to the application of a multilevel formulation table increased the capacity to calculate and develop 6 formulations for the feeding of Rainbow Trout with high potential for success, which represents a fundamental advance in the optimization of aquaculture, since it is based on rigorous technical and economic criteria for the design of nutritionally balanced formulations that maximize the growth of Trout with a minimized environmental impact.

Referencias

Barroso, F. G., Sánchez-Muros, M. J., Rincón, M. Á., Rodriguez-Rodriguez, M., Fabrikov, D., Morote, E., & Guil-Guerrero, J. L. (2019). Production of n-3-rich insects by bioaccumulation of fishery waste. *Journal of Food Composition and Analysis*, *82*(June). https://doi.org/10.1016/j.jfca.2019.103237,

Bolton, C., Muller, N., Hyland, J., Johnson, M., Valente, C., Davies, S., & Wan, A. (2021). Black soldier fly

larval meal with exogenous protease in diets for rainbow trout (Oncorhynchus mykiss) production meeting consumer quality. Journal of Agriculture and Food Research, 6, 100232. https://doi.org/10.1016/j.jafr.2021.100232.

Bonafaccia, G., Marocchini, M., & Kreft, I. (2003). Composition and technological properties of the flour and bran from common and tartary buckwheat. *Food Chemistry*, *80*(1), 9–15. https://doi.org/https://doi.org/10.1016/S0308-8146(02)00228-5.

Bortone, E. (2007). *Diseño de plantas de alimentos balanceados especializadas para peces y crustáceos - Engormix*. https://www.engormix.com/balanceados/articulos/diseno-plantas-alimentos-balanceados-t27297.htm.

Castro, E., & Avilia, L. (s/f). *Control de calidad de insumos y dietas acuicolas*. FAO. Recuperado el 11 de julio de 2019, de http://www.fao.org/tempref/FI/CDrom/aquaculture/a0845t/volume2/docrep/field/003/ab482s/AB482S06.htm.

Christa, K., & Soral-Smietana, M. (2008). Buckwheat grains and buckwheat products - nutritional and prophylactic value of their components - a review. *Czech Journal of Food Sciences*, *26*(3), 153–162. https://cjfs.agriculturejournals.cz/artkey/cjf-200803-0001.php.

Conchillo, A., Valencia, I., Puente, A., Ansorena, D., & Astiasarán, I. (2006). Componentes funcionales en Aceites de Pescado y de Alga. *Nutrición Hospitalaria*, *21*(3).

Dumas, A., Raggi, T., Barkhouse, J., Lewis, E., & Weltzien, E. (2018). The oil fraction and partially defatted meal of black soldier fly larvae (Hermetia illucens) affect differently growth performance, feed efficiency, nutrient deposition, blood glucose and lipid digestibility of rainbow trout (Oncorhynchus mykiss). *aquaculture*, #pagerange#. https://doi.org/10.1016/j.aquaculture.2018.03.038.

Guerrero-Muñoz, J. (2012). La nutrición y la alimentación eficiente de los peces. *Agrinal Colombia s.a*, 1–12.

Halver, J. E. (1972). *Fish nutrition*. Academic Press.

Hilton, J. W., & Slinger, S. J. (1981). *Nutrition and Feeding of Rainbow Trout* (D. of F. and Oceans, Ed.). Government of Canada Fisheries and Oceans.

Kroeckel, S., Harjes, A.-G. E., Roth, I., Katz, H., Wuertz, S., Susenbeth, A., & Schulz, C. (2012). When a turbot catches a fly: Evaluation of a pre-pupae meal of the Black Soldier Fly (Hermetia illucens) as fish meal substitute — Growth performance and chitin degradation in juvenile turbot (Psetta maxima). *Aquaculture*, *364–365*, 345–352. https://doi.org/10.1016/j.aquaculture.2012.08.041.

Lindsay, G. J. H. (1984). Adsorption of rainbow trout (Salmo gairdneri) gastric lysozymes and chitinase by cellulose and chitin. *Aquaculture*, *42*(3), 241–246. https://doi.org/https://doi.org/10.1016/0044-8486(84)90104-2.

Makkar, H. P. S., Tran, G., Heuzé, V., & Ankers, P. (2014). State-of-the-art on use of insects as animal feed. *Animal Feed Science and Technology*. https://doi.org/10.1016/j.anifeedsci.2014.07.008.

Mancini, S., Medina, I., Iaconisi, V., Gai, F., Basto, A., & Parisi, G. (2017). *Impact of black soldier fly larvae meal on the chemical and nutritional characteristics of rainbow trout fillets*. https://doi.org/10.1017/S1751731117003421.

National Research Council. (1993). *Nutrient Requirements of Fish*. http://www.nap.edu/catalog/2115.html.

Ngugi, C. C., Oyoo-Okoth, E., Manyala, J. O., Fitzsimmons, K., & Kimotho, A. (2017). Characterization of the nutritional quality of amaranth leaf protein concentrates and suitability of fish meal replacement in Nile tilapia feeds. *Aquaculture Reports*, *5*, 62–69. https://doi.org/10.1016/j.aqrep.2017.01.003.

Orna, E. (2010). Manual de alimento balanceado para truchas. *Embajada de España en Perú*, 30. http://docplayer.es/6836244-Manual-de-alimento-balanceado-para-truchas.html.

Paucar, L. M. (2014). C*ontrol de calidad de la harina de pescado* (p. 20). Universidad Nacional del Santa ing. agroindustrial. http://biblioteca.uns.edu.pe/saladocentes/archivoz/curzoz/semana_13.pdf.

Poczyczyński, P., Gomułka, P., Woźniak, M., & Szostak, I. (2014). *Preliminary Study on the Partial Substitution of Fish Oil with Amaranth Oil in diets for Rainbow trout (Oncorhynchus mykiss) Fingerlings: Effects on Body Composition and Fatty Acids Contents*. *462*, 457–462. https://doi.org/10.4194/1303-2712-v14.

Renna, M., Schiavone, A., Gai, F., Dabbou, S., Lussiana, C., Malfatto, V., Prearo, M., Capucchio, M. T., Biasato, I., Biasibetti, E., De Marco, M., Brugiapaglia, A., Zoccarato, I., & Gasco, L. (2017). Evaluation of the suitability of a partially defatted black soldier fly (Hermetia illucens L.) larvae meal as ingredient for rainbow trout (Oncorhynchus mykiss Walbaum) diets. *Journal of Animal Science and Biotechnology*, 13. https://doi.org/10.1186/s40104-017-0191-3.

Segura-Cazorla, M. (2014). *Composición Bromatológica Hermetia Illucens*. Universidad de Almería.

Spranghers, T., Ottoboni, M., Klootwijk, C., Ovyn, A., Deboosere, S., De Meulenaer, B., Michiels, J., Eeckhout, M., De Clercq, P., & De Smet, S. (2017). Nutritional composition of black soldier fly (Hermetia illucens) prepupae reared on different organic waste substrates. *Journal of the Science of Food and Agriculture*, *97*(8), 2594–2600. https://doi.org/10.1002/jsfa.8081.

Tacon, A. (1989). N*utricion y alimentacion de peces y camarones cultivados (manual de capacitación)*.

Apoyo a las actividades regionales de acuicultura en america latina y el caribe", aquila ii (gcp/rla/102/ita). http://www.fao.org/3/AB492S/AB492S00.htm#TOC

Takeuchi, T., & Watanabe, T. (1977). Dietary levels of methyl laurate and essential fatty acid requirement of rainbow trout. *Bull. Jpn. Soc. Sci. Fish*.

Venskutonis, P. R., & Kraujalis, P. (2013). Nutritional Components of Amaranth Seeds and Vegetables: A Review on Composition, Properties, and Uses. *Comprehensive Reviews in Food Science and Food Safety*, *12*(4), 381–412. https://doi.org/10.1111/1541-4337.12021

Received: *April15th, 2025*

Accepted: *July 22th, 2025*

Villegas, Wilmer: *Chemical Engineer, Universidad de los Andes. Adjunct Researcher, Laboratory of Food Science, Engineering and Biotechnology, Faculty of Engineering, Universidad de los Andes. Quality Analyst, Packaging Laboratory, Cervecería Polar C.A.*
https://orcid.org/0009-0005-5303-0750

Noboa, Glenda*. MSc in Chemical Engineering (U.L.A). Associate Professor. Dept. of Industrial and Applied Chemistry, School of Chemical Engineering. School of Engineering. Head of the Food Science, Engineering and Biotechnology Laboratory. E-mail: glenda@ula.ve* *https://orcid.org/0009-0008-4585-8437*

Izaguirre, César*. Degree in Chemistry. ULA. Interfaculty Postgraduate Course in Food Science and Technology. SCIENCES-UCV. Master's Degree. Researcher of the School of Chemical Engineering. Laboratory of Food Science, Engineering and Biotechnology ULA. E-mail: cmizag@gmail.com* *https://orcid.org/0009-0004-0351-8515*

González, Aura Marina*, Chemical Engineer, MSc Applied Chemistry ULA Faculty of Sciences, Doctorate in Applied Sciences ULA Engineering Faculty, Full Professor, Researcher in Science and Technology of Applied Chemistry. Email: auragonza274@gmail.com.*
https://orcid.org/0009-0003-4147-1044

De Lima, Aída, *Chemical Engineer ULA, MSc Chemical Engineering ULA. Assistant Professor, attached to the Department of Industrial and Applied Chemistr. School of Chemical Engineering. ULA Engineering Faculty, researcher in food science and technology. Email: aidajdl@gmail.com.*
https://orcid.org/0009-0003-3850-0019

Prato, José G. *PhD. Ingeniería Química. Grupo de Investigación: Estudios Interdisciplinarios, Facultad de Ingeniería, Universidad Nacional de Chimborazo, 060103 Riobamba, Ecuador. Correo electrónico: pratoj@gmail.com.*
https://orcid.org/0000-0001-8381-404X;

Gómez, Ruben *(†). MSc. Food Engineering. National College of Food Technology, University of Reading, Weybridge, England. Senior Lecturer, School of Chemical Engineering, College of Engineering, U.L.A. E-mail: rcgomezr@gmail.com* *https://orcid.org/0009-0006-4138-5826*

Artículo de Investigación. Revista Ciencia e Ingeniería. Vol. 46, No. 3 pp. 343-352, agosto-noviembre, 2025.
ISSN 1316-7081. ISSN Elect. 2244-8780 Universidad de los Andes (ULA)

Q-learning based algorithm for learning children's difficulties in multiplication tables

Algoritmo basado en Q-learning para el aprendizaje de las dificultades de los niños en las tablas de multiplicar

Pérez, Jesús[1*]; Aguilar, Jose [2,3]; Dapena, Eladio[4]
[1]LaSDAI, Universidad de Los Andes, Mérida, Venezuela.
[2]CEMISID, Universidad de Los Andes, Mérida, Venezuela.
[3]IMDEA Networks Institute, Leganés, Madrid, España.
[4]Universidad Intercontinental de la Empresa UIE, La Coruña, España.
* jesuspangulo@ula.ve

Abstract

In order to help children with their difficulties in multiplication tables, this paper presents a learning system based on the Q-learning algorithm, which allows software agents to learn what multiplication tables are difficult for a child. The results indicate that our learning system is effective to learn the children's levels of difficulties (low, medium, high, and very high) in the multiplication tables, when an agent randomly asks all operations of the multiplication tables (64 operations, since 2 until 9). In addition, our learning system allows knowing what multiplication tables have more difficulty with respect to the others, after asking at least once an operation for each multiplication table.

Keywords: Agent, social robot, Q-learning, reinforcement learning.

Resumen

Para ayudar a los niños con sus dificultades con las tablas de multiplicar, este artículo presenta un sistema de aprendizaje basado en el algoritmo Q-learning, que permite a los agentes de software aprender qué tablas de multiplicar son difíciles para un niño. Los resultados indican que nuestro sistema de aprendizaje es eficaz para aprender los niveles de dificultad de los niños (bajo, medio, alto y muy alto) en las tablas de multiplicar, cuando un agente pregunta aleatoriamente todas las operaciones de las tablas de multiplicar (64 operaciones, del 2 al 9). Además, nuestro sistema de aprendizaje permite saber qué tablas de multiplicar presentan mayor dificultad con respecto a las demás, tras preguntar al menos una operación por cada tabla.

Palabra clave: Agente, robot social, Q-learning, aprendizaje por refuerzo.

1 Introduction

The software agents are being used to help children in mathematical learning, such as: an agent asks deep questions on the learning material during a computer game (Pareto, 2014); an agent guides algebra lessons with prescriptive instructional guidance and anxiety treating messages (Kim *et al.*, 2016); children guide to the agent to play correctly a game (Axelsson *et al.*, 2013); and an agent integrated into a learning environment acts as a tutor and motivator (Mohammadhasani *et al.*, 2018).

Recently, the typical agents used are social robots. For example, children complete mathematical problems with robots (Ramachandran *et al.*, 2017); children solve tests of multiple-choice math questions while robots give verbal feedback (Brown & Howard, 2014); children participate in a game-based learning activity to learn arithmetic with the guidance of robots (Vrochidou *et al.*, 2018); children practice multiplication with problems that include whole numbers, while robots guide the practice (Liles, 2021).

In general, the agents as social robots have been shown to be effective for increasing cognitive and affective outcomes of children, achieving outcomes similar to those of human tutoring on restricted tasks

(Belpaeme *et al.*, 2018). In addition, the social robots can provide a personalized learning and social support (Michaelis & Mutlu, 2019). Therefore, the social robots are promising to continue helping children.

Particularly, in the context of mathematical learning, multiplication is a fundamental area in which many students manifest learning difficulties (Zhang *et al.*, 2016). According to Zhang *et al.* (2013), helping students with mathematics difficulties to develop sufficient multiplication problem-solving skills, is a priority for educators and researchers. It means that helping children with difficulties in multiplication tables, also known as times tables, is relevant.

According to Park *et al.* (2019), the current personalized education technologies are capable of delivering adaptive interventions that play an important role in addressing the needs of diverse young learners. In this context, children's difficulties in multiplication tables are different for every child, therefore, social robots need to learn the particular difficulties in multiplication tables for every child.

According to Castro-González *et al.* (2011), learning is an active area in robotic, and reinforcement learning is one of the learning methods that has been most successfully implemented in robots. Among the different solution methods, Q-learning is performing extremely well in the field of robotic (Jang *et al.*, 2019). For example, a robot uses Q-learning to select stories that are optimized for each child's linguistic skill progression (Park *et al.*, 2019). In our case, a Q-learning based algorithm will allow learning the particular difficulties in multiplication tables for every child.

In this paper, we present how a Q-learning based algorithm can be used for learning the children's difficulties in the multiplication tables. The paper is organized as follows: in section 2, we present the main concepts related to our proposition; in section 3, we describe our proposed learning system; in section 4, we show the experimental tests; and in section 5, we present the conclusions and future works.

2 Preliminary concepts

Reinforcement learning allows learning what to do through trial and error interactions with an environment. The task of reinforcement learning is to use observed rewards to learn an optimal policy for the environment (Aguilar, 2014; Russell & Norvig, 2016). The distinction between problems and solution methods is very important in reinforcement learning (Sutton & Barto, 2018): the problems are formalized using ideas from the dynamical system theory, for example, through the Markov Decision Processes (MDP); and the solution methods allow solving such problems.

In general, a learning agent interacts over time with its environment to achieve a goal, therefore, the learning agent must be able to perceive the state of its environment; take actions that affect the state; and receive rewards relating to the state. In this context, a MDP is composed of states, actions, transitions between states, and a reward function. Formally, a MDP is a tuple $<S,A,T,R>$ (Van Otterlo & Wiering, 2012), in which S is a finite set of states, A is a finite set of actions, T is a transition function defined as $T:S\times A\times S\rightarrow[0,1]$, and R is a reward function defined as $R:S\times A\times S\rightarrow R$. According to the problem, a MPD can have or not the transition function.

There are three types of systems that can be modelled by a MDP (Van Otterlo & Wiering, 2012): fixed horizon (tasks in which each episode consists of a fixed number of steps), indefinite horizon (tasks in which each episode can have an arbitrary length, but ends), and infinite horizon (tasks where the system does not end at all). An episode happens when the agent reaches a goal state and the process restarts in a new initial state; and a step is related to each action that the agent must take to reach a goal state. It means that a MDP can have one or more starting and goal states.

Given a MDP $<S,A,T,R>$, a policy is a computable function that outputs for each state $s\in S$ (except goal states) an action $a\in A$ (or $a\in A(s)$). Formally, a deterministic policy π is a function defined as $\pi:S\rightarrow A$ (Van Otterlo & Wiering, 2012). It is also possible to define a stochastic policy as $\pi:S\times A\rightarrow[0,1]$, such that for each state $s\in S$ (except goal states), it holds that $\pi(s,a)\geq 0$ and $\sum_{(a\in A)}\pi(s,a)=1$. Then, solving a given MDP means computing an optimal policy $\pi*$.

Solution methods for solving a MDP can be divided in several ways. On one side, there are two categories (Russell & Norvig, 2016): passive learning, where the agent's policy is fixed and the task is to learn the utilities of the states; and active learning, where the agent must learn the policy. In other side, there are three fundamental classes of methods (Sutton & Barto, 2018): dynamic programming, Monte Carlo methods, and temporal-difference learning. Also, the algorithms can be divided in two classes (Van Otterlo & Wiering, 2012): model-based, where a model of the MDP is known beforehand, and can be used to compute value functions and policies; and model-free, where the agent interacts with the environment, generating samples of state transitions and rewards, in order to estimate state-action value functions.

Q-learning method belongs to active learning,

temporal-difference learning, and model-free algorithms. Jang *et al.* (2019) covered all variants of Q-learning algorithms, and they conclude that improved Q-learning algorithms might perform poorly while solving simple problems in a simple environment, but they outperform basic Q-learning algorithms when the problem at hand is complex and under a sophisticated environment. It means that a basic Q-learning shows an excellent learning ability in simple environments. In our case study, we will use a basic Q-learning because our problem is relatively simple (4 states and 8 actions).

Q-learning uses an off-policy method to separate the acting policy from the learning policy. The basic idea in Q-learning is to incrementally estimate Q-values for actions, based on rewards and the agent's Q-value function. Specifically, the agent makes a step in the environment from state s to s' using action a, and receives a reward R(s'); then, the update takes place on the Q-value of action a in the state s from which this action was executed. According to Watkins & Dayan (1992), equation for the Q-value is as follows (see equation 1):

$$Q(s,a) = (1- \alpha)\, Q(s,a) + \alpha\, [R(s') + \gamma \max_{a'} Q(s',a')] \qquad (1)$$

Equation 1 uses two hiperparameters: the learning rate α that determines the update rate, and the discount factor γ that determines the present value of future rewards. Formally, $\alpha \in [0, 1]$ and $\gamma \in [0, 1]$.

In active learning methods as Q-learning, the principal issue is the exploration (Russell & Norvig, 2016), because the agent must interact with the environment to learn by trial and error a correct policy. However, also the exploitation is used to get the right action that maximizes the expected reward on the one step (Sutton & Barto, 2018). First, the agent has to explore the environment by performing actions and perceiving their consequences through rewards, and then it can exploit the knowledge. In addition, if the environment is not stationary, the agent must explore to keep its policy up-to-date (Van Otterlo & Wiering, 2012). This naturally induces an exploration-exploitation trade-off, which has to be balanced to obtain an optimal policy.

3 Our learning system

3.1 Problem formulation

Social robots communicate through human-like interactions and must learn from these interactions. In this paper, social robots must learn children's difficulties in multiplication tables. In general, mathematical difficulties are determined by a low performance on tests of mathematics (Zhang *et al.*, 2013). Therefore, social robots must emulate tests through the interactions. A simple mathematic test consists in a social robot asking all multiplication tables to a child. It means that the problem will be formulated for one child, and social robots must have one model for every child.

In a mathematic test, a social robot must randomly ask all operations of the multiplication tables of one digit (from the multiplication table of 2 to the multiplication table of 9), and a child must answer it. In the problem formulation as a MDP, each multiplication table represents an action, and every answer represents a state. The idea is to reward every answer, in order to benefit negative answers, because in this way the policy π of the MDP will return actions (multiplication tables) with more difficulty to the child.

The states are qualifications related to difficulties: conscious difficulty (child knows that he doesn't know the correct answer), unconscious difficulty (child doesn't know that he doesn't know the correct answer), moderate difficulty (child knows the correct answer, but he is not sure), and without difficulty (child knows the correct answer). The rewards must mostly benefit conscious and unconscious difficulties; and it must less benefit the moderate difficulty.

The states can be determined indirectly combining two dichotomic parameters: speed of answer and validity. The speed of answer can be slow or fast, and the validity can be incorrect or correct. Specifically, a conscious difficulty is an answer slow and incorrect; an unconscious difficulty is an answer fast and incorrect; a moderate difficulty is an answer slow and correct; and without difficulty is an answer fast and correct.

Formally, the problem is formulated as a MDP, denoted as a tuple <A,S,R>, where A is the set of actions or multiplication tables {multiplication table of 2, multiplication table of 3, multiplication table of 4, multiplication table of 5, multiplication table of 6, multiplication table of 7, multiplication table of 8, multiplication table of 9}; S is the set of states or answer's qualifications {conscious difficulty, unconscious difficulty, moderate difficulty, without difficulty}; and R is the reward function as follows (see equation 2):

$$R(s) = \begin{cases} 0.99 & if\ s = conscious\ difficulty \\ 0.66 & if\ s = unconscious\ difficulty \\ 0.33 & if\ s = moderate\ difficulty \\ 0 & if\ s = without\ difficulty \end{cases} \qquad (2)$$

The problem is modelled as an indefinite horizon, because each episode must end, but episodes can have arbitrary length. Each episode starts in without difficulty state (initial state) and the goal is to reach a conscious

difficulty state or unconscious difficulty state (goal states). In addition, there is a fixed number of operations (steps) to end the test. The total operations are 64 (8 operations for each multiplication table) and the idea is to learn the policy for the formulated problem taking these operations, such that a social robot can know the multiplication tables that are difficult for a child.

3.2 Solution method

The formulated problem in the previous section has not a transition function because the problem is a model-free. Also, the problem does not have a policy, which means that it is an off-policy problem. The solution method used for this kind of problems is Q-learning, which goal is estimate Q-values. In our problem, the Q-values will allow knowing the difficulties in multiplication tables for every child.

Table 1. Learning algorithm

Step	Instruction
1.	Initialize Q(s,a) = 0
2.	s = initial state
3.	For each a in O:
3.1.	Take action a
3.2.	Observe s', R(s')
3.3.	Update Q(s, a) using equation 1
3.4.	s = s'
3.5.	If (s == goal state) then s = initial state

In the process of estimation of Q-values, our algorithm requires only exploration, because it must determine the end Q-values in the least amount of iterations. According to the amount of operations required for the test, we use a set of operations called O, which contains 64 operations (8 operations for each multiplication table). Because our problem was modelled like an indefinite horizon, we use an initial state, but several goal states in the algorithm. The algorithm used is shown in Table 1.

In lines 1 and 2, the algorithm begins with all Q-values in zero and in a specific initial state (without difficulty). Then, each action belonging to the set of 64 operations O (line 3) is performed (line 3.1) and based on child answers (line 3.2), the Q-value is updated (line 3.3), a transition is made to a new state (line 3.4), and it is compared in order to restart the initial state when it reach a goal state (line 3.5). The 64 operations are randomly taken, and the algorithm ends when all operations are processed.

In our formulated problem, future rewards are not important because there is not interdependence among the states to reach a goal state. Therefore, according to Vlachogiannis & Hatziargyriou (2004), the value of the discount factor is set to 0.005. On the other hand, the selection of the learning rate α for our algorithm will be fixed with helping of a sensitivity analysis, according to the best performance to our problem (see section 4). Finally, when the algorithm ends, the social robot knows the multiplication tables that are difficult for the child, through the Q-values, where the greatest values represent the multiplication tables with the greatest difficulties.

4 Testing

4.1 Experimental protocol

The experimental goal is to verify that our learning system allows learning children's difficulties in multiplication tables. The experiments will be successful when the Q-values indicate the multiplication tables that are difficult for the children. The experimental protocol is divided in four experiments: 1) convergence, in order to know the convergence Q-values; 2) sensitivity analysis of the learning rate α, in order to select the best value for our model; 3) learning fixed profile of two children to know how the model learns in two instances; and 4) learning of a variable profile of one child, in order to analyze how the model can adapt to variable performance of a child.

In each experiment, it is necessary to instance our model at least one time, and to simulate the children answers. The children answer is simulated with profiles, where each profile is related to the child's knowledge about each multiplication table. For that, we specified two attributes: difficulty level (low, medium, high, and very high) of each multiplication table, and answer's probabilities of each difficulty level.

The answer's probabilities for difficulty levels try to simulate that in each level of difficulty there is an answer with higher probability, but it can be another. In Table 2, we present the probability distribution, where the low difficulty level means that the child can answer without difficulty 80% of the time, with moderate difficulty 10% of the time; and the rest is distributed between unconscious difficulty (5% of the time) and conscious difficulty (5% of the time). The others levels in Table 2 can be interpreted in the same way.

Table 2. Answer's probabilities of each difficulty level

Difficulty	P(cd)	P(ud)	P(md)	P(wd)
Low	0.05	0.05	0.1	0.8
Medium	0.05	0.05	0.8	0.1
High	0.1	0.8	0.05	0.05
Very High	0.8	0.1	0.05	0.05

cd = "conscious difficulty" state, ud = "unconscious difficulty" state, md =

"moderate difficulty" state, and wd = "without difficulty" state.

In order to carry out the experiments, we define three profiles for the children: bad (it simulates a child with bad performance in the tests of the multiplication tables), regular (it simulates a child with medium performance), and good (it simulates a child with good performance). In Table 3, we present the profiles mapped to each multiplication table, where bad profile means that high difficulty is mapped to multiplication tables of 2, 3, 4 and 5; and very high difficulty level with multiplication tables of 6, 7, 8 and 9. The others profiles in Table 3 can be interpreted in the same way.

The profiles are used in the four experiments as follows: in the convergence and the sensitivity analysis of the learning rate, we use the regular profile because it allows analysing how our model learns each level of difficulty; in the learning fixed profile of two children, we use the bad and good profiles to train one instance of our model for each child; and in the learning of a variable profile of one child, we use the bad and good profiles in only one instance of our model, in order to simulate a child with an initial bad performance and later it changes to a good performance.

Table 3. Difficulty level of each multiplication table in the three children profiles

Multipl. Table	Profile		
	Bad	**Regular**	**God**
2	High	Low	Low
3	High	Low	Low
4	High	Medium	Medium
5	High	Medium	Medium
6	Very High	High	Low
7	Very High	High	Low
8	Very High	Very High	Medium
9	Very High	Very High	Medium

4.2 Results

4.2.1 Convergence

Q-learning allows convergence in Q-values after several iterations (Watkins & Dayan, 1992). The goal of this experiment is to know the Q-values of convergence for each level of difficulty. For that, the model is instanced using the regular profile (see Table 3), and according to Castro-González *et al.* (2011), the rate learning (α) is set to 0.3. Then, we run our learning algorithm for 256 operations (32 random operations for each multiplication table, using a uniform distribution). In the Figure 1, we show the average Q-values for each step (operation) in 100 runs, and we appreciate that the four levels of difficulty converge after the step 100 in Q-values close to: 0.13 for low level of difficulty; 0.35 for medium level of difficulty; 0.63 for high level of difficulty; and 0.86 for very high level of difficulty. These results follow our goal, the Q-values of the states that represent the greatest difficulty for children are the biggest.

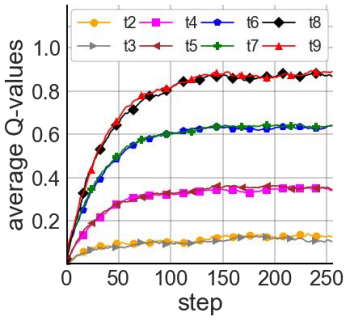

Figure 1. Average Q-values of initial state for a regular profile, using α = 0.3 and 256 steps

In order to get a better idea of the convergence of Q-values, in Figure 2 we show the standard deviations of the average Q-values presented on the Figure 1. It allows checking that the four levels of difficulty converge after the step 100, being the standard deviations between 0.06 and 0.13. These results are the references to use our learning system, however, we need to work with a smaller number of steps (ideally 64 steps because this cover the multiplication test).

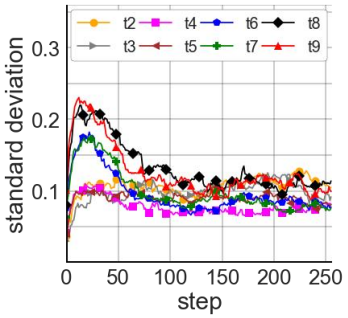

Figure 2. Standard deviations of average Q-values of initial state for a regular profile, using α = 0.3 and 256 steps

4.2.2 Sensitivity analysis

The goal of this experiment is to understand the relationships between an input and the outputs of our model, in order to select the appropriate value of the input, according to the expected behavior of our model. The input of interest is the learning rate (α), the outputs of interest are the end Q-values, and the expected behavior is that end Q-values of the initial state (without difficulty) in the last operation (operation 64) indicates the multiplication tables

that are difficult for a child (specified in a profile).

For that, our model is instanced using the regular profile, we test our learning algorithm on 100 runs for different values of α, and the results are shown in the Table 4. The end Q-values shown are average of 100 runs with its standard deviations. Because the regular profile has associated all levels of difficulty (low, medium, high, and very high), in Table 4 we show the results of only one multiplication table (which is representative) for each difficulty level (for example, multiplication table of 3 for low difficulty).

In Table 4, we appreciate that the learning rate (α) has an incidence in the end Q-values. In general, α represents how much the Q-values are updated; it means that higher values of α allow faster convergence of the Q-values. That behavior can be appreciated in our results. For example, the results for the smallest α tested (0.1) have the smallest standard deviations (between 0.05 and 0.08), but they have far Q-values with respect to the convergence values; and the results for the highest α tested (1) are close Q-values with respect to the convergence values, but they have high standard deviations (between 0.13 and 0.29).

Since the learning rate 0.4 allows getting Q-values close to the convergence values with standard deviation between 0.10 and 0.14, we will select this learning rate for our algorithm. In order to understand better the behavior of our model while is running our algorithm, we show in the Figure 3 the average Q-values for each step (operation) of the multiplication test (64 operations). In Fig 3, we appreciate that multiplication tables with low level of difficulty have end Q-values close to 0.11 (multiplication tables off 2 and 3, see Table 3); multiplication tables with medium level of difficulty have end Q-values close to 0.32; multiplication tables with high level of difficulty have end Q-values close to 0.60; and multiplication tables with very high level have end Q-values close to 0.82.

Table 4. Sensitivity analysis of learning rate

α	Low (T3)		Medium (T5)		High (T7)		Very High (T9)	
	$\bar{Q}$	σ	$\bar{Q}$	σ	$\bar{Q}$	σ	$\bar{Q}$	σ
0.1	0.06	0.05	0.17	0.05	0.31	0.05	0.42	0.08
0.2	0.09	0.09	0.25	0.06	0.48	0.07	0.63	0.11
0.3	0.11	0.11	0.30	0.07	0.57	0.09	0.75	0.13
0.4	0.11	0.12	0.32	0.10	0.60	0.10	0.82	0.14
0.5	0.12	0.16	0.33	0.11	0.64	0.11	0.83	0.16
0.6	0.13	0.18	0.34	0.12	0.64	0.14	0.88	0.16
0.7	0.13	0.22	0.36	0.13	0.62	0.17	0.87	0.18
0.8	0.11	0.18	0.35	0.14	0.66	0.17	0.89	0.21
0.9	0.15	0.27	0.34	0.16	0.63	0.16	0.85	0.23
1	0.14	0.29	0.31	0.13	0.65	0.19	0.88	0.26

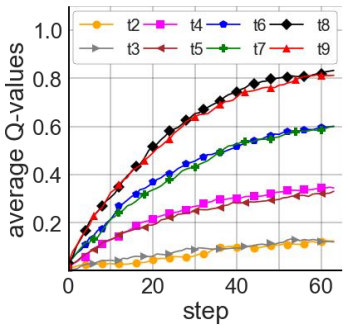

Figure 3. Average Q-values of initial state for a regular profile, using α = 0.4 and 64 steps

4.2.3 Learning fixed profile of two children

The goal of this experiment is to analysis the behavior of our learning system with the basic test of multiplication tables. For that, we create two instances of our model in order to test with two profiles (each profile simulates one child). The first profile is bad, and the second one is good (see Table 3). In Figure 4, we show the results of the bad profile, where can be appreciated that the end Q-values (step 64) are close to the convergence Q-values of our model: the multiplication tables of 2, 3, 4 and 5 have end Q-values close to 0.60; and the multiplication tables of 6, 7, 8 and 9 have end Q-values close to 0.82. It means that a social robot could know the specific multiplication tables that are difficult for a child of bad performance, and in addition, it could know the levels of difficulty of each one, making comparisons with the convergence Q-values.

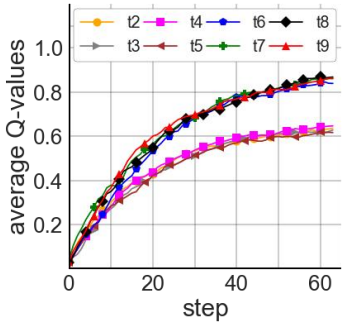

Figure 4. Average Q-values of initial state for a bad profile, using α = 0.4 and 64 steps

In Figure 5, we show the results of the good profile, where can be appreciated that the end Q-values are close to the convergence Q-values of our model: the multiplication tables of 2, 3, 6 and 7 have end Q-values close to 0.11; and the multiplication tables of 4, 5, 8 and 9 have end Q-values close to 0.32. In this case, the end Q-values are close to the convergence Q-values. In this way, a social robot could know the specific multiplication tables that are not difficult for a child with good performance, and knows the levels of

difficulty of each one, making comparisons with the convergence Q-values.

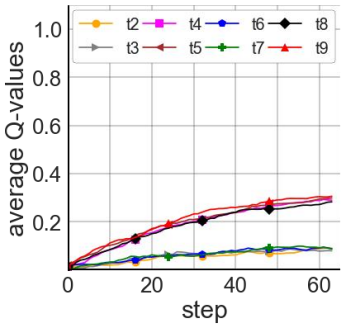

Figure 5. Average Q-values of initial state for a good profile, using α = 0.4 and 64 steps

4.2.4 Learning of a variable profile of one child

The goal of this experiment is to analysis the behavior of our learning system when the basic test of multiplication tables is applied to a child who has changed his profile. For that, we use the bad and good profiles in the same instance of our model. When we run our learning system with the bad profile, we get the results as is shown in Figure 4, and later, when we run it with the good profile, we get the results that are shown in Figure 6, where can be appreciated that the initial Q-values are the same end Q-values of the Fig 4. These Q-values are modified until the last step to get the end Q-values, which are close to 0.4 for multiplication tables with medium level of difficulty and are close to 0.2 for multiplication tables with low level of difficulty. It means that the Q-values in this case are far to the convergence Q-values, in comparison with the other cases, however, a social robot could know which multiplication tables are more difficult for a child in comparison with the other multiplication tables, through the Q-values. In general, our learning system follows the change of profile of the child.

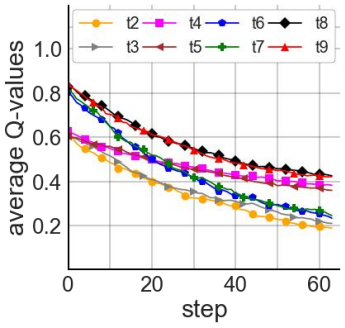

Figure 6. Average Q-values of initial state from bad to good profile, using α = 0.4 and 64 steps

5 Conclusions

In our learning system, the Q-values converge after of the step 100 as follows (see Figure 1): 0.13 for multiplication tables with low level of difficulty; 0.35 for multiplication tables with medium level of difficulty; 0.63 for multiplication tables with high level of difficulty; and 0.86 for multiplication tables with very high level of difficulty. These Q-values have a standard deviation between 0.06 and 0.13, and can be used to get the level of difficulty of each multiplication table in a given context. However, in our case of study, 100 steps (it means that social robot asks 100 operations to the child) is so much. One option is to use the Q-values before the step 100, but implies a higher standard deviation (see Figure 2). Because a basic multiplication test consists in asks one time all operations of the multiplication tables, 64 operations are acceptable for our case study.

The sensitivity analysis for different values of the learning rate, allows appreciating that for the highest values of the learning rate, the Q-values are close faster to convergence Q-values, but the standard deviation is higher: a learning rate of 0.1 has a standard deviation between 0.05 and 0.08, and a learning rate of 1 has a standard deviation between 0.13 and 0.29. A learning rate of 0.4 is an equilibrium between the fast convergence and the standard deviation values, and allows getting Q-values close to the convergence Q-values in the step 64, which is acceptable for our case study.

Our learning system allows knowing the multiplication tables that are difficult or not for children with several profiles: regular (see Figure 3), bad (see Figure 4) and good (see Figure 5). This is possible comparing the end Q-values with the convergence Q-values as follows: the end Q-value of a child has the same level of difficulty in that multiplication table as the nearest convergence Q-value. In this sense, an end Q-value nearest to 0.13 means a low level of difficulty; nearest to 0.35 means a medium level of difficulty; nearest to 0.63 means a high level of difficulty; and nearest to 0.86 means a high level of difficulty.

Our learning system allows knowing the multiplication tables that are difficult for a child that change his profile. In general, our learning system is able to know which multiplication tables are more difficult for a child after asks him at least one operation for each multiplication table in all the case studies.

There are several future works. A first future work must extend this study with information of the context, like more actions guided by the educational paradigms and based on the learning profiles of the children. Also, another future work must analyze the sorting of the Q-values to get the order of difficulty, which can be useful for a social robot in order to help children through specific learning strategies adequate to them. For example, once the system knows which multiplication tables are more difficult for the child, which policy of actions to follow in order to reduce that

difficulty. Some of the possible results would be practice sessions of all the multiplication tables, making emphasis on the ones that the child has more difficulty without knowing, or fun strategies to reduce the difficulty without asking the multiplication tables.

Also, in the field of social robotics, it will be necessary to include other actions linked to the body of the robot, such as its mobility and expressions (non-verbal language like emotional expressions through the face (Pérez *et al.*, 2020)), to make the learning process more harmonious. Finally, the article has used two parameters to determine the status (response time of the child, and validity of the response). A future work should interpret human characteristics (for example, affective states (Pérez *et al.*, 2024)) when asked, to enrich the model because it gives evidence of knowledge.

References

Aguilar, J. (2014). Introducción a los Sistemas Emergentes. Talleres Gráficos, Universidad de Los Andes: Venezuela.

Axelsson, A., Anderberg, E., & Haake, M. (2013). Can Preschoolers Profit from a Teachable Agent Based Play-and-Learn Game in Mathematics? In Lecture notes in computer science (pp. 289–298). https://doi.org/10.1007/978-3-642-39112-5_30

Belpaeme, T., Kennedy, J., Ramachandran, A., Scassellati, B., & Tanaka, F. (2018). Social robots for education: A review. Science Robotics, 3(21). https://doi.org/10.1126/scirobotics.aat5954

Brown, L., & Howard, A. (2014). The positive effects of verbal encouragement in mathematics education using a social robot. In 2014 IEEE integrated STEM education conference (pp. 1-5). http://doi.org/10.1109/ISECon.2014.6891009

Castro-González, Á., Malfaz, M., & Salichs, M. A. (2011). Learning the selection of actions for an autonomous social robot by reinforcement learning based on motivations. International Journal of Social Robotics, 3(4), 427–441. https://doi.org/10.1007/s12369-011-0113-z

Jang, B., Kim, M., Harerimana, G., & Kim, J. W. (2019). Q-Learning Algorithms: A Comprehensive Classification and applications. IEEE Access, 7, 133653–133667. https://doi.org/10.1109/access.2019.2941229

Kim, Y., Thayne, J., & Wei, Q. (2016). An embodied agent helps anxious students in mathematics learning. Educational Technology Research and Development, 65(1), 219–235. https://doi.org/10.1007/s11423-016-9476-z

Liles, K. R. (2019). Ms. An (Meeting Students' Academic Needs): Engaging Students in Math Education. Lecture Notes in Computer Science, 645–661. https://doi.org/10.1007/978-3-030-22341-0_50

Michaelis, J. & Mutlu, B. (2019). Supporting interest in science learning with a social robot. In Proceedings of the 18th ACM international conference on interaction design and children (pp. 71-82). https://doi.org/10.1145/3311927.3323154

Mohammadhasani, N., Fardanesh, H., Hatami, J., Mozayani, N., & Fabio, R. A. (2018). The pedagogical agent enhances mathematics learning in ADHD students. Education and Information Technologies, 23(6), 2299–2308. https://doi.org/10.1007/s10639-018-9710-x

Park, H. W., Grover, I., Spaulding, S., Gomez, L., & Breazeal, C. (2019). A Model-Free affective reinforcement learning approach to personalization of an autonomous social robot companion for early literacy education. Proceedings of the AAAI Conference on Artificial Intelligence, 33(01), 687–694. https://doi.org/10.1609/aaai.v33i01.3301687

Pareto, L. (2014). A teachable agent game engaging primary school children to learn arithmetic concepts and reasoning. International Journal of Artificial Intelligence in Education, 24(3), 251–283.https://doi.org/10.1007/s40593-014-0018-8

Pérez, J., Aguilar, J., & Dapena, E. (2020). MIHR: a Human-Robot Interaction Model. IEEE Latin America Transactions, 18(09), 1521–1529. https://doi.org/10.1109/tla.2020.9381793

Pérez, J., Dapena, E., & Aguilar, J. (2024). Emotions as implicit feedback for adapting difficulty in tutoring systems based on reinforcement learning. Education and Information Technologies, 29(16), 21015–21043. https://doi.org/10.1007/s10639-024-12699-8

Ramachandran, A., Huang, C. M., & Scassellati, B. (2017). Give me a break! Personalized timing strategies to promote learning in robot-child tutoring. In Proceedings of the 2017 ACM/IEEE International Conference on Human-Robot Interaction (pp. 146-155). https://ieeexplore.ieee.org/document/8534798

Russell, S. J., & Norvig, P. (2016). Artificial Intelligence: A Modern Approach (3rd ed.). Prentice Hall Press: Upper Saddle River, USA.

Sutton, R. & Barto, A. (2018). Reinforcement Learning: An Introduction. A Bradford Book: USA.

Van Otterlo, M., & Wiering, M. (2012). Reinforcement learning and Markov decision processes. In Adaptation, learning, and optimization (pp. 3–42). https://doi.org/10.1007/978-3-642-27645-3_1

Vlachogiannis, J., & Hatziargyriou, N. (2004). Reinforcement learning for reactive power control. IEEE Transactions on Power Systems, 19(3), 1317–1325. https://doi.org/10.1109/tpwrs.2004.831259

Vrochidou, E., Najoua, A., Lytridis, C., Salonidis, M., Ferelis, V., & Papakostas, G. A. (2018). Social robot NAO as a self-regulating didactic mediator: A case study of teaching/learning numeracy. In 2018 26th international conference on software, telecommunications and computer networks (SoftCOM) (pp. 1-5). https://doi.org/10.23919/softcom.2018.8555764

Watkins, C. J. C. H., & Dayan, P. (1992). Q-learning. Machine Learning, 8(3), 279–292. https://doi.org/10.1007/bf00992698

Zhang, D., Ding, Y., Lee, S., & Chen, J. (2016). Strategic development of multiplication problem solving: Patterns of students' strategy choices. The Journal of Educational Research, 110(2), 159–170. https://doi.org/10.1080/00220671.2015.1060928

Zhang, D., Xin, Y. P., Harris, K., & Ding, Y. (2013). Improving multiplication strategic development in children with math difficulties. Learning Disability Quarterly, 37(1), 15–30. https://doi.org/10.1177/0731948713500146

Received: *December 28th, 2024*

Accepted: *March 22th, 2025*

Pérez, Jesús: *Postdoctorado en Investigación Educativa (2022), Dr. en Ciencias de la Educación (2019), MSc. en Educación Superior (2014), Ing. de Sistemas (2014), Ing. en Electrónica (2012). Es Profesor Agregado en la Universidad de Los Andes (ULA), e Investigador del Laboratorio de Sistemas Discretos, Automatización, e Integración (LaSDAI).* *https://orcid.org/0000-0002-6585-2648*

Aguilar, Jose: *Ingeniero de Sistemas en 1987 (ULA), MSc. en Ciencias de la Computación en 1991 (Universite Paul Sabatier-Francia), Doctorado en Ciencias de la Computación en 1995 (Universite Rene Descartes-Francia) y Postdoctorado en Ciencias de Computación en 2000 (Universidad de Houston). Actualmente es investigador Senior en IMDEA Networks Institute. Email: aguilar@ula.ve* *https://orcid.org/0000-0003-4194-6882*

Dapena, Eladio: *Doctor Ingeniero Industrial, UC3M, España (2002). Automatización Industrial (Esp.), UFSC, Brasil (1998). Ingeniería de Sistemas, ULA, Venezuela (1990). Profesor jubilado Universidad de Los Andes (ULA). Profesor Titular Universidad Intercontinental de la Empresa UIE. Email: eladio.dapena@uie.edu*
https://orcid.org/0000-0002-9135-0967

Artículo de Investigación. Revista Ciencia e Ingeniería. Vol. 46, No. 3 pp. 353-360, agosto-noviembre, 2025.
ISSN 1316-7081. ISSN Elect. 2244-8780 Universidad de los Andes (ULA)

Petrogenetic study of the El Verdalito Granodiorite through petrologic and petrographic analysis

Estudio petrogenético de la Granodiorita El Verdalito mediante análisis petrológico y petrográfico

Rosales, Rafael[1*]; Andara, Ángel[1]; Torres, Gusbel[1]; Gómez, Jessica[2]; Maldonado, Maricarmen[3]; Caraballo, José[3]; Lujano, José[3]; Uzcátegui, Francyret[3];
[1]Grupo de Investigaciones TERRA. Escuela de Ingeniería Geológica. Universidad de Los Andes. Venezuela.
[2]Laboratorio de Palinoestratigrafía y Paleobotánica, Centro de Investigaciones Científicas, Argentina.
[3]Escuela de Ingeniería Geológica - Universidad de los Andes-Venezuela, Venezuela.
* rafaeljrosales@ula.ve

Abstract

Outcropping along the Rafael Caldera Highway in Mérida, Venezuela, the El Verdalito granodiorite stands out as a prominent igneous body due to its geological and petrographic characteristics. This study aims to deepen its understanding through petrological and petrographic analyses of its mineralogy to comprehend its petrogenesis and evolution. U/Pb zircon dating estimates a crystallization age of approximately 440 ± 19 million years. Regarding its petrographic characteristics, the El Verdalito granodiorite displays a range of primary textures with variable grain sizes, showing a dominance of plagioclase phenocrysts with normal zoning, along with quartz and alkali feldspars, and accessory minerals such as biotite, muscovite, epidote, sericite, and chlorite. Analyses reveal primary textures resulting from recrystallization, as well as secondary alterations from hydrothermal fluids. The presence of immobile elements determines the tectonic setting of formation and evolution, suggesting magma generated in a pre-collisional subduction zone.

Keywords: Granodiorite, Petrogenesis, Petrography, Geochemistry, Andes Cordillera, Tectonics.

Resumen

Aflorando a lo largo de la autopista Rafael Caldera en Mérida, Venezuela, la granodiorita de El Verdalito simboliza un cuerpo ígneo muy llamativo debido a sus características tanto geológicas como petrográficas, por ello, se busca profundizar su estudio a través de análisis petrológicos y petrográficos de su mineralogía, con el fin de comprender su petrogénesis y evolución. Mediante la datación U/Pb en circones, se estima una edad de cristalización de aproximadamente 440 ± 19 millones de años. En cuanto a sus características petrográficas, la granodiorita de El Verdalito muestra una serie de texturas primarias con variedad de tamaños de granos. Presenta dominancia de fenocristales de plagioclasa con zonación normal, como también cuarzo y feldespatos alcalinos, así como también minerales accesorios como lo pueden ser las micas biotita, moscovita, epidota, sericita y clorita. Los análisis revelan texturas primarias producto de la recristalización, asimismo, alteraciones secundarias provenientes de fluidos hidrotermales. La presencia de elementos inmóviles determina el ambiente tectónico de formación y evolución, sugiriendo un magma generado en una zona de subducción pre-placa.

Palabra clave: Granodiorita, Petrogénesis, Petrografía, Geoquímica, Cordillera de los Andes, Tectónica.

1 Introduction

Between 1974 and 1976, the Ministry of Energy and Mines documented for the first time the El Verdalito Granodiorite, located on the geological map of Tovar–Guaraque–Mesa Bolívar–Bailadores, Mérida State, Venezuela. This igneous body crops out in the Chama Canyon within the Venezuelan Andes and spans approximately 1.7 kilometers in a North–South direc-

tion and 1.5 kilometers East–West.

Classified as a granodiorite by Van der Lelij in 2013 and corroborated by Professor Rafael J. Rosales R. in 2020, it is found in discordant contact with Cretaceous rocks and is presumed to have intruded formations belonging to the Tostós Association. Sample 08VDL03, located at latitude N 8°28'49" and longitude W 71°34'13", yielded a U–Pb zircon age of 449.3 ± 2.5 Ma (Van der Lelij, 2013), suggesting it is contemporaneous with the Estanques Granite and other similarly aged plutonic bodies in the region.

This study employs analytical techniques such as thin section petrography and geochemical analysis to characterize in detail the mineralogical composition of this igneous body. Additionally, a petrological and petrographic assessment is conducted with the aim of contributing to the understanding of the petrogenesis of the El Verdalito Granodiorite.

2 Materials and methods

The study was conducted at the Optical Mineralogy and Petrography Laboratory of the Universidad de Los Andes. Following the standard cutting and polishing protocols established by MacKenzie et al. (1997), thin sections were prepared and examined using a Nikon ECLIPSE E200 POL polarizing light microscope. This enabled the detailed identification and description of crystallinity, grain size, textural patterns (both primary and secondary textures), and modal mineralogical composition (primary and secondary minerals, expressed as volume percentages).

Rock classification was performed using the classification triangles of Le Bas et al. (1991). The normative and relative modal percentages of the major minerals observed in the thin sections were calculated and plotted on the diagram to determine the appropriate rock nomenclature.

For the geochemical analysis of the granodiorite, the geochemical dataset for the Venezuelan Andes provided by Van der Lelij (2013) was used. Several classification and tectonic discrimination diagrams were applied, including the TAS (Total Alkali-Silica) diagram by Le Maitre (1982), the AFM (Al_2O_3–FeO–MgO) diagram, and the alkalinity and aluminosity diagrams by Maniar and Piccoli (1989). Additionally, the tectonic discrimination diagram by Pearce (1976), the immobile element ratio diagram by Winchester and Floyd (1976), and the R1–R2 diagrams proposed by De la Roche (1980) and Batchelor et al. (1984) were employed. Trace element relationships such as Th–Ta–Hf/3 (Wood, 1980) and Th vs. Co (Hastie et al., 2007) were also analyzed to gain insights into the magmatic evolution and geodynamic setting of formation.

3 Results and Discussion

3.1 Petrography of the El Verdalito Granodiorites

Through petrographic examination of thin sections from samples GVM-101, GVM-102, GVM-103, and GVM-104 under the microscope, it has been determined that all samples exhibit minerals with slight variations in the modal percentages of quartz, orthoclase, and plagioclase. See Table 1. The samples contain 22.5% or less of mafic (dark colored) minerals, classifying them as felsic. The average Color Index (CI) is estimated to be below 25%, thus the rock is inferred to be leucocratic. According to the classification of Le Bas et al. (1991), the samples classify the rock as a granodiorite (Fig. 1).

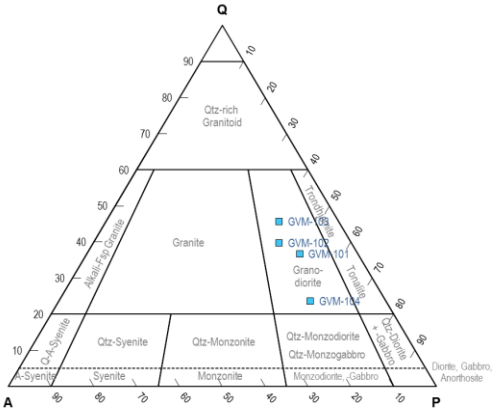

Figure 1. Modal APQ ternary classification diagram for plutonic rocks (Le Bas et al., 1991).

The observed modal variations indicate that the igneous body exhibits mineralogical—and possibly chemical—heterogeneities at different spatial scales within its emplacement. These differences could be related to local fluctuations in crystallization conditions, such as temperature, pressure, and magma chemistry, as well as to subsequent processes involving fluid interaction and magmatic differentiation.

Table 1. Modal percentages of thin sections taken from the El Verdalito Granodiorite.

Sample	GVM-101	GVM-102	GVM-103	GVM-104
Quartz (Qtz)	28.50	33.40	39.30	20.80
Orthoclase (Or)	10.50	12.30	8.60	12.20
Microcline (Mc)	0	1.80	3.30	3.30
Plagioclase (Pl)	38.50	36.40	34.80	51.60
Muscovite (Ms)	9.50	10.30	3.60	5.90
Biotite (Bt)	5.0	1.50	3.50	1.20
Zircon (Zr)	0	0	0	0.50
Chlorite (Chl)	2.50	0	1.70	1.0
Sericite (Se)	1.0	0.30	0	1.60
Epidote (Ep)	4.0	3.50	3.40	2.30
Hornblende (Hb)	0	0	0	2.0
Opaques (Op)	0.50	0.50	1.80	0.60

Regarding the observed textures, perthites (Fig. 2a) and antiperthites were identified. According to Winter (2001), the characteristic texture of granitic rocks is indicative of exsolution and suggests fluctuations in magma crystallization temperature— a typical feature of rocks formed through slow cooling under plutonic conditions. Along the same lines, myrmekites (Fig. 2b) were identified by their vermicular intergrowth of quartz within acidic plagioclase crystals. Additionally, Castro (2015) infers that changes in temperature, pressure, and/or magma composition during crystallization and progressive undercooling result in variations in the proportions of albite and anorthite as the crystal grows, leading to zoning in plagioclase (Fig. 2c).

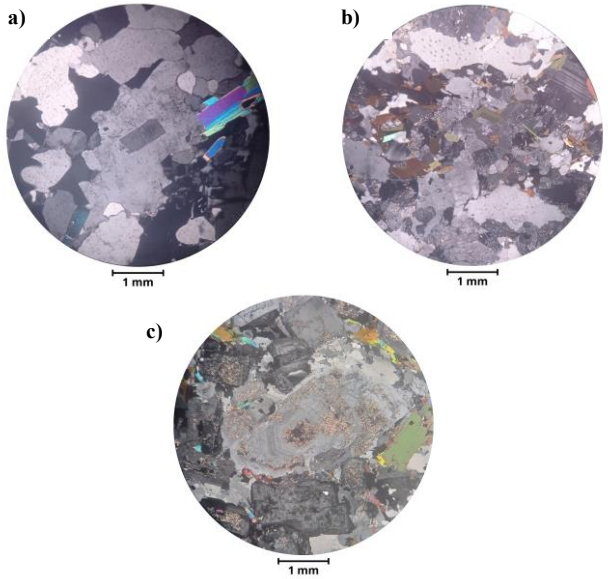

Figure 2. Microphotographs of the El Verdalito Granodiorite. 4x objective. a) Sample GVM-101. Perthitic texture, resulting from cooling below the solvus curve. Poikiloblastic texture, indicating recrystallization processes either metamorphic in nature or related to the crystallization sequence of phenocrysts. b) Sample GVM-103. Myrmekitic texture, generated by the intergrowth of quartz and plagioclase, associated with post-magmatic reactions. c) Sample GVM-103. Zoned plagioclase texture, resulting from variations in albite and anorthite proportions during crystallization. Secondary sericitization texture affecting both alkali feldspars and plagioclase.

In most of the thin sections examined, a prominent poikilitic texture (Fig. 2a) was observed. This texture results from varying nucleation and growth rates of crystal nuclei, which dictate the order of crystallization. It is established that if one mineral species encapsulates another, it must have crystallized first. This term is also associated with metamorphic processes related to mineral adjustments in a recrystallization environment influenced by pressure and temperature fluctuations.

Moreover, the analyzed samples display a holocrystalline degree of crystallinity, indicating complete crystallization, with no residual glass material present. This characteristic suggests progressive cooling without significant interruptions, aligning with the phaneritic texture noted in the medium- to coarse-grained crystals. The serial inequigranularity, wherein grains of varying sizes coexist, indicates non-uniform crystallization, potentially arising from fluctuations in magmatic input or environmental conditions during cooling. Consequently, phenocrysts exhibit a hypidiomorphic form, developing subhedral habits, a typical feature of magmas that experience multiple stages of crystallization, indicating that certain crystals had extended growth periods prior to final solidification.

Additionally, the rock has undergone substantial hydrothermal alterations, evidenced by secondary textures such as chloritization, saussuritization, and sericitization (Fig. 2c) within the plagioclase, orthoclase, and microcline. Best (2003) suggests that during post-magmatic stages, the granodiorite was subjected to hydrothermal fluids enriched in volatile elements, likely sourced from the crystallization process of the magma or from adjacent intrusions. This alteration has not only transformed the primary mineralogy but has also enhanced the diversity of mineral phases present, including sericite, chlorite, and epidote.

Furthermore, the photomicrograph in Fig. 3 illustrates a hornblende crystal with scalloped edges, indicative of an incomplete habit, suggesting a peritectic replacement process. This edge morphology is characteristic of the partial dissolution of the original mineral under unstable conditions within the system, possibly due to variations in pressure, temperature, or the chemical composition of the magma.

The hornblende mineral is surrounded by biotite, muscovite, and plagioclase, indicative of environments where magmatic differentiation processes or interactions with residual fluids occur. This phenomenon contributes to the mineralogical diversification of the igneous body and reflects changes in crystallization conditions during the emplacement of the pluton.

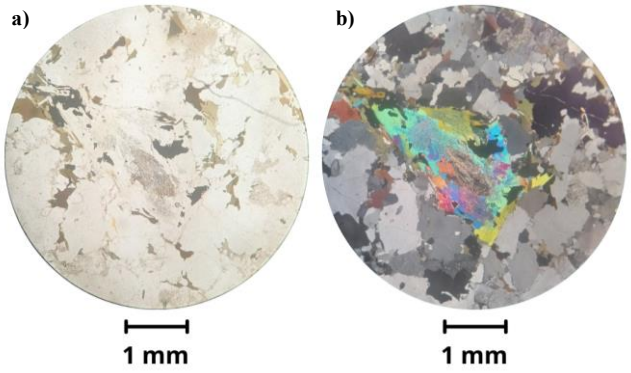

Figure 3. Microphotograph of the El Verdalito Granodiorite. 4x objective. Sample GVM-104. Evidence of peritectic replacement of hornblende by biotite due to partial system instability

As previously stated, this type of reaction is common under metamorphic conditions or during the later stages of magmatic crystallization. This may indicate modifications in the physical and chemical conditions as temperature de-

creases or changes in the chemical composition of the system that favor the formation of micas over hornblende. Furthermore, hornblende may react with a water-rich fluid phase to produce micas under the moderate temperature conditions characteristic of metamorphism.

3.2 Geochemistry of the El Verdalito Granodiorite

According to the geochemical data from the Andes in Mérida provided by Van der Lelij (2013), the El Verdalito granodiorite, coded as 08VDL03, contains 64.89 wt% SiO_2, classifying it as an intermediate-composition rock with a low to moderate content of mafic minerals and a slightly felsic character.

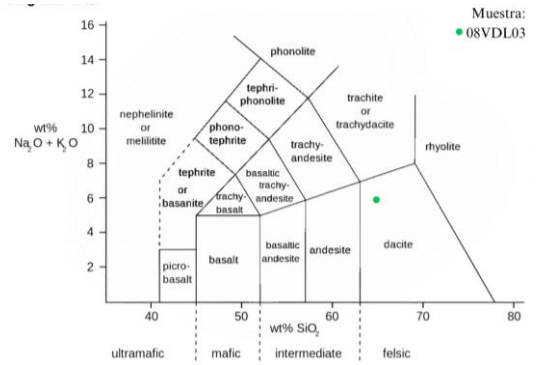

Figure 4. TAS diagram (Le Maitre, R. W., 2002). Sample source: Van der Lelij (2013).

Initially, the TAS (Total Alkali-Silica) diagram by Le Maitre (1982) places the sample within the dacite field, with a tendency toward andesitic composition (Fig. 4), suggesting magmatic evolution from a more mafic parental source. The silica enrichment observed in the sample is indicative of advanced differentiation, consistent with a subduction-related environment, where magmas typically follow a calc-alkaline trend, as further confirmed by analysis using the AFM (Al_2O_3–FeO–MgO) diagram.

The AFM diagram, used to discriminate between calc-alkaline and tholeiitic magmas, reinforces the calc-alkaline classification of the granodiorite (Fig. 5), which is typical of volcanic arc magmas generated in subduction zones. This process involves the early crystallization of mafic minerals, which increases the silica content in the residual magma and promotes the formation of intermediate to felsic rocks, such as the igneous body in question.

Continuing with the classification, the alkalinity and aluminosity indices were analyzed, yielding values of A/NK = 1.75 and A/CNK = 1 (Fig. 6), placing the rock in the metaluminous field with a trend toward peraluminous composition. This indicates a balanced relationship between aluminum oxides and alkalis. A metaluminous composition is common in subduction-related magmas that have undergone slight crustal enrichment, suggesting that the parental magma interacted with crustal materials during its ascent.

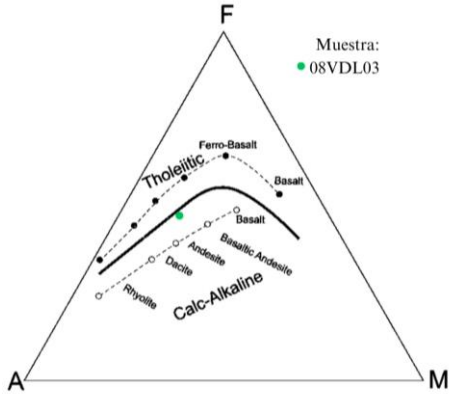

Figure 5. AFM diagram showing the line separating tholeiitic and calc-alkaline fields (Irving et al., 1971). Sample source: Van der Lelij (2013).

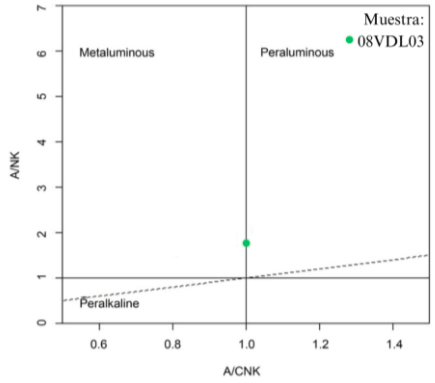

Figure 6. A/CNK–A/NK. Shand's Alumina Saturation Index (molecular Al/(Ca+Na+K)) versus the Alkali Saturation Index (molecular Al/(Na+K)) (Maniar, P. D., et al., 1989). Sample source: Van der Lelij (2013).

Additionally, in the Winchester and Floyd (1976) diagram—based on immobile element ratios such as Nb/Y versus SiO_2—the sample plots at the transition between dacite and rhyodacite, see Fig. 7. This positioning suggests that the El Verdalito granodiorite represents a magma that has undergone significant evolution from an andesitic composition, accumulating silica and transitioning toward felsic compositions.

To refine the tectonic interpretation, FeO, MgO, and $CaO–Al_2O_3$ ratios were analyzed using the Jensen (1976) diagram, which places the El Verdalito granodiorite in the calc-alkaline field, specifically within the andesite zone. This supports the intermediate nature of the rock and confirms its association with a subduction-related environment, where calc-alkaline magmas are predominant.

To better constrain the tectonic setting, the Pearce (1976) and Wood (1980) diagrams—focused on immobile element ratios such as Th–Ta and Th–Hf/3 (see Fig. 8)—confirm that the origin of the igneous body is associated with a volcanic arc. According to Polat (2006), these immobile elements are not significantly altered by post-magmatic

processes, thus preserving the original geochemical signature of the tectonic environment, validating the association with magmas generated in subduction zones.

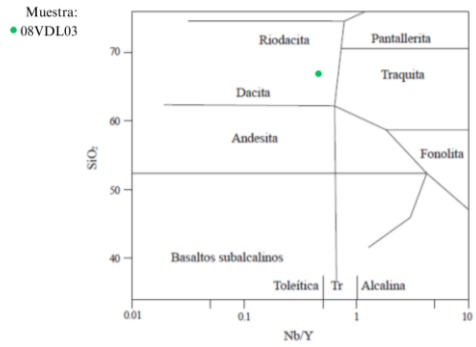

Figure 7. Winchester and Floyd diagram (1976). Immobile element ratios (Rb, Zr, Ti, Y) versus SiO_2. Sample source: Van der Lelij (2013).

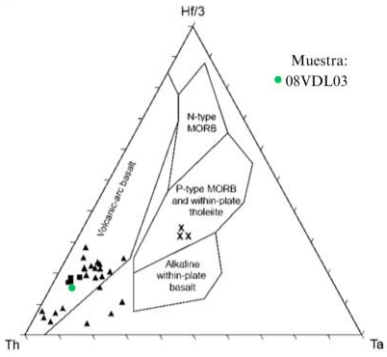

Figure 8. Th–Hf/3–Ta ternary diagram for tectonomagmatic classification (Wood, D. A., 1980). Sample source: Van der Lelij (2013).

Finally, the R1–R2 diagram used to determine the tectonic setting, following De la Roche (1980) and Batchelor et al. (1984), places the granodiorite in a pre-collisional tectonic context. Fig. 9. This result suggests that the parental magma originated during an early stage of tectonic convergence, prior to full plate collision. This phase of high tectonic compression allowed magma ascent and facilitated deep cooling and crystallization, as noted by Best (2003).

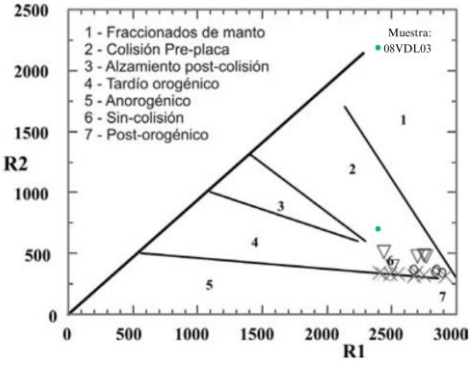

Figure 9. Diagram for tectonic setting discrimination (Batchelor et al., 1984). Sample source: Van der Lelij (2013).

4 Conclusion

4.1 Petrogenesis and tectonic context of the El Verdalito Granodiorite

The El Verdalito granodiorite is the result of a complex magmatic evolution in a subduction setting influenced by the tectonic interaction between the Caribbean and South American plates. Petrographic analyses have revealed characteristic textures indicative of crystallization processes under fluctuating thermal and chemical conditions. These textures suggest solidification in a dynamic context, likely due to the injection of new magmatic pulses and interaction with metasomatic fluids, which altered the original conditions of the magma.

From a geochemical perspective, the parental magma displays an intermediate, calc-alkaline composition, having evolved through fractional crystallization and prolonged differentiation during its ascent through the continental crust. This process led to the formation of a high-potassium, metaluminous rock, typical of arc magmatic environments associated with subduction zones.

The pre-collisional tectonic setting provides a comprehensive explanation for both the magmatic and tectonic evolution of this granodiorite, which exhibits affinity with other igneous bodies in the Venezuelan Andes that display similar evolutionary patterns. In this regard, the El Verdalito granodiorite can be interpreted as part of a regional magmatic cycle, where subduction processes and subsequent tectonic collision have played a fundamental role in generating differentiated magmas and shaping the crust in this region.

4.2 Magma–crust interaction during the ascent and emplacement of the El Verdalito Granodiorite

During the ascent of the El Verdalito granodiorite, a complex interaction occurred between the magma and the Earth's crust. Throughout its magmatic evolution, beginning in a subduction setting, the body underwent chemical and mineralogical changes due to the incorporation of crustal materials, resulting in compositional enrichment and the development of distinct textures. Some of these petrographic features, such as poikilitic texture, reflect modifications in magma composition, leading to the assimilation of crustal elements that, upon partial melting, contributed to its differentiation and textural complexity.

The magma–crust interaction enabled sequential crystallization of minerals, consistent with a prolonged process of fractional differentiation, evidenced by plagioclase zoning and the late-stage appearance of mineral phases such as hornblende and micas. These findings underscore how the dynamic interaction between magma and crust played a crucial role in the chemical and textural evolution of this igneous body, closely tied to the long-standing tectonic subduction activity in the region.

4.3 Post-magmatic alteration stage of the El Verdalito Granodiorite

The post-magmatic alteration stage of the El Verdalito granodiorite is characterized by a series of mineralogical transformations reflecting the interaction of the rock with hydrothermal fluids under cooling conditions. These alterations include processes such as sericitization of plagioclase, chloritization of biotite, and saussuritization of plagioclase, which indicate a history of exposure to fluids rich in volatile elements. Sericitization reflects potassium incorporation during late-stage alteration, while chloritization suggests the progressive replacement of mafic minerals by more stable phases in a decreasing-temperature environment.

These post-magmatic alterations, in addition to modifying the original mineralogy, also provide insights into the cooling environment and geotectonic processes that affected the igneous body after its emplacing. The diversity of secondary mineral phases, such as sericite, chlorite, and epidote, reinforces the notion of an active hydrothermal environment, possibly associated with a fracture system that enabled fluid ingress. Thus, the post-magmatic alteration stage adds an important layer of complexity to the evolution of the granodiorite, linking its history to the prolonged tectonic activity in the Venezuelan Andes region.

References

Audemard, F.E., Audemard F.A. (2002). Structure of the Mérida Andes, Venezuela: relations with the South America-Caribbean geodynamic interaction. Tectonophysics, 345,1-4, 299-327.

Bailey, J.C., (1981). Geochemical criteria for a refined tectonic discrimination of orogenic andesites. Chemical Geology, 32. 139-154.

Bass M., Shagam R. (1959). Edades Rb-Sr de las rocas cristalinas de Los Andes merideños, Venezuela. En III Congreso Geológico Venezolano, Caracas, 1, 377-381.

Batchelor, R., Bowden, P. (1984). Petrogenetic interpretation of granitoid rock series using multicationic parameters. Chemical Geology, 48, 43-55.

Bellizzia A., Pimentel N. (1994). Terreno Mérida: Un cinturón alóctono herciniano en la Cordillera de Los Andes de Venezuela. En V Simposio Bolivariano Exploración Petrolera, Caracas, 5, 271-290.

Best, M. G. (2003). Igneous and metamorphic petrology (2nd ed.). Blackwell Publishing.

Burkley, J. (1976). Geochronology and Geochemistry of the Estanques Granite, Venezuela. Journal of the Geological Society of Venezuela, 31, 42-58.

De la Roche H., (1964). Sur l'expression graphique des relations entre la composition chimique et la composition minéralogique quantitative des roches cristallines. Présentation d'un diagramme destiné à l'étude chimico-minéralogique des massifs granitiques ou granodioritiques. Application aux Vosges cristallines. Sciences de la Terre, 9(3), 293-337.

Castro Dorado, A. (2012). Petrografía de rocas ígneas y metamórficas. Servicio de Publicaciones de la Universidad de Huelva.

De la Roche H. (1976). Sur la contribution des données chimiques à une systématique générale des roches ignées, avec, en appendice, "A diagram for a chemical classification of igneous rocks referred to their mineral contents". Sciences de la Terre, 23, 17-35.

De la Roche H. (1978). La chimie des roches présentée et interprétée d'après la structure de leur faciès minéral dans l'espace des variables chimiques. Fonctions spécifiques et diagrammes qui s'en déduisent. Application aux roches ignée. Chemical Geology, 21, 63-87.

De La Roche H., Grandclaude P., Marchal M. (1980). A Classification of Volcanic and Plutonic Rocks Using R1-R2 Diagram and Major Element Analyses Its Relationships with Current Nomenclature. Chemical Geology, 29, 183-210.

González de J. C. (1980). Geología de Venezuela y de sus Cuencas Petrolíferas. Caracas: Foninves.

Grauch R. L. (1972). Preliminary report of a Late (?) Paleozoic metamorphic event in the Venezuelan Andes. Geological Society of America, 132, 465-473.

Irving, T. N. y Baragar, W. R. (1971). A guide to the Chemical classification of the common volcanic rocks. Earth Science, 8, 523-548.

Le Bas, M. J., Le Maitre, R. W., Streckeisen, A., & Zanettin, B. (1991). A Chemical Classification of Volcanic Rocks Based on the Total Alkali-Silica Diagram. Journal of Petrology, 27(3), 745-750. https://doi:10.1093/petrology/27.3.745

Le Bas M.J., Streckeisen A. (1991). The IUGS Systematic of Igneous Rocks. Geological Society London, 148, 825-833.

Le Maitre R. W. (2002). Igneous rocks a classification and glossary of terms. Recommendations of the IUGS subcommission on the Systematics of Igneous Rocks. Cambridge: Cambridge University Press.

Le Maitre, R. W. (1982). Numerical Petrology: Statistical Interpretation of Geochemical Data. Elsevier, 281 pp.

MacKenzie, W. S., Donaldson, C. H., & Guilford, C. (1997). Atlas of Igneous Rocks and Their Textures. Pearson Education, 148 pp.

Maniar, P. D., Piccoli, P. M. (1989). Tectonic discrimination of granitoids. Geological Society of America, 101, 635-643.

Pearce J. A. (1976). Statistical analysis of major element patterns in basalts. Mineral Petrology, 17, 15-43.

Pearce J. A., Norry M. J. (1979). Petrogenetic implications of Ti, Zr, Y, and Nb variations in volcanic rocks. Mineral Petrology, 69, 33-47.

Pearce J. A., Harris N. B. W., Tindle A. G. (1984). Trace element discrimination diagrams for the tectonic interpretation of granitic rocks. Petrololy, 25, 956-983.

Polat A., Kerrich R. (2006). Reading the Geochemical Fingerprints of Archean Hot Subduction Volcanic Rocks: Evidence for Accretion and Crustal Recycling in a Mobile Tectonic Regime. American Geophysical Union Monograph Series, 164, 189-213.

Schubert C. (1969). Geologic structure of a part of the Barinas Mountain front, Venezuelan Andes. Geological Society of America, 80, 3, 443-548.

Streckeisen A. (1967). Classification and nomenclature of igneous rocks. Final report of an inquiry. Mineral, 107, 144-240.

Streckeisen, A. (1976). Classification of the common igneous rocks by means of their chemical composition. Mineral, 1, 1-15.

Streckeisen A., Le Maître R.W. (1979). A chemical approximation to the modal QAPF classification of the igneous rocks. Mineral, Abh., 136, 169-206.

Van der Lelij R., Spikings R., Ulianov A. (2011). From the Rheic Ocean to the Proto-Caribbean Sea in Venezuela: 300 Ma of Magmatism in the Northern Andes. Geophysical Research, 13.

Van der Lelij, R., Spikings, R.A., Gerdes, A., Chiaradia, M., Vennemann T., Mora, A. (2019). Multi-proxy isotopic tracing of magmatic sources and crustal recycling in the Palaeozoic to early Jurassic active margin of NorthWestern Gondwana. Gondwana Research, 66, 227-245.

Van der Lelij, R., Spikings, R.A., Ulianov, A., Chiaradia, M., Mora, A. (2016). Palaeozoic to Early Jurassic history of the northwestern corner of Gondwana, and implications for the evolution of the Iapetus, Rheic and Pacific Oceans. Gondwana Research, 31, 271-294.

Van Der Lelij, R., (2013). Reconstructing north-western Gondwana with implications for the evolution of the lapetus and Rheic Oceans: a geochronological, thermochronological and geochemical study. Tesis de Doctorado para la obtención del título de Doctor en Ciencias, mención Ciencias de la Tierra, Faculté des sciences de l´Université de Geneve, Ginebra, Suiza.

Van der Lelij R. Spikings R.A. Kerr A.C., Kounov A., Cosca M., Chew D., Villagómez D. (2010). Thermochronology and tectonics of the Leeward Antilles: Evolution of the southern Caribbean Plate boundary zone. Tectonics, 29, 6, 1-30.

Winter J. D. (2001). Igneous and Metamorphic Petrology. New Jersey: Prentice-Hall.

Wood D. A. (1980). The application of a Th-Hf-Ta diagram to problems of tectonomagmatic classification and to establishing the nature of crustal contamination of basaltic lavas of the British Tertiary Volcanic Province. Earth Planet Sci, 50, 11-30

Received: *March 21th, 2025*

Accepted: *July 26th, 2025*

Rosales, Rafael: *Assistant Professor at the School of Geological Engineering, Universidad de Los Andes. Geological Engineer. PhD candidate in Applied Economics at Universidad de Los Andes. Research interests: Interaction between quantitative and qualitative variables impacting sustained oil production through econometric models. Lecturer in Petrology, Optical Mineralogy, Igneous-Metamorphic Petrography, Mineral Deposits, Basin Analysis, and Field Geology at the School of Geological Engineering, ULA–Mérida.*

https://orcid.org/0009-0007-5988-9421

Andara, Ángel: *Full Professor at Universidad de Los Andes (ULA). PhD in Geology from the University of Oviedo, Spain. Research interests: Crystal growth, thermodynamics of solid solution–aqueous solution systems, analysis and characterization of crystalline materials, and sorption of contaminant metals on mineral surfaces. Collaborating member of the Crystal Growth and Experimental Water Geochemistry group at the Department of Geology, University of Oviedo, Spain. Email: angel.andara@gmail.com*

https://orcid.org/ 0009-0009-2302-6274

Torres, Gusbel: *Instructor Professor at the School of Geological Engineering, Universidad de Los Andes. Master's degree in Renewable Natural Resources and Environmental Management from Universidad de Los Andes, CIDIAT. Research interests include Renewable Resources and Environmental Management, Soil erosion control, and environmental impacts associated with the oil industry. Professor in the areas of Petroleum Geology, Sedimentology, and Well Logging. Email: gusbel@ula.ve*

https://orcid.org/0009-0004-0015-6184

Gómez, Jessica: *Postdoctoral Fellow at the Laboratory of Palynostratigraphy and Paleobotany, Center for Scientific*

Research and Technology Transfer to Production (CICYTTP), affiliated with the National Scientific and Technical Research Council (CONICET). Ph.D. in Geological Sciences from the National University of San Juan, Argentina. Research lines: Late Ordovician palynostratigraphy of western Gondwana; bio-chemostratigraphic correlations in the Late Ordovician; high-resolution stratigraphic analysis of the South American Paleozoic. Member of the Board of Directors (2025–2027) of the Latin American Association of Paleobotany and Palynology. Email: jcgomez@conicet.gov.ar

https://orcid.org/0000-0003-3104-2716

Maldonado, Maricarmen: *Geological Engineer (Universidad de Los Andes, 2011). Former Wellbore Stability Engineer at PDVSA (Exploration & Production), where she worked on wellbore stability control, well cost analysis, and supervision of well operations (2013–2016). Research interests include wellbore stability and operations, petroleum geology and geochemistry, GIS applications to subsurface studies, and hydrogeochemistry of thermal springs (undergraduate thesis). Email: ing.mcmt@gmail.com*

https://orcid.org/0009-0002-3894-0375

Caraballo, José Alejandro: *Undergraduate student in Petrography at the professional cycle of the School of Geological Engineering, Universidad de Los Andes. Email: jacaraballog@gmail.com*

https://orcid.org/0009-0004-7226-9380

Lujano, José: *Undergraduate student in Petrography at the professional cycle of the School of Geological Engineering, Universidad de Los Andes. Email: jlujano21@gmail.com*

https://orcid.org/0009-0001-6117-494X

Uzcátegui, Francyret: *Undergraduate student in Petrography at the professional cycle of the School of Geological Engineering, Universidad de Los Andes. Email: anakary@ula.ve*

https://orcid.org/0009-0002-2438-2560